DEVELOPMENT OF AN EMPIRICALLY BASED COMPUTER PROGRAM TO PREDICT THE AERODYNAMIC CHARACTERISTICS OF AIRCRAFT. VOLUME I. EMPIRICAL METHODS

Roy T. Schemensky

General Dynamics

Prepared for:

Air Force Flight Dynamics Laboratory

November 1973

NOTICE

When Government drawings, specifications, or other data are used for any purpose other than in connection with a definitely related Government procurement operation, the United States Government thereby incurs no responsibility nor any obligation whatsoever; and the fact that the government may have formulated, furnished, or in any way supplied the said drawings, specifications, or other data, is not to be regarded by implication or otherwise as in any manner licensing the holder or any other person or corporation, or conveying any rights or permission to manufacture, use, or sell any patented invention that may in any way be related thereto.

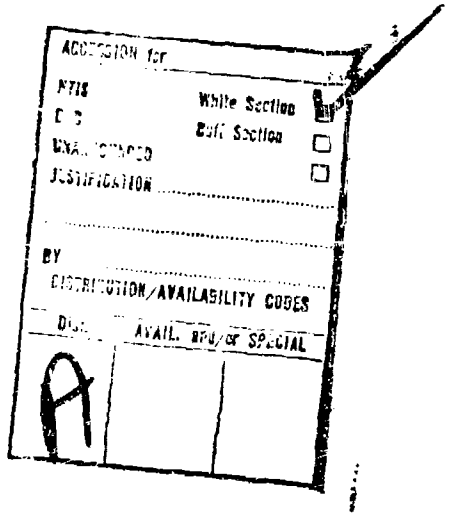

Copies of this report should not be returned unless return is required by security considerations, contractual obligations, or notice on a specific document.

AIR FORCE/56780/5 June 1974 - 200

ib

Unclassified

Security Classification

AD 780 100

DOCUMENT CONTROL DATA - R & D

(Security classification of title, body of abstract and indexing annotation must be entered when the overall report is classified)

1. ORIGINATING ACTIVITY (Corporate author)
Convair Aerospace Division
General Dynamics Corporation
Fort Worth, Texas

2a. REPORT SECURITY CLASSIFICATION
Unclassified

2b. GROUP

3. REPORT TITLE
Development of an Empirically Based Computer Program to Predict the Aerodynamic Characteristics of Aircraft
Volume I: Empirical Methods

4. DESCRIPTIVE NOTES (Type of report and inclusive dates)
Final Report - December 1972 through October 1973

5. AUTHOR(S) (First name, middle initial, last name)
Roy T. Schemensky

6. REPORT DATE	7a. TOTAL NO. OF PAGES	7b. NO. OF REFS
	198	43

8a. CONTRACT OR GRANT NO.	9a. ORIGINATOR'S REPORT NUMBER(S)
F33615-73-C-3043	AFFDL-TR-73-144 Vol. I
b. PROJECT NO. 1476	
c.	9b. OTHER REPORT NO(S) (Any other numbers that may be assigned this report)
d.	

10. DISTRIBUTION STATEMENT
Approved for public release; Distribution Unlimited

11. SUPPLEMENTARY NOTES	12. SPONSORING MILITARY ACTIVITY
	AFFDL/FXM

13. ABSTRACT

This report (Volume I, Emperical Methods) presents the methods, equations, and substantiating data for an empirically based computer program for the rapid and accurate evaluation of the aerodynamic characteristics of large aircraft (bombers, tankers, and transports) from takeoff through landing and through the subsonic, transonic, and supersonic speed regimes. The program calculates lift, moment, and drag characteristics at both low- and high-lift conditions, including the effects of ground proximity during landing and takeoff. The input requires the configuration geometry and the aerodynamic conditions for which solutions are desired. The program includes the capability of analyzing both fixed-wing and variable-sweep-wing configurations as well as the aerodynamic characteristics of the most recent supercritical wing designs. The accuracy of the program is verified through comparisons of the predicted results with experimental data for several configurations. Details of the input and output for this program along with a FORTRAN source deck listing and sample problem are contained in Volume II, Program User Guide. Although this program was developed to handle the bomber, tanker, transport class of aircraft, it is also applicable to fighter type aircraft without maneuver devices.

DD FORM 1 NOV 68 1473

Unclassified

Security Classification

14. KEY WORDS	LINK A		LINK B		LINK C	
	ROLE	WT	ROLE	WT	ROLE	WT
Aerodynamic Characteristics						
Drag Prediction						
Lift Prediction						
Moment Prediction						
High-Lift Prediction						
Computer Program						
Transport Aircraft						
Drag Due to Lift						
Vortex Lift						

*U.S.Government Printing Office: 1974 — 756-435/605

DEVELOPMENT OF AN EMPIRICALLY BASED COMPUTER PROGRAM TO PREDICT THE AERODYNAMIC CHARACTERISTICS OF AIRCRAFT

Volume I Empirical Methods

R. T. SCHEMENSKY

ic

FOREWORD

This report was prepared by the Convair Aerospace Division of General Dynamics Corporation, Fort Worth, Texas, for the Air Force Flight Dynamics Laboratory under Contract F33615-73-C-3043, Project 147601. The work reported here was performed in the period December 1972 through October 1973.

The results of this work are documented in two volumes. Volume I presents the methodology developed in this study; Volume II contains the user manual for a computer program which automates these methods.

The work was accomplished under the direction of Mr. J. Kenneth Johnson of the Air Force Flight Dynamics Laboratory (FXM). The author wishes to acknowledge the valuable assistance of Mr. Eugene L. Crosthwait, Convair Aerospace Division, in the development of the empirical methods for the wing lift and wave drag characteristics.

This technical report has been reviewed and is approved.

Philip P. Antonatos
Chief, Flight Mechanics Division
Air Force Flight Dynamics Laboratory

ABSTRACT

This report (Volume I, Empirical Methods) presents the methods, equations, and substantiating data for an empirically based computer program for the rapid and accurate evaluation of the aerodynamic characteristics of large aircraft (bombers, tankers, and transports) from takeoff through landing and through the subsonic, transonic, and supersonic speed regimes. The program calculates lift, moment, and drag characteristics at both low- and high-lift conditions, including the effects of ground proximity during landing and takeoff. The input requires the configuration geometry and the aerodynamic conditions for which solutions are desired. The program includes the capability of analyzing both fixed-wing and variable-sweep-wing configurations as well as the aerodynamic characteristics of the most recent supercritical wing designs. The accuracy of the program is verified through comparisons of the predicted results with experimental data for several configurations. Details of the input and output for this program along with a FORTRAN source deck listing and sample problem are contained in Volume II, Program User Guide. Although this program was developed to handle the bomber, tanker, transport class of aircraft, it is also applicable to fighter type aircraft without maneuver devices.

TABLE OF CONTENTS

TABLE OF CONTENTS (Cont'd)

TABLE OF CONTENTS (Cont'd)

TABLE OF CONTENTS (Cont'd)

LIST OF FIGURES

LIST OF FIGURES (Cont'd)

LIST OF FIGURES (Cont'd)

LIST OF FIGURES (Cont'd)

LIST OF FIGURES (Cont'd)

LIST OF FIGURES (Cont'd)

LIST OF FIGURES (Cont'd)

LIST OF SYMBOLS

A	Area
AR	Aspect ratio
b	Wing span
C_D	Drag coefficient
C_{D_L}	Drag due to lift
C_{DR}	Drag rise
C_f	Skin friction coefficient
C_f/C	Flap chord to wing chord ratio
C_L	Lift coefficient
C_{L_d}	Wing design lift coefficient
C_{ℓ_d}	Section camber lift coefficient
$C_{L_{DB}}$	Value of C_L for flow separation
C_P	Pressure coefficient
$C_{L_{PB}}$	Value of C_L where drag polar ceases to be parabolic
C_R	Root chord
$\bar{c}$	Mean geometrical chord
C_{L_α}	Lift-curve slope
d	Body diameter
e	Net polar span efficiency
e_o	Wing-body polar span efficiency
e_w	Theoretical wing-alone polar span efficiency
i	Incidence angle
K	Polar shape factor

LIST OF SYMBOLS (Cont'd)

ℓ	Length
M	Mach number
MAC	Mean geometrical chord
M_{CR}	Critical Mach number
R	Leading-edge suction factor
R_N	Reynolds number
S	Surface area
t/c	Wing thickness-to-chord ratio
X	Longitudinal location
Y	Lateral location
Z	Vertical location
α	Angle of attack
β	$\sqrt{M^2-1}$ or $\sqrt{1-M^2}$
ΔC_L	Polar displacement at minimum drag
ΔC_{L_o}	Lift displacement at $\alpha = 0$
Δy	Airfoil leading-edge sharpness parameter
Λ	Sweep angle
λ	Taper ratio
ϕ_{TE}	Airfoil section trailing-edge angle
δ	Deflection
η	Efficiency factor

Subscripts

BT	Boattail
c/4	Quarter-chord

Subscripts (Continued)

c/2	Mid-chord
CG	Center of gravity
e	Effective value or exposed
EXP	Exposed
f	Flap
HT	Horizontal tail
i	Inboard
LE	Leading edge
LER	Airfoil leading-edge radius
MAX	Maximum value
MIN	Minimum value
N	Nose or number of wing panels
o	Zero lift or outboard
PB	Value at $C_{L_{PB}}$
PLAN	Planform
REF	Reference
S	Slat or airfoil surface
s	Exposed airfoil surface
t	Tail surface
TE	trailing edge
WB	Wing-Body
Wet	Wetted area

1. INTRODUCTION

The need for a computer program for performing rapid and accurate evaluation of the aerodynamic characteristics of an aircraft is evident during evaluation of a preliminary design configuration when both time and geometry definition are limited. A quick-response program is also needed for performing preliminary design trade-off studies. This report presents documentation for an empirically based computer program that will predict, with minimum aircraft geometry input requirements, the aerodynamic characteristics of large aircraft (bombers, tankers, and transports) from takeoff and landing through the subsonic, transonic, and supersonic speed regimes.

Some of the methods contained in the AeroModule program (Reference 1) developed at General Dynamics' Convair Aerospace Division, Fort Worth Operation, are utilized in the Large-Aircraft Aerodynamic Prediction Program. The AeroModule program was developed to provide lift and drag estimates for use in a computerized aircraft design synthesis program. The Large-Aircraft program has extended the AeroModule methods to include moment calculations along with improving the methods used to predict lift and drag.

Input to the Large Aircraft program requires the configuration geometry and the aerodynamic conditions for which solutions are desired. Aircraft geometry is represented by a series of component bodies and airfoil surfaces. The geometry input requirements are minimized by use of internally calculated values where possible. Component wetted areas can either be calculated internally from other input or input directly, as desired. The program includes the capability of analyzing both fixed-wing and variable-sweep-wing configurations along with either conventional or supercritical wing designs.

The output from the Large Aircraft program consist of tabulated C_L, C_D, C_m, and angle-of-attack predictions for a given Mach number and altitude or Reynolds number condition. In addition, a breakdown is given of each drag item such as drag rise, wave, friction, base, trim, camber, etc. Also, other aerodynamic parameters such as lift-curve slope, $C_{L_{max}}$, polar-shape factors, wing-body aerodynamic center, etc., are listed. The output format is designed to provide the program user with a quick scan of the significant aerodynamic parameters along with an in-depth look.

The methods, equations, and substantiating data for the Large Aircraft program are presented in the following sections. Details of the input and output of this program along with a FORTRAN source deck listing and sample problems are contained in Volume II, Program User Guide.

Although this program was developed to handle the bomber, tanker, transport class of aircraft, it is also applicable to fighter type aircraft without maneuver devices. The program is referred to throughout the text as the Large Aircraft Program.

2. GEOMETRY

The Large-Aircraft Aerodynamic Prediction Program requires a minimum of input data since most of the geometric parameters used in the aerodynamic methods are calculated internally within the program. Some geometric parameters such as wetted areas and mean geometric chords can be either generated internally by the program or accepted as input data. The conventions and equations used by the Large Aircraft program to determine the geometric parameters used in aerodynamic calculations are described in this section.

2.1 Component Geometry

The basic aircraft geometry is represented by a series of components. The fuselage, canopy, and stores are represented by a series of bodies; the nacelles are represented by another series of bodies (open nosed); and the wing, tail surfaces, pylons, and ventrals are represented by a series of single-panel airfoil surfaces. For cranked or complex wing planforms the wing can also be represented by a series of interconnected surface panels. Provision is also incorporated into the program for computing the geometric parameters for variable-wing-sweep configurations.

2.1.1 Body Geometry

The minimum geometry input requirements for the body components are length, width, height, nose length, and boattail length; in addition, for open-nosed bodies, the inlet and exit area must be specified. If the maximum cross-sectional area of the component, A_{MAX}, is not input, the value is calculated by

$$A_{MAX} = \frac{\pi}{4} \text{ (width x height)} \tag{2-1}$$

Also, if wetted area for the component is not input, a value is then calculated. The wetted area for close-nosed bodies is determined by

$$A_{WET} = \left\{ 2.8\, \ell_N + 2.5 \ell_{BT} \left(1 + \sqrt{\frac{A_{BASE}}{A_{MAX}}}\right) + 4(\ell - \ell_N - \ell_{BT}) \right\} \sqrt{\frac{\pi}{4} A_{MAX}} \tag{2-2}$$

For open-nosed bodies, wetted area is determined by

$$A_{WET} = \left\{2.5\ell_N\left(1 + \sqrt{\frac{A_{INLET}}{A_{MAX}}}\right) + 2.5\ell_{BT}\left(1 + \sqrt{\frac{A_{EXIT}}{A_{MAX}}}\right) + 4(\ell - \ell_N - \ell_{BT})\right\}\sqrt{\frac{\pi}{4} A_{MAX}} \quad (2\text{-}3)$$

2.1.2 Airfoil Surface Geometry

The input required to define the planform for the airfoil surface components that represent surfaces other than the main wing are exposed taper ratio, exposed root chord, and the leading- and trailing-edge sweep angles.

The aspect ratio and the exposed area of each component are calculated by the equations

$$AR_S = \frac{(1-\lambda_S)}{(1+\lambda_S)} \quad \frac{4}{\tan(\Lambda_{LE})_S - \tan(\Lambda_{TE})_S} \quad (2\text{-}4)$$

$$S_{EXP} = \left[(C_R)_S\ (1+\lambda_S)\right]^2 \frac{AR_S}{4} \quad (2\text{-}5)$$

If the component wetted area and mean geometric chord are not input, they are calculated by the equations

$$\bar{c}_S = \frac{2}{3}(C_R)_S\left[1 + \frac{\lambda_S^2}{1+\lambda_S}\right] \quad (2\text{-}6)$$

$$S_{WET} = S_{EXP}\left[2 + .1843(t/c)_S + 1.5268(t/c)_S^2 - .8395(t/c)_S^3\right] \quad (2\text{-}7)$$

The wetted area is essentially twice the exposed area with a small factor to account for thickness.

For trim calculations the location of the horizontal tail quarter-chord point on the MAC is calculated from

$$X_{HT} = \frac{b_{HT}}{6}\left[\frac{1+2\lambda_{HT}}{1+\lambda_{HT}}\right] \tan(\Lambda_{LE})_{HT} + \frac{\bar{C}_{HT}}{4} + (X_{LE})_{HT} \qquad (2\text{-}8)$$

where b_{HT} is the exposed area span of the horizontal tail calculated from $b_{HT} = \sqrt{AR_{HT} \cdot SEXP}$. The moment arm of the tail at any angle of attack is computed from

$$\ell_{HT} = X_H \cos(\Omega - \alpha) \qquad (2\text{-}9)$$

where

$$X_H = \sqrt{(Z_{HT} - Z_{CG})^2 + (X_{HT} - X_{CG})^2}$$

and

$$\Omega = \arctan\left\{\frac{(Z_{HT} - Z_{CG})}{(X_{HT} - X_{CG})}\right\}$$

X_{CG} and Z_{CG} are the longitudinal and vertical locations of the moment reference point and Z_{HT} is the vertical location of the quarter-chord point on the horizontal tail MAC.

2.1.3 Wing Geometry

If the main wing is defined as one panel, the aspect ratio, taper ratio, leading-edge sweep, planform area, and the location of the wing relative to the fuselage are required input to define the planform geometry. The geometry for a complex wing planform is represented as a series of panels, as shown below in the sketch.

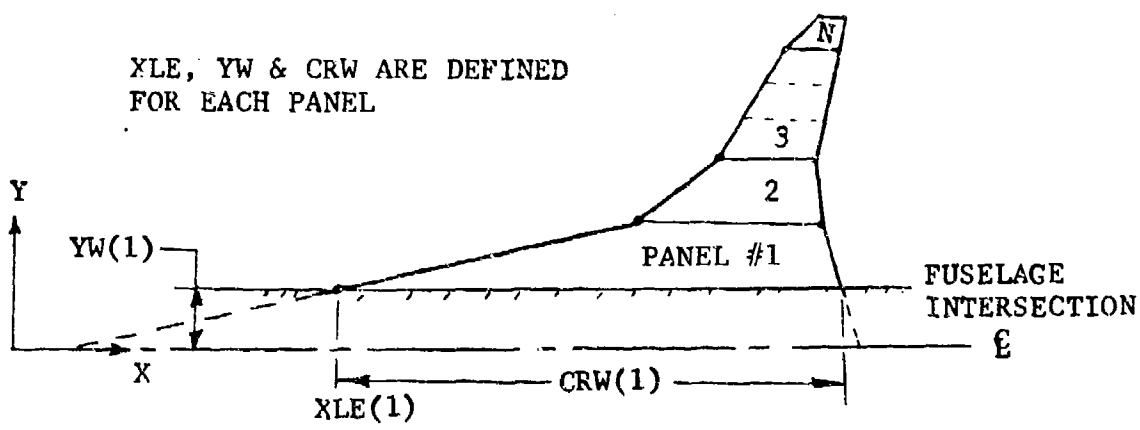

The total wing is defined by up to ten panels. The leading-edge location and chord length of each panel edge is specified along with the average section camber and thickness of each panel. Average values of thickness and camber are computed by the root-mean-square equations

$$t/c = \sqrt{\frac{\sum_N (t/c)_i^2 S_i}{S_{EXP}}} \tag{2-10}$$

$$C_{L_d} = \sqrt{\frac{\sum_N (C_{\ell_d})_i^2 S_i}{S_{EXP}}} \tag{2-11}$$

where $S_{EXP} = \sum_N S_i$ is the sum of the exposed areas of all the panels. Certain aerodynamic calculations, such as wing wave drag and lift-curve slope, require the use of an "equivalent" trapezoidal wing that approximates the planform of the arbitrary wing. The sweep angle of the equivalent wing is obtained by area-weighting the sweep according to the equations

$$(\tan\Lambda_{LE})_e = \frac{\sum_{i=1}^{N} (\tan\Lambda_{LE})_i S_i}{S_{EXP}} \tag{2-12}$$

$$(\cos\Lambda_{c/4})_e = \frac{\sum_{i=1}^{N} (\cos\Lambda_{c/4})_i S_i}{S_{EXP}} \tag{2-13}$$

$$(\cos\Lambda_{c/2})_e = \frac{\sum_{i=1}^{N} (\cos\Lambda_{c/2})_i S_i}{S_{EXP}} \tag{2-14}$$

$$(\tan\Lambda_{TE})_e = \frac{\sum_{i=1}^{N} (\tan\Lambda_{TE})_i S_i}{S_{EXP}} \tag{2-15}$$

If the wing panel wetted areas and mean geometric chord are not input, they are calculated by use of equations similar to Equations 2-6 and 2-7.

For a multiple-panel wing, if the planform area is not input, a value is calculated by summing the panel exposed areas and adding the area obtained by extending the innermost panel to the centerline of the aircraft. In the case of a wing whose innermost panel represents a strake with a large leading-edge sweep angle, extending this panel to the centerline of the aircraft would result in an extremely large planform area. In this case the value of the theoretical planform area of the wing, ignoring the strake, should be input. The aspect ratio is defined as

$$AR = b^2/S_{PLAN} \tag{2-16}$$

Lift and drag parameters are calculated by use of the aspect ratio defined with the wing planform area, and the final results are then referenced to the reference area, S_{REF}, which is input. In most typical cases, S_{PLAN} equals S_{REF}.

2.2 Variable-Sweep Configuration

The planform for a variable-sweep configuration is defined by a trapezoidal movable panel and an optional glove panel, as shown in the sketch below.

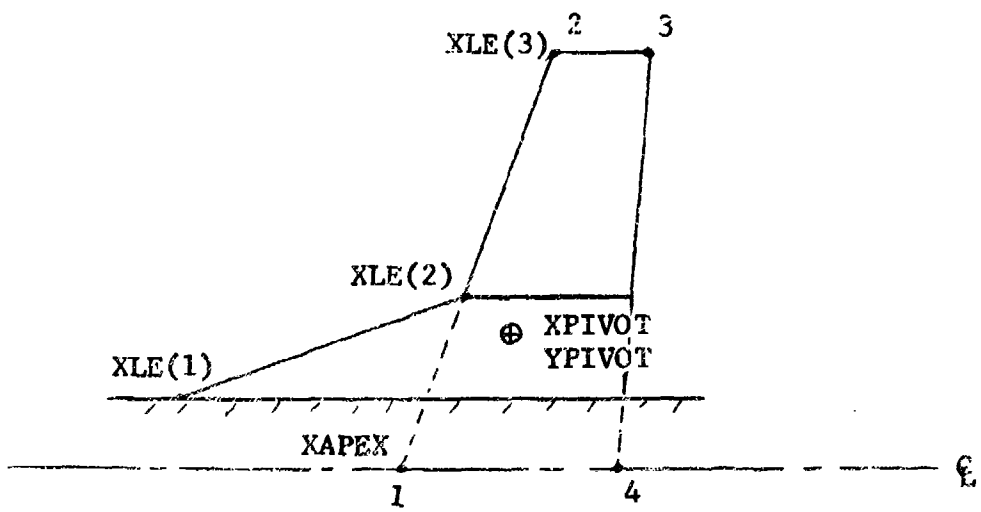

The procedure first defines the coordinates of Points 1, 2, 3, and 4 from the input. (The input planform area is equal to twice the area enclosed by these four points.) When the movable panel is rotated about the pivot point, the resulting geometry is as sketched below. The coordinates of Points 2, 3, 5, and 6 are

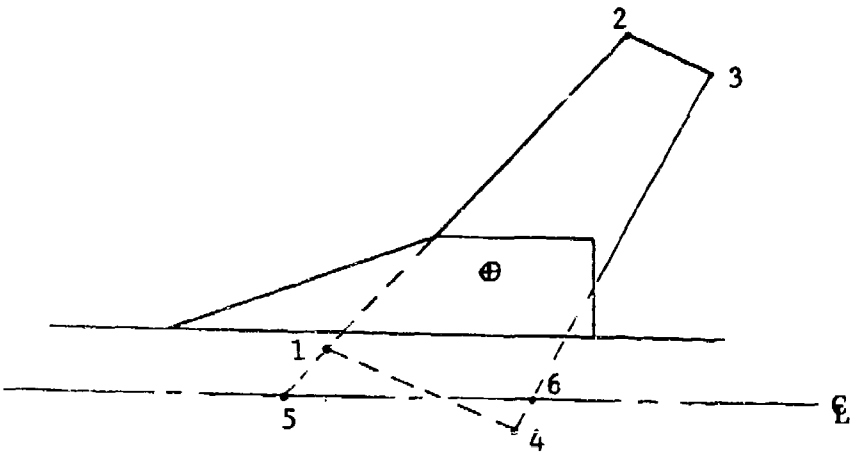

then determined. The planform area is calculated as twice the area enclosed by these four points. Since the tip chord is assumed streamwise at the forward reference sweep, the distance from Point 2 to the centerline is the semi-span, b/2. The aspect ratio is thus defined as

$$AR = b^2/S_{PLAN} \qquad (2\text{-}16)$$

The taper ratio is calculated as

$$\lambda = C_T/C_R \qquad (2\text{-}17)$$

where C_T and C_R are as defined in the following sketch.

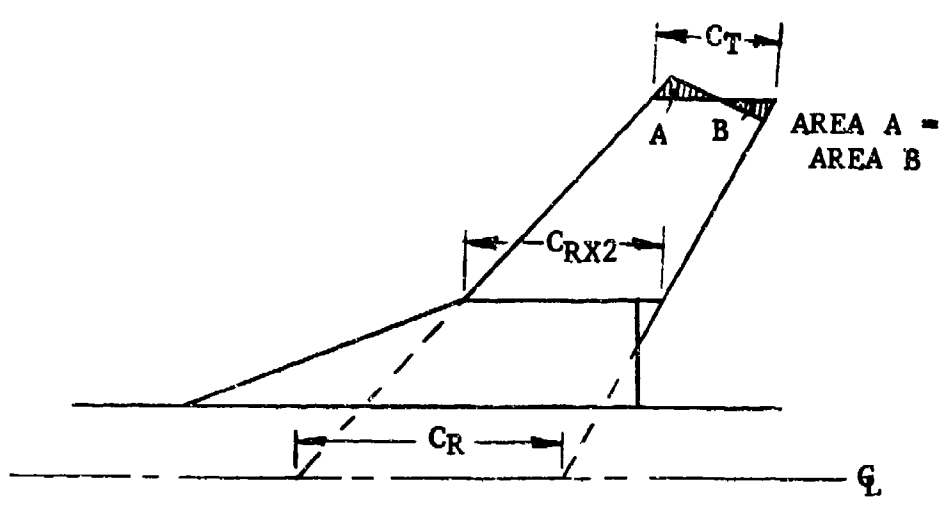

The mean aerodynamic chord (MAC) and wetted area of the outboard panel are calculated by use of the tip chord, C_T, and the chord, C_{RX2}. The $(MAC)_{calculated}$ is expressed for the outboard panel as

$$(MAC)_{calculated} = \frac{2}{3} C_{RX2}\left[1 + \frac{\lambda'^2}{1+\lambda'}\right] \qquad (2\text{-}18)$$

where $\lambda' = C_T/C_{RX2}$. The wetted area $(A_{wet})_{calculated}$ is computed using twice the exposed area of the panel and the thickness correction to wetted area expressed by Equation 2-7. These calculated values for MAC and A_{wet} are compared with the optional input values at the forward reference sweep and the aft reference sweep conditions. If the calculated and input values differ, as might occur for non-trapezoidal planforms, the input values are used and the incremental differences between the two are used for interpolation purposes in the calculation of MAC and A_{wet} at intermediate sweep angles. The equations are as follows:

$$MAC = MAC_{calc.} + \Delta MAC_1 + (\Delta MAC_2 - \Delta MAC_1)\frac{\Lambda - \Lambda_1}{\Lambda_2 - \Lambda_1} \qquad (2\text{-}19)$$

$$A_{wet} = A_{wet_{calc.}} + \Delta A_{wet_1} + (\Delta A_{wet_2} - \Delta A_{wet_1})\frac{\Lambda - \Lambda_1}{\Lambda_2 - \Lambda_1} \qquad (2\text{-}20)$$

where

$$\Delta MAC = MAC_{calc.} - MAC_{input}$$

$$\Delta A_{wet} = A_{wet_{calc.}} - A_{wet_{input}}$$

and where the subscript 1 refers to the forward reference sweep position, and the subscript 2 refers to the aft reference sweep position.

The maximum-thickness sweep angle, $\Lambda_{(t/c)_{max}}$, used in friction drag calculations, is calculated from the quarter-chord sweep of the panel and the input $\Lambda_{(t/c)_{max}}$ at the forward and aft reference sweep positions. The equation is

$$\Lambda_{(t/c)_{max}} = \Lambda_{c/4} + \Delta\Lambda_1 + (\Delta\Lambda_2 - \Delta\Lambda_1)\frac{\Lambda - \Lambda_1}{\Lambda_2 - \Lambda_1} \qquad (2\text{-}21)$$

where

$$\Delta\Lambda = (\Lambda_{c/4})_{calc.} - (\Lambda_{(t/c)_{max}})_{input}$$

The streamwise camber and thickness of the outboard panel at a given sweep are calculated by

$$(C_{L_d})_{calc.} = (C_{L_d})_{ref} \cdot \frac{C'/C}{(C'/C)_{ref}} \qquad (2\text{-}22)$$

$$(t/c)_{calc.} = (t/c)_{ref} \cdot \frac{C'/C}{(C'/C)_{ref}} \qquad (2\text{-}23)$$

where

$$C'/C = 0.5\left\{\frac{\cos\Lambda_{LE}}{\cos(\Lambda_{LE} - \Lambda_{c/2})} + \frac{\cos\Lambda_{TE}}{\cos(\Lambda_{c/2} - \Lambda_{TE})}\right\} \qquad (2\text{-}24)$$

Equation 2-24 is the relationship between the chord perpendicular to the mid-chord sweep, C', and the streamwise chord, C. For a variable-sweep wing, C' remains constant so that the camber and thickness perpendicular to the mid-panel sweep also remain constant. Finally, the outboard panel thickness is compared with the aft reference sweep input value and, if the calculated and input values differ, the input value is used for interpolation

purposes in the calculation of t/c at intermediate sweep angles. The equation is as follows:

$$(t/c) = (t/c)_{calc.} + (\Delta t/c) \cdot \frac{\Lambda - \Lambda_1}{\Lambda_2 - \Lambda_1} \qquad (2\text{-}25)$$

where $(\Delta t/c) = (t/c)_{input} - (t/c)_{calc.}$ at aft sweep.

The variation of wing twist with sweep can be calculated from

$$\tau = \arctan \left(\frac{\Delta Z}{C}\right)_{tip} \qquad (2\text{-}26)$$

where ΔZ is the vertical position of the leading edge (assuming the wing is twisted about the trailing edge) and C is the streamwise chord at the tip in the swept position. The tip displacement is calculated at the forward reference sweep position through the equation

$$(\Delta Z)_{tip} = (C_R \lambda) \tan \tau$$

The streamwise chord at the tip is calculated from

$$C_{tip} = C_R - (b/2)(\tan \Lambda_{LE} - \tan \Lambda_{TE})$$

The tip displacement is assumed to be independent of sweep.

The variation of wing incidence with sweep is calculated from

$$i = i_{ref} \left(1 - \tan \Delta\Lambda_{LE} \cdot \tan \Lambda_{TE_1}\right) \cos \Delta\Lambda_{LE} \qquad (2\text{-}27)$$

where $\Delta\Lambda_{LE} = \Lambda_{LE} - \Lambda_{LE_1}$. In calculating the variations of twist and incidence with wing sweep, it is assumed that the wing pivot is perpendicular to the wing chord plane.

2.3 Airfoil Section Geometry

Several airfoil section parameters are used in the aerodynamic predictions. These parameters are generated internally in the program for the NACA 6-series and 4-digit airfoil sections along with biconvex and supercritical airfoil sections. The procedure determines the leading-edge radius as a function of thickness

ratio, t/c, for these airfoils, as shown in Figure 1. The distance of the position of maximum thickness from the leading edge, $X_{t/c_{max}}$, is listed in Table I. A leading-edge sharpness parameter, Δy, expressed as

$$\Delta y = A(t/c) \tag{2-28}$$

is defined for uncambered airfoils, where A is a function of the airfoil leading-edge geometry (shown plotted in Figure 2.2.1-8 of Reference 2). The trailing-edge angle of the upper surface of the airfoil is computed from

$$\phi_{TE} = B(t/c) + C(C_{\ell_d}) \tag{2-29}$$

A, B, C values used in the Large Aircraft program are listed in Table I.

If the airfoil section cannot be approximated by one of the sections contained within the Large Aircraft program, the user can input geometry to define any arbitrary airfoil section.

Two examples of the designation for a six-series airfoil are given by:

64-210 and
64A210

The 6 for the first digit indicates a 6-series airfoil. The second digit (4) designates the chordwise location (in tenths) of the minimum pressure for the basic symmetric airfoil at zero lift. The third digit (2) designates the camber design lift coefficient (in tenths). The last two digits (10) designate the airfoil thickness (in percent). The letter A appearing in some 6-digit series designations indicates that a modified thickness and camber distribution is used.

An example of the designation for a 4-digit airfoil is given by:

0012-34

where the 12 designates the thickness (in percent chord), the 4 designates the position of maximum thickness (in tenths), and the 3 designates the leading-edge radius (3 designates 1/4 normal, 6 designates normal, and 9 designates 9X normal leading-edge radius).

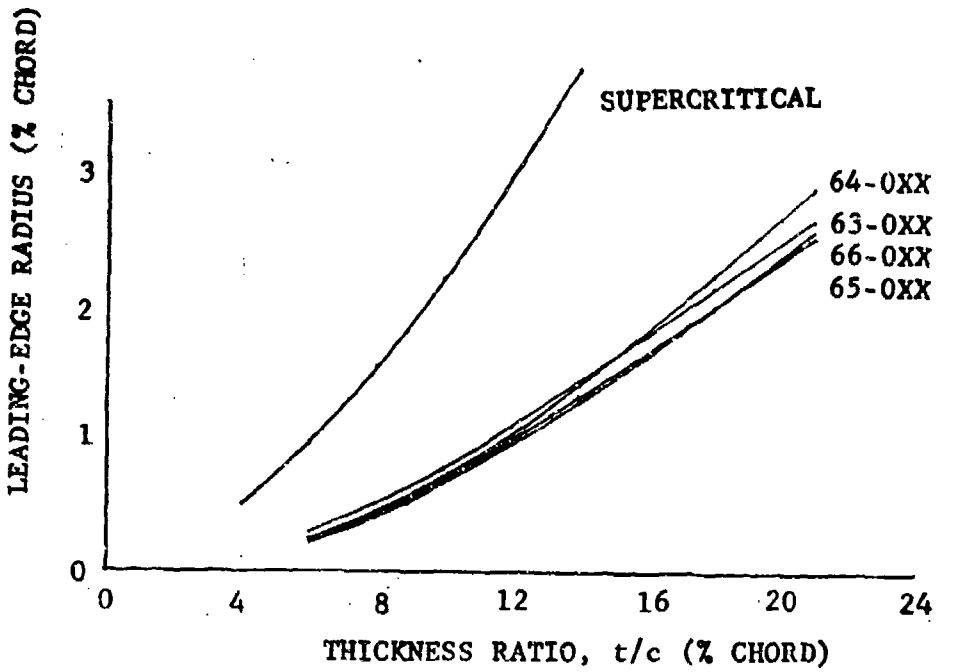

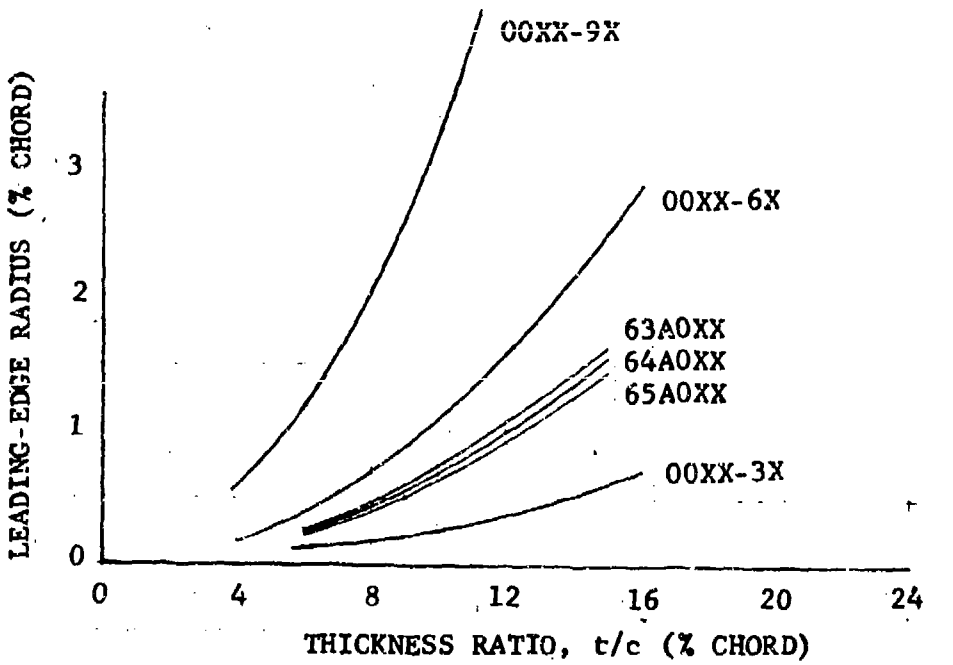

Figure 1 Variation of Leading-Edge Radius with Thickness Ratio of Airfoils

Table 1

TABULATED AIRFOIL SECTION PARAMETERS

Airfoil Type	$X_{(t/c)_{max}}$	A	B	C
63-series	.35	22.0	34.6	14.8
64-series	.375	21.7	38.4	14.8
65-series	.41	19.2	46.4	14.8
66-series	.44	18.35	60.2	14.8
63A	.37	22.0	57.5	14.05
64A	.39	21.2	59.5	14.05
65A	.42	19.2	66.5	14.05
Supercritical	.3471	27.0	30	40.0
Biconvex	.50	11.75	95.0	0.0
00XX-62	.2	24.0	50.0	13.8
-63	.3	24.0	63.0	13.8
-64	.4	22.0	82.8	13.8
-65	.5	20.0	113.0	13.8
-66	.6	20.0	153.0	13.8
-33	.3	19.0	63.0	13.8
-34	.4	17.0	82.8	13.8
-35	.5	15.0	113.0	13.8
-93	.3	29.0	63.0	13.8
-94	.4	27.0	82.8	13.8
-95	.5	25.0	113.0	13.8

3. MINIMUM DRAG

The drag of an aircraft can be represented as the sum of minimum drag, plus drag due to lift, plus drag due to trim. The drag bookkeeping system used in the Large Aircraft program has minimum drag comprised of the drag items that are "assumed" to be independent of lift, such as friction, form, interference, wave, base, camber, roughness and proturberance. Drag due to lift is comprised of the drag items that vary with lift, such as induced drag, profile drag increment due to lift, and flow separation drag. Transonic drag rise, which varies with lift, is separated for bookkeeping purposes into an increment added to minimum drag and an increment added to drag due to lift. In cases where the fuselage has an upswept aft end, the increment in fuselage drag between an upswept fuselage and a symmetrical fuselage is tabulated in the program output as a function of lift. The drag buildup does not include incremental drag contributions due to propulsion installation such as spillage drag, bleed, nozzle effects, etc. In many thrust-drag accounting systems the propulsion related drag increments are included in the propulsion force buildup since these drag increments vary with power setting. If a horizontal tail is present on the configuration, the untrimmed lift and drag is computed for a zero tail deflection condition. The effect of horizontal tail deflection for trim is determined by computing the lift and drag increment relative to the zero tail setting.

The methods used to determine each of the minimum drag contributions and the fuselage aft-end upsweep drag are described in the following subsections. Drag rise, drag due to lift, and trim drag are discussed in Sections 5, 4, and 7, respectively.

3.1 Friction, Form, and Interference Drag

A large part of the subsonic minimum drag is comprised of the sum of friction, form, and interference drag of all the aircraft components. The drag of each component is computed as

$$C_D = \left(C_f \cdot \frac{A_{wet}}{S_{REF}}\right) \cdot FF \cdot IF \qquad (3\text{-}1)$$

where C_f is the compressible flat-plate skin-friction coefficient, A_{wet} is the component wetted area, and FF and IF are the component form and interference factors.

3.1.1 Friction Drag

The flat-plate, compressible, turbulent, skin-friction coefficient is determined from the general equation given in Reference 3,

$$C_f = \frac{1}{F_1} C_{f_i}(R_{N_L} \cdot F_2) \tag{3-2}$$

where F_1 and F_2 are functions of the freestream Mach number and wall temperature. The incompressible skin-friction coefficient, C_{f_i}, is evaluated at the equivalent Reynolds number, $R_{N_L} F_2$. White and Christoph (Reference 3) developed expressions for the transformation functions F_1 and F_2 along with a more accurate explicit equation, based on Prandtl/Schlichting type relations, for computing the incompressible, turbulent, flat-plate friction coefficient (C_{f_i}) with the following results:

$$F_1 = t^{-1} f^{-1}$$

$$F_2 = t^{1+n} f$$

$$C_{f_i} = \frac{0.430}{\left(\log_{10} R_{N_L}\right)^{2.56}}$$

For an adiabatic wall condition, t and f are given by

$$t = T_\infty / T_{aw} = \left[1 + r \frac{\gamma-1}{2} M_\infty^2\right]^{-1}$$

$$f = 1 + 0.044\ r\ M_\infty^2\ t$$

Using a recovery factor r = 0.89 and a viscosity power-law exponent n = 0.67, recommended in Reference 3, results in the following expression for C_f:

$$C_f = t\ f^2 \frac{0.430}{\left(\log_{10}(R_{N_L} \cdot t^{1.67} \cdot f)\right)^{2.56}} \tag{3-3}$$

where

$$t = \left[1 + 0.178\ M_\infty^2\right]^{-1}$$

$$f = 1 + 0.03916\ M_\infty^2 \cdot t$$

The Reynolds number, R_{N_L}, is based either on component length or an admissible surface roughness, whichever produces a smaller value of Reynolds number, as follows:

$$R_{N_L} = \text{minimum} \begin{cases} (R_N/ft) \cdot L \\ K_1 \cdot (L/K)^{1.0489} \end{cases} \quad (3\text{-}4)$$

where

R_N/ft is determined from standard atmospheric tables or is input.
L is the characteristic length of the component.
K is the admissible surface roughness and is an input quantity.

and,

$$K_1 = 37.587 + 4.615M + 2.949M^2 + 4.132M^3$$

For mixed laminar-turbulent flow, transition location is specified for the upper and lower surfaces of the wing. For the laminar portion of the flow, the Blasius skin-friction relation

$$C_f = 1.328/\sqrt{R_{N_{X_r}}} \cdot \left(\frac{C_f}{C_{f_i}}\right)_{\text{Laminar}} \quad (3\text{-}5)$$

where $C_f/C_{f_i} = (1 + 0.1256M^2)^{-.12}$, is used up to the transition point. At the transition point, X_r, the laminar momentum thickness is matched by an iterative process to a turbulent momentum thickness, which begins some fictitious distance, ΔX, ahead of transition. The skin-friction coefficient for the turbulent part of the flow is calculated from Equation 3-3, where the Reynolds number is calculated from

$$R_{N_L} = (\Delta X + L - X_r) \cdot (R_N/ft) \quad (3\text{-}6)$$

The value of C_f with transition is finally given by

$$C_f = \left(\frac{\Delta X}{L} + \frac{L-X_r}{L}\right) C_{f_{Turb.}} \quad (3\text{-}7)$$

Calculated values of C_f versus R_{N_L} are presented in Figures 2 through 7 for mixed laminar-turbulent flow.

3.1.2 Form Factors

The component form factors, FF, account for the increased skin friction caused by the supervelocities of the flow over

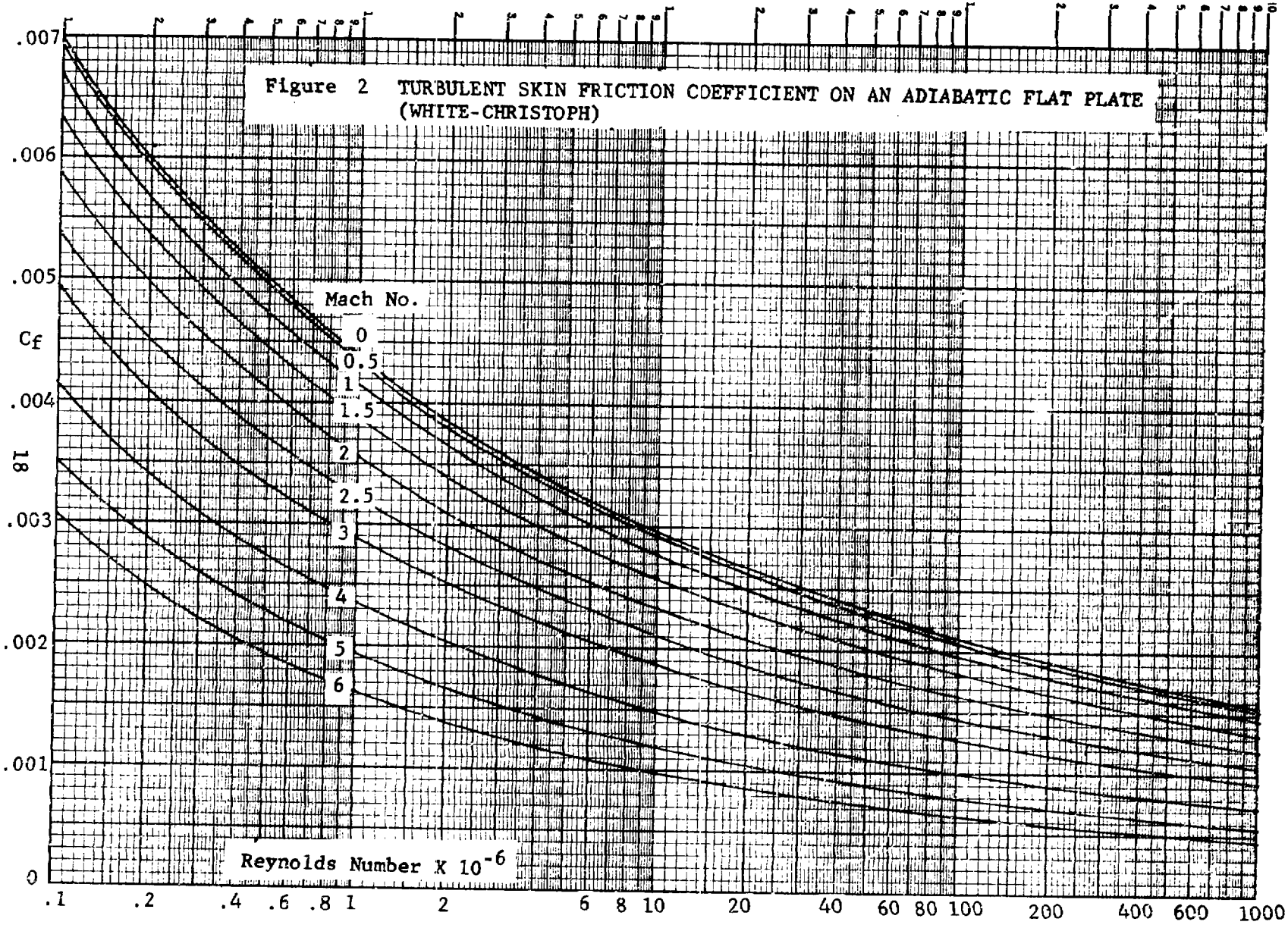
Figure 2 TURBULENT SKIN FRICTION COEFFICIENT ON AN ADIABATIC FLAT PLATE (WHITE-CHRISTOPH)
.007
.006
.005
.004
.003
.002
.001
0
C_f
Mach No.
0
0.5
1
1.5
2
2.5
3
4
5
6
Reynolds Number X 10^{-6}
.1
.2
.4
.6
.8
1
2
6
8
10
20
40
60
80
100
200
400
600
1000

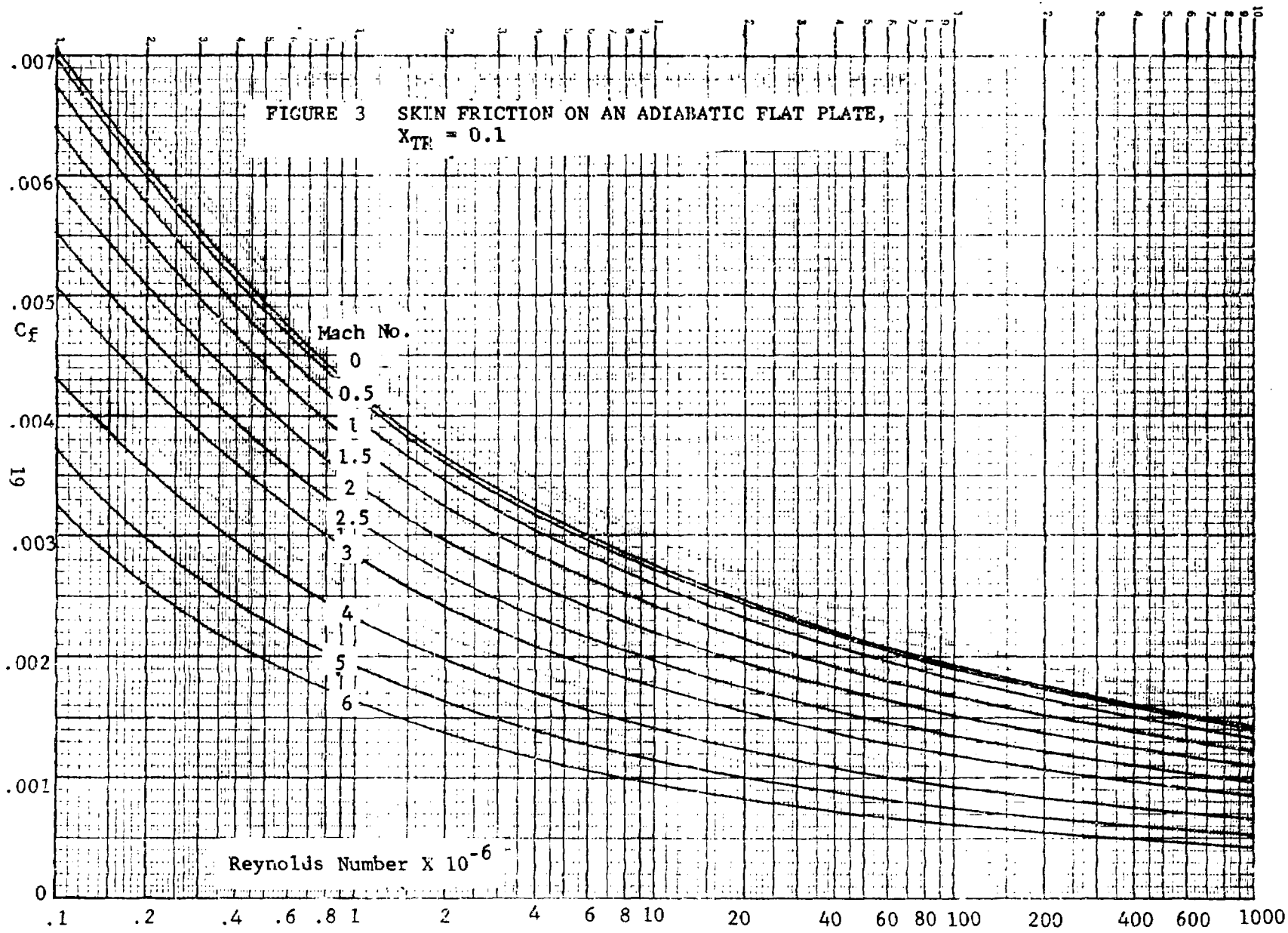

FIGURE 3 SKIN FRICTION ON AN ADIABATIC FLAT PLATE, $X_{TF} = 0.1$

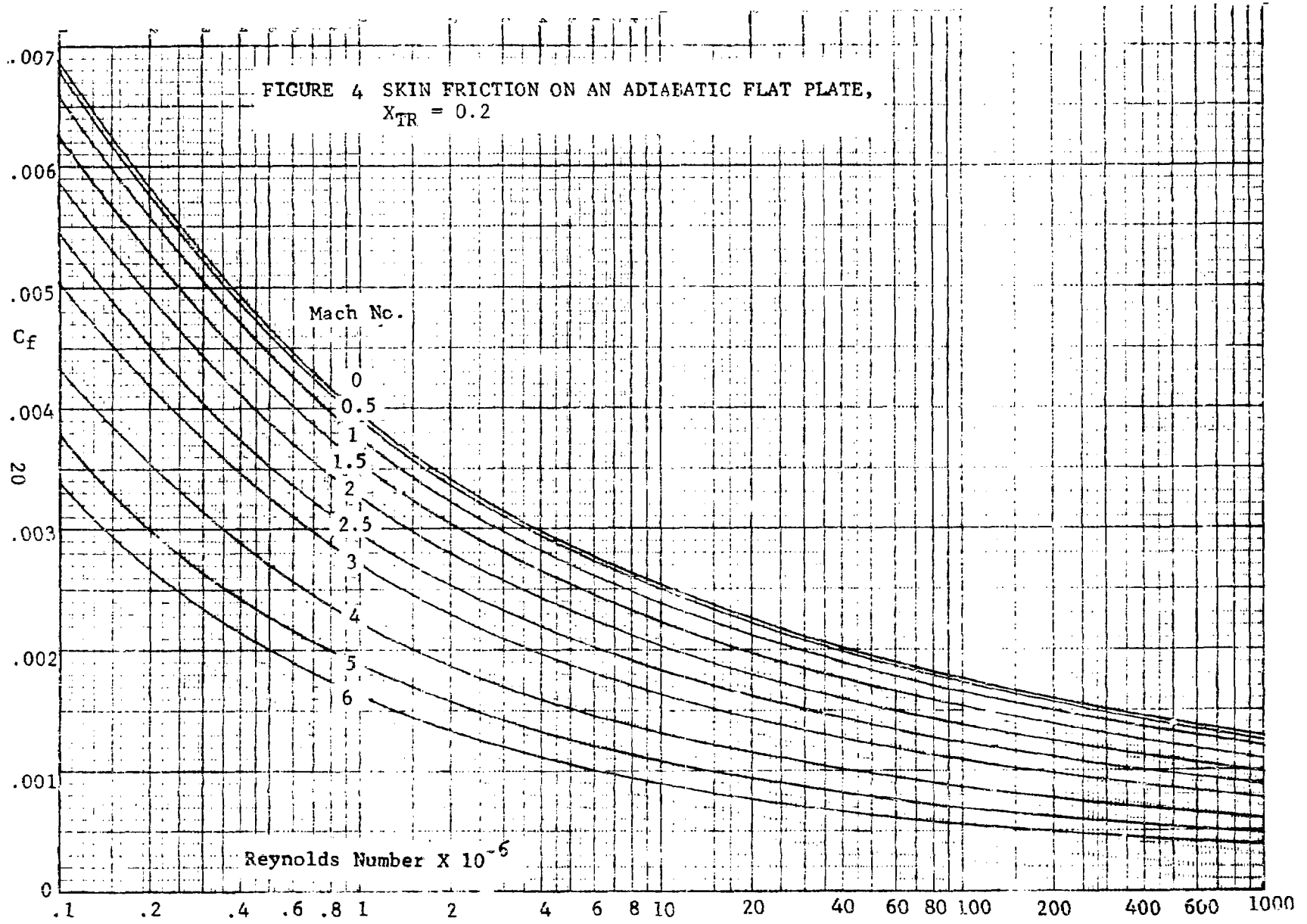
FIGURE 4 SKIN FRICTION ON AN ADIABATIC FLAT PLATE, $X_{TR} = 0.2$
.007
.006
.005
C_f
.004
.003
.002
.001
0
Mach No.
0
0.5
1
1.5
2
2.5
3
4
5
6
Reynolds Number X 10^{-6}
.1
.2
.4
.6
.8
1
2
4
6
8
10
20
40
60
80
100
200
400
600
1000

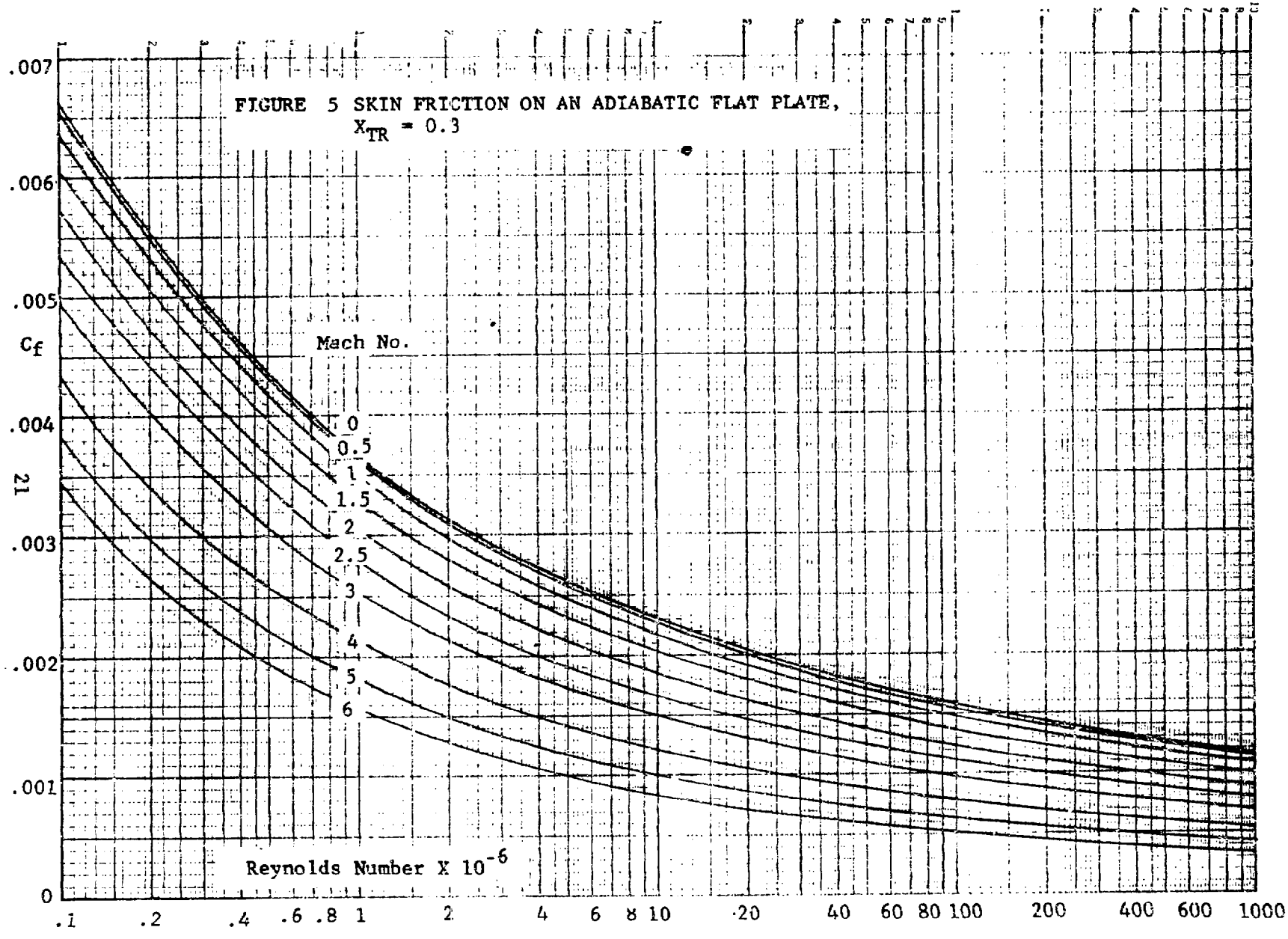

FIGURE 5 SKIN FRICTION ON AN ADIABATIC FLAT PLATE, $X_{TR} = 0.3$

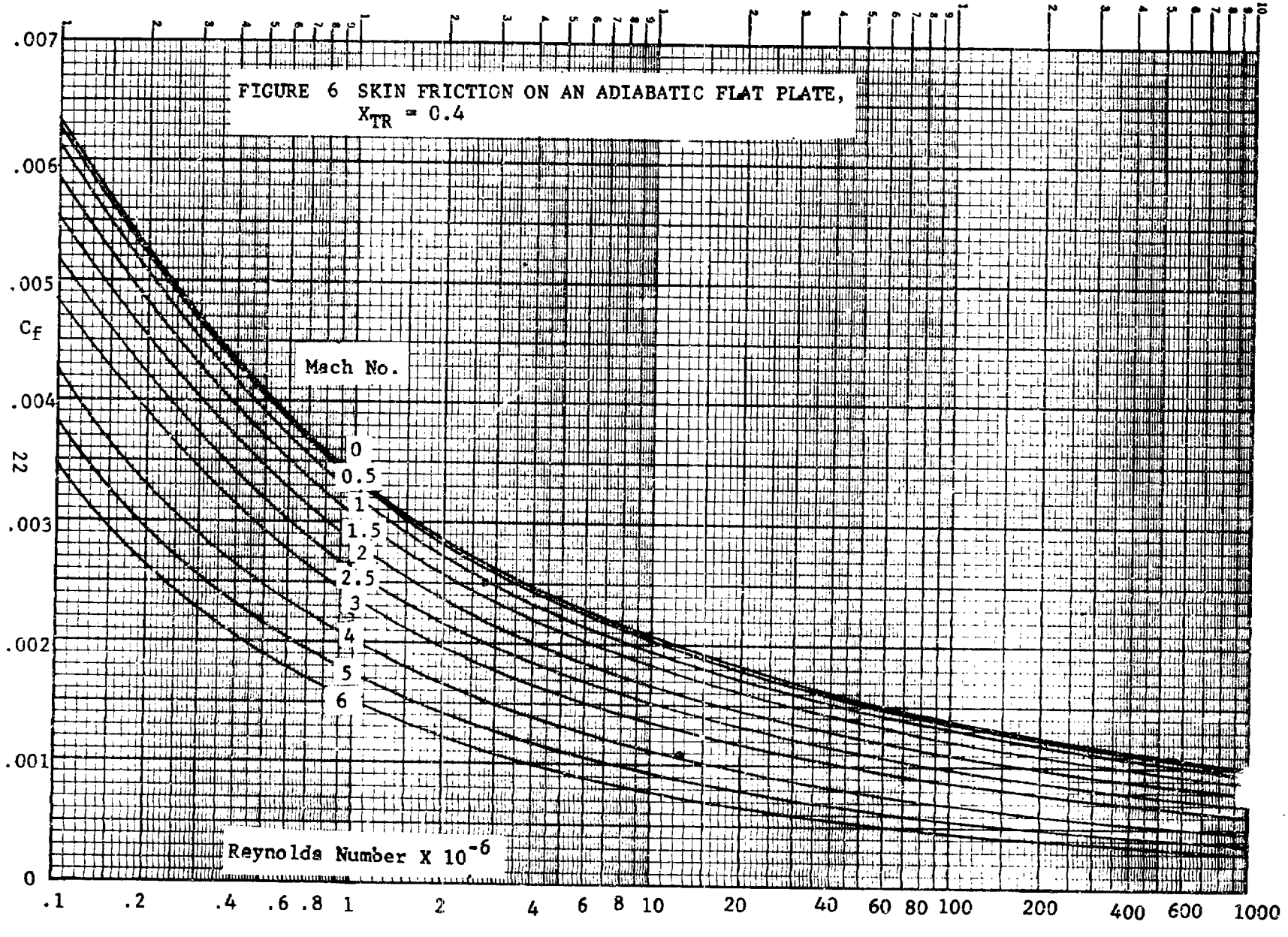
FIGURE 6 SKIN FRICTION ON AN ADIABATIC FLAT PLATE, $X_{TR} = 0.4$
.007
.006
.005
C_f
.004
.003
.002
.001
0
Mach No.
0
0.5
1
1.5
2
2.5
3
4
5
6
Reynolds Number X 10^{-6}
.1
.2
.4
.6
.8
1
2
4
6
8
10
20
40
60
80
100
200
400
600
1000

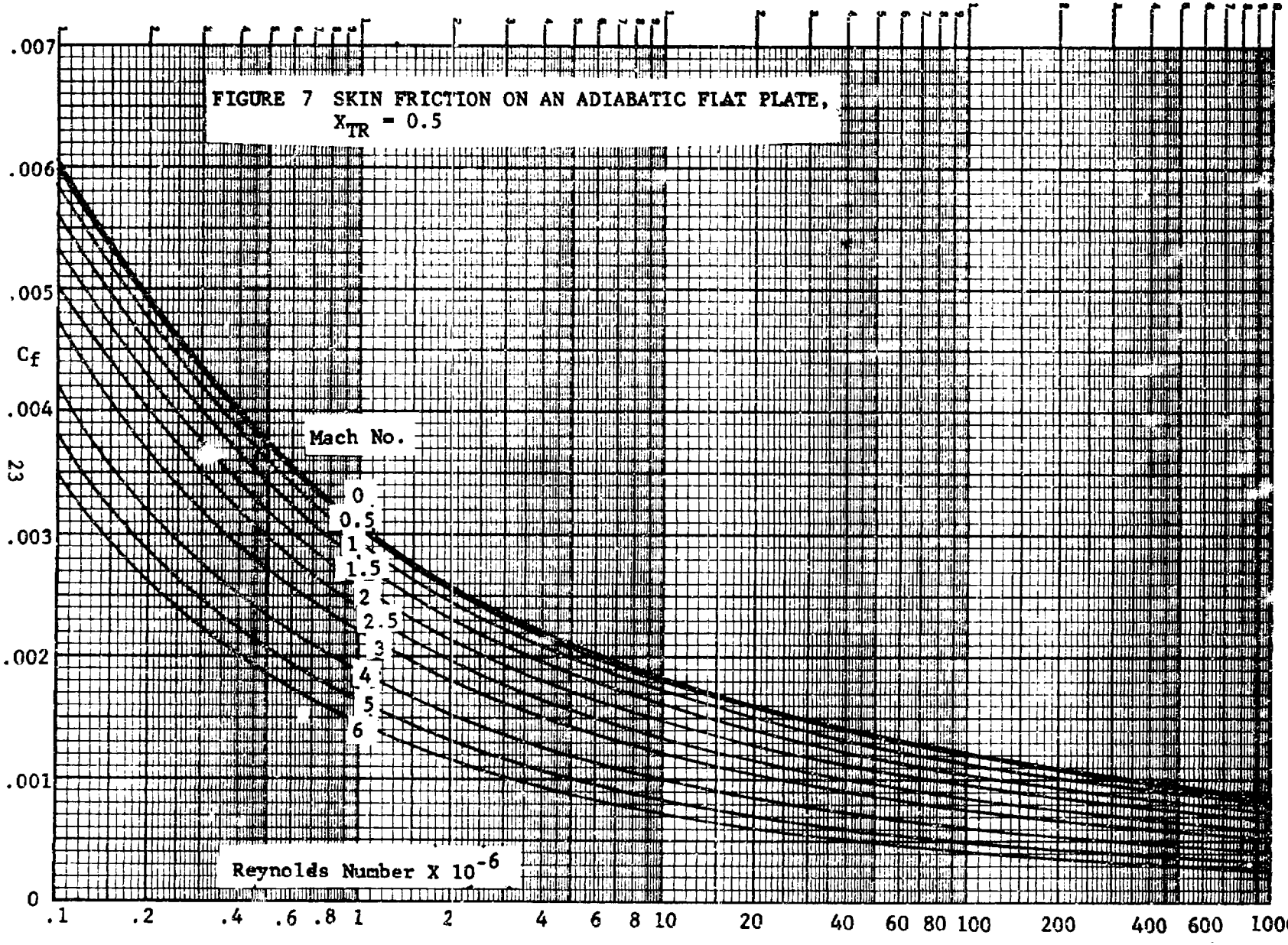
FIGURE 7 SKIN FRICTION ON AN ADIABATIC FLAT PLATE, X_{TR} = 0.5
.007
.006
.005
C_f
.004
.003
.002
.001
0
Mach No.
0
0.5
1
1.5
2
2.5
3
4
5
6
Reynolds Number X 10^{-6}
.1
.2
.4
.6
.8
1
2
4
6
8
10
20
40
60
80
100
200
400
600
1000

the body or surface and the boundary-layer separation at the trailing edge. The form factor for the "body" component is computed as

$$FF = 1 + 60/FR^3 + 0.0025 \cdot FR \qquad (3\text{-}8)$$

where

$$FR = \frac{\text{Component Length}}{\sqrt{\text{Width x Height}}}$$

For "nacelle" components, the form factor is given by

$$FF = 1 + 0.35/FR \qquad (3\text{-}9)$$

Equations 3-8 and 3-9 were obtained from the Convair Aerospace Handbook (Reference 4) and also appear in the DATCOM (Reference 2).

The airfoil form factors depend upon airfoil type and streamwise thickness ratio. For 6-series airfoils, the form factor is given by

$$FF = 1 + 1.44(t/c) + 2(t/c)^2 \qquad (3\text{-}10)$$

For 4-digit airfoils, the form factor is given by

$$FF = 1 + 1.68(t/c) + 3(t/c)^2 \qquad (3\text{-}11)$$

For biconvex airfoils, the form factor is given by

$$FF = 1 + 1.2(t/c) + 100(t/c)^4 \qquad (3\text{-}12)$$

And for supercritical airfoils, the form factor is given by

$$FF = 1 + K_1 C_{l_d} + 1.44(t/c) + 2(t/c)^2 \qquad (3\text{-}13)$$

The factor $K_1 C_{l_d}$ in Equation 3-13 is an empirical relationship which shifts the 6-series form-factor equation to account for the increased supervelocities caused by the supercritical-section design camber C_{l_d}. The factor K_1 (derived from experimental data) is shown plotted in Figure 8 as a function of the Mach number relative to the wing Mach critical. Equations 3-10 and 3-11 were obtained from informal discussions with NASA/LRC personnel; Equation 3-12 appears in both the DATCOM and the Convair Handbook.

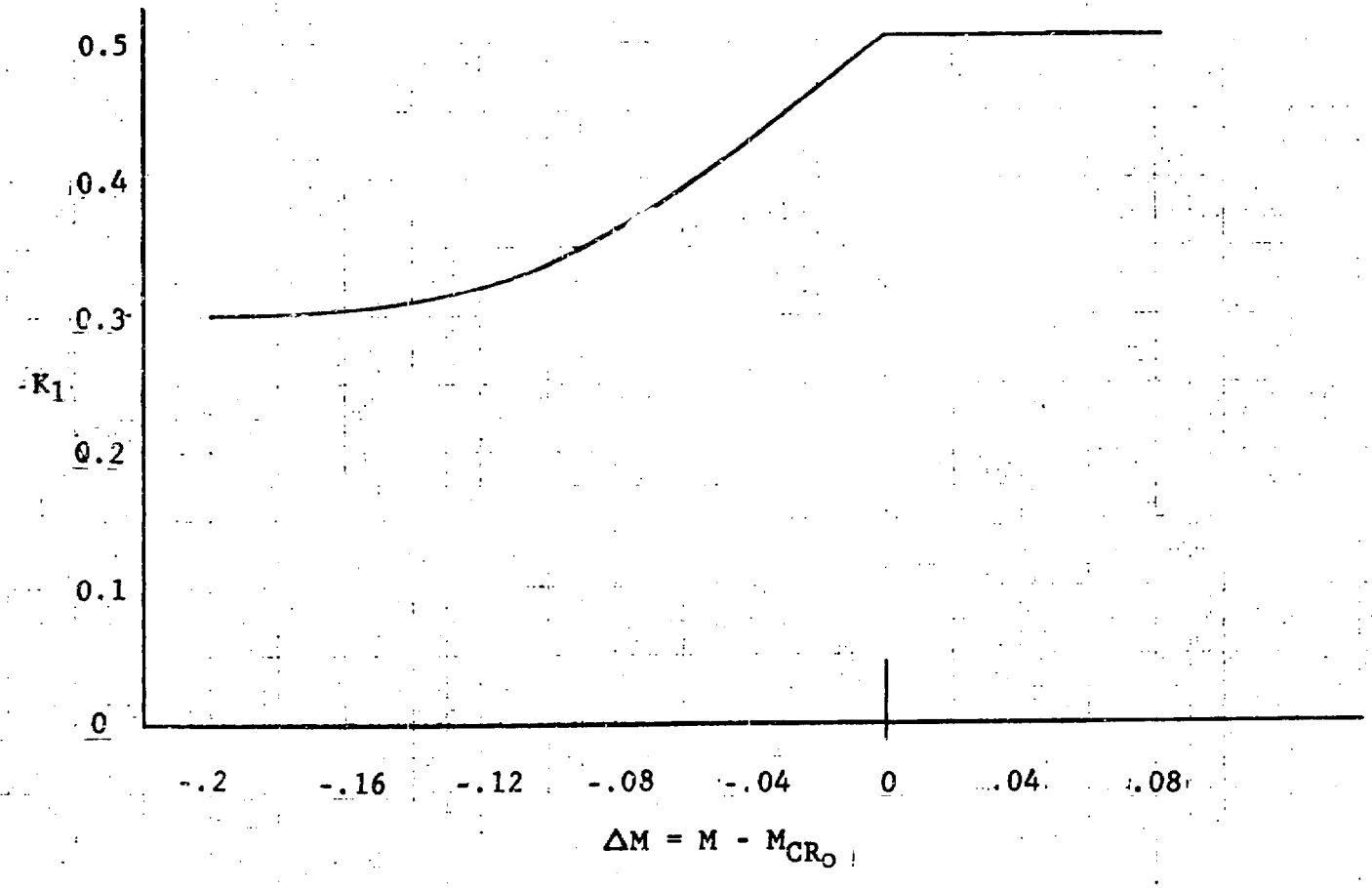

Figure 8 Supercritical Wing Compressibility Factor

3.1.3 Interference Factors

The component interference factors, IF, account for the mutual interference between components. For the fuselage, the interference factor is given by

$$IF = R_{W-B} \tag{3-14}$$

where R_{W-B} is shown plotted in Figure 9 as a function of fuselage Reynolds number and Mach. For other bodies such as stores, canopies, landing gear fairings, and engine nacelles, the interference factor would be an input factor based on experimental experiences with similar configurations. The Convair Aerospace Handbook (Reference 4) recommends using

IF = 1.0 for nacelles and stores mounted out of the local velocity field of the wing

IF = 1.25 for stores mounted symmetrically on the wing tip

IF = 1.3 for nacelles and stores if mounted in moderate proximity of the wing

IF = 1.5 for nacelles and stores mounted flush to the wing or fuselage.

The interference factor for the main wing is computed as

$$IF = R_{LS} \cdot R_{W-B} \tag{3-15}$$

where R_{W-B} is the wing-body interference factor presented in Equation 3-14, and R_{LS} is the lifting surface interference factor presented in Figure 10. For supercritical wings the wing interference factor is set equal to one. Other airfoil surfaces such as horizontal or vertical tails use an interference factor determined by

$$IF = R_{LS} \cdot H_f \tag{3-16}$$

where H_f is the hinge factor obtained from input (use $H_f = 1.0$ for an all movable surface, 1.1 if the surface has a flap for control). The factors R_{W-B} and R_{LS} are plotted in Reference 3 and also appear in the DATCOM.

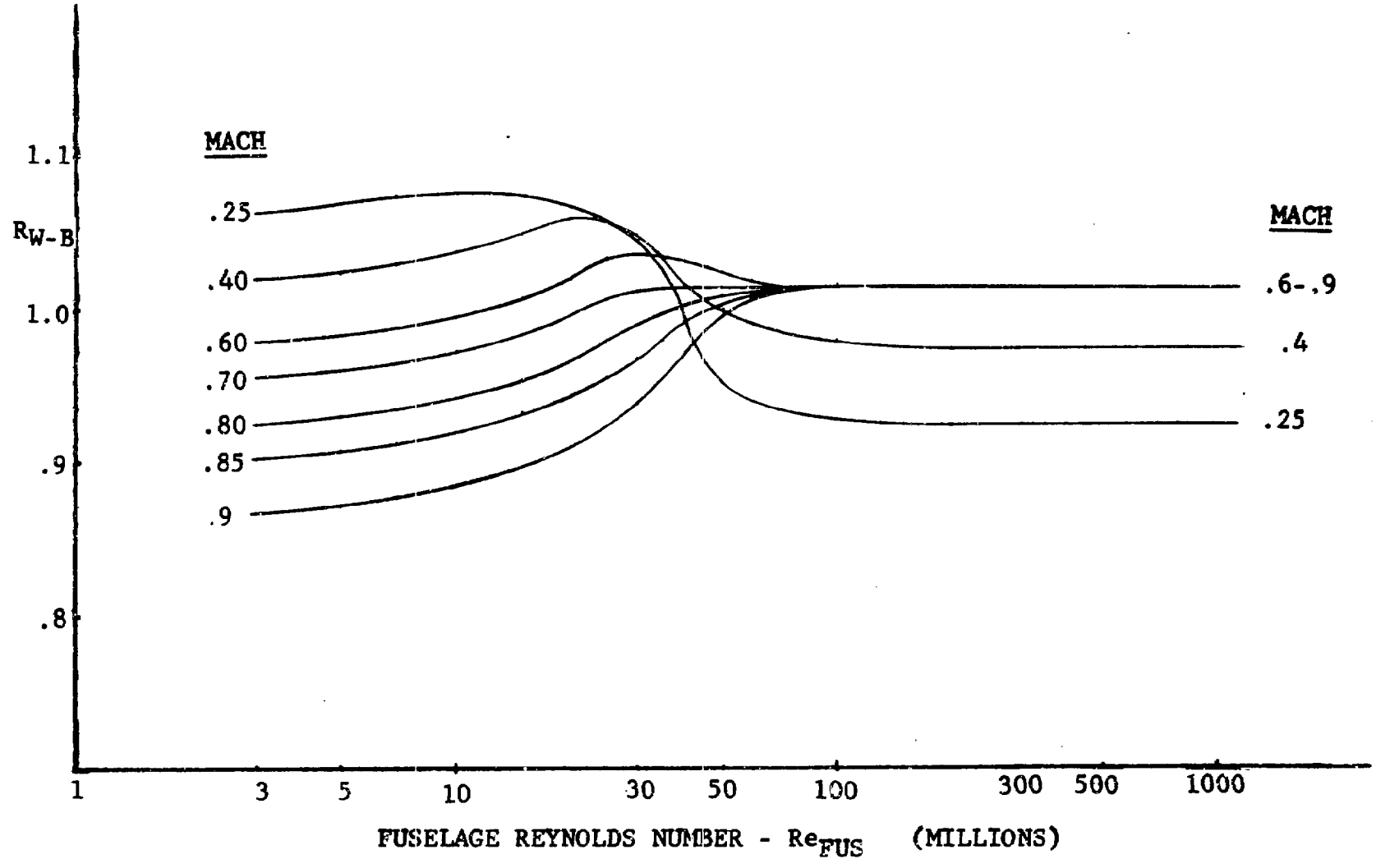

Figure 9 Wing-Body Correlation Factor for Subsonic Minimum Drag

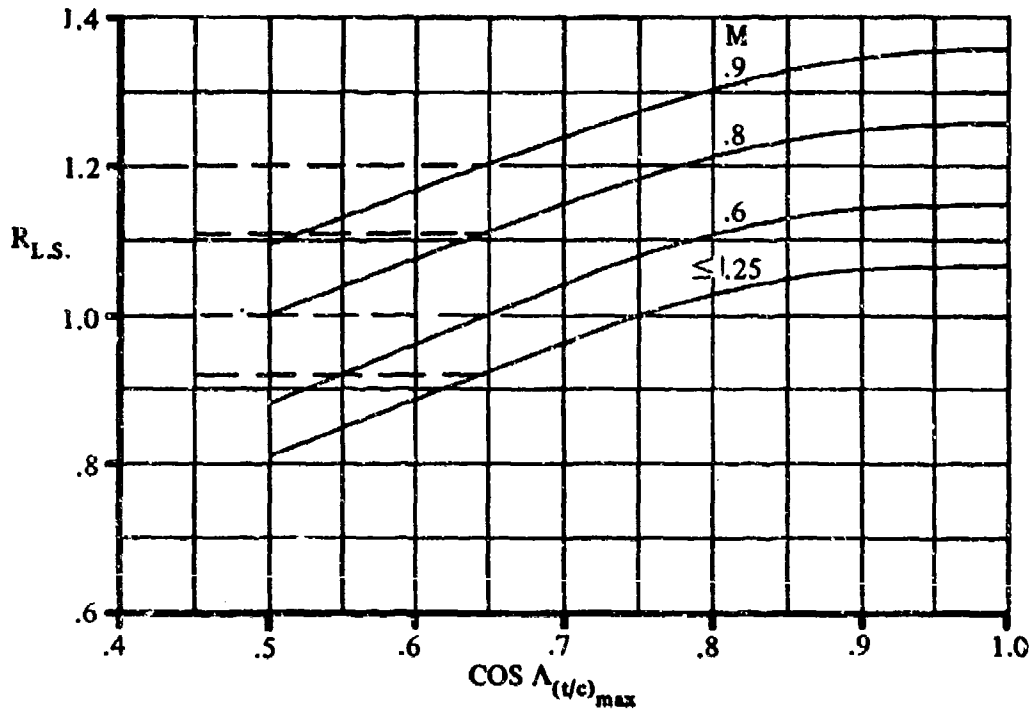

Figure 10 Lifting Surface Correlation Factor For Subsonic Minimum Drag

3.2 Camber Drag

The minimum drag contribution of the wing twist and camber is related to the lift coefficient of the polar displacement, ΔC_L, by the equation

$$C_{D_{CAMBER}} = \frac{e}{1-e} K\Delta C_L^2 \tag{3-17}$$

This increment is called camber drag and represents a drag increment between minimum profile drag and $C_{D_{MIN}}$. The span efficiency value, e, is related to the induced drag factor, K, by the equation

$$e = \frac{1}{\pi \cdot AR \cdot K}$$

If, for some reason, $e \geq 1$, an alternate equation, obtained from Reference 4, is used:

$$C_{D_{CAMBER}} = 0.7(\Delta C_L)^2 \frac{S_{EXPOSED}}{S_{REF}} \tag{3-18}$$

3.3 Base Drag

Data presented in Reference 5 were used to establish equations from which the base drag of bodies could be determined. The trends of these data show three different phases: (1) a gradual rise of $C_{D_{Base}}$ at transonic speeds up to M = 1, (2) a relatively constant drag level supersonically up to about M = 1.8, and (3) a steadily decreasing value of drag above M = 1.8. The resulting empirical equations are given as

$$C_{D_{Base}} = \begin{cases} (0.1 + 0.1222M^8)\frac{S_{Base}}{S_{Ref}}, & M \leq 1 \\ 0.2222S_{Base}/S_{Ref}, & 1.0 < M \leq 1.8 \\ 1.42S_{Base}/S_{Ref})/(3.15 + M^2), & M \geq 1.8 \end{cases} \tag{3-19}$$

3.4 Wave Drag

Supersonic wave drag is determined on the basis of a component buildup for which simplified shapes are assumed. Three basic simplified shapes are used to represent the airplane: bodies, nacelles, and wings. The component buildup assumes that the total wave drag is the sum of the isolated wave drag of each component and does not allow for the mutual interference between components. However, the component-buildup method does give wave-drag results comparable to average configurations which have some degree of favorable and unfavorable interference.

3.4.1 Wing Wave Drag

The technique used to estimate wing wave drag evolved from a method that applies transonic similarity theory to straight wings. Data correlations at Mach 1 were performed on a large number of unswept wing configurations with blunt and sharp leading-edge airfoils. For the Large Aircraft program, these results were represented by an analytical function common to both types. The equations were then modified for $M > 1$ to produce a peak value at low supersonic speeds and then to decrease at high Mach numbers to values predicted by straight-wing linear theory for equivalent two-dimensional configurations. Finally, sweep effects were included. The resulting semi-empirical equations are presented below:

$$\tilde{C}_D = \frac{2K_tK_wK_cK_b}{\tilde{\beta}K_bK_w\cdot(F_\beta)^m + \left[\dfrac{1/\tilde{AR}_e}{1+(1+\lambda)F_\beta\tilde{\beta}^{(1+K_w)}} + \dfrac{\tilde{AR}_e{}^3}{1+\frac{1}{3}\tilde{AR}_e{}^3\tilde{\beta}^4}\right]}$$

$$+ \frac{3.33\ K_tK_wK_cK_b}{\tilde{\beta}K_bK_w{}^{3.8}(F_\beta)^m + \left[\dfrac{2/\tilde{AR}_e{}^3}{1+(\frac{2}{3}+\lambda)F_\beta\tilde{\beta}^{(1+K_w{}^{3.8})}} + \dfrac{1}{1+3\tilde{AR}_e\tilde{\beta}^4}\right]} \qquad (3\text{-}20)$$

where

$$\tilde{C}_D = C_D/(t/c)^{5/3}$$

K_t = airfoil thickness distribution factor

$$= 1 + 4\left[\frac{1}{2} - \frac{X_t}{c}\left(1+\frac{1}{2}\sqrt{\frac{r_o}{t}}\right)\right]^2 - \frac{1}{4}\sqrt{\frac{r_o}{t}}\ \left(1-\frac{X_t}{c}\right)^2$$

K_b, K_w, airfoil factors

$K_b = 1.0$, $K_w = 1.2$ for double-wedge sections
$K_b = 1.069$, $K_w = 1.0$ for curved-type sections

X_t = location of section maximum y ordinate

r_o = section leading-edge radius

K_c = airfoil camber factor

$$1 + \frac{5}{2}(h/t)^2$$

h = section camber (maximum y ordinate)

$$K_p = \frac{\cos\Lambda_{LE} + \frac{1/2}{(1+\lambda)^2}(\tan^2\Lambda_{LE} - \tan^2\Lambda_{TE})}{1 + \frac{1}{(1+\lambda^2)^2}(\tan\Lambda_{LE} + \tan\Lambda_{TE})^2}$$

$$F_\beta = 0.3 + 0.7\ K_p^{(1+2\lambda^{1/3})}$$

$$\tilde{\beta} = \beta/(t/c)^{1/3} = \sqrt{M^2-1}/(t/c)^{1/3}$$

$$m = \frac{1+\lambda^2(2-\lambda)^3}{2}(\beta_{lim}/\beta)^Z \qquad \text{at} \quad \beta > \beta_{lim}$$

$$= \frac{1+\lambda^2(2-\lambda)^3}{2} \qquad \text{at} \quad \beta \leq \beta_{lim}$$

$$Z = \cos\Lambda_{LE} + \cos\Lambda_{TE}$$

$$\beta_{lim} = \left|\tan\Lambda_{LE}\right|$$

and where $\tilde{AR}_e$ is the straight-wing $\tilde{AR}$ having the same value of $C_D/(t/c)^{5/3}$ at $M = 1.0$ as $\tilde{AR}$, where $\tilde{AR} = AR(t/c)^{1/3}$.

The value of $\tilde{AR}_e$ is determined by solving the following equation by use of an iterative method:

$$\frac{2}{\frac{1}{\tilde{AR}_e} + \tilde{AR}_e^3} + \frac{3.33}{\frac{2}{\tilde{AR}_e^3} + 1} = \left(\frac{2}{\frac{1}{\tilde{AR}} + \tilde{AR}^3} + \frac{3.33}{\frac{2}{\tilde{AR}^3} + 1}\right)K_p$$

The term $\beta_{\ell_{im}}$ represents the approximate value of β at which $C_D/(t/c)^{5/3}$ will maximize, provided the body is essentially cylindrical where the wing is attached. If the body is area-ruled, the peak value of $C_D/(t/c)^{5/3}$ may or may not be closely approximated.

3.4.2 Body Wave Drag

The fuselage body wave drag is computed by dividing the body into two parts, consisting of a simplified pointed nose and a simplified boattail. That is,

$$C_{D_{W_{BODY}}} = C_{D_{P_N}} \cdot \frac{A_{MAX}}{S_{REF}} + C_{D_{PBT}} \cdot \frac{A_{MAX}}{S_{REF}} \qquad (3\text{-}21)$$

Nose wave drag, $C_{D_{P_N}}$, is determined from Linnell's empirical equation

$$(f_N^2+1)C_{D_{P_N}} = \frac{1.2 + 1.15(\beta/\sqrt{f_N^2+1})}{1 + 1.9(\beta/\sqrt{f_N^2+1})} \qquad (3\text{-}22)$$

for the supersonic wave drag of parabolic noses (Reference 6). For Mach numbers between 1.2 and 1.0, the nose wave drag is determined from the curves of Figure 11, which were derived from the transonic drag rise of ogive noses, as presented in Figure III.B.10-9 of Reference 4, and using Equation 3-22 as a supersonic limit. The nose fineness ratio, f_N, is calculated from the nose length, ℓ_N, and the maximum cross-sectional area, A_{MAX}, as

$$f_N = \ell_N / \sqrt{(\tfrac{4}{\pi})A_{MAX}}$$

Boattail wave drag, $C_{D_{PBT}}$, is determined as a function of boattail fineness ratio (f_B), base diameter to maximum diameter (d_B/d), and Mach number. This is done by computing $C_{D_{PBT}}$ at five values of (d_B/d) and interpolating to the desired value. The general form of these equations is given below:

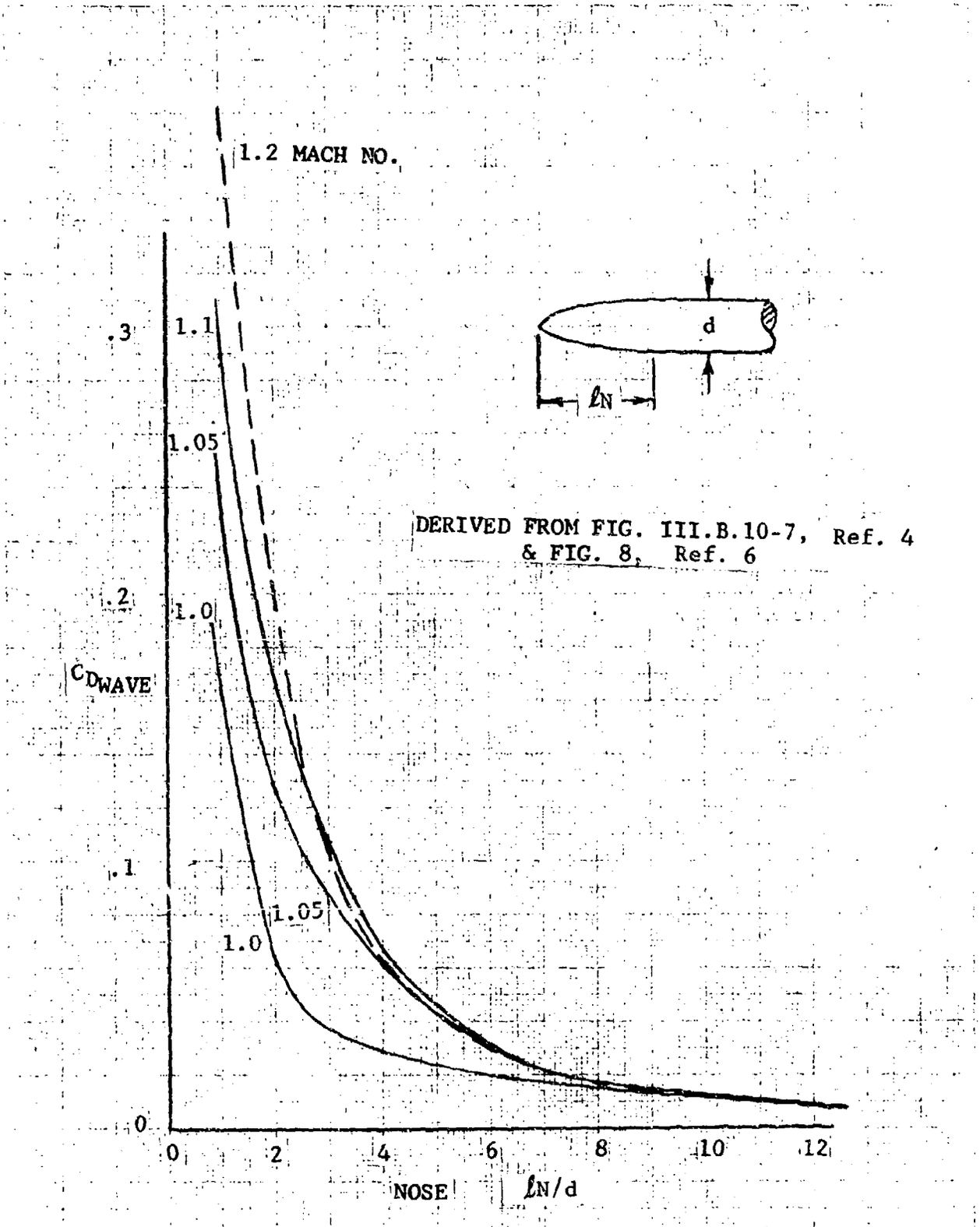

DERIVED FROM FIG. III.B.10-7, Ref. 4
& FIG. 8, Ref. 6

Figure 11 Transonic Wave Drag of Parabolic Noses

For $\beta/f_N \leq 1$ and $d_B/d = \frac{d_B(I)}{d}$,

$$C_{D_{PBT}}(I) = \frac{1}{f_B^2}\left[A_o(I)+A(I)\cdot\beta/f_B+A_2(I)\cdot(\beta/f_B)^2+A_3(I)\cdot(\beta/f_B)^3\right] \quad (3\text{-}23)$$

For $\beta/f_N > 1$,

$$C_{D_{PBT}}(I) = \frac{1}{f_B^2}\ A_4(I)\cdot(f_N/\beta) \quad (3\text{-}24)$$

The polynominal coefficients of Equations 3-23 and 3-24, determined from a least-square fit of Fig. III.B.10-9 of Reference 4 for ogive boattails, are tabulated below:

I	d_B/d	A_o	A_1	A_2	A_3	A_4
1	0	1.165	-0.5112	-0.5372	0.3964	0.513
2	0.4	1.067	-1.709	1.6632	-0.686	0.3352
3	0.6	0.7346	-1.4618	1.5795	-0.6542	0.198
4	0.8	0.2555	-0.5008	0.5024	-0.2077	0.0494
5	1.0	0	0	0	0	0

3.4.3 Nacelle Wave Drag

The nacelle wave drag is calculated by a method similar to that used for the fuselage:

$$C_{D_{W_{Nac}}} = (C_{D_{ON}} + C_{D_{PBT}})\ \frac{A_{MAX}}{S_{REF}} \quad (3\text{-}25)$$

The equation used to calculate $C_{D_{ON}}$ for open-nose bodies is

$$C_{D_{ON}} = \left[(1 - r_{IN}/R)/f_N\right]^{1.5}/\beta^{\frac{1}{2}} \quad (3\text{-}26)$$

where

$$r_{INLET} = \sqrt{A_{INLET}/\pi}$$

$$R = \sqrt{A_{MAX}/\pi}$$

This equation is a curve fit of Figure III.B.10-6 of Reference 4.

3.5 Fuselage Aft-End Upsweep Drag

The main parameters affecting the fuselage aft-end upsweep drag are the upsweep angle and the crossflow drag coefficient of the rear fuselage sections in the local flow, including modification by wing downwash. Data in Reference 7 indicate that the afterbody drag increases rapidly with upsweep angle β, but decreases with increasing fuselage angle of attack. The curves in Figure 12, obtained from the data presented in Reference 7, are used to predict aft-end drag as a function of angle of attack.

3.6 Miscellaneous Drag Items

In the preliminary design stage of aircraft drag estimation, the drag due to surface irregularities such as gaps and mismatches, fasteners, small protuberances, and leakage due to pressurization are estimated by adding a miscellaneous drag increment which would be some percentage of the total friction, form, and interference drags. The miscellaneous drag varies between 10 and 20 percent of the total friction, form, and interference drags for typical aircraft. The Large Aircraft program computes miscellaneous drag by use of a percentage factor specified as input to the program.

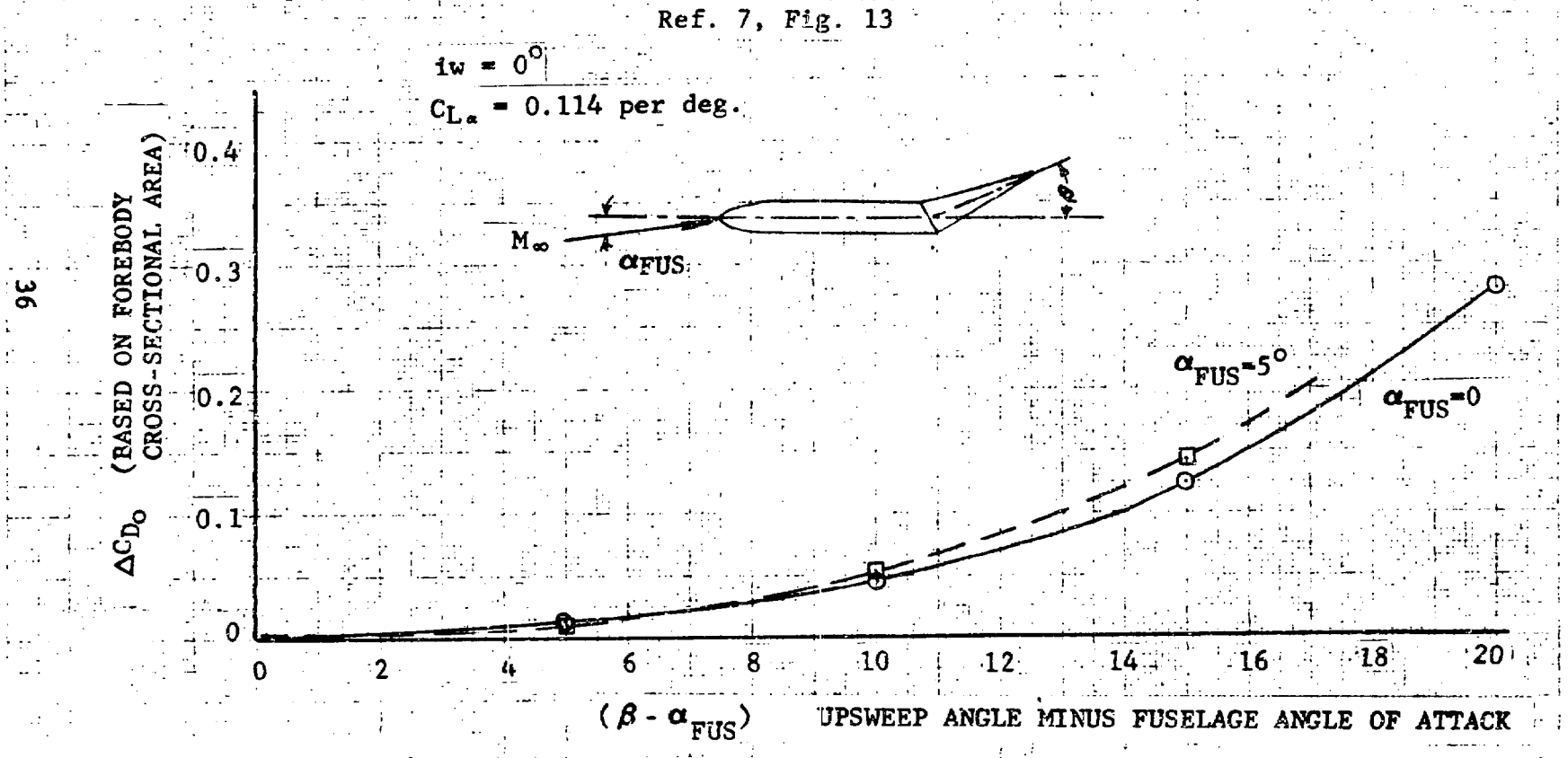

Figure 12 Effect of Fuselage Upsweep on Drag

4. DRAG DUE TO LIFT

The Large Aircraft program predicts drag due to lift by one of several methods, depending on the aerodynamic conditions at which a solution is desired. The various regions are illustrated in Figure 13; they are discussed in the following subsections in the numerical order shown in the figure.

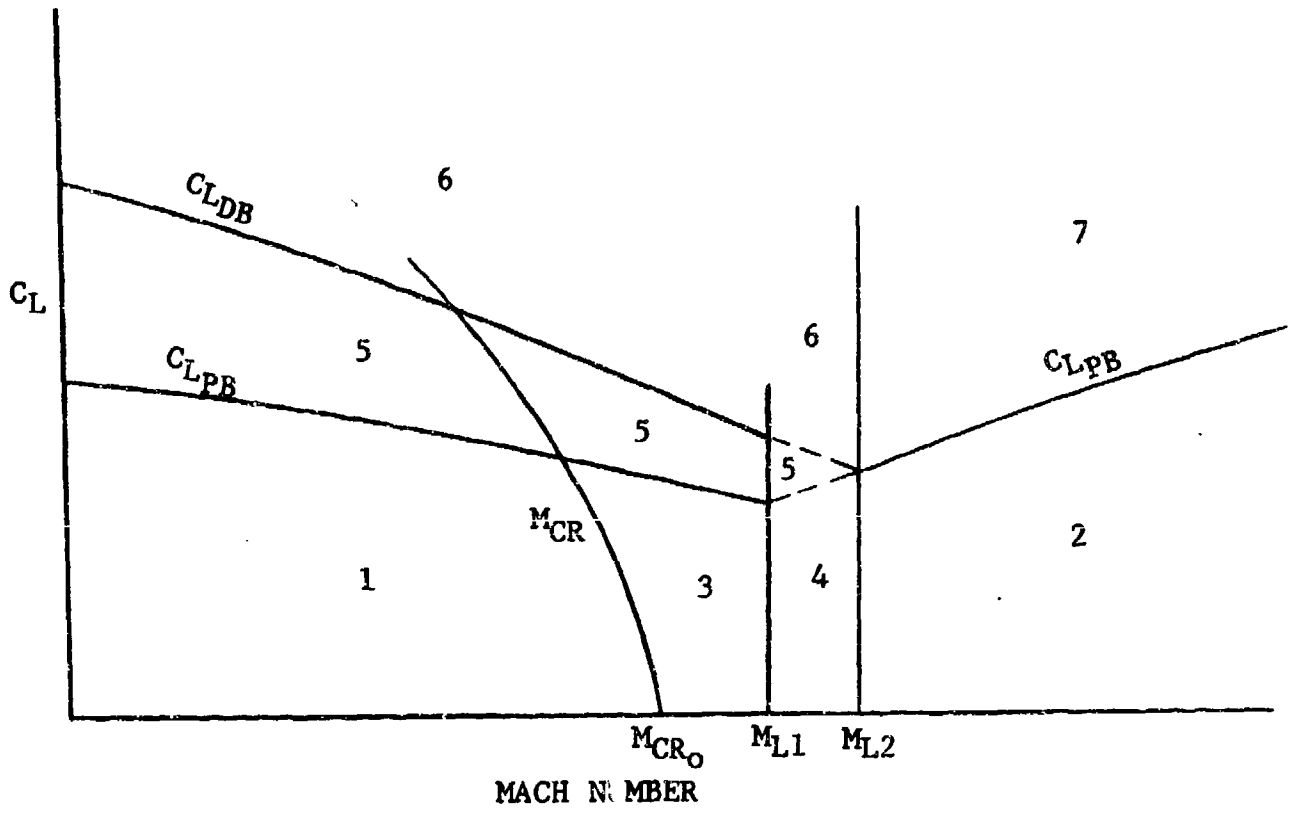

Figure 13 Lift and Speed Regions for Calculation of Drag Due to Lift

4.1 Subsonic Polar Prediction below Polar Break

Region 1 is bounded by the critical Mach number and by the C_L at which the polar break occurs ($C_{L_{PB}}$). In this subsonic, low-lift region, the drag due to lift can be determined from

$$C_{D_L} = K(C_L - \Delta C_L)^2 \tag{4-1}$$

where the drag due to lift factor, K, is predicted from

$$K = \frac{1-R}{C_{L_\alpha}} + \frac{R}{\pi AR\ e_o} \tag{4-2}$$

In this equation, a leading-edge suction parameter R, is used to relate K to the lower bound of drag, $1/\pi AR$, for full leading-edge suction (R=1.0) and to the upper bound of drag, $1/C_{L_\alpha}$, for zero leading-edge suction. Body effects are accounted for in Equation 4-2 by computing e_o, shown plotted in Figure 14 as a function of taper ratio and body-diameter-to-span ratio (d/b).

The correlation of leading-edge suction on induced drag was first developed by Frost (Reference 8) and was later extended for additional planform effects and higher subsonic Mach numbers (Reference 9). A study by NASA (Reference 10) showed that airfoil camber, conical camber, sharp leading edges, leading-edge flaps, Reynolds number, and sweep have significant effects on the suction parameter. H. John (Reference 11) improved the correlation of R for plane wings at low Reynolds number by including airfoil thickness along with leading-edge radius.

The procedure followed in the Large Aircraft program to determine R is as follows:

1. Using the leading-edge radius and the leading-edge sweep for each wing panel, determine Ω from the equation

$$\Omega = \begin{cases} R_{N_{LER}} \times 10^{-3} \cot\Lambda_{LE} \sqrt{1-M^2\cos^2\Lambda_{LE}}; & \Lambda_{LE} \geq 20^\circ \\ R_{N_{LER}} \times 10^{-3}(5-6.511\Lambda_{LE}) \sqrt{1-M^2\cos^2\Lambda_{LE}}; & \Lambda_{LE} < 20^\circ \end{cases} \tag{4-3}$$

(Λ_{LE} in radians)

   The switch from the cotangent term is made to prevent Ω from going to infinity as sweep approaches zero.

   The value of Ω is then used to read R_T from Figure 15, which is a plot of leading-edge suction for thin, round-nose, uncambered airfoils developed in Reference 9.

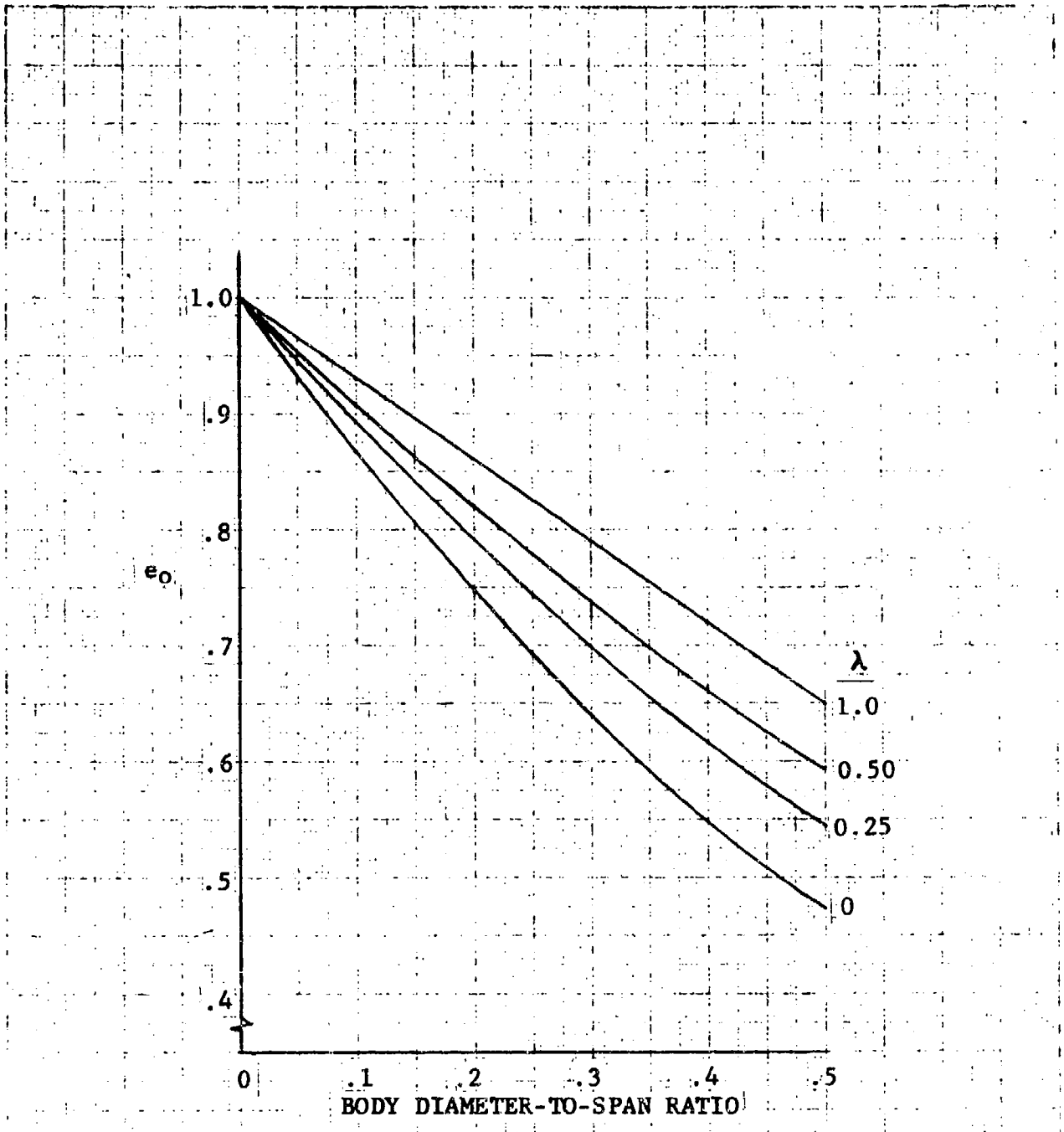

Figure 14 Body Effects on Wing Span Efficiency

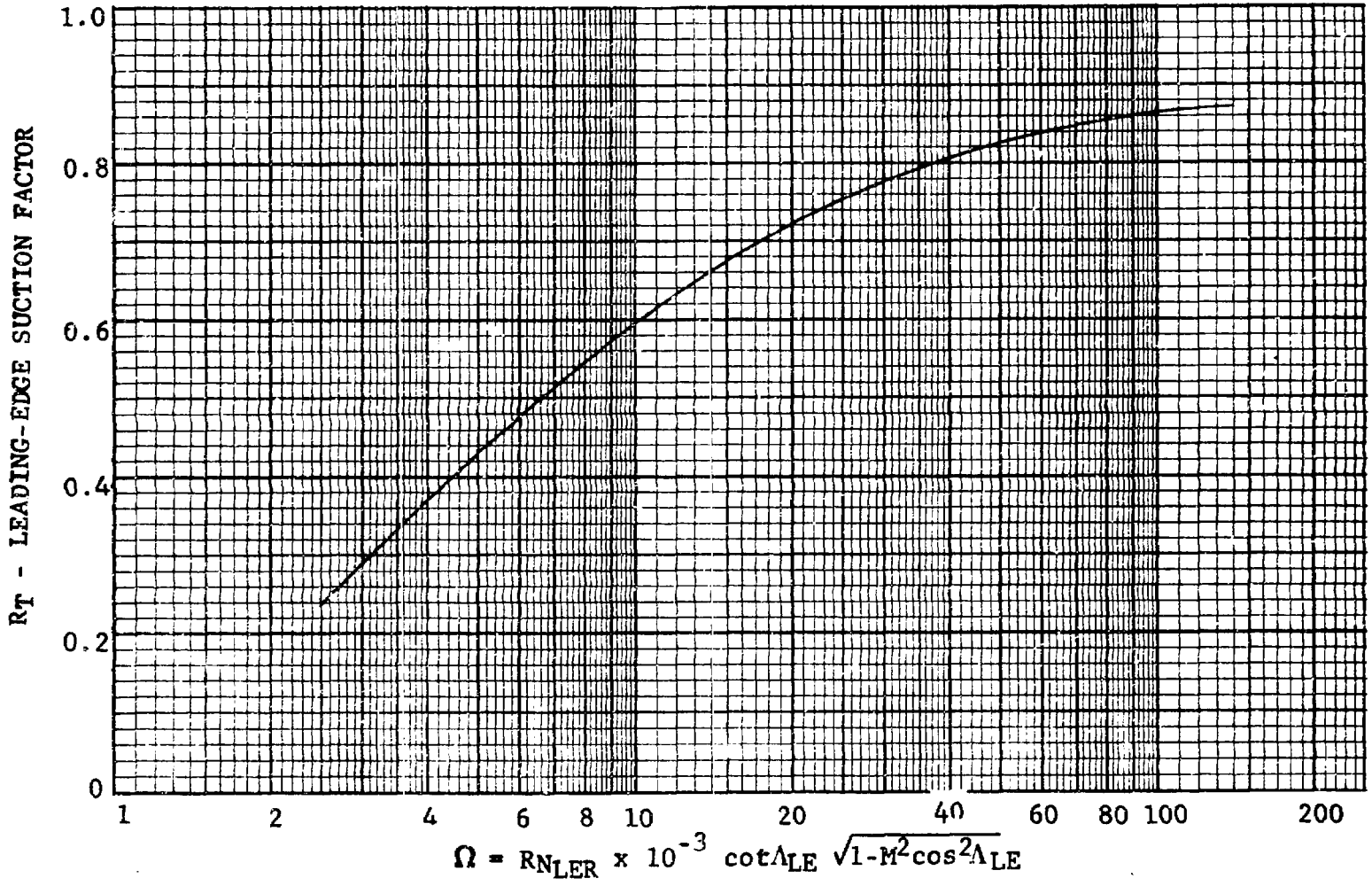

Figure 15 Effect of Reynolds Number on Leading-Edge Suction for Blunt-Uncambered Airfoils

2. Using the leading-edge sweep of the wing panel, determine R_{MIN} from Figure 16. The plot of Figure 16 was obtained from the results reported in Reference 10 for sharp-leading-edge wings. The leading-edge-suction value for sharp-leading-edge wings is independent of Reynolds and Mach numbers.

3. If the value of R_T determined from step (1) is less than the value of R_{MIN} determined from step (2), set R_T equal to R_{MIN}.

4. Using the wing panel thickness and leading-edge radius Reynolds number, determine a thickness correction to leading-edge suction, R_T, from Figure 17. Figure 17 was determined from the data presented in Reference 11. The increment in suction parameter ΔR_T is then added to the value of R_T determined from step (3).

5. Determine the effect of either section camber or conical wing camber on the R factor from

$$R_i = R_T + (0.824 - R_T) \cdot (C_{L_d} + C_{L_{con}})/0.6 \qquad (4\text{-}4)$$

If $R_i > 0.874$, $R_i = 0.874$.

Correlation with experimental data and the results of Reference 10 indicate that R does not decrease as much for low Reynolds number when the wing is cambered compared to an uncambered wing.

The accompanying sketch shows the relative effect that Equation 4-4 will predict for cambered wings.

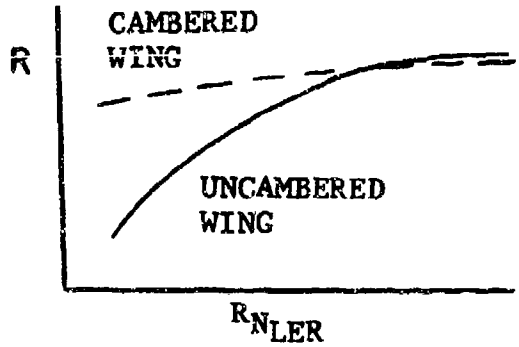

6. Obtain the effective R for the composite wing from a span-weighted average of the individual R_i for each panel as follows:

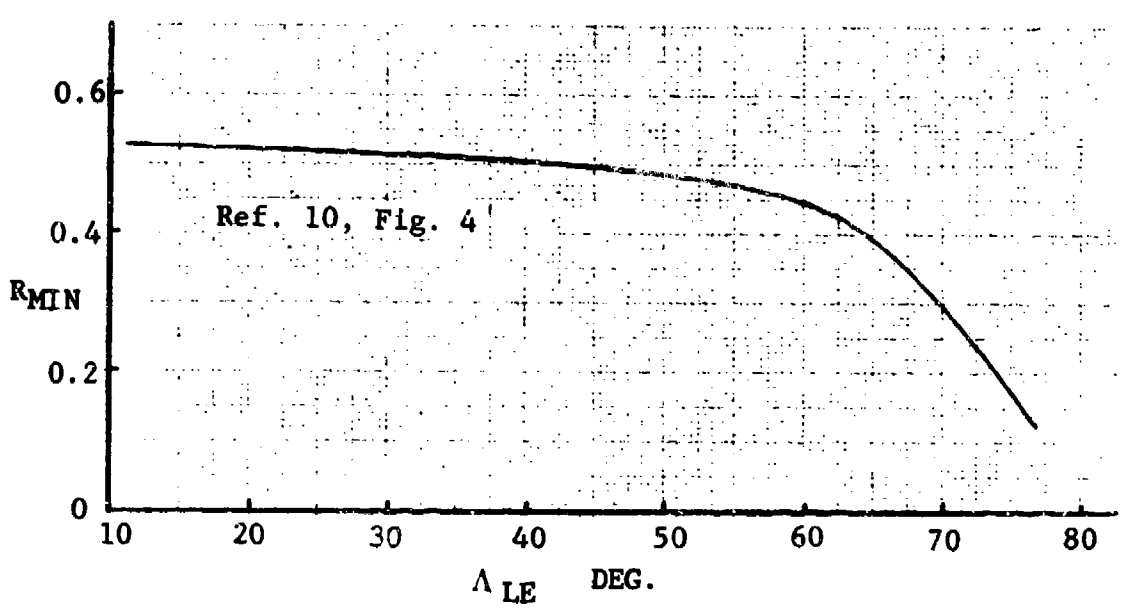

Figure 16 Leading-Edge Suction for Sharp Airfoils

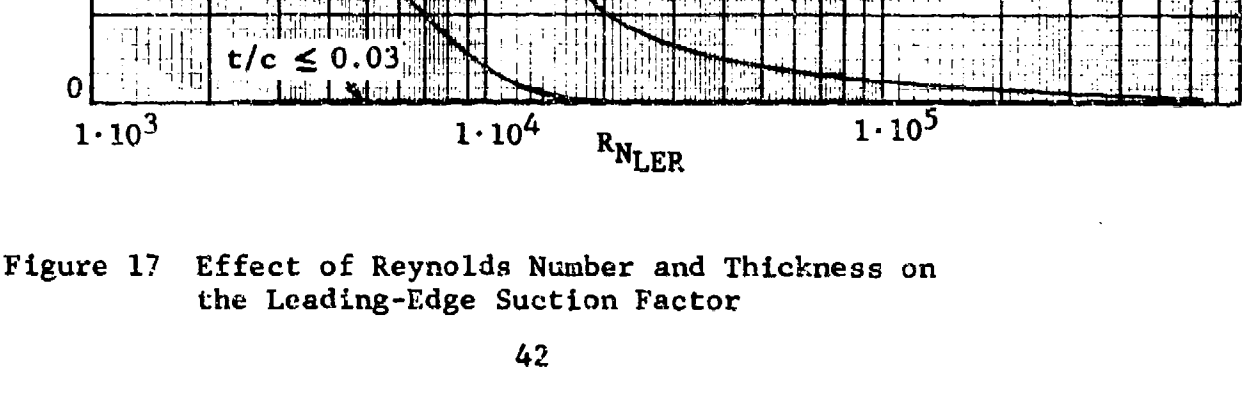

Figure 17 Effect of Reynolds Number and Thickness on the Leading-Edge Suction Factor

$$\bar{R} = \sum_{i=1}^{N} R_i \cdot \frac{YW(i+1) - YW(i)}{(b/2 - d/2)}$$

where YW(i+1) - YW(i) is the width of the ith panel.

7. Using Figure 18 and the parameter $AR \cdot \lambda/\cos\Lambda_{LE}$, calculate the effect of wing planform on R. The increment ΔR due to planform is then added to $\bar{R}$, determined from step (6), to obtain the final R value used in Equation 4-2.

The polar displacement, ΔC_L, is related to the lift coefficient for minimum profile drag, $C_{L_{OPT}}$, by the equation

$$\Delta C_L = (1 - \frac{1}{\pi AR\ K})C_{L_{OPT}}$$

The lift coefficient for minimum profile drag is related to the camber, twist, and asymmetry of the configuration. Figures 19 and 20 present data (Reference 13) for the effect of NACA camber and conical camber on $C_{L_{OPT}}$. For supercritical wings, the limited amount of data available for correlation indicate that

$$C_{L_{OPT}} = 0.5195(C_{L_d})^{0.75} \qquad (4\text{-}5)$$

where C_{L_d} is the wing section design lift coefficient.

4.2 Supersonic Polar Prediction below Polar Break

The drag polar in the supersonic region beyond the second limit Mach number below polar break (Region 2) is predicted by Equation 4-1, where

$$K = \frac{1-\tilde{R}}{C_{L_\alpha}} + \frac{\tilde{R}}{\pi AR\ e_o} \qquad (4\text{-}6)$$

This equation is similar to Equation 4-2 for the subsonic induced-drag factor except for the use of $\tilde{R}$, which is a transonic leading-edge suction factor. For Mach numbers greater than Mach critical, the suction factor is predicted from

$$\tilde{R} = R_o/(1 + n\Delta M + (n\Delta M)^2) \qquad (4\text{-}7)$$

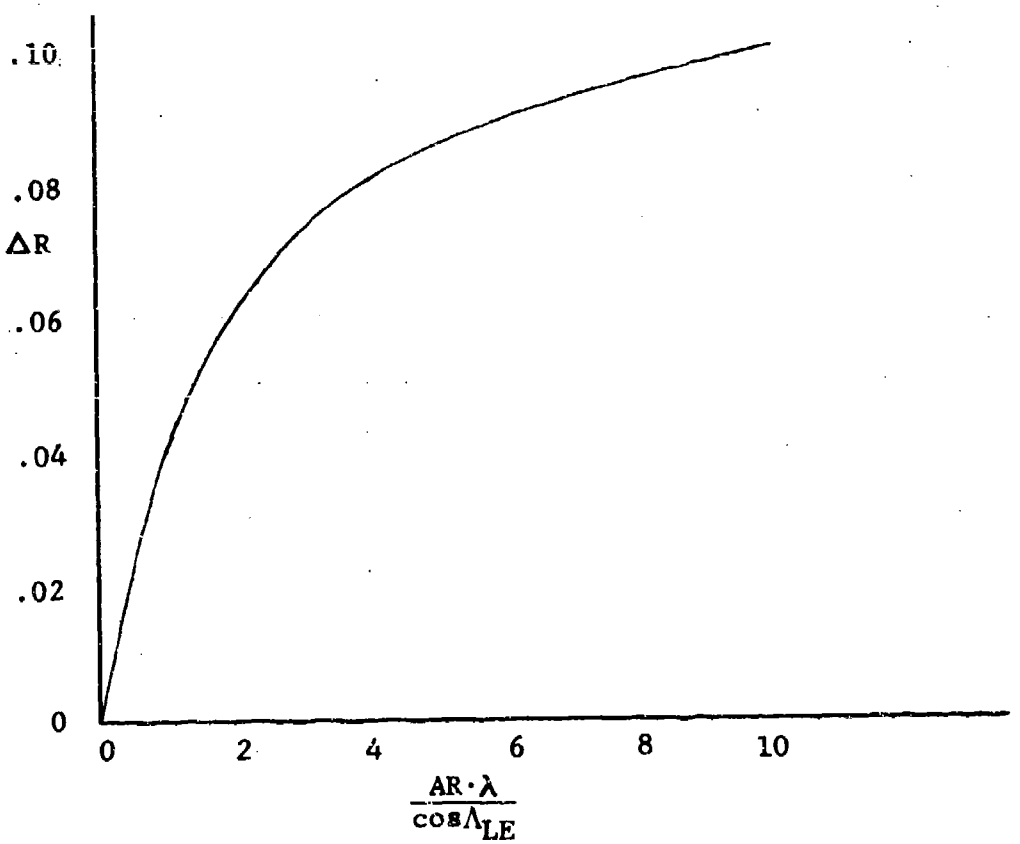

Figure 18 Effect of Wing Planform on Lead ng-Edge Suction

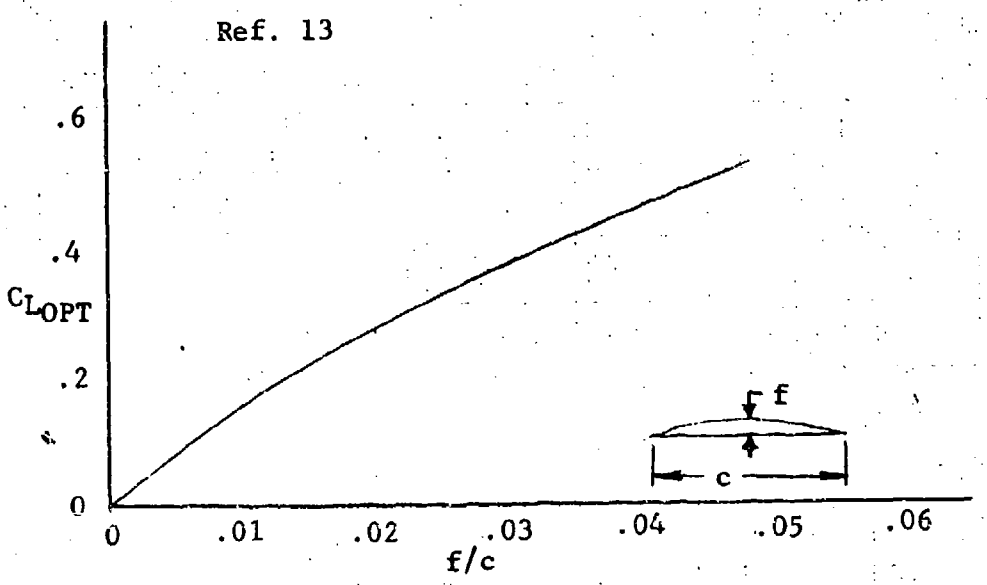

Figure 19 Lift Coefficient for Minimum Profile Drag - NACA Camber

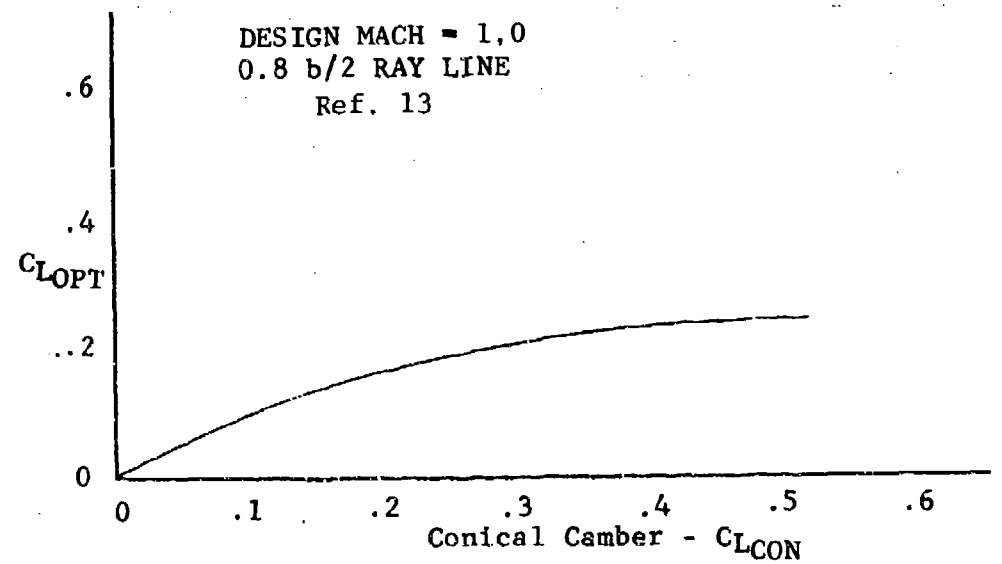

Figure 20 Lift Coefficient for Minimum Profile Drag - Conical Camber

where R_o = leading-edge suction factor at the critical Mach number at zero lift, M_{CR_o}

$$n = 12(\cos\Lambda_{LE})^{1.6}$$

$$\Delta M = M - M_{CR_o}$$

The variation of $(\tilde{R}/R_o)$ for Mach numbers greater than M_{CR_o} is shown in Figure 21. This method of predicting polar shape factor produces a continuous decrease in leading-edge suction so that in the limit, as the Mach number approaches the sonic leading-edge condition, the polar shape approaches $(1/C_{L_\alpha})$.

The supersonic polar displacement for NACA camber is calculated from

$$\Delta C_L = \begin{cases} C_{L_d}(0.25-0.225\beta\cot\Lambda_{LE}); & \beta\cot\Lambda_{LE} < 1.11 \\ 0; & \beta\cot\Lambda_{LE} \geq 1.11 \end{cases} \qquad (4\text{-}8)$$

and the supersonic polar displacement for conical camber is calculated from

$$\Delta C_L = \begin{cases} C_{L_{con}}(0.111-0.1\beta\cot\Lambda_{LE}); & \beta\cot\Lambda_{LE} < 1.11 \\ 0; & \beta\cot\Lambda_{LE} \geq 1.11 \end{cases} \qquad (4\text{-}9)$$

These equations were obtained from a simple curve fit of the data presented in Figures 94 through 97 of Reference 13.

4.3 Transonic Polar Prediction

In the transonic region bounded by Mach critical (M_{CR}) and the first limit Mach number (M_{L1}) (Region 3), the induced drag is computed by adding drag rise to the basic polar:

$$C_{D_L} = K(C_L - \Delta C_L)^2 + C_{DR_{CL}} \qquad (4\text{-}10)$$

The basic polar shape is calculated up to M_{CR_o} in the same manner as described for Region 1. Beyond M_{CR_o}, the basic polar does not change. An incremental drag-rise term ($C_{DR_{C_L}}$) is calculated as a

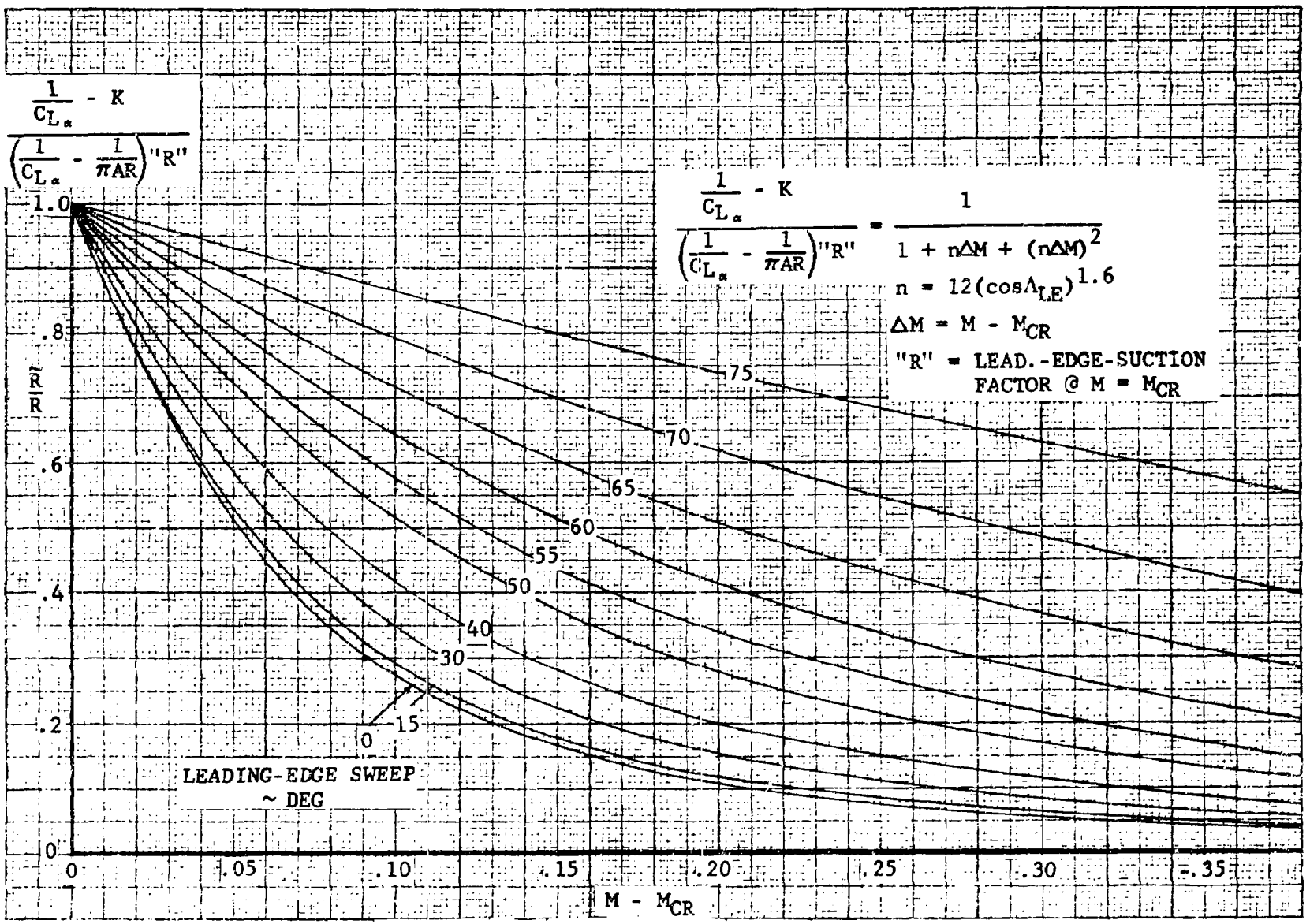

Figure 21 Transonic Suction Factor

function of lift and is added to the basic polar to determine the total drag due to lift. A complete description of the techniques used to determine the drag-rise increment is given in Subsection 5.3.

In the transonic region above the first limit Mach number, M_{L1} (Region 4), the drag-rise term in Equation 4-10 becomes less accurate. Therefore, the drag polar in Region 4 is calculated by interpolation between the polar shape factors calculated in Regions 3 and 2. The equations for K and ΔC_L are given by

$$K = K_{L1} + (K_{L2} - K_{L1}) \frac{M-M_{L1}}{M_{L2}-M_{L1}} \tag{4-11}$$

$$\Delta C_L = \Delta C_{L_{L1}} + (\Delta C_{L_{L2}} - \Delta C_{L_{L1}}) \frac{M-M_{L1}}{M_{L2}-M_{L1}} \tag{4-12}$$

where $M_{L1} < M < M_{L2}$. The polar shape factors, K_{L1} and $C_{L_{L1}}$, are determined from a least-square curve fit of the polar shape computed by Equation 4-10 at M_{L1}. The polar shape factors K_{L2} and $C_{L_{L2}}$ are computed from Equations 4-6 and 4-8 at M_{L2}. The limit Mach numbers are determined from

$$M_{L1} = M_{CR_0} + 0.05$$

If $M_{L1} < 0.95$, then $M_{L1} = 0.95$

If $M_{L1} > 1.00$, then $M_{L1} = 1.0$

$$M_{L2} = M_{L1} + 0.15$$

4.4 Subsonic Polar Prediction above Polar Break

The polar region between the polar break lift coefficient ($C_{L_{PB}}$) and the initial-stall lift coefficient ($C_{L_{DB}}$) is the region in which leading-edge separation and reattachment occurs, causing the polar to deviate from a parabolic shape (Region 5 in Figure 13). Whether or not this region exists (i.e., the flow reattaches after separation and allows the wing to reach a higher lift coefficient before final separation occurs at the trailing edge) is determined by the type of airfoil, the Reynolds number, and the leading-edge wing sweep. For thin wings, low Reynolds numbers, or highly swept wings, the values of $C_{L_{PB}}$ and $C_{L_{DB}}$ are equal.

Leading-edge sharpness is a measure of the type of separation likely to occur. Blunt, thick airfoils generally exhibit trailing-edge separation, while very thin airfoils exhibit leading-edge separation. Airfoils of moderate thickness are likely to separate and reattach at the leading edge, followed by trailing-edge separation (stall) at higher lift coefficients. Associated with the leading-edge separation and reattachment is a loss in leading-edge suction, which produces an increase in drag due to lift. Above $C_{L_{DB}}$, the flow separates completely along the wing and the drag increases more rapidly.

The prediction method in the Large Aircraft program utilizes the sharpness parameter of the airfoil, Δy, as defined in Equation 2-28. If Δy is less than or equal to 1.65, leading-edge flow separation is assumed to occur. Also, if the leading-edge sweep is greater than or equal to 50 degrees, it is assumed that leading-edge separation occurs. If Δy is greater than 2.05, a leading-edge separation and reattachment occurs, followed by a trailing-edge separation. For values of Δy between 1.65 and 2.05, a transition region exists in which the behavior varies between the condition of full leading-edge separation at $\Delta y = 1.65$ and full leading-edge flow reattachment at $\Delta y = 2.05$.

Because the polar-break lift coefficient is a function of many variables, it has proved to be a difficult quantity to predict. Data correlations at subsonic and transonic speeds performed during the development of the Large Aircraft program indicate that the polar-break point can better be determined with angle of attack as the parameter rather than lift coefficient. These correlations resulted in a method that determines the angle of attack at polar break as a function of Mach number, Δy, sweep angle, and wing camber. Consequently, the polar break, C_L, is calculated as

$$C_{L_{PB}} = C_{L_\alpha} \cdot (\alpha_{PBO} + \Delta\alpha_{PB}) \qquad (4\text{-}13)$$

where $(\alpha_{PBO}/\cos\Lambda_{c/4})$ is shown plotted in Figure 22 as a function of Δy and $M \cos\Lambda_{c/4}$. The term $\Delta\alpha_{PB}$ accounts for section camber and is determined from

$$\Delta\alpha_{PB} = (12.05 - 4.1\ M \cos\Lambda_{c/4})\left(\frac{C_{\ell_d}}{\cos\Lambda_{c/4}}\right)$$

which was derived principally from correlating the experimental data in Reference 12. For wings with conical camber, an increment in $C_{L_{PB}}$ is obtained from Figure 23.

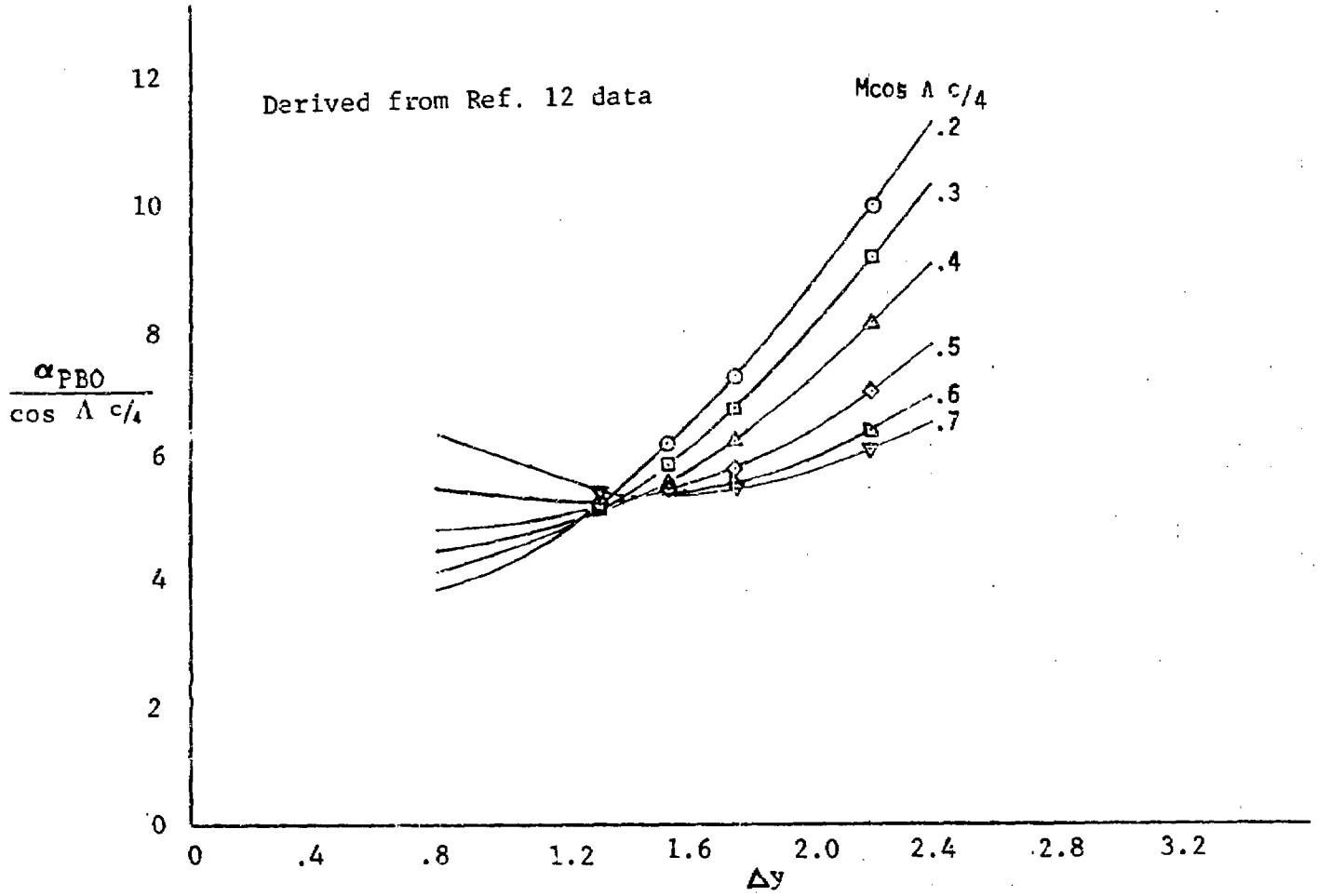

Figure 22 Airfoil Leading-Edge Shape Effect on α_{PB_o}

The drag due to lift is expressed in Region 5 as

$$C_{D_L} = K(C_L-\Delta C_L)^2 + K'(C_L-C_{L_{PB}})^2 \qquad (4\text{-}14)$$

$$C_{L_{PB}} < C_L < C_{L_{DB}}$$

where $K' = 0.518/\sqrt{AR}$ (Reference 1).

The upper boundary of Region 5 represents the lift coefficient at which trailing-edge separation occurs. It is predicted as

$$C_{L_{DB}} = C_{L_{PB}} + T\left[R_{N_{\bar{C}}} \cdot \left(\frac{\partial C_L}{\partial R_N}\right) - \delta C_L\right]$$

where

$$T = \begin{cases} 0 & ; \quad \Delta y \leq 1.65 \\ (\Delta y - 1.65)/0.4; & 1.65 < \Delta y < 2.05 \\ 1.0 & ; \quad \Delta y \geq 2.05 \end{cases}$$

and $(\partial C_L/\partial R_N)$ and δC_L are shown plotted in Figures 24 and 25.

The drag polar above $C_{L_{DB}}$ (Region 6 in Figure 13) increases sharply from the subsonic attached-flow condition. The polar prediction for lift coefficients above $C_{L_{DB}}$ is determined by a modification of the empirical method presented in Reference 13 whereby

$$C_{D_L} = C_{D_{DB}} + K_D C_L^2 + \Delta C_{DB} \qquad (4\text{-}15)$$

$$C_L > C_{L_{DB}}$$

where $C_{D_{DB}}$ is the predicted lift dependent portion of profile drag at $C_{L_{DB}}$, $K_D C_L^2$ is the theoretical induced drag, and ΔC_{DB} is a correlated separation drag increment obtained as a function of $C_{L_{DB}}$. The lift dependent profile drag at $C_{L_{DB}}$ is given by

$$C_{D_{DB}} = K(C_{L_{DB}}-\Delta C_L)^2 + K'(C_{L_{DB}}-C_{L_{PB}})^2 - K_D C_{L_{DB}}^2 \qquad (4\text{-}16)$$

where the theoretical induced drag factor, K_D, is predicted from

$$K_D = \frac{1}{\pi AR\, e'} \qquad (4\text{-}17)$$

where e' is a modification of the classical theoretical

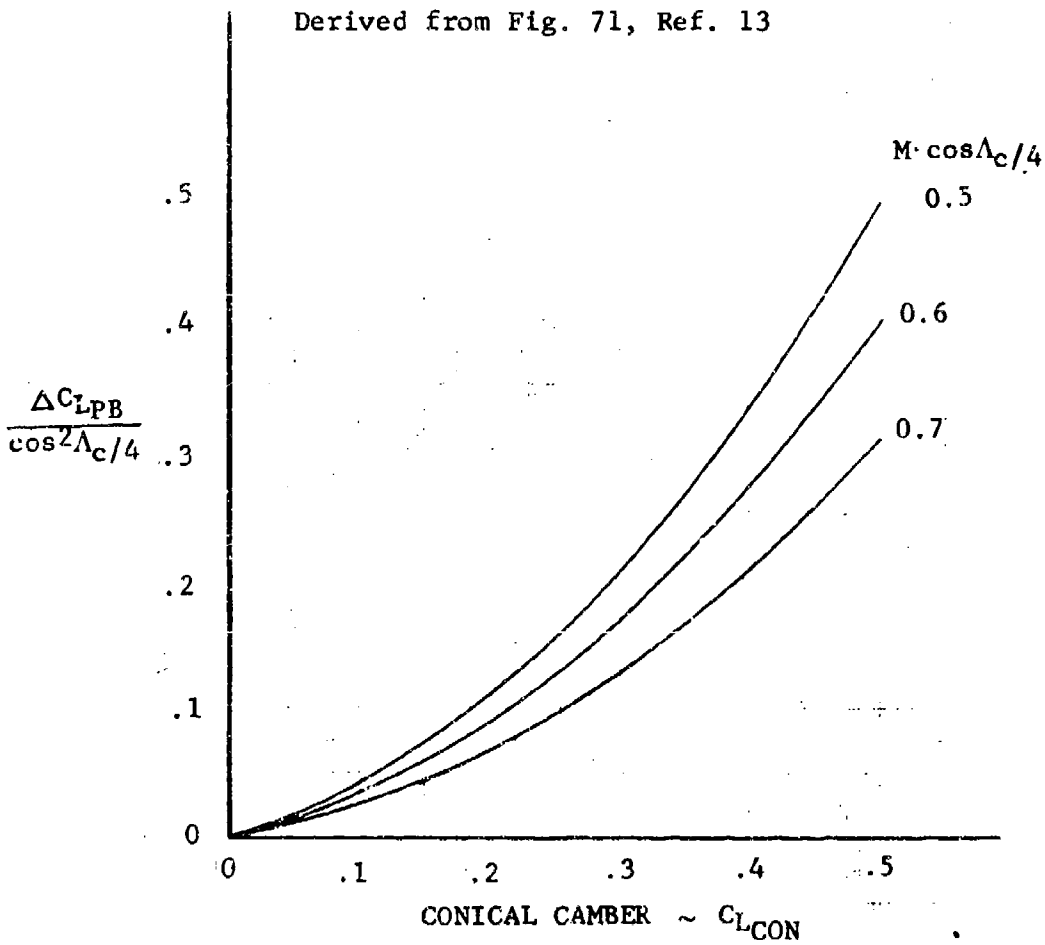

Figure 23 Conical Camber Effect on $C_{L_{PB}}$

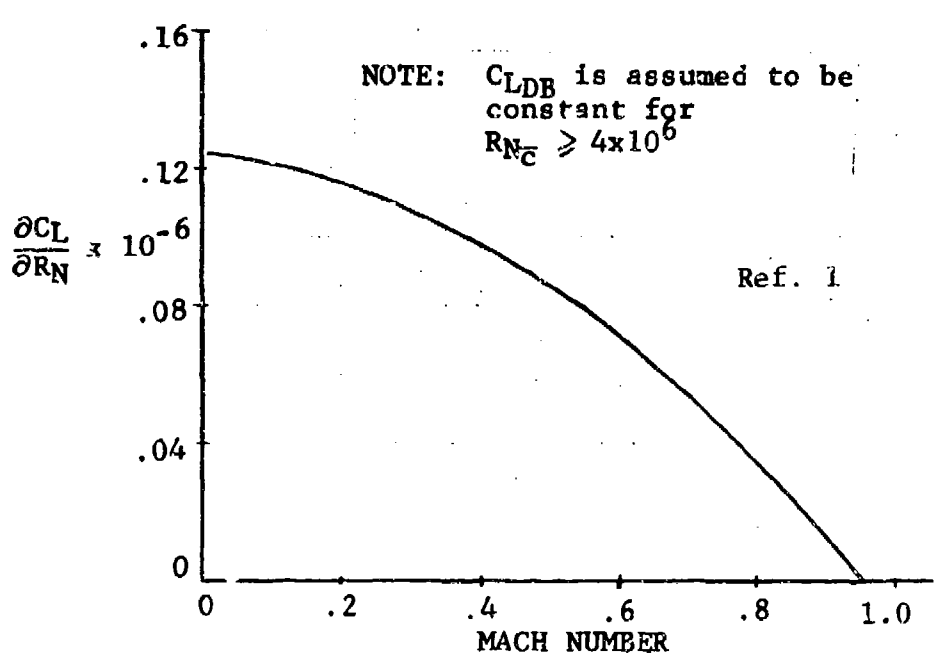

Figure 24 Reynolds Number Effect on $C_{L_{DB}}$

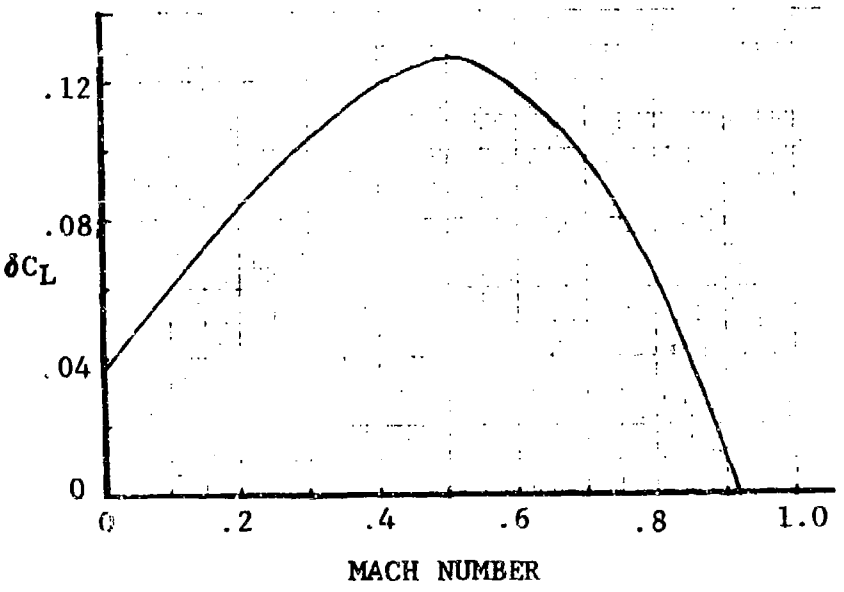

Figure 25 Correlation Lift Coefficient for $C_{L_{DB}}$

drag-due-to-lift factor $1/\pi AR$ to account for nonelliptical span loadings and body effects. The factor e' is calculated from

$$e' = e'_w \left[1 - (d/b)^2\right] \tag{4-18}$$

where the wing planform efficiency factor e'_w is as plotted in Figure 26 as a function of taper ratio, sweep, and aspect ratio. The data of Figure 26 were obtained from a Weissinger lifting-line solution presented in Reference 13.

The drag above $C_{L_{DB}}$ represents the separation drag component when major separation effects are present. Simon et al. (Reference 13) measured this drag relative to the profile drag at the drag-break lift coefficient and present correlated curves of ΔC_{DB} versus C_L, $C_{L_{DB}}$, and Mach number. The $\Delta C_{D_{DB}}$ data were curve fitted and result in the equation

$$\Delta C_{DB} = K_B(C_L - C_{L_{DB}})^2 + .08\sqrt{K_B(C_L - C_{L_{DB}})^2} \quad ; \quad C_L > C_{L_{DB}} \tag{4-19}$$

The factor K_B is shown plotted in Figure 27. The program does not vary K_B with Mach number since the drag-rise term is included in the polar buildup above $C_{L_{DB}}$.

For conventional wings the polar predicted by Equation 4-15 is continued up through $C_{L_{MAX}}$. For low-aspect-ratio or cranked wings (see Section 6) that develop vortex lift at the higher lift coefficients, the zero-suction drag polar predicted by

$$C_{D_L} = C_L \tan \alpha \tag{4-20}$$

is compared against the drag polar predicted by Equation 4-15 and the drag due to lift is set equal to whichever is lowest. This produces a drag polar as shown in the sketch below. The C_L-α variation for vortex lift is predicted by the methods given in Section 6.

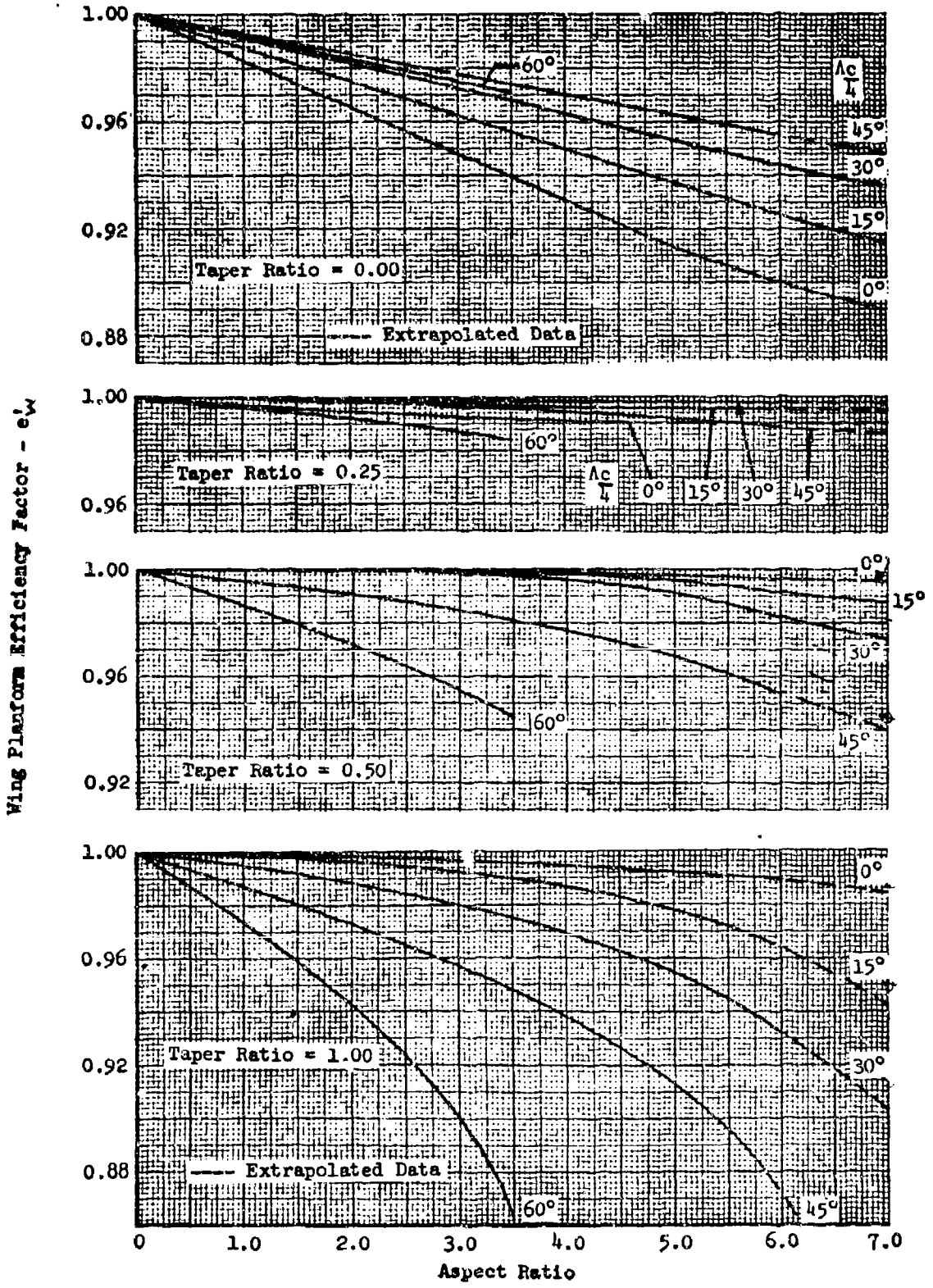

Figure 26 Weissenger Theoretical Wing Planform Efficiency Factor

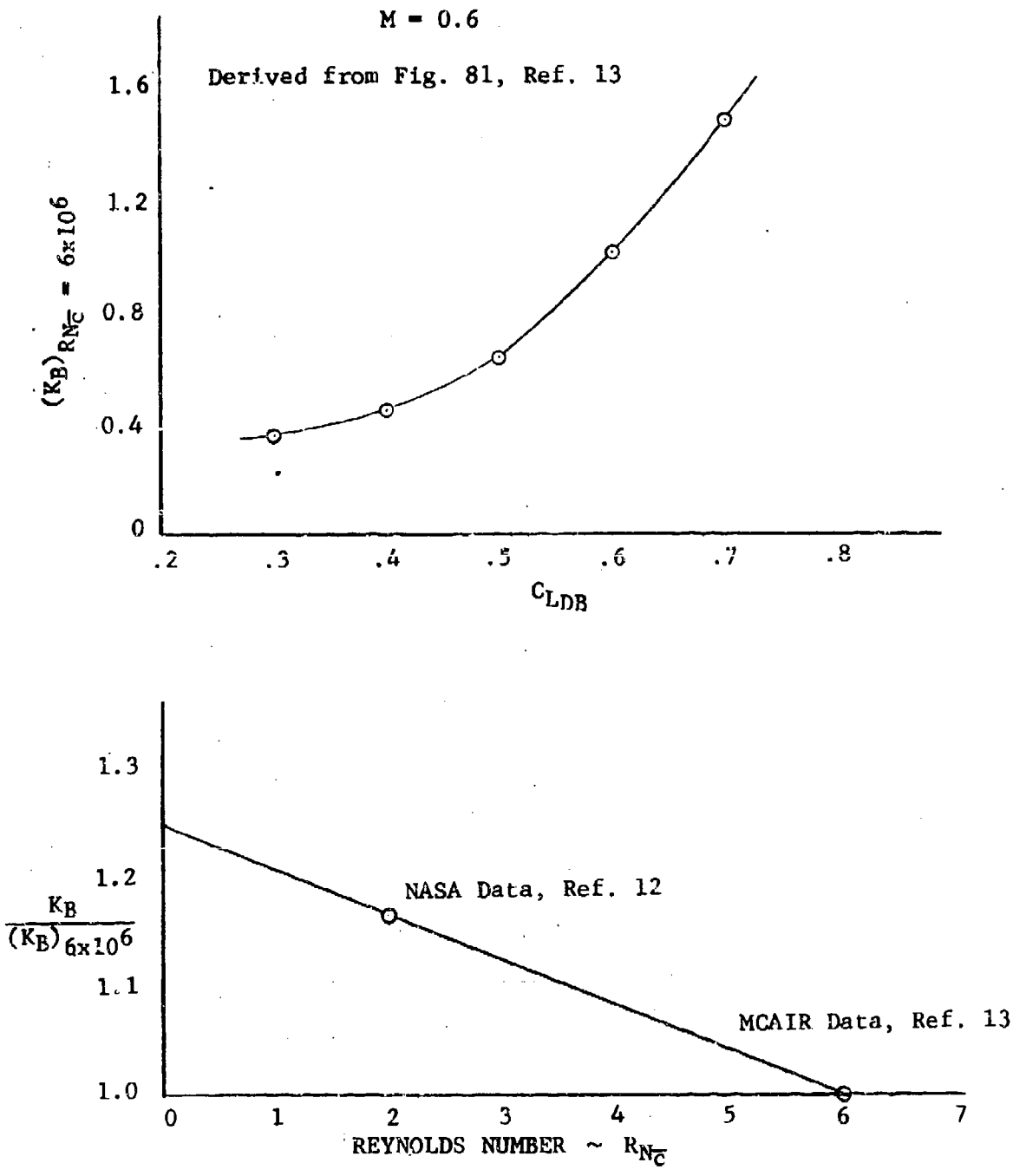

Figure 27 Separation Drag Factor

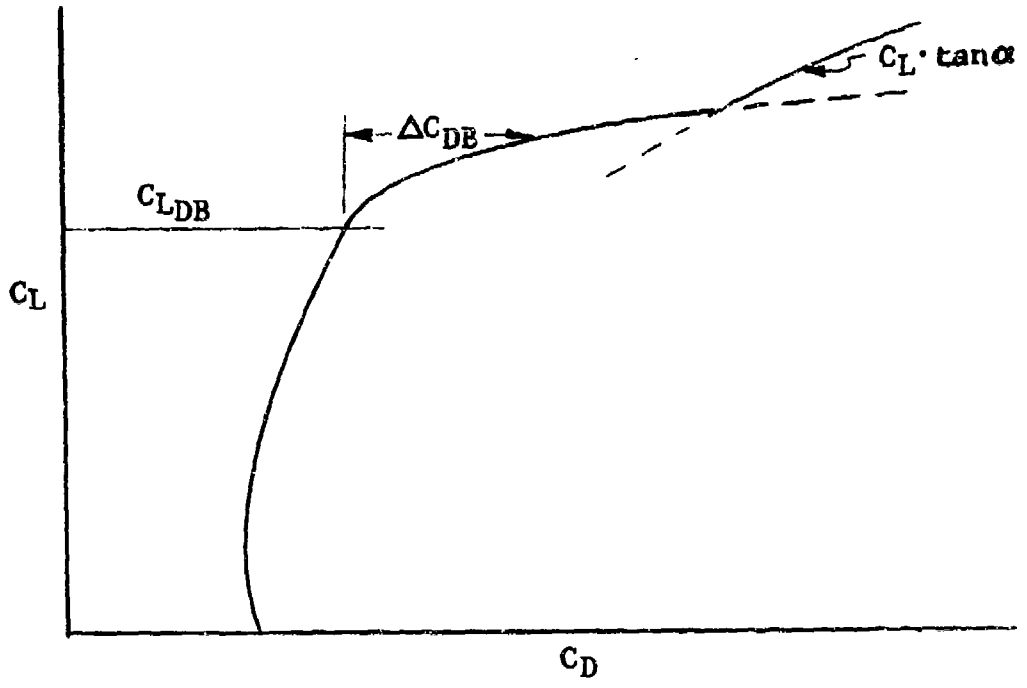

4.5 Supersonic Polar Prediction Above Polar Break

Supersonic Region 7 above polar break is predicted by the semi-empirical method developed in Reference 13. The equation for predicting supersonic drag due to lift above polar break is given by

$$C_{D_L} = (K-K')(C_{L_{PB}} - \Delta C_L)^2 + K'(C_L - \Delta C_L)^2; \quad C_L > C_{L_{PB}} \qquad (4\text{-}21)$$

where K and ΔC_L are the polar parameters in the low-lift region discussed in Subsection 4.2.

The polar-break lift coefficient, $C_{L_{PB}}$, is correlated as a function of sweep, aspect ratio, camber, etc. in Reference 13. A curve fit of the data in Reference 13 results in the following equations for $C_{L_{PB}}$.

$$C_{L_{PB}} = C_{LS_1} + 1.25(C_{LS_9} + \Delta C_{LS_9} - C_{LS_1})(\beta \cot \Lambda_{LE} - .1) + 0.5 C_{l_d} \qquad (4\text{-}22)$$

where the factors C_{LS_1}, C_{LS_9}, and ΔC_{LS_9} are shown plotted in Figure 28 as a function of aspect ratio.

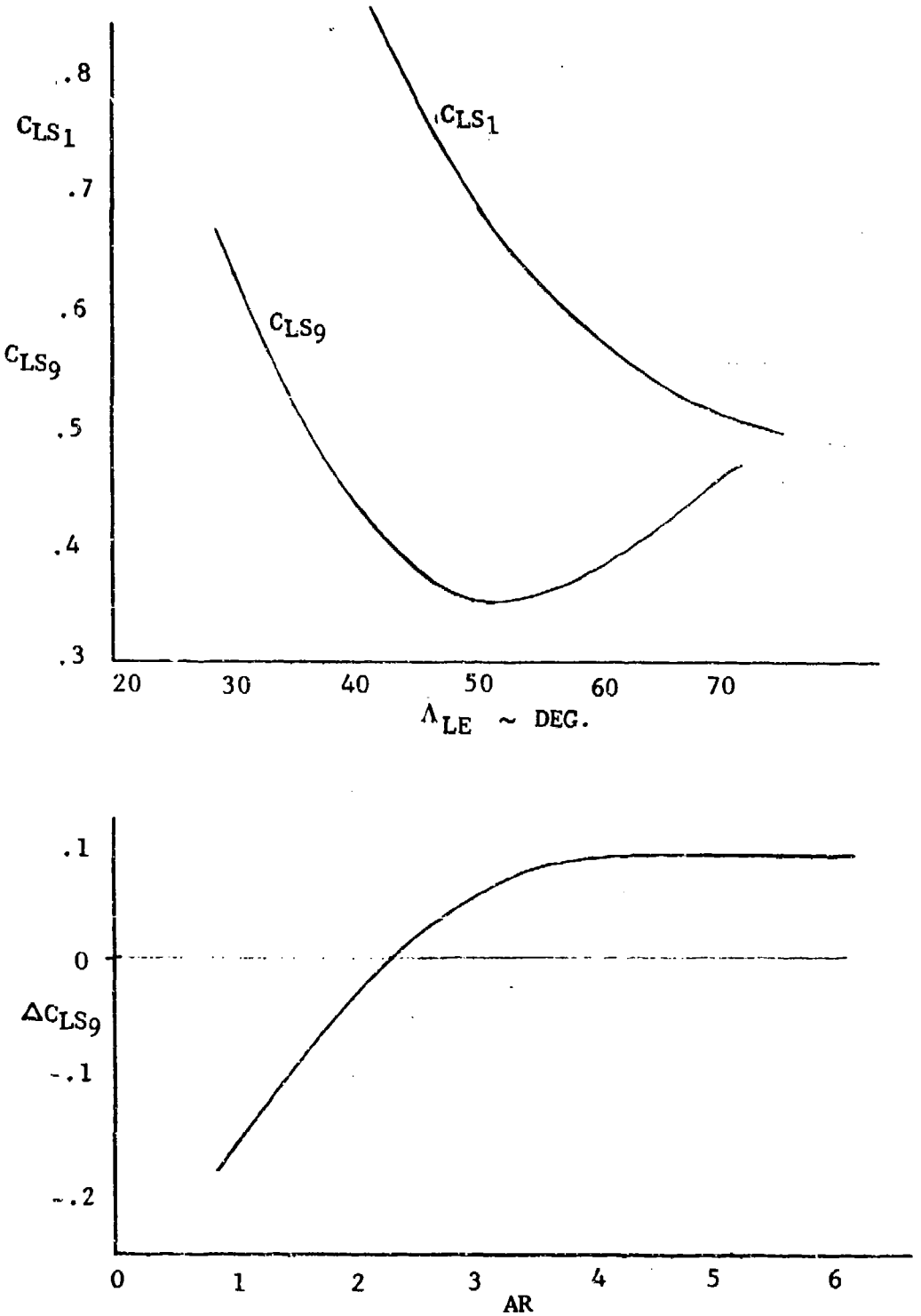

Figure 28 Supersonic Polar Break Lift Factors

The polar shape factor, K', above $C_{L_{PB}}$ is computed in Reference 13 as

$$K' = \frac{H}{C_{L_\alpha}} \tag{4-23}$$

where

$$H = \begin{cases} 1.1; & AR\tan\Lambda_{LE} \leq 3.5 \\ 1.1 + 0.1(AR\tan\Lambda_{LE} - 3.5); & AR\tan\Lambda_{LE} > 3.5 \end{cases} \tag{4-24}$$

5. CRITICAL MACH NUMBER AND DRAG RISE

The drag-divergence Mach number or Mach critical, is defined as the Mach number at which a rapid drag rise intercepts the subsonic trend in drag. The British method of predicting the critical Mach number for two-dimensional airfoils (Reference 14) appears to be the most accurate empirical method available. The British method uses the Sinnott "crest criteria", where the low-speed pressure at the airfoil crest is related to the drag-divergence Mach number.

The Large Aircraft program uses a method analogous to the British two-dimensional critical Mach number prediction procedure in order to predict the critical Mach number for a finite-aspect-ratio swept wing. The critical Mach number is defined as the value of freestream Mach number which produces a local supersonic flow measured normal to the sweep of the isobar at the crest. The local Mach number normal to the crest isobar is taken to be 1.02 for conventional airfoils and 1.05 for supercritical airfoils in order to define freestream critical Mach number. The sonic condition at the crest can be predicted by means of a simple equation in which the incompressible pressure at the crest of the airfoil and compressibility factors are used.

The value of 1.02 local Mach number for the weak shock at crest condition for drag rise used in Sinnott's transonic airfoil theory (Reference 15) was established empirically. Reference 14 shows that this method should predict M_{CR} to within +0.015 for the majority of conventional two-dimensional airfoils. However, as shown in Reference 14, with "peaky" airfoils (as in the supercritical airfoil) the onset of rapid drag rise may be delayed until the shock is substantially downstream of the crest. The predicted value of M_{CR} based on a local Mach of 1.02 at the crest may thus be conservative by more than 0.02, and a local Mach of 1.05 is necessary to achieve good correlation.

The following subsections discuss the methods used to predict the pressure distribution around an airfoil and to determine M_{CR} from the pressure at the crest along with the method used to estimate the drag rise above M_{CR}.

5.1 Pressure Coefficient Calculations

The incompressible, inviscid pressure distribution around the airfoil is first defined, from which the pressure at the crest can be determined. The method of Weber (Reference 16) was used for the pressure distribution calculations. This method requires the airfoil surface coordinates to be determined at the chordwise locations defined by

$$X(\nu) = \frac{1}{2}\left(1 + \cos\frac{\nu\pi}{N}\right) \quad \text{where } 0 \leq \nu \leq N \tag{5-1}$$

N may be any integer, but, in this program, N is set equal to 32.

The Weber formula is essentially a second-order linear theory whereby the pressures are determined from multiplication of the matrix of thickness and camber ordinates of the airfoil by a matrix of constants given in Reference 16.

The formula for the incompressible pressure distribution on an infinite sheared wing was obtained from the incompressible form of Equation 93 in Reference 16, resulting in

$$\begin{aligned}
1 - C_p = {} & \left[\frac{1}{1 + \left[\frac{S^{(2)}(X) \pm S^{(5)}(X)}{\cos\Lambda}\right]^2}\right] \\
& \times \Bigg(\Bigg\{\cos\alpha\left[1 + S^{(1)}(X)\cos\Lambda \pm S^{(4)}(X)\cos\Lambda\right] \\
& \pm \sin\alpha\cos\Lambda\left\{1 + \frac{S^{(3)}(X)}{\cos\Lambda}\right\}\left(\frac{1-X}{X}\right)^{\frac{1}{2}}\Bigg\}^2 \\
& \pm\Bigg\{\cos\alpha\left[S^{(1)}(X)\sin\Lambda \pm S^{(4)}(X)\sin\Lambda\right] \\
& \pm \sin\alpha\sin\Lambda\left\{1 + \frac{S^{(3)}(X)}{\cos\Lambda}\right\}\left(\frac{1-X}{X}\right)^{\frac{1}{2}}\Bigg\}^2\Bigg) \\
& + \sin^2\Lambda\cos^2\alpha\left\{1 - \frac{1}{1+\left[\frac{S^{(2)}(X)\pm S^{(5)}(X)}{\cos\Lambda}\right]^2}\right\}
\end{aligned} \tag{5-2}$$

For C_p on the upper surface the + is used, and for the lower-surface C_p the - is used. Also,

$$S^{(1)}(X) = \sum_{\mu=1}^{N-1} S^{(1)}_{\mu\nu} \quad Z_{t\mu}$$

$$S^{(2)}(X) = \sum_{\mu=1}^{N-1} S^{(2)}_{\mu\nu} \quad Z_{t\mu}$$

$$S^{(3)}(X) = \sum_{\mu=1}^{N-1} S^{(3)}_{\mu\nu} \quad Z_{t\mu} + S^{(3)}_{N} \sqrt{\rho/2c}$$

$$S^{(4)}(X) = \sum_{\mu=1}^{N-1} S^{(4)}_{\mu\nu} \quad Z_{s\mu}$$

$$S^{(5)}(X) = \sum_{\mu=1}^{N-1} S^{(5)}_{\mu\nu} \quad Z_{s\mu}$$

Tables of the $S^{(\ )}_{\mu\nu}$ matrices of constants are given in Reference 16. $Z_{t\mu}$ and $Z_{s\mu}$ are the thickness and camber distribution at the control point μ given by

$$Z_{t\mu} = \frac{1}{2}(y_u + y_\ell)$$

and

$$Z_{s\mu} = \frac{1}{2}(y_u - y_\ell)$$

where y_u and y_ℓ are the upper- and lower-surface ordinates defined at the control point μ given by

$$X(\mu) = \frac{1}{2}\left(1 + \cos\frac{\mu\pi}{N}\right)$$

5.2 Critical Mach Number Calculation from Crestline Pressure

The procedure followed to determine M_{CR} for swept wings is similar to the procedure outlined in Reference 14 to predict the M_{CR} for two-dimensional sections. In the procedure, Equation 5-2 is used to compute the pressure distribution around the airfoil at a sweep angle determined from

$$\Lambda = \begin{cases} \arccos(\cos\Lambda_{c/2})^n ; \Lambda_{c/2} \leq 40^\circ \\ \arccos\left[\dfrac{(\cos\Lambda_{c/2})^n + .76604^n}{2}\right] ; \Lambda_{c/2} > 40^\circ \end{cases} \qquad (5\text{-}3)$$

where $\Lambda_{c/2}$ is the wing mid-chord sweep at the semi-span of the wing and the factor n is determined from

$$n = \frac{AR}{1.4+AR}$$

The sweep angle Λ represents an effective isobar sweep at the mid-span region of the wing as affected by the root and tip regions of the wing. The procedure used to determine M_{CR} based on the crest pressures is as follows:

1. Determine a chordwise incompressible, inviscid pressure distribution for an angle of incidence (α). Integrate the pressure distribution to obtain the lift coefficient (C_{L_i}).

2. Determine the chordwise position of the crest for each α, the crest being defined as the point at which the airfoil surface is tangential to the undisturbed freestream direction ($\theta = \alpha$).

3. Determine the incompressible pressure coefficient at the crest ($C_{P_{crest}}$).

4. Use $C_{P_{crest}}$ to determine M_{CR} from the relation

$$C_{P_{crest}} = \frac{(P/P_t)(1+0.2M_{CR}^2\cos^2\Lambda)^{3.5} - 1}{0.7M_{CR}^2 / \sqrt{1-M_{CR}^2\cos^2\Lambda}} \qquad (5\text{-}4)$$

where (P/P_t) is the ratio of local static pressure to freestream stagnation pressure as determined from

$$P/P_t = \left[1 + 0.2M_l^2\right]^{3.5}$$

where M_l is the local Mach number normal to the isobar sweep Λ at the crest of the airfoil. M_l is set equal to 1.02 for conventional airfoils and 1.05 for "peaky" or supercritical airfoils. Equation 5-4 uses a Prandtl-Glauert compressibility factor to correct the incompressible pressure coefficient for Mach number rather than the Karman-Tsien factor used in Reference 14. References 17 and 18 recommend using the Prandtl-Glauert factor instead of the Karman-Tsien factor in the M_{CR} prediction method for highly cambered airfoils or general airfoils at high-lift coefficients. The relationship determined by Equation 5-4 is plotted in Figure 29.

5. Use the Prandtl-Glauert compressibility factor (β_D) evaluated at M_{CR} to obtain the lift coefficient C_{L_D} from

   $$C_{L_D} = C_{L_i}/\beta_D$$

6. Repeat Steps 1 through 5 for a set of incidences in order to obtain a drag-rise boundary from the set of points (C_{L_D}, M_{CR}).

The critical Mach number predicted by the above six steps is prevented from exceeding the critical Mach number of the fuselage alone (shown plotted in Figure 30). For aircraft that are not area-ruled, where the isobars are allowed to unsweep at the wing-fuselage juncture, the method would tend to overpredict M_{CR} when the value approaches the fuselage M_{CR}. The prediction-versus-test M_{CR} correlation shown in Figure 31 is thus applied for conventional-wing predictions.

5.3 Drag Rise

For Mach numbers less than M_{CR} the drag increases slowly with increasing Mach number. This drag component is known as compressible drag, or drag creep. Methodology for estimating this component of drag for conventional or supercritical wings was included in the subsonic drag buildup in Subsection 3.1. For Mach numbers greater than M_{CR}, drag rise begins and increases rapidly with Mach. Figure 32 illustrates the drag bookkeeping system followed in the Large Aircraft program

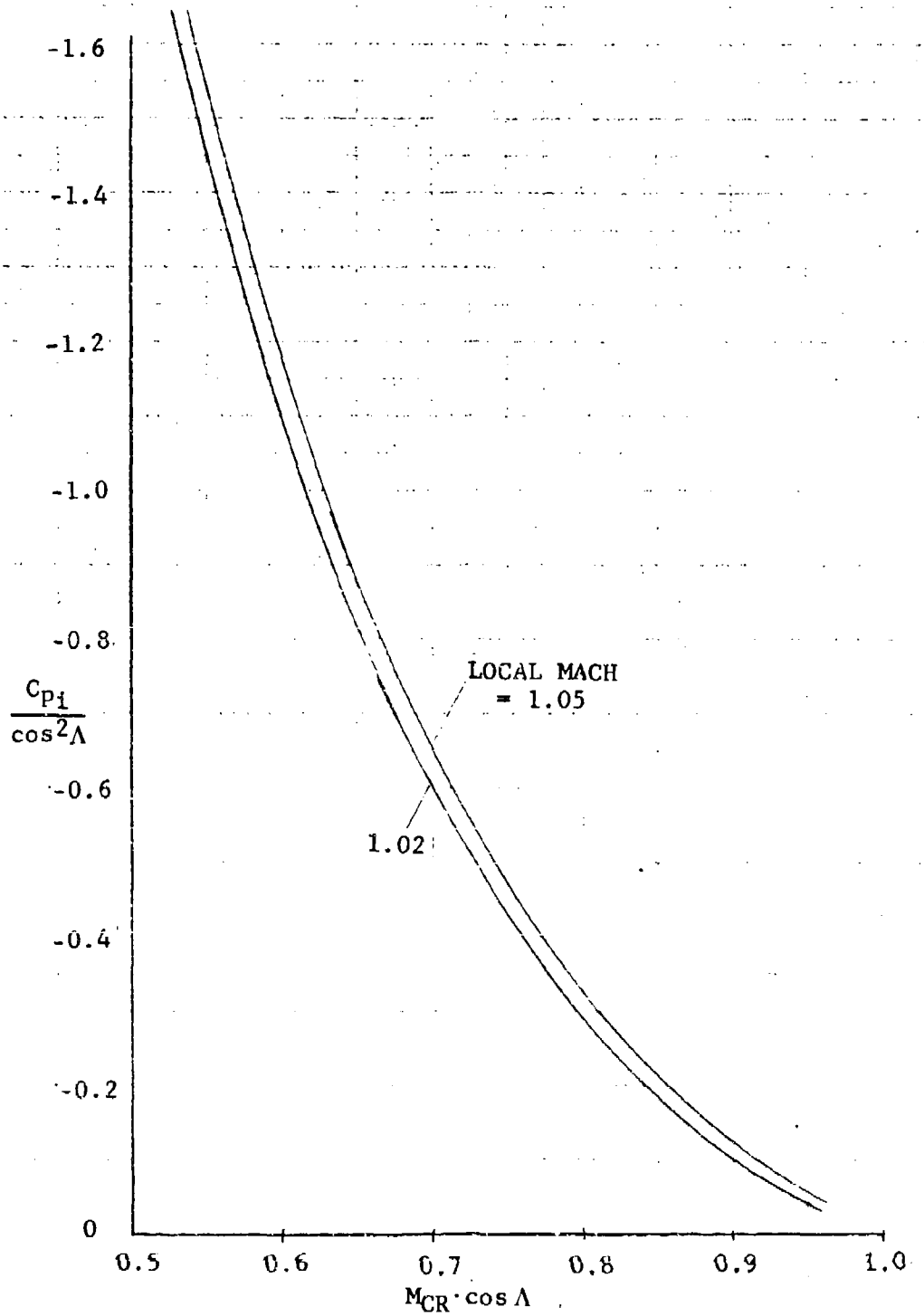

Figure 29 Mach Critical Prediction Chart

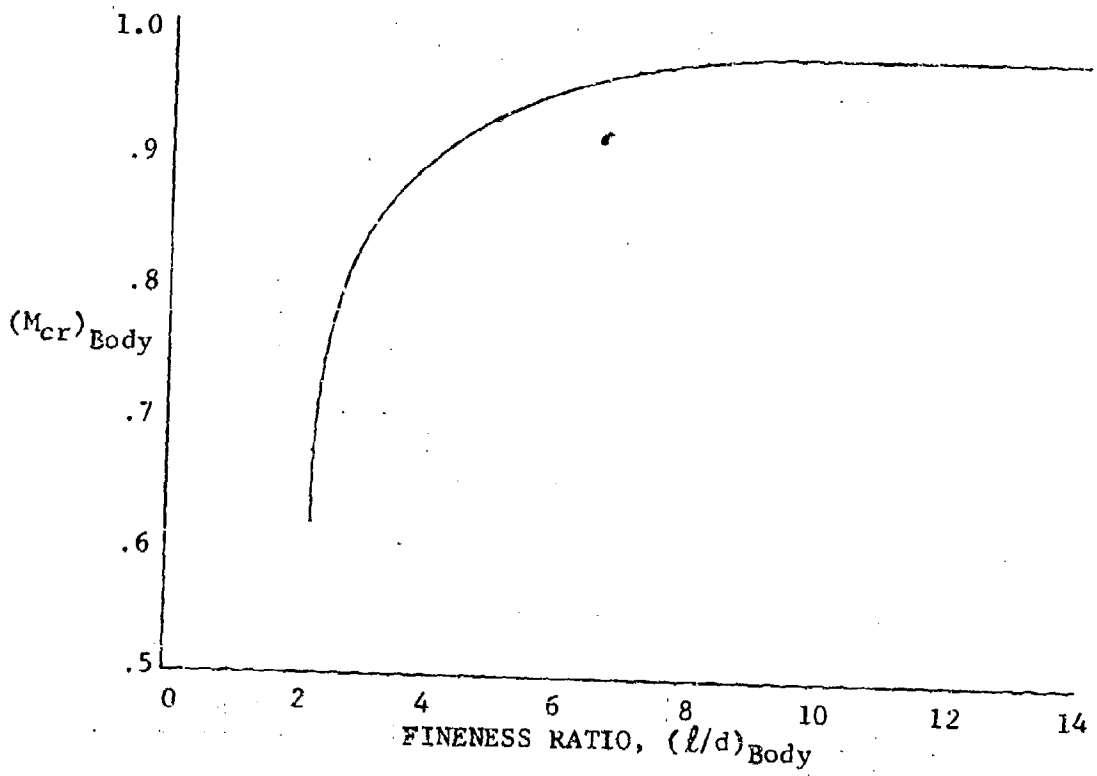

Figure 30 Prediction of Fuselage Critical Mach Number

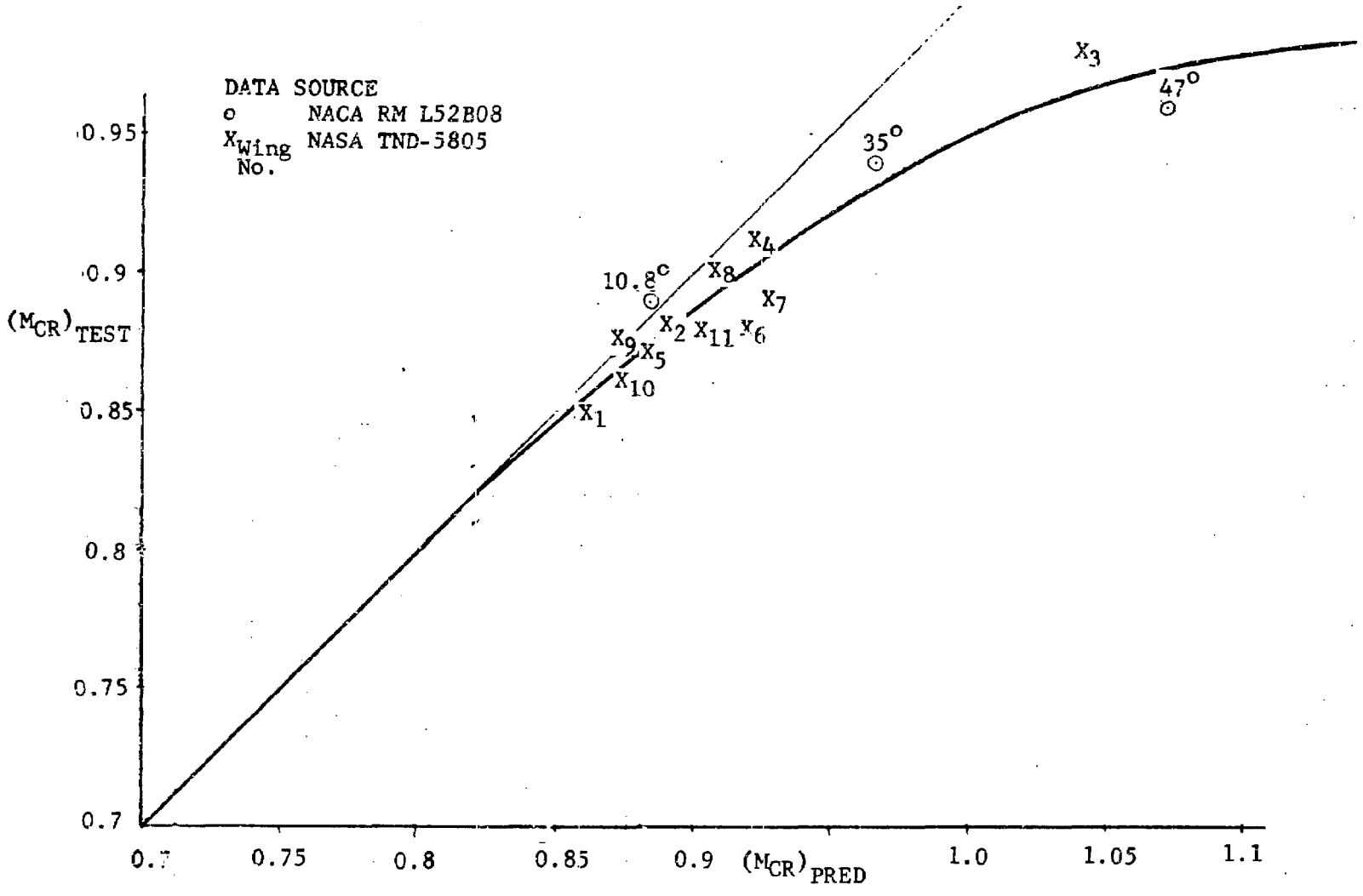

Figure 31 Correlation of Critical Mach Number for Conventional Wings

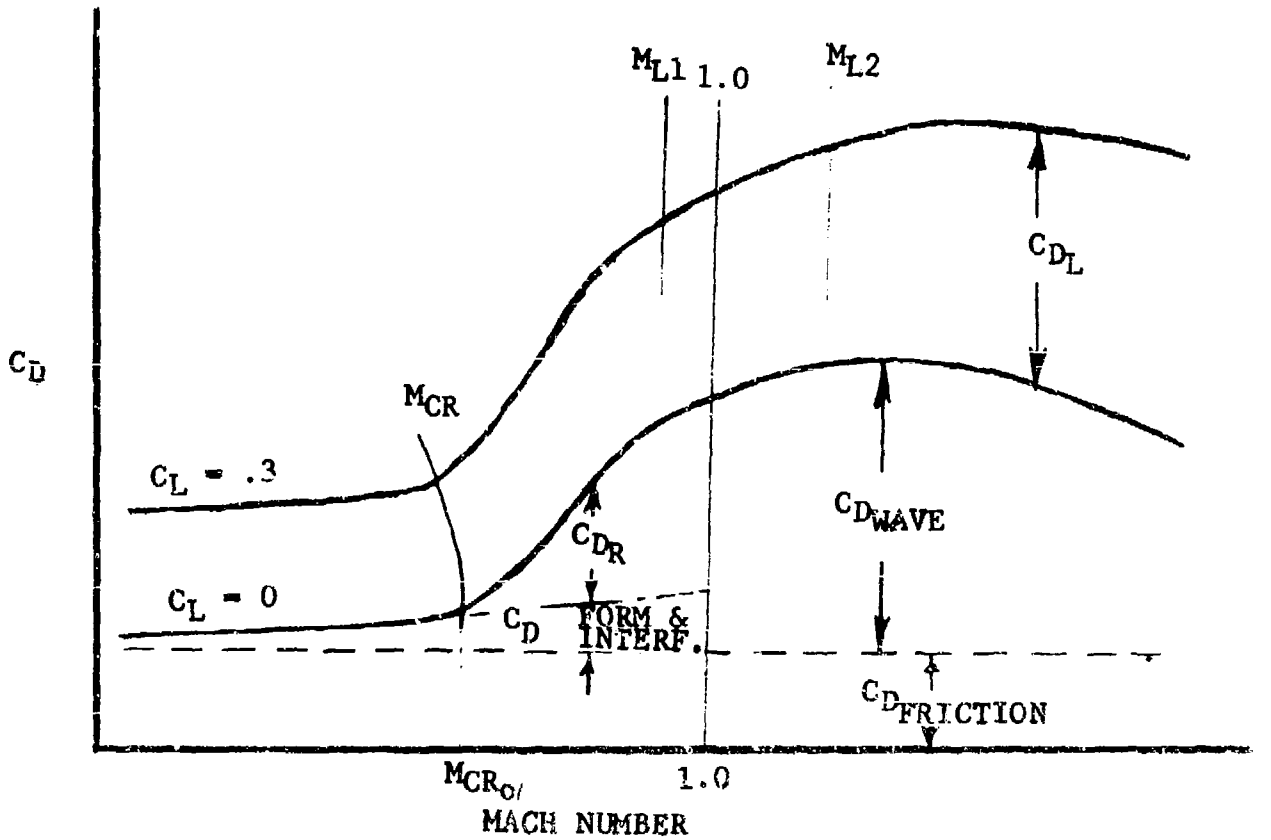

Figure 32 Transonic Drag Buildup

whereby beyond Mach 1.0 the drag rise and the interference plus form drag are replaced by wave drag. The drag rise is separated into two components, drag rise due to lifting surfaces and drag rise due to all other components on the aircraft. The drag rise due to lifting surfaces is represented by

$$C_{D_{RL}} = P_L\,(M-M_{CR})^2 \qquad (5\text{-}5)$$

where

$$P_L = 25 \cdot (t/c + 2f/c)\cdot(\cos\Lambda_{c/2})^3$$

The factor P_L is a function of the wing section thickness, t/c, maximum ordinate of the camber, f/c, and the midchord sweep, $\Lambda_{c/2}$. The total drag rise, at zero lift, due to lifting and non-lifting components is determined by

$$C_{D_{R_o}} = a_2(M-M_{CR_o})^2 + a_3(M-M_{CR_o})^3 \qquad (5\text{-}6)$$

where a_2 and a_3 are defined to produce a continuous zero-lift drag curve between M_{CR_o} and Mach 1.0. The drag rise is curve-fitted to begin at M_{CR_o} with zero slope and end at Mach = 1.0, matching the value and slope of the wave-drag curve. The coefficients a_2 and a_3 are calculated from

$$a_2 = \frac{3(C_{D_{W1}} - C_{D_{F\&I}}) - (1 - M_{CR_o})C_{D'_{W1}}}{(1 - M_{CR_o})^2}$$

$$a_3 = \frac{(1 - M_{CR_o})C_{D'_{W1}} - 2(C_{D_{W1}} - C_{D_{F\&I}})}{(1 - M_{CR_o})^3}$$

where $C_{D_{W1}}$, $C_{D_{F\&I}}$, and $C_{D'_{W1}}$ represent the Mach 1.0 value of the wave drag, form plus interference drag, and the slope of the wave drag, respectively. The non-lifting contribution to the drag rise is assumed to begin at M_{CR_o} and not vary with lift; using Equations 5-5 and 5-6, an equation for total drag rise at any lift condition can be determined from

$$C_{D_R} = P_L(M-M_{CR})^2 + (a_2-P_L)(M-M_{CR_o})^2 + a_3(M-M_{CR_o})^3 \qquad (5\text{-}7)$$

The change in M_{CR} with lift causes the subsonic drag polar to increase after M_{CR} (see Figure 32). For bookkeeping, the drag rise is separated into a minimum drag contribution and a contribution due to lift. The increment to the minimum drag is determined from Equation 5-6, and the increment at lift is determined by

$$C_{D_{R_{CL}}} = C_{D_R} - C_{D_{R_o}} \tag{5-8}$$

6. LIFT

The untrimmed lift of an aircraft can be represented by the equation

$$C_L = C_{L_\alpha} (\alpha - \alpha_{L_O})$$

For moderate to high aspect ratios and moderate sweeps, the lift equation is linear with (α) so that the lift-curve slope (C_{L_α}) is constant. The total lift-curve slope of the aircraft is given by

$$C_{L_\alpha} = (C_{L_\alpha})_{W-B} + (C_{L_\alpha})_T + (C_{L_\alpha})_B \qquad (6\text{-}1)$$

which is the sum of the wing (including body carry-over effects), horizontal tail, and the forward portion of the fuselage.

The following subsections describe the methods by which C_{L_α} and α_{L_O} are calculated along with the method of calculating the lift in the nonlinear range up to $C_{L_{MAX}}$.

6.1 Wing Lift-Curve Slope

The value of $(C_{L_\alpha})_{W-B}$ is predicted by the use of several rather involved semi-empirical equations. These equations were developed to predict wing lift-curve slope as a continuous expression in the subsonic, transonic, and supersonic regions. The value of $(C_{L_\alpha})_{W-B}$ is expressed as

$$(C_{L_\alpha})_{W-B} = (C_{L_\alpha})_{Basic} \cdot K_t \cdot K_b \cdot \frac{S_{PLAN}}{S_{REF}} \qquad (6\text{-}2)$$

where $(C_{L_\alpha})_{Basic}$ is the wing-alone C_{L_α} with no thickness effects. The factors K_t and K_b account for the effect of airfoil-thickness plus camber and fuselage interference, respectively. The equation for $(C_{L_\alpha})_{Basic}$ was evolved from the Polhamus (Reference 19) equation for trapezoidal wing .

$$C_{L_\alpha} = \frac{(\frac{a_o}{2})AR/57.3}{(\frac{a_o}{2\pi}) + \sqrt{(\frac{a_o}{2\pi})^2 + \left[1 - (M\cos\Lambda_{c/2})^2\right](\frac{AR}{2\cos\Lambda_{c/2}})^2}} \qquad (6\text{-}3)$$

for subsonic flow and the linear-theory level of

$$C_{L_\alpha} = \frac{4/57.3}{\sqrt{M^2-1}} \qquad (6\text{-}4)$$

for supersonic flow at the leading edge ($M > 1/\cos\Lambda_{LE}$).

To extend the Polhamus equation for use with non-trapezoidal wing planforms, Spencer (Reference 20) replaces $\cos\Lambda_{c/2}$ with the effective cosine mid-chord sweep determined by Equation 2-13.

When Equation 6-3 results were compared with subsonic experimental data, it was deduced that better agreement would be achieved if the predicted peak C_{L_α} were to occur at $M < 1.0$ (for moderate and high AR) and if the rate of increase in C_{L_α} with increasing M were larger. Consequently, Equation 6-3 was altered to

$$(C_{L_\alpha})_{Basic} = \frac{AR/57.3}{1+\sqrt{1+\left[1-(\cos\Lambda_{c/2})_e^{4/3}\left(\frac{M}{M^*}\right)^{8/3}\right]\left[\frac{AR}{2(\cos\Lambda_{c/2})_e}\right]^2}} \qquad (6\text{-}5)$$

where the sectional lift-curve slope a_o equals 2π, and M* is the limiting M for the application of Equation 6-5. M* is a function of AR and $\Lambda_{c/2}$ and is defined by

$$M^* = M_o^* + (1-M_o^*)\left[1-(\cos\Lambda_{c/2})_e\right]^2 \qquad (6\text{-}6)$$

where

$$M_o^* = (10 + 0.91AR^3)/(10 + AR^3)$$

In effect, M* is the Mach number at which the rate of increase in C_{L_α} with M begins to decrease. Note that, at M=0, Equations 6-3 and 6-5 are identical. However, it was also found desirable (for improved correlation) to limit $(\cos\Lambda_{c/2})_e$ to the range $0.94 \geq \cos\Lambda_{c/2} \geq 0$. Thus, in applying Equation 6-5, sweep angles of less than 20 degrees are treated as having a value of $\cos\Lambda_{c/2} = 0.94$.

For thin wings, experimental levels of C_{L_α} characteristically reach a peak at speeds somewhat greater than M*. With low sweep and moderate to high AR, the peak occurs below M=1, while with high sweep and/or low AR, the peak may be at or above sonic speeds. At speeds well above sonic, C_{L_α} then decreases with increasing M and, when the leading-edge becomes supersonic ($M > \cos\Lambda_{LE}^{-1}$), the level approaches the two-dimensional-theory level of $C_{L_\alpha} = 4/(57.3\sqrt{M^2-1})$. To emulate these trends, Equation 6-5, was modified by a factor term and an adder term, each to be applied only at $M > M^*$. These new terms are included in the modified equation:

$$(C_{L_\alpha})_{Basic} = \frac{1/57.3}{(1/C_{L_{\alpha o}})(\frac{M^*}{M})^Z + \beta'/4}; \quad M > M^* \qquad (6\text{-}7)$$

where $C_{L_{\alpha o}}$ is defined as $(C_{L_\alpha})_{Basic}$ at $M = M^*$ in radians, and

$$\beta' = (M-M^*)\left[1 + (M^*/M)^Y\right]^2$$

$$Y = \frac{1+\pi AR}{3+\pi AR}\left(2 - 2/3\sqrt{\lambda} - \lambda^2\right)$$

and

$$Z = M^* C_{L_{\alpha o}} + \frac{AR^2}{3\,\frac{\pi AR}{C_{L_{\alpha o}}}\left(\frac{\pi AR}{C_{L_{\alpha o}}} - 1\right)(\cos\Lambda_{c/2})_e^{2/3}}$$

Wings having thick airfoils undergo a degradation in C_{L_α} beginning at $M > M^*$. The level of C_{L_α} versus M dips, usually reaching a minimum at $M < 1.0$, and then recovers to a second peak level at $M > 1.0$. To account for this phenomenon, the basic C_{L_α} equations have been modified by a factor, K_t, as defined by

$$K_t = \begin{cases} 1 - \left[4\sigma_1(1-\sigma_1)\right]^3 \cdot \gamma & ; \; M_1 \leq M \leq M_2 \\ 1 - \left[4\sigma_2(1-\sigma_2)\right]^3 \cdot \gamma & ; \; M_2 \leq M \leq M_3 \\ 1.0 & M_1 \geq M \geq M_3 \end{cases} \qquad (6\text{-}8)$$

where γ, σ_1, σ_2, M_1, M_2, M_3 are as defined by the equations below:

$$\gamma = \frac{9\Delta(t/c)/(\cos\Lambda_{c/2})_e}{1+\frac{1}{2}AR[\Delta(t/c)/(\cos\Lambda_{c/2})_e]}$$

where

$$\Delta(t/c) = t/c - (t/c)_{\alpha_{im}}$$

$$(t/c)_{\alpha_{im}} = \frac{1}{4.4AR(\cos\Lambda_{c/2})_e^{3/2}} \qquad (6\text{-}9)$$

The equation for γ is applicable for

$$0 \leq \frac{\Delta(t/c)}{(\cos\Lambda_{c/2})_e} \leq 0.07$$

$$0 \leq \frac{AR\Delta(t/c)}{(\cos\Lambda_{c/2})_e} \leq 0.10$$

If $\Delta(t/c)/(\cos\Lambda_{c/2})_e > 0.07$, use 0.07

If $AR\,\Delta(t/c)/(\cos\Lambda_{c/2})_e > 0.10$, use 0.10

$$\sigma_1 = \tfrac{1}{2}\,\frac{M-M_1}{(M_2-M_1)}$$

$$\sigma_2 = \tfrac{1}{2}\,(1 + \frac{M-M_2}{M_3-M_2})$$

$$M_1 = 1-2(t/c)(\cos\Lambda_{c/2})_e^{3/2}\left[1+\frac{3}{2}(C_{L_d})^{3/2}\right]\frac{AR^3}{4+AR^3} \qquad (6\text{-}10)$$

$$M_2 = M_1 + t/c$$

Note: $0 \leq M_1 \leq M^*$

If $M_1 > M^*$, use $M_1 = M^*$

$$M_3 = 1.0 + t/c$$

The derivation of Equation 6-8 is based on the data trends and analyses of Reference 21 and on other limited data (e.g., References 22 and 23). It should be noted that a C_{L_α} "bucket" is

predicted only if the wing streamwise airfoil t/c exceeds the limit thickness defined by Equation 6-9. The limit-thickness boundary was established from the statistical boundaries presented in Reference 24.

Another factor in the wing C_{L_α} prediction equation (Eq. 6-1), is the fuselage interference factor, defined by

$$K_b = (1 + d/b)(1 - d/b)^f \qquad (6\text{-}11)$$

where

$$f = \frac{16+3AR^2}{8+5AR^2}$$

b = wing total span
d = body total width at wing junction

The factor K_b accounts for the change in wing lift due to the body segment which enshrouds the wing and to the wing-induced lift on that body segment. Based on semi-empirical derivations presented in Reference 25, K_b is independent (to the first order) of M. It is noted that the total lift of a wing/body configuration is derived by adding the body-alone lift to that obtained for the wing-alone as modified by the factor K_b.

Application of Equations 6-2, 6-5, 6-7, 6-8, and 6-11, for the prediction of $(C_{L_\alpha})_{W-B}$ will yield trends as sketched in Figure 33. It is noted that the technique is strongly dependent on the value of (t/c) in the transonic speed regime if (t/c) exceeds the limiting value defined in Equation 6-9.

Substantiation of the C_{L_α} prediction technique described above in the form of comparisons with a wide range of experimental data is presented in References 1 and 26. The derivation of C_{L_α} for Mach numbers greater than M*, presented in original Reference 26, relied heavily on transonic-bump test data, which characteristically produces a trend such as shown in Figure 33. The new derivation (Equation 6-7) relies on sting-mounted test data, which produces a less abrupt transition in (dC_{L_α}/dM) in the transonic region.

6.2 Supercritical Wing Lift-Curve Slope

The wing lift-curve slope technique described above in Section 6.1 would underpredict C_{L_α} when compared against supercritical wing data. In a study of the factors affecting

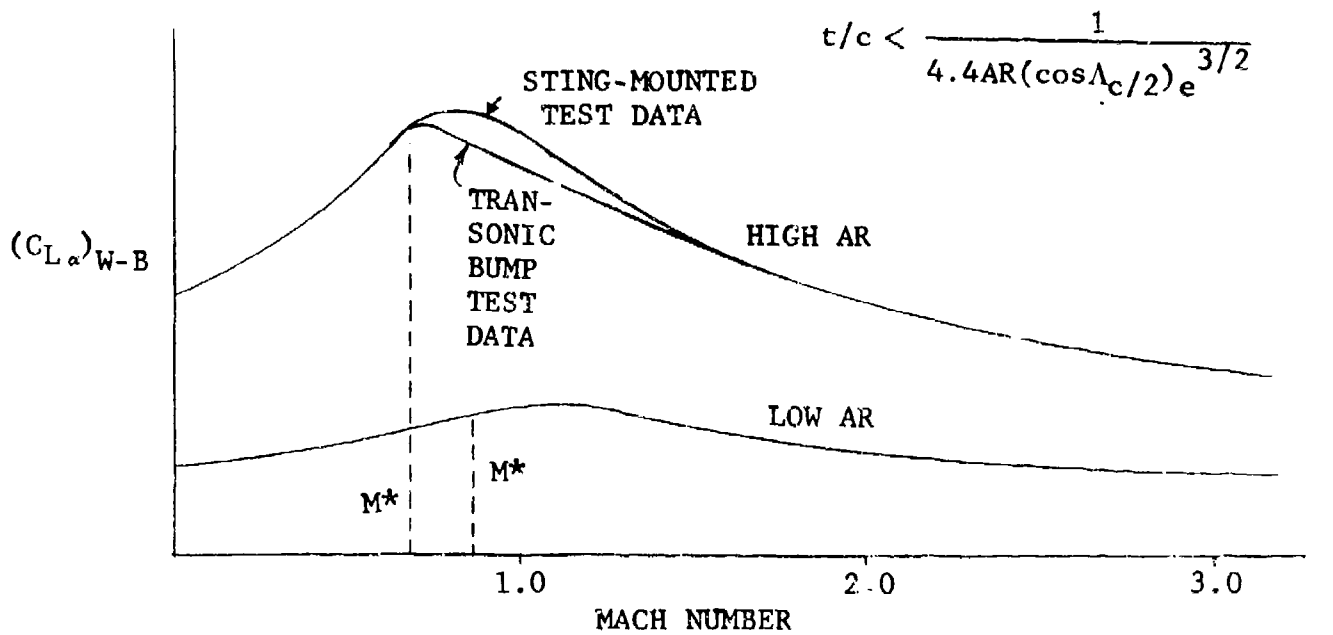

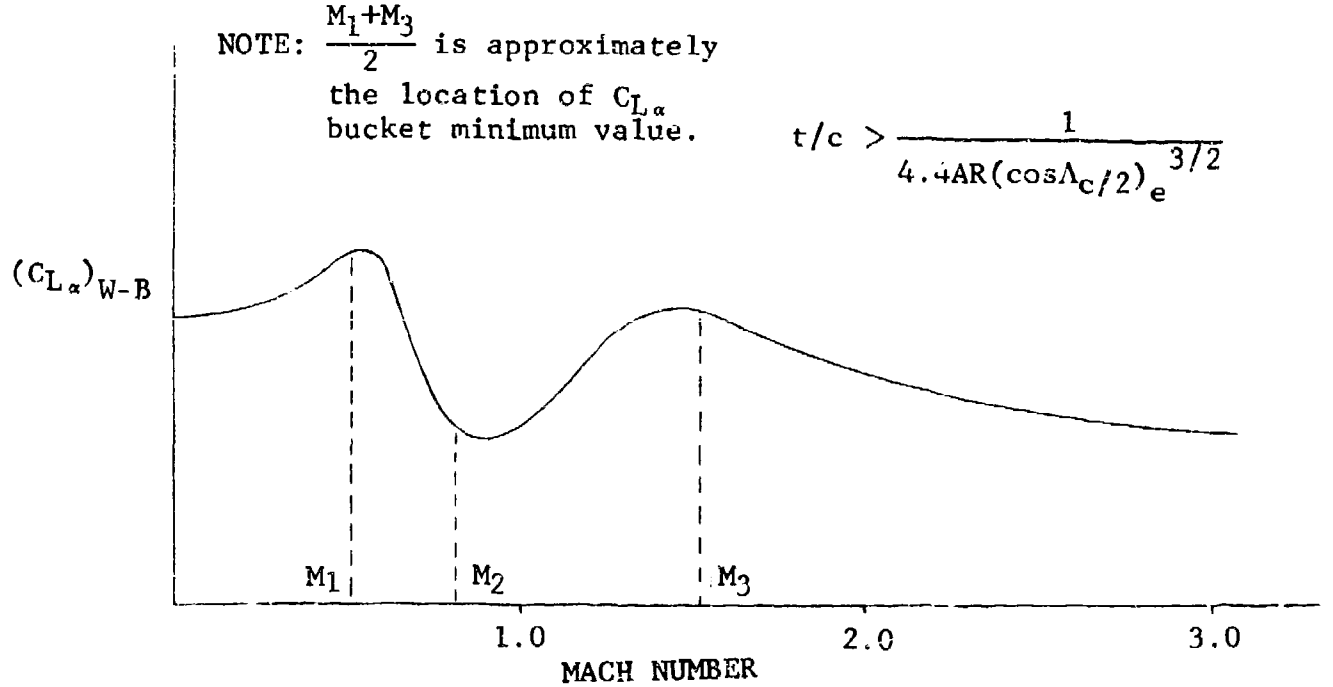

Figure 33 Typical Lift-Curve Slopes

lift, it was concluded that the reason C_{L_α} was being underpredicted is due primarily to the thickness correction factor, K_t (Equation 6-8), and the incompressible sectional lift-curve slope, a_o (Equation 6-3).

For supercritical wings, the onset of the lift divergence Mach number, M_1, is delayed to a higher value as compared to conventional wings. For supercritical wings, the factors M_1, M_2, and γ in Equation 6-8 are modified as follows:

$$(M_1)_{SCW} = (M_1)_{CONV} + 0.09$$

$$(M_2)_{SCW} = (M_2)_{CONV} + 0.045$$

$$(\gamma)_{SCW} = (\gamma)_{CONV} \cdot \frac{(M_3-M_1)_{SCW}}{(M_3-M_1)_{CONV}}$$

This modification delays the thickness correction factor to a higher Mach number and also decreases the extent by which K_t is reduced at M_2.

Supercritical wings have a higher sectional lift-curve slope compared with conventional wings. The program uses

$$\frac{a_o}{2\pi} = 1 + \frac{1.174\ t/c}{\sqrt{1-M^2}}$$

for supercritical wings in place of $a_o/2\pi = 1$ for conventional wings.

6.3 Tail Lift-Curve Slope

The lift-curve slope of the horizontal tail can be estimated from the equation

$$(C_{L_\alpha})_T = (C_{L_\alpha}')_T \left[K_{W(B)} + K_{B(W)}\right] \left(1 - \frac{\partial \epsilon}{\partial \alpha}\right) \frac{q_t}{q_\infty} \frac{S_T}{S_{REF}} \qquad (6\text{-}13)$$

where $(C_{L_\alpha}')_T$ is the exposed-area lift-curve estimate for the tail; $K_{W(B)}$ and $K_{B(W)}$ are the Pitts, Nelson, and Kaattari body-lift carry-over factors (Reference 27); $\partial\epsilon/\partial\alpha$ is the downwash gradient; q_t/q_∞ is the dynamic pressure ratio; and S_T is the

exposed tail area. The exposed-area lift-curve for the tail is estimated by use of the exposed planform of the tail and the method described in Section 6.1.

6.3.1 Downwash at the Tail

An empirical method of estimating the low-speed downwash gradient behind straight-tapered wings is given in the DATCOM by

$$\left(\frac{\partial \epsilon}{\partial \alpha}\right)_o = 4.44 \left[K_A K_\lambda K_H (\cos \Lambda_{c/4})^{\frac{1}{2}} \right]^{1.19} \qquad (6\text{-}14)$$

The factors K_A, K_λ, and K_H are wing aspect ratio, wing taper ratio, and horizontal-tail-location factors, respectively, determined from

$$K_A = 1/AR - 1/(1+AR^{1.7})$$

$$K_\lambda = \frac{10-3\lambda}{7}$$

and

$$K_H = \frac{(1-h_t/b)}{(2\ell_t'/b)^{1/3}}$$

where AR and λ are the wing aspect and taper ratios, respectively, h_t is the height of the tail relative to the wing chord plane and ℓ_t' is the distance between the exposed MAC of the wing and the exposed MAC of the tail. At higher speeds the effect of compressibility on downwash is approximated by

$$\frac{\partial \epsilon}{\partial \alpha} = \left(\frac{\partial \epsilon}{\partial \alpha}\right)_o \frac{(C_{L_\alpha})_M}{(C_{L_\alpha})_o} \qquad (6\text{-}15)$$

where $(C_{L_\alpha})_o$ and $(C_{L_\alpha})_M$ are the wing lift-curve slopes at low speed (M=0.1) and at the appropriate Mach number, respectively.

6.3.2 Dynamic Pressure at the Tail

The method for estimating the dynamic-pressure q_t/q_∞ at the tail is based on the DATCOM method which relates the dynamic-pressure ratio to the drag coefficient of the wing. The steps involved in determining the dynamic pressure at some distance aft of the wing root chord, outlined in Section 4.4.1 of the DATCOM report, are as follows

1. Calculate the half-width of the wing wake by

$$\frac{Z_w}{c} = 0.68\sqrt{C_{D_o}\left(\frac{x}{c} + 0.15\right)} \qquad (6\text{-}16)$$

where x is the longitudinal distance measured from the wing-root-chord trailing edge, Z_w is the half-width of the wake at any position x, and C_{D_o} is the wing zero-lift drag coefficient.

2. Calculate the downwash in the plane of symmetry at the vortex sheet by

$$\epsilon = \frac{1.62}{\pi AR}\left(C_{L_\alpha} \cdot 2\right) \qquad (6\text{-}17)$$

3. Determine the vertical distance Z from the vortex sheet to the quarter-chord point of the MAC of the horizontal tail by

$$Z = x \tan\left(\gamma + \epsilon - 2\right) \qquad (6\text{-}18)$$

where $\gamma = \tan^{-1}\left(h_t/\ell_t\right)$.

4. Determine the dynamic-pressure-loss ratio at the wake center by

$$\left(\frac{\Delta q}{q}\right)_o = \frac{2.42(C_{D_o})^{1/2}}{\left(\frac{x}{c} + 0.3\right)} \qquad (6\text{-}19)$$

5. Determine the dynamic-pressure-loss ratio for points not on the wake centerline by

$$\frac{\Delta q}{q_\infty} = \left(\frac{\Delta q}{q}\right)_o \cos^2\left(\frac{\pi}{2}\frac{Z}{Z_w}\right) \tag{6-20}$$

6. Determine the dynamic pressure ratio at an arbitrary distance x aft of the wing-root-chord trailing edge by

$$\frac{q_t}{q_\infty} = 1 - \frac{\Delta q}{q_\infty} \tag{6-21}$$

6.4 Body Lift-Curve Slope

As shown in Reference 28, the linearized lift-curve slope for a body can be expressed as

$$(C_{L_\alpha})_B = k_1 \left(\frac{L}{L_N}\right)^{1/3} \frac{F}{S_{Ref}} \tag{6-22}$$

where L is the body length, L_N is the forebody length, F is the body cross-sectional area, and k_1 is a linear-potential lift-curve-slope parameter. The factor k_1 (a function of body width b, body height, h, and the perimeter of an elliptical body with equal area, p) is determined from the curve given in Figure 34, which is taken from Reference 28.

6.5 Angle of Attack at Zero Lift

The angle of attack at zero lift, α_{Lo}, is determined from

$$\alpha_{Lo} = (\alpha_{Lo})_{CAMBER} + (\alpha_{Lo})_{TWIST} + (\alpha_{Lo})_{INCIDENCE} \tag{6-23}$$

The effect of camber, C_{L_d} on α_{Lo} is calculated from

$$(\alpha_{Lo})_{CAMBER} = \left(\frac{\partial \alpha_{Lo}}{\partial C_{\ell_d}}\right) C_{L_d} \tag{6-24}$$

where $(\partial\alpha_{Lo}/\partial C_{\ell_d})$ is shown plotted in Figure 35, which is obtained from two-dimensional data.

The increment in α_{Lo} due to wing twist, τ, is calculated from

$$(\alpha_{Lo})_{TWIST} = -\left(\frac{\partial \alpha_{Lo}}{\partial \tau}\right)\tau \tag{6-25}$$

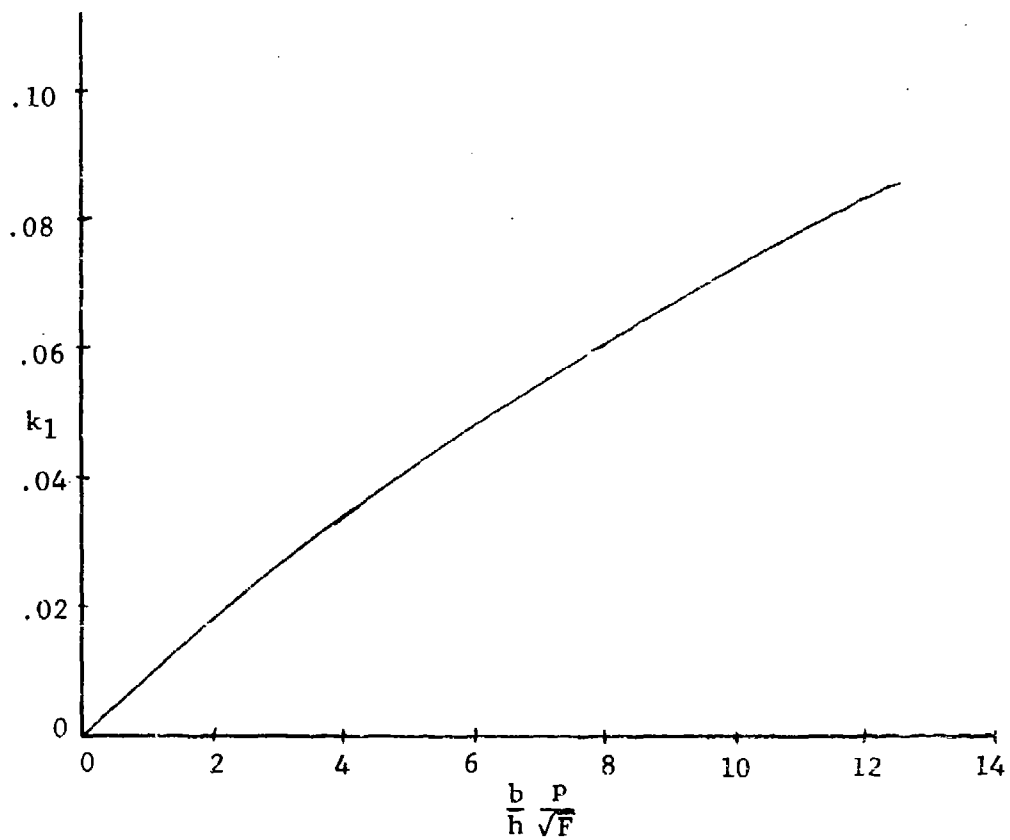

Figure 34 Factor Used in Determination of Body Lift-Curve Slope

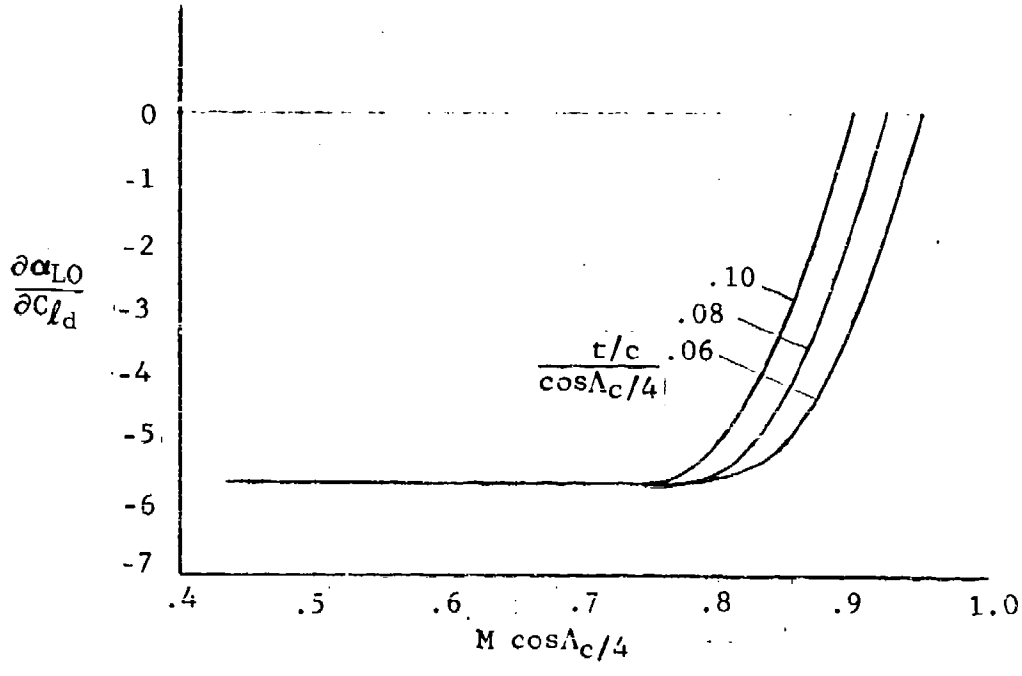

Figure 35 Camber Factor for Zero-Lift Angle of Attack

where $\partial\alpha_{L_0}/\partial\tau = 0.093 - 0.000571\Lambda_\beta + 0.5761\lambda - 0.2645\lambda^2$ and $\Lambda_\beta = \tan^{-1}(\tan\Lambda_{c/4}/\beta)$ (deg) The equation for $(\partial\alpha_{L_0}/\partial\tau)$ was obtained from a curve fit of the parametric data reported by Gilman and Burdges (Reference 29) for wings with linear-element twist.

The angle of attack in the program is measured relative to the wing root-chord reference plane. For variable-sweep configurations the angle of attack for any sweep position is measured from the wing chord plane in the forward sweep position. The increment in α_{L_0} due to wing and horizontal tail incidence is calculated from

$$(\alpha_{L_0})_{INCIDENCE} = \frac{(C_{L_\alpha})_{BODY}(i_w) + (C_{L_\alpha})_{TAIL}(i_w - i_t)}{C_{L_\alpha}} + (i_w - i_{w_{REF}}) \qquad (6\text{-}26)$$

where

$$(C_{L_\alpha})_{BODY} = (C_{L\alpha})_{NOSE} + \left(\frac{K_{B(W)}}{K_{W(B)} + K_{B(W)}}\right)(C_{L\alpha})_{W-B}$$

When $M > 1$, the contribution of camber and twist to α_{L_0} is set equal to zero and only the incidence effect is continued supersonically.

6.6 Nonlinear Lift of High-Aspect-Ratio Wings

The lift characteristics of a high-aspect-ratio wing is illustrated in the sketch. A high aspect ratio is defined as $AR > AR_{LOW}$, where AR_{LOW} is defined in Section 6.9 (Equation 6-37). The lift varies linearly with angle of attack up to C_{L_S}, after which the lift variation becomes non-linear.

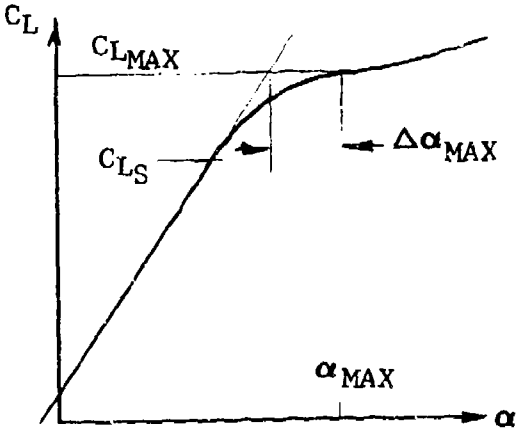

The angle of attack for a specified lift coefficient is calculated from

$$\alpha = \frac{C_L}{C_{L_\alpha}} + \alpha_{L_o} + \Delta\alpha \tag{6-27}$$

where

$$\Delta\alpha = \begin{cases} 0; & C_L \leq C_{L_S} \text{ or } M > 1.0 \\ \left(\dfrac{C_L - C_{L_S}}{C_{L_{max}} - C_{L_S}}\right)^2 \cdot \Delta\alpha_{max}; & C_{L_S} < C_L \leq C_{L_{max}} \\ \left(\dfrac{C_L - C_{L_S}}{C_{L_{max}} - C_{L_S}}\right)^2 \cdot \Delta\alpha_{max} + 5^o; & C_L > C_{L_{max}} \end{cases} \tag{6-28}$$

and $C_{L_S} = C_{L_\alpha}(\alpha - \alpha_{L_o} - 2\Delta\alpha_{max})$

The prediction of $C_{L_{max}}$ and $\Delta\alpha_{max}$ for high-aspect-ratio wings is discussed in Section 6.9.

6.7 Nonlinear Lift of Low-Aspect-Ratio Wings

The subsonic characteristic of a low-aspect-ratio wing is illustrated in the sketch. The total lift is equal to the potential lift plus the vortex-induced lift from the leading edge and tip of the wing. The equation

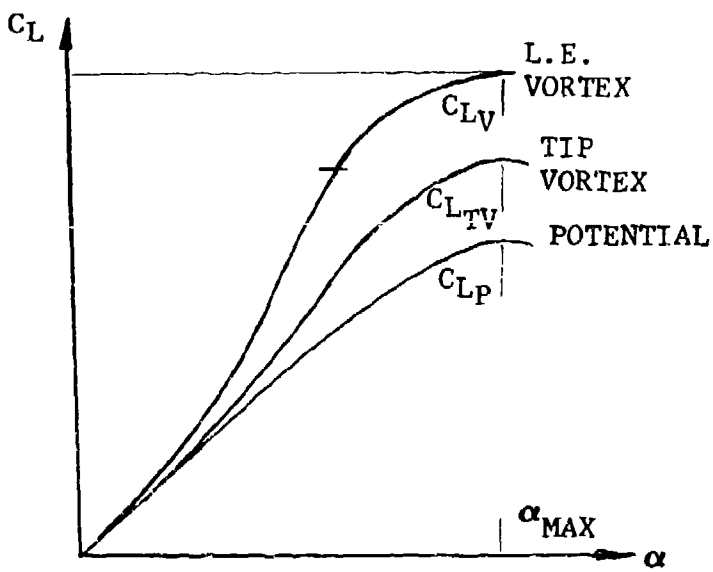

for lift can be expressed as

$$C_L = C_{L_P} + C_{L_V} + C_{L_{T_V}} \tag{6-29}$$

The method of predicting each of these terms is discussed in the following subsections.

6.7.1 Potential-Flow Lift

The potential-flow lift is determined from

$$C_{L_P} = K_p \sin\alpha\cos^2\alpha + C_{L_o} \tag{6-30}$$

where K_p is the lift-curve slope given by small-disturbance potential-flow lifting-surface theory, and the trigonometric terms account for the leading-edge separation effects (Reference 30). The value of K_p is the lift-curve slope (C_{L_α}), converted to radians, obtained from Equation 6-1. The factor C_{L_o} is the lift at zero angle of attack predicted by

$$C_{L_o} = -C_{L_\alpha}\alpha_{L_o}$$

6.7.2 Leading-Edge Vortex Lift

The leading-edge vortex lift is determined from

$$C_{L_V} = (1-R) \cdot F_{VB} \cdot K_V \sin^2\alpha\cos\alpha \tag{6-31}$$

In this equation, developed in Reference 31, the sharp-leading-edge suction analogy of Polhamus is modified to account for round-leading-edge and vortex-breakdown effects.

In Figure 36 (taken from Reference 36) the theoretical variation of the vortex lift factor K_V with aspect ratio and cutout factor is shown. The factor F_{VB} (shown in Figure 37) is a vortex-breakdown factor, which was obtained from the ratio of experimental data to theoretical for sharp-leading-edge delta wings. The factor R in Equation 6-31 is a leading-edge suction parameter (Reference 33). For a sharp leading edge, the suction parameter is near zero; for a rounded leading edge, the suction parameter is near unity at low alphas. The variation of R versus α is shown in Figure 38 as a function of thickness ratio.

Ref. 32, Fig. 3

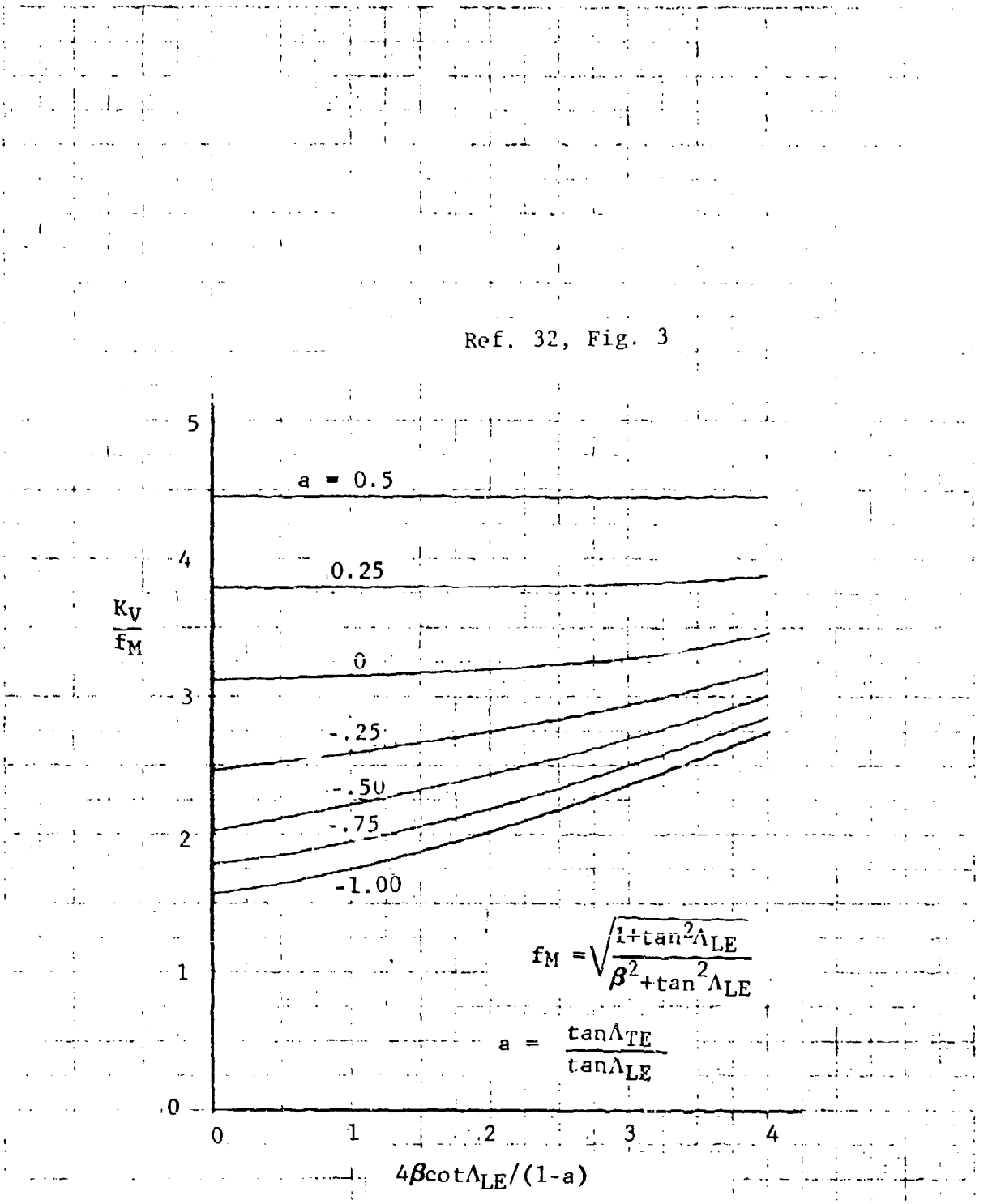

Figure 36 Variation of Vortex-Lift Constant with Planform Parameters

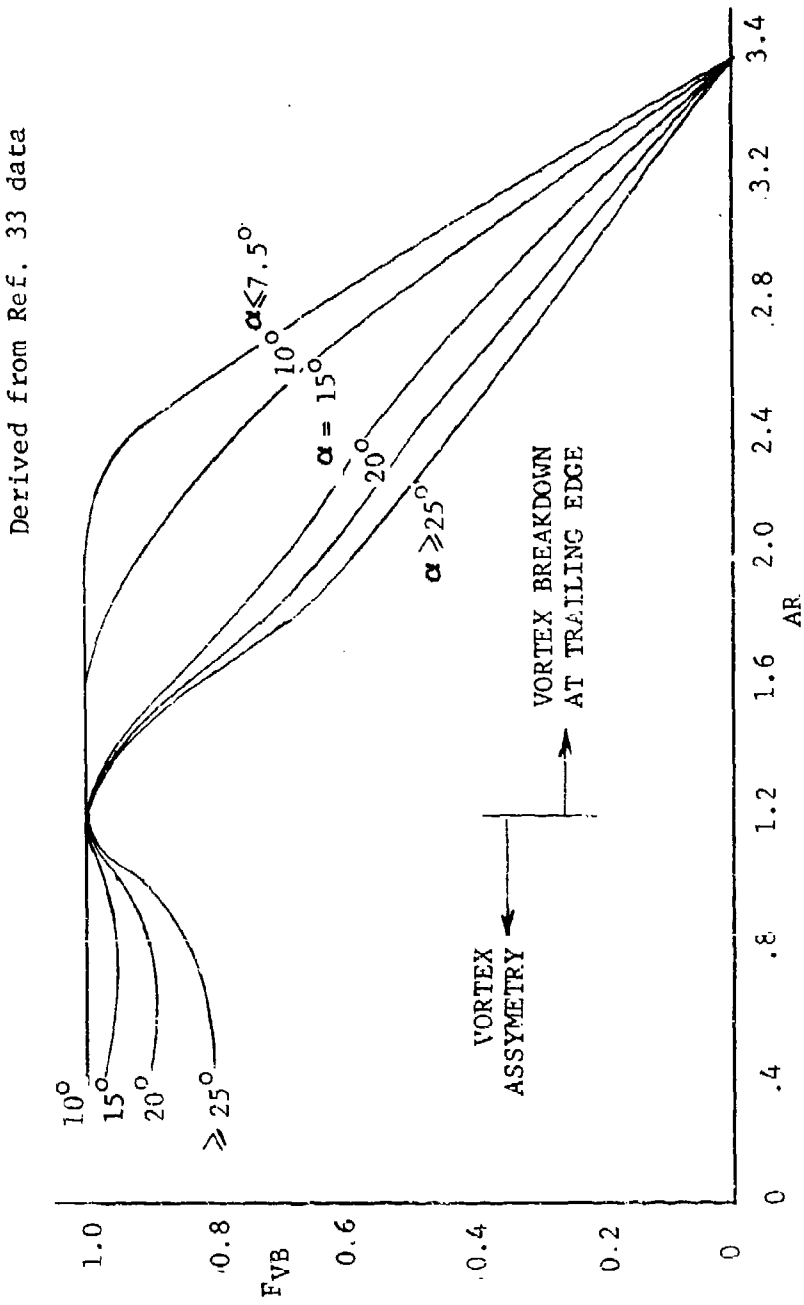

Figure 37 Variation of Vortex Breakdown Factor with Aspect Ratio and Angle of Attack

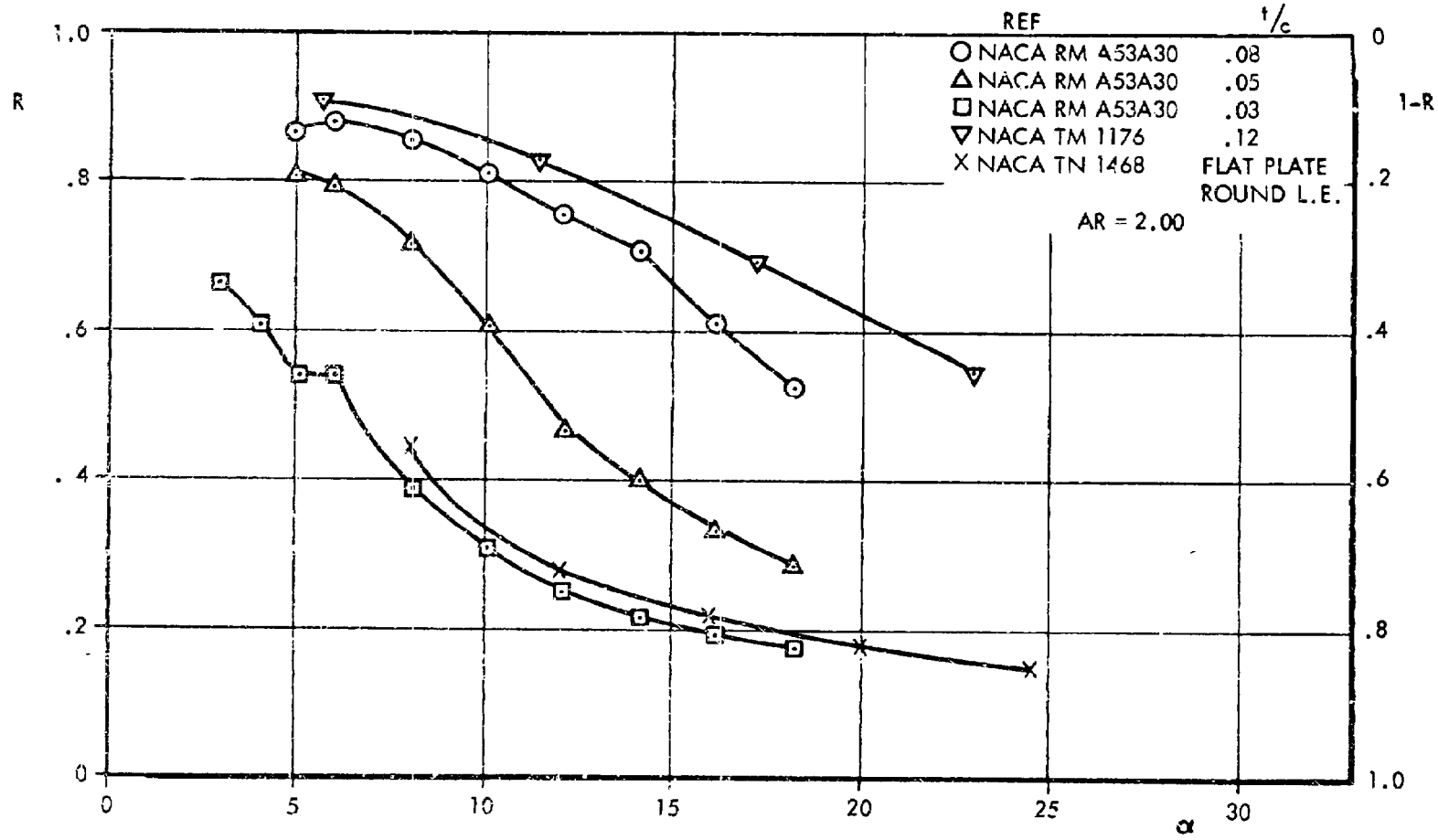

Figure 38 Experimental Variation of Leading-Edge Suction Parameter R with Angle of Attack For Round-Leading-Edge Delta Wings

6.7.3 Tip-Vortex Lift

For wings having a tip chord greater than zero, a tip vortex forms that induces an additional lift contribution on the wing. At low angles of attack the flow around the wing leading edge and tip is attached, and a vortex sheet is formed at the trailing edge (Figure 39a). At slightly higher angles of attack (Figure 39b), the flow possibly will make the turn around the leading edge of the wing without separating, but the flow around the tip separates. In this stage, the flow forms a vortex sheet consisting of a horizontal part originating from the trailing edge and two vertical sheets attached to it originating from the two sides of the wing. Küchemann (Reference 34) noted that a spanwise cross-section through the vortex sheet has the same shape as that obtained behind a wing with end plates. The height of the "end-plate vortex" or tip vortex is approximated by

$$h/b = \frac{\alpha}{2}\,\frac{C_T}{\bar{c}}\,\frac{1}{AR} \tag{6-32}$$

where C_T is the tip chord. With the height of the tip vortex known, the incremental tip-vortex lift can be expressed as

$$C_{L_{T_V}} = \left\{ \frac{Z+\sqrt{1+Z^2}}{xZ+\sqrt{1+(xZ)^2}} - 1 \right\} K_p \sin\alpha \tag{6-33}$$

where

$$Z = 2\cos\Lambda_{c/2}/AR$$

$$x = 1.0014-1.969(h/b)+3.0021(h/b)^2-2.0072(h/b)^3 \tag{6-34}$$

Equation 6-33 was derived (Reference 34) by modifying the Helmbold lift equation, where the effect of the end-plates are expressed as a factor 1/x to the aspect ratio. Equation 6-34 is a curve fit of the end-plate effect shown in Figure III.A.4-1 of Reference 4.

It can be seen from Equation 6-32 that the end-plate effect becomes smaller with increasing aspect ratio. This explains why the end-plate effect of the tip vortex has rarely been noticed for wings of moderate and large aspect ratios, although it always existed. The tip-vortex method is shown

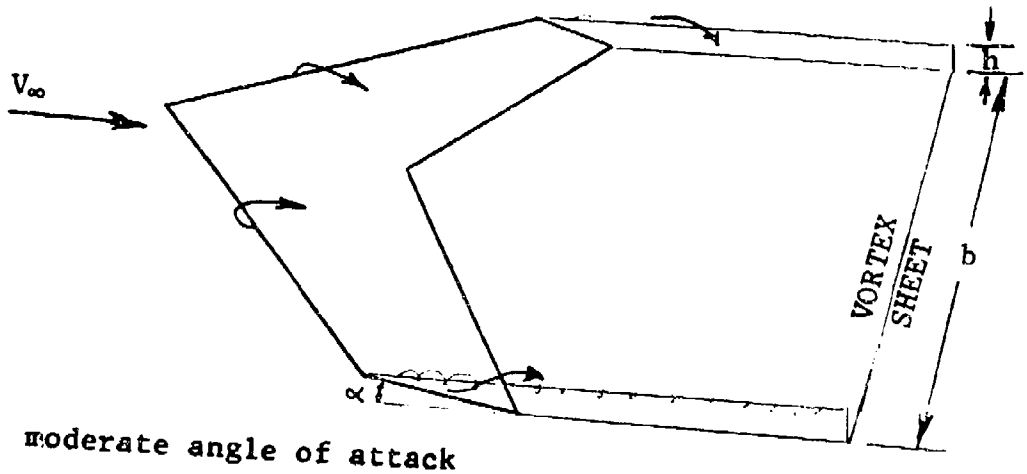

39b moderate angle of attack

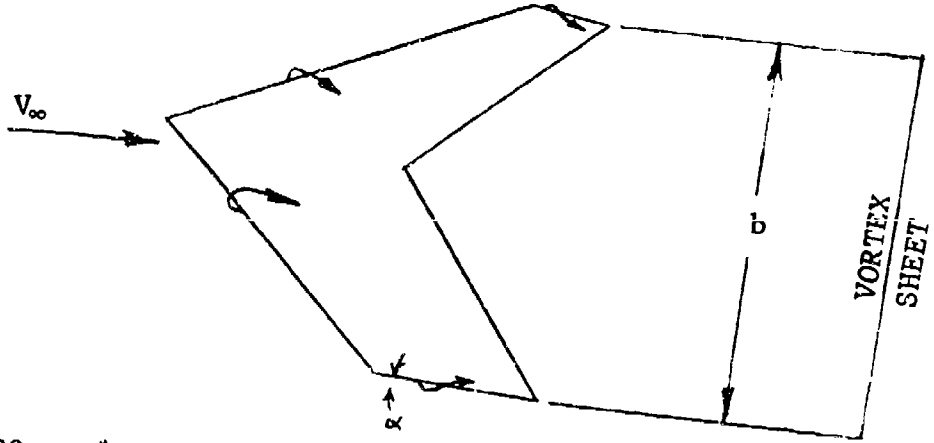

39a low angle of attack

Figure 39 Sketch of Possible Flow Patterns

in Reference 34 to give good agreement with experimental data for unswept rectangular wings ranging in aspect ratio from 0.5 to 2.0. It is stated in Reference 34 that the end-plate analogy can be used for straight or swept wings.

The nonlinear lift calculated by Equation 6-29 is limited by the maximum lift coefficient, $C_{L_{max}}$, of the wing. The value of $C_{L_{max}}$ and the angle at which maximum lift occurs, α_{max}, are predicted by the low-aspect-ratio method given in Section 6.9. The leading-edge vortex is then limited by the condition

$$C_{L_V} \leq C_{L_{MAX}} - (C_{L_P})_{MAX} - (C_{L_{TV}})_{MAX} \qquad (6\text{-}35)$$

where $(C_{L_P})_{MAX}$ and $(C_{L_{TV}})_{MAX}$ are the values calculated for the potential lift and the tip-vortex lift at the maximum-lift angle of attack. If $(C_{L_P})_{MAX} > (C_L)_{MAX}$, it is assumed that the leading-edge and tip vortices are too weak to add much lift to the wing, and the high-aspect-ratio method discussed in Section 6.6 is then used to predict the lift up to stall.

Results of applying the nonlinear lift prediction procedure are shown in Figures 40 through 43. The data were taken from Reference 35, which reports on a test of a series of clipped delta wings. The program results are shown as the solid lines for the complete lift and as dashed lines for the initial value of the lift-curve slope, C_{L_α}. The results, in general, are good and indicate a substantial amount of the lift is due to the vortices.

6.8 Nonlinear Lift of Cranked Wings

The method available in the Large Aircraft program for predicting the subsonic lift variation of cranked wings is based on the technique presented in Reference 9. This method assumes that as the outboard panel of a cranked wing experiences stall, the inboard panel still continues to lift. This behavior is believed to be caused by the influence of the leading-edge vortex of the inboard panel. Consequently, the flow field is similar to that of a low-aspect-ratio delta wing with leading-edge separation.

The method employs the results of a data correlation accomplished to provide a technique for determining the nonlinear lift of double-delta wings. It is hypothesized that the nonlinear lift of a cranked wing should be similar

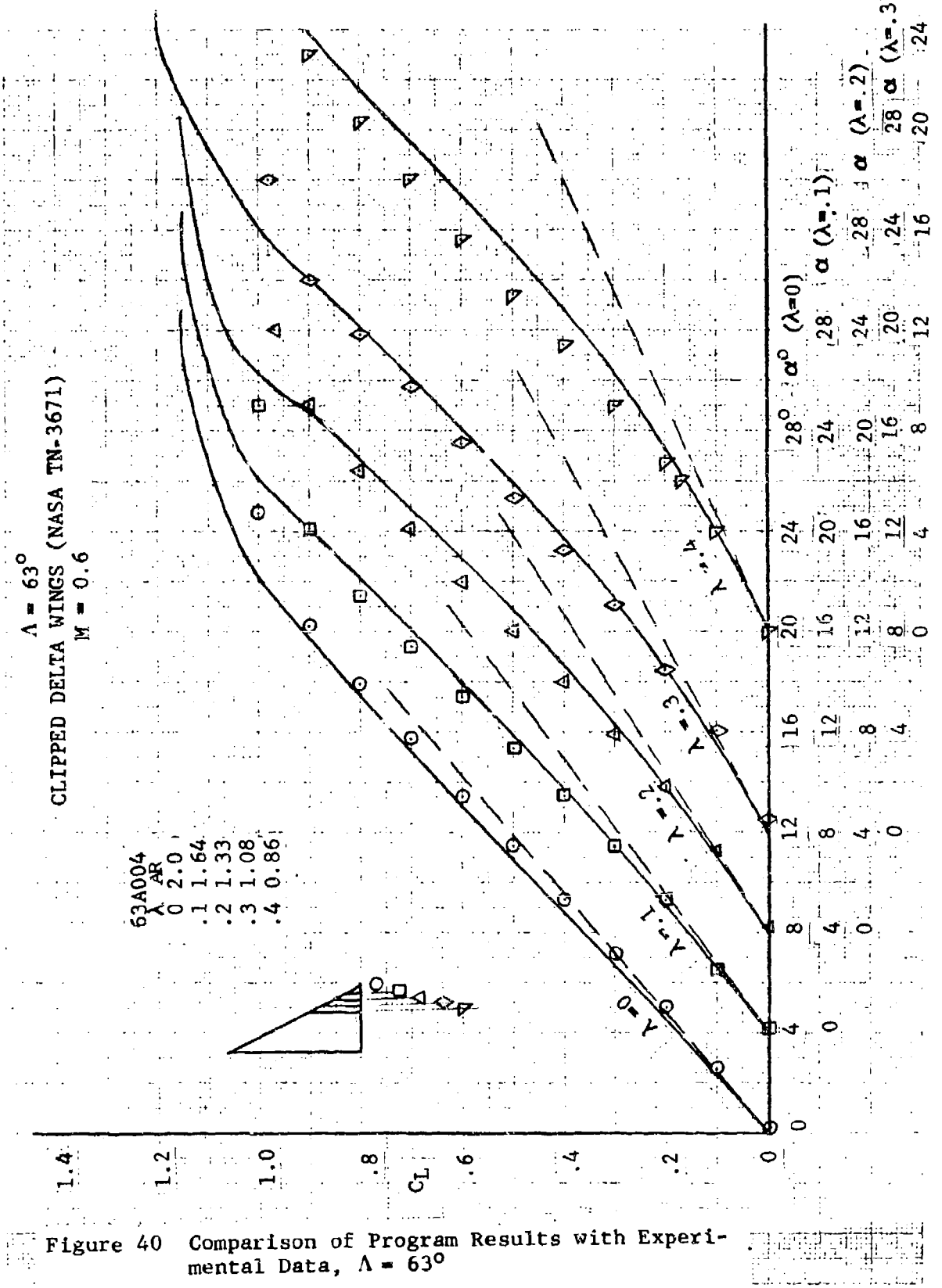

Figure 40 Comparison of Program Results with Experimental Data, Λ = 63°

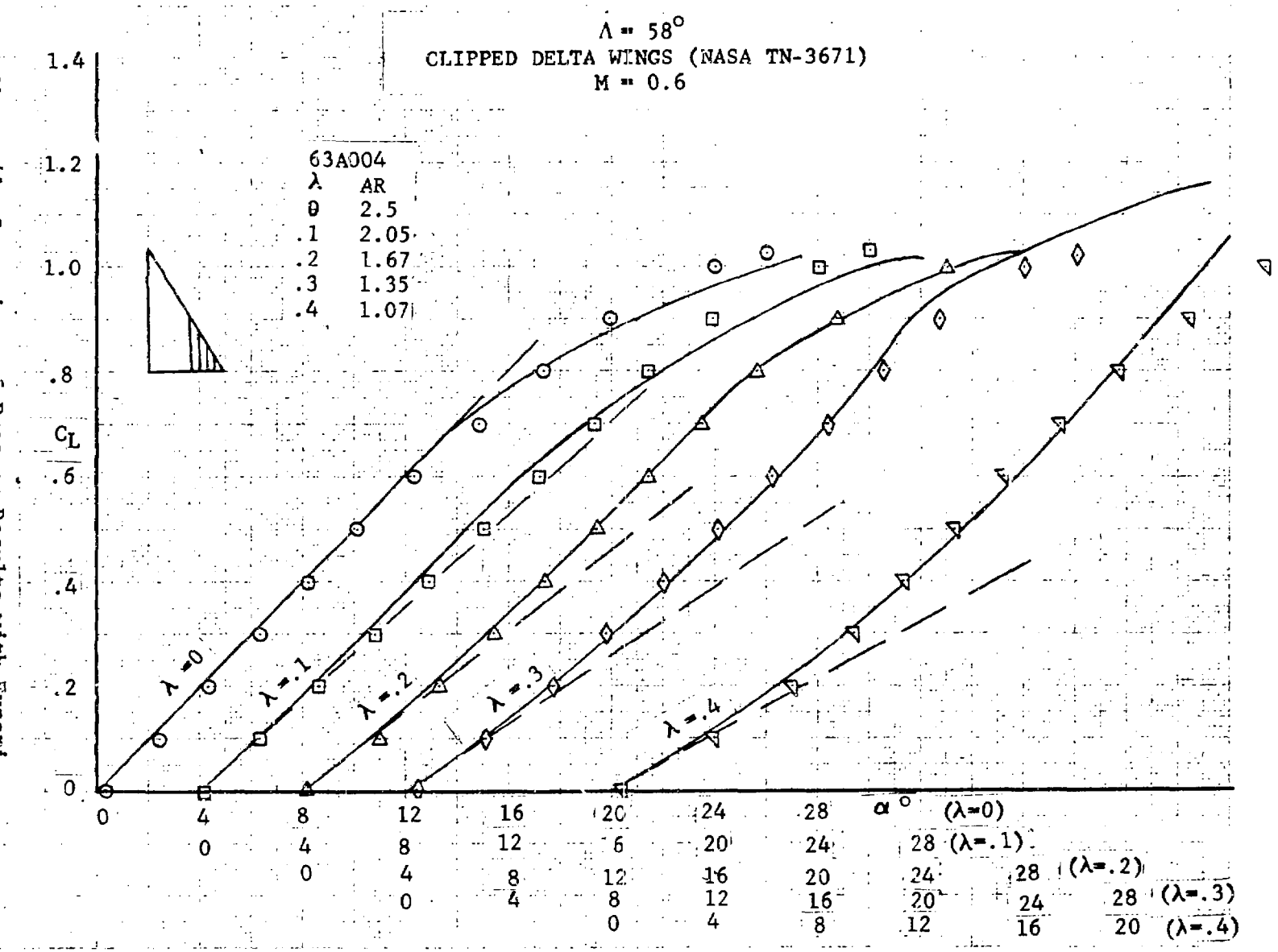

Figure 41 Comparison of Program Results with Experimental Data, Λ = 58°

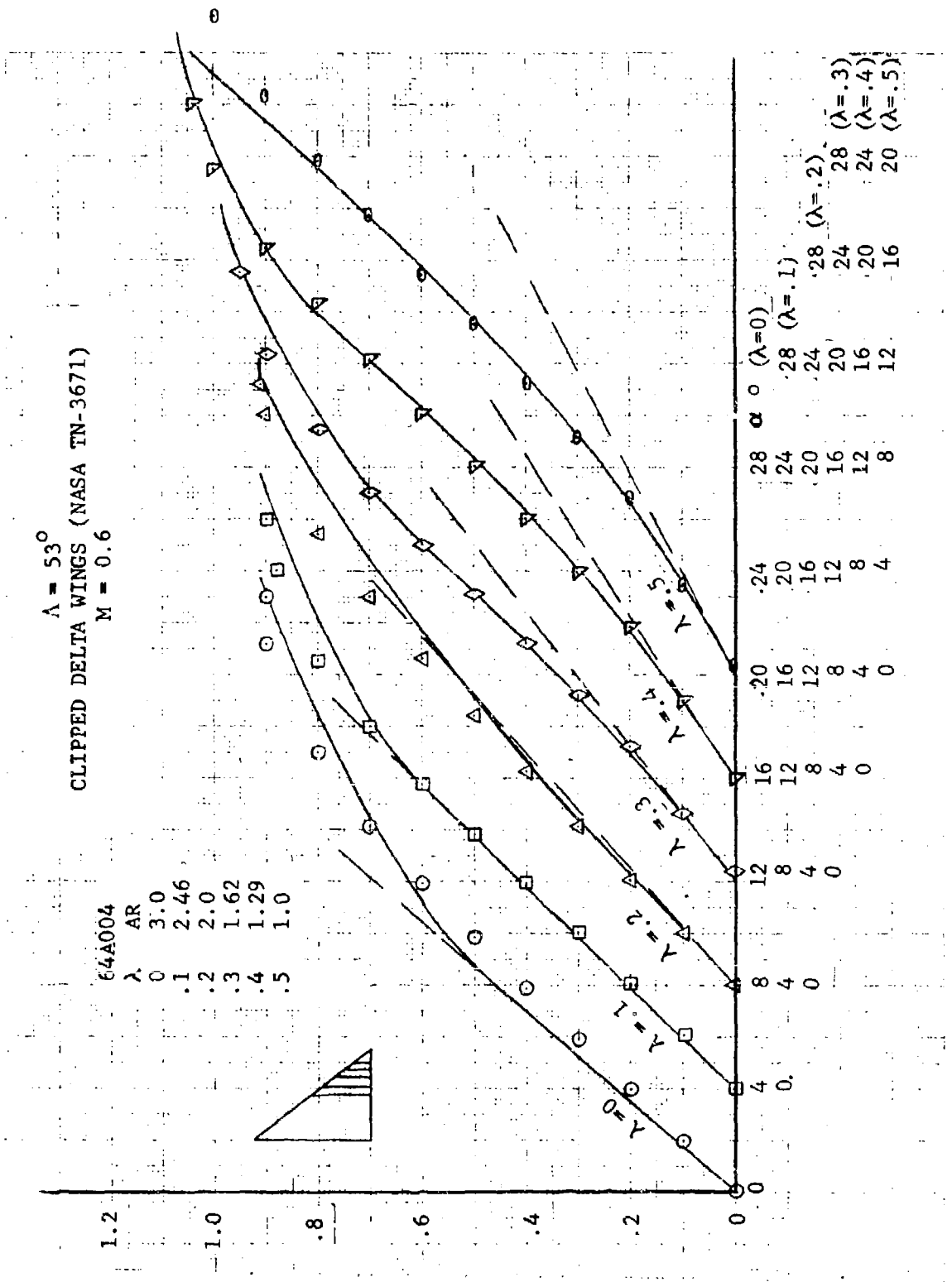

Figure 42 Comparison of Program Results with Experimental Data, $\Lambda = 53^{\circ}$

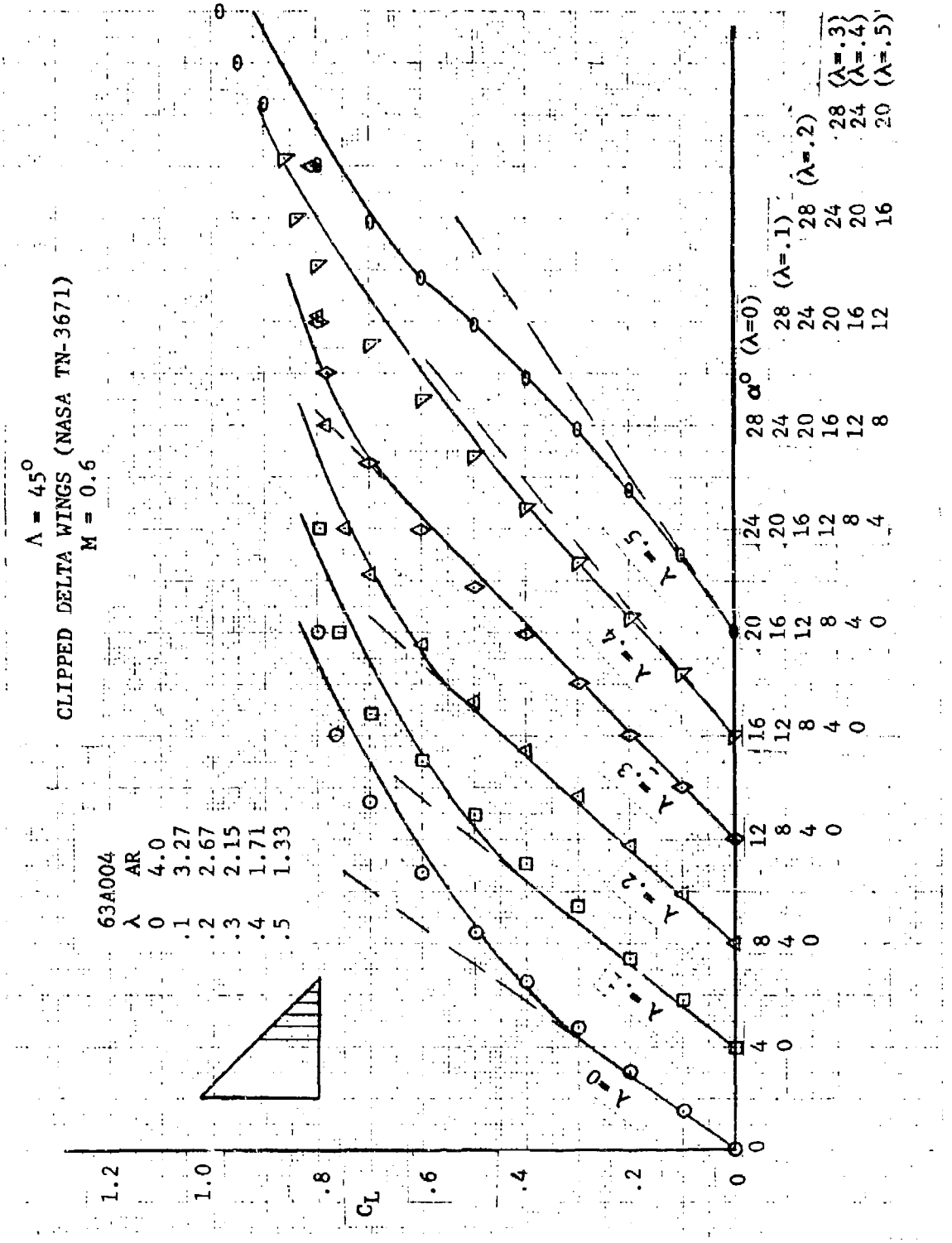

Figure 43 Comparison of Program Results with Experimental Data, $\Lambda = 45°$

to that of a double-delta wing. The nonlinear-lift curve construction technique for cranked wings is shown in Figure 44.

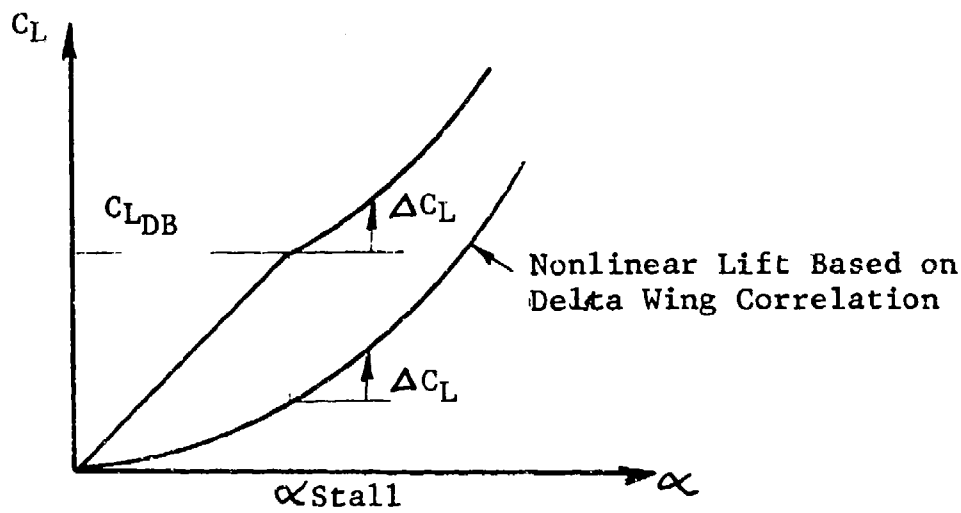

Figure 44 Construction of Nonlinear Lift Curve for Cranked Wings

Except for some slight refairing of the data correlation curves to account for aspect ratios of less than 1.0, the method employed in the program is essentially the same as that presented in Reference 9. The nonlinear angle of attack for a given C_L is calculated from

$$\alpha = \left[\frac{1}{a} \frac{C_L}{C_{L_\alpha}} \frac{A_i}{\eta_B} \right]^{1/n} \qquad (6\text{-}36)$$

where

C_{L_α} is the linear lift-curve slope (including outboard panel)

A_i is the aspect ratio of the inboard panel, defined as shown in Figure 45.

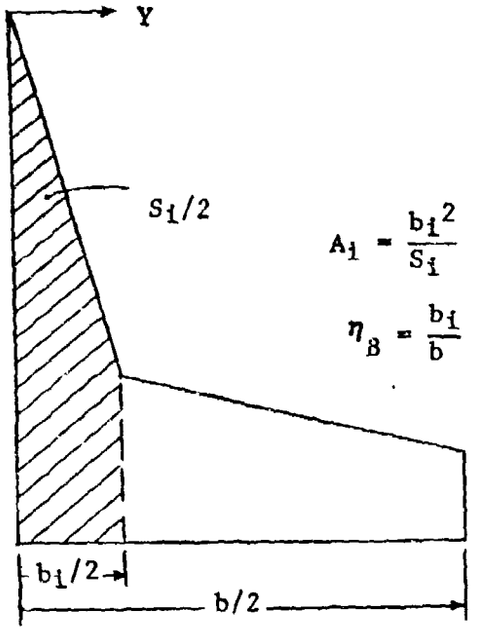

Figure 45 Definition of Cranked-Wing Planform for Calculation of Angle of Attack in Nonlinear Lift Range

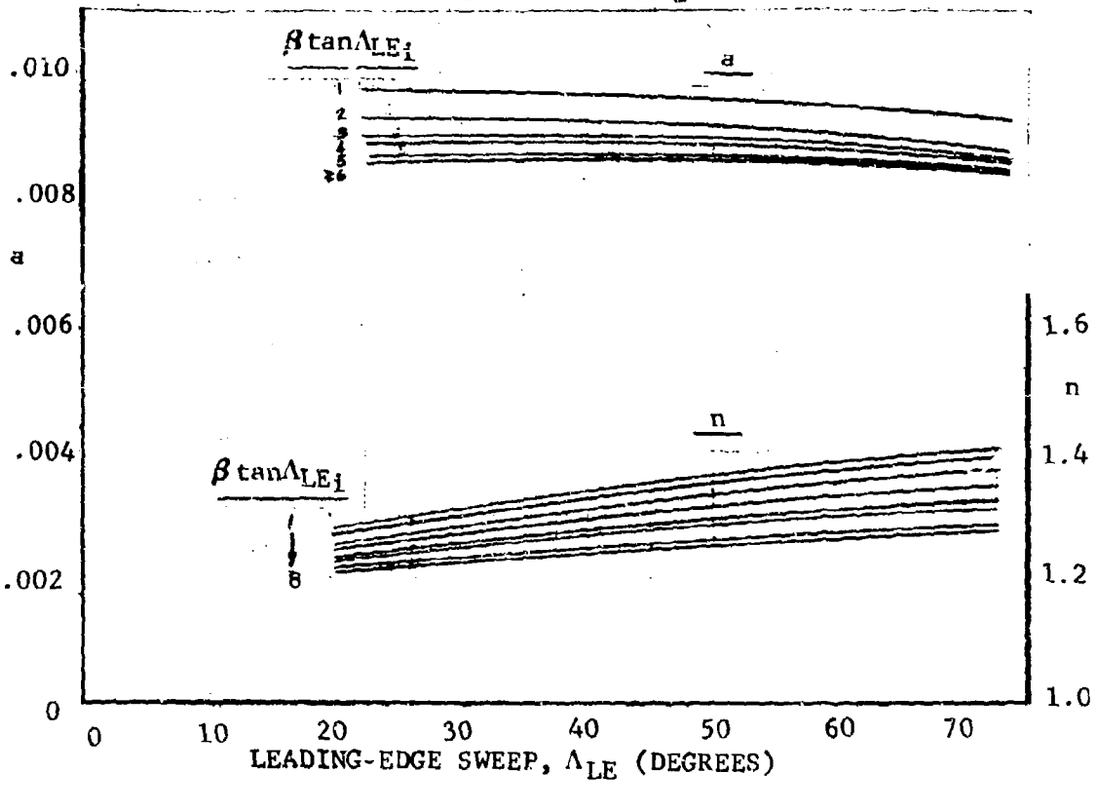

Figure 46 Parameters Used in Calculation of Angle of Attack in Nonlinear Lift Range

η_B is the nondimensional spanwise ordinate for the break point in the cranked wing

a,n are correlation constants (shown in Figure 46) derived by modifying the Reference 9 method.

In the program it is assumed that α_{stall} is the angle of attack corresponding to $C_{L_{DB}}$, as shown in Figure 13 of Section 4. The accuracy of the nonlinear angle-of-attack prediction technique is, of course, strongly dependent on knowing α_{stall}.

6.9 Maximum-Lift Coefficient

The method used in the Large Aircraft program to estimate the maximum lift and angle of attack for maximum lift is based on the DATCOM method for both the low- and high-aspect-ratio wings (Reference 2). The maximum lift of high-aspect-ratio wings at subsonic speeds is directly related to the maximum lift of the wing airfoil sections. The wing planform shape is a secondary influence on the maximum lift obtainable. However, for low-aspect-ratio wings, the wing planform is the primary effect on maximum lift, while sectional characteristics are secondary. The program uses the criteria established in the DATCOM method by the equation

$$AR_{LOW} = \frac{3}{(C_1+1)\cos\Lambda_{LE}} \tag{6-37}$$

where C_1 is a function of taper ratio, as given in Figure 54. If $AR > AR_{LOW}$, the high-aspect-ratio method is used, and if $AR \leq AR_{LOW}$, the low-aspect-ratio method is used. These two methods are described in the following subsections.

6.9.1 High-Aspect-Ratio Method

The DATCOM method is an empirically derived method based on experimental correlations of high-aspect-ratio, untwisted, and constant-section wings. The equations for maximum lift and the angle of maximum lift are as follows:

$$C_{L_{MAX}} = \left(\frac{C_{L_{MAX}}}{C_{\ell_{MAX}}}\right) C_{\ell_{MAX}} + \Delta C_{L_{MAX}} \tag{6-38}$$

$$\alpha_{MAX} = \left(\frac{C_{L_{MAX}}}{C_{L\alpha}}\right) + \alpha_{Lo} + \Delta\alpha_{MAX} \qquad (6\text{-}39)$$

The first term in Equation 6-38 is the maximum lift coefficient at M=0.2; the second term is the lift increment to be added for Mach numbers greater than 0.2.

The factor $(C_{L_{MAX}}/C_{\ell_{MAX}})$ is computed by a curve fit of the curves in Figure 4.1.3.4-14a in the DATCOM given by

$$\frac{C_{L_{MAX}}}{C_{\ell_{MAX}}} = A - B\,\Delta y' \qquad (6\text{-}40)$$

where

$$\Delta y' = \begin{cases} 0; & \Delta y < 1.4 \\ \Delta y - 1.4; & 1.4 \leq \Delta y \leq 2.5 \\ 1.1; & y > 2.5 \end{cases}$$

and the terms A and B are plotted in Figure 47 as a function of sweep. (The Δy is defined by Equation 2-16.)

The increment to $C_{L_{MAX}}$ due to Mach number is computed from a curve fit of the curves of Figure 4.1.3.4-15 in the DATCOM, given by

$$C_{L_{MAX}} = C + (D-C)\left(\frac{\Lambda_{LE}}{60}\right) \qquad (6\text{-}41)$$

where the terms C and D are plotted in Figure 48 as a function of Δy and Mach number.

The section maximum lift coefficient at M=0.2, $C_{\ell_{MAX}}$ is computed from

$$C_{\ell_{MAX}} = (C_{\ell_{MAX}})_{Base} + \Delta C_{\ell_{MAX}} \qquad (6\text{-}42)$$

where $(C_{\ell_{MAX}})_{Base}$ and $\Delta C_{\ell_{MAX}}$ are shown plotted in Figures 49 and 50 as a function of the sharpness factor, maximum-thickness location, and camber.

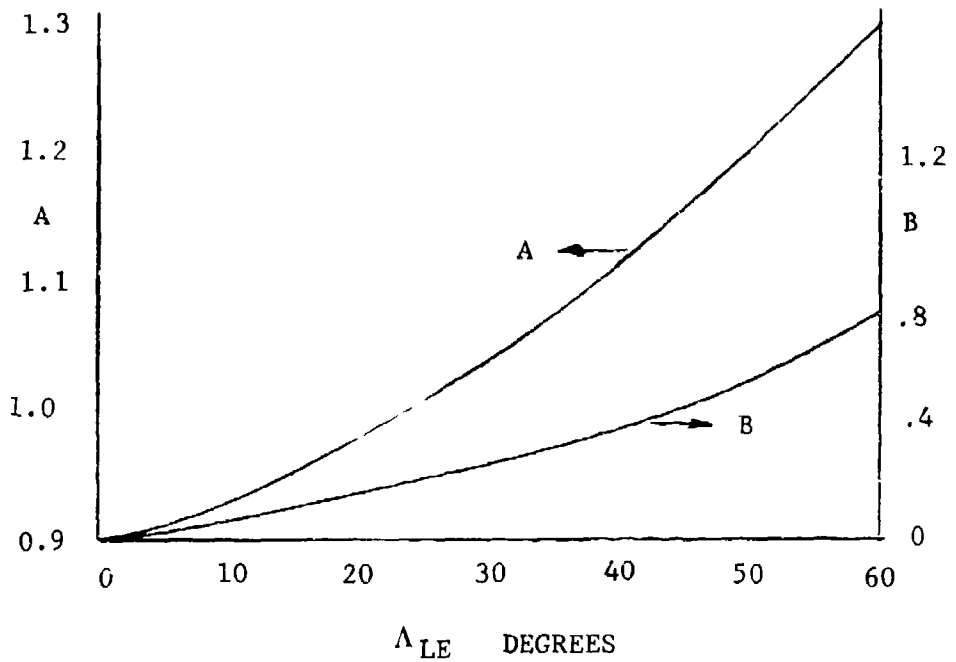

Figure 47 Factors for Determining Subsonic Maximum Lift

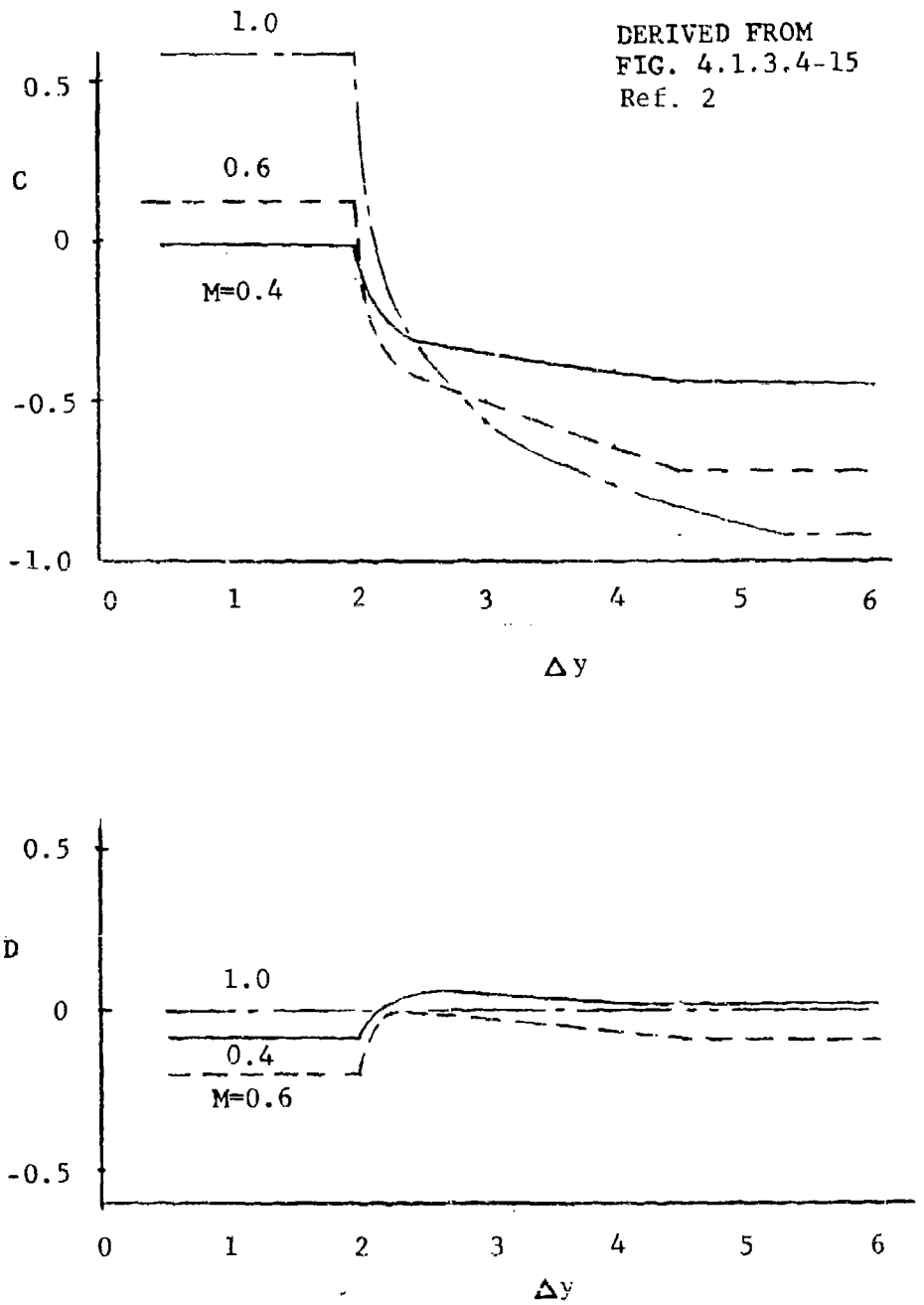

Figure 48 Factors for Determining Mach Number Correction for Maximum Lift

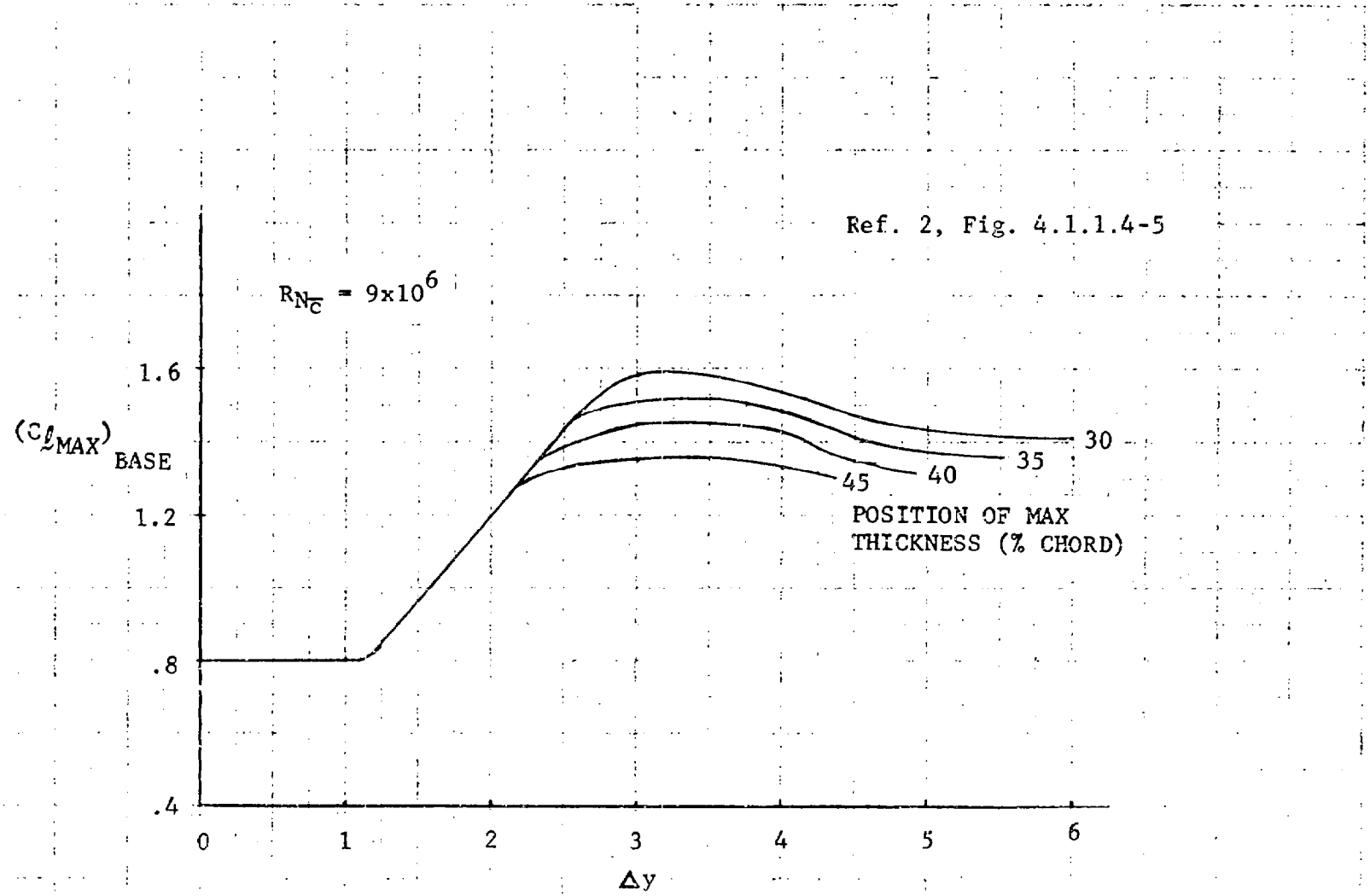

Figure 49 Section Maximum Lift for Uncambered Airfoils

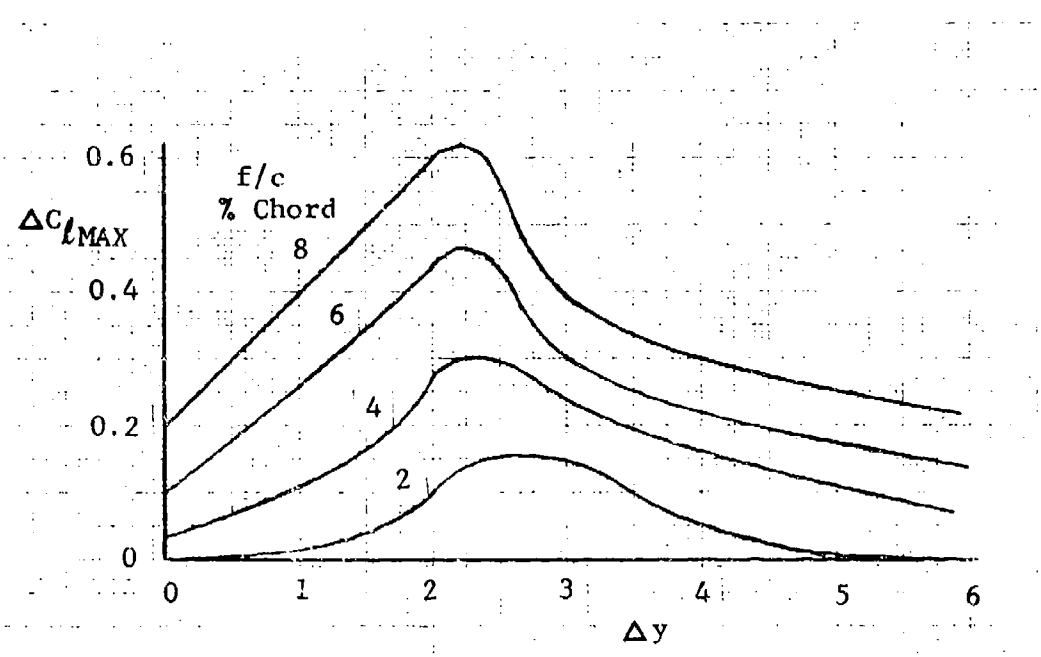

Figure 50 Effect of Airfoil Camber on Maximum Lift

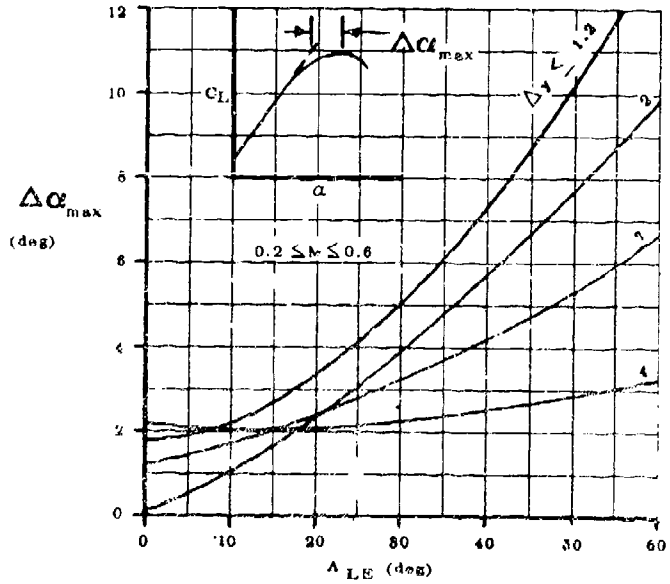

Figure 51 Angle-of-Attack Increment for Subsonic Maximum Lift of High-Aspect-Ratio Wings

The angle-of-attack increment for maximum lift, $\Delta\alpha_{MAX}$, is obtained from Figure 51, which is taken from Section 4.1.3.4 in the DATCOM.

6.9.2 Low-Aspect-Ratio Method

The empirical equations in DATCOM for estimating subsonic maximum lift and angle of attack for untwisted low-aspect-ratio wings are

$$C_{L_{MAX}} = (C_{L_{MAX}})_{Base} + \Delta C_{L_{MAX}} \tag{6-43}$$

$$\Delta\alpha_{MAX} = (\alpha_{MAX})_{Base} + \Delta\alpha_{MAX} \tag{6-44}$$

The base value of $C_{L_{MAX}}$ is obtained from Figure 52 if the position of maximum airfoil thickness, X_T, is forward of the 35-percent chord point, and from Figure 53 if X_T is aft of the 35-percent chord. The values of $\Delta C_{L_{MAX}}$, C_1, and C_2 are obtained from Figure 54, the base α_{MAX} from Figure 55, and the value of $\Delta\alpha_{MAX}$ from Figure 56. (Figures 52 through 56 are taken from Section 4.1.3.4 of the DATCOM.)

6.9.3 Tail-Lift Contribution to $C_{L_{MAX}}$

Because the horizontal tail usually has a smaller aspect ratio compared to the wing and is in a downwash field that counteracts the effect of angle of attack to some extent, it is assumed that the tail does not stall before the wing. The lift generated by the tail at the angle of attack of wing stall is added to the wing maximum lift coefficient to obtain the configuration maximum lift coefficient. The configuration maximum lift is given by

$$C_{L_{MAX}} = (C_{L_{MAX}})_{Wing} + (\Delta C_{L_{MAX}})_{Tail} \tag{6-45}$$

where

$$(\Delta C_{L_{MAX}})_{Tail} = (C_{L_\alpha})_T \cdot 57.3 \sin\alpha_{max}(\cos\alpha_{max})^2$$

The term $(C_{L_\alpha})_T$ is the lift-curve slope of the horizontal tail as determined in Section 6.3.

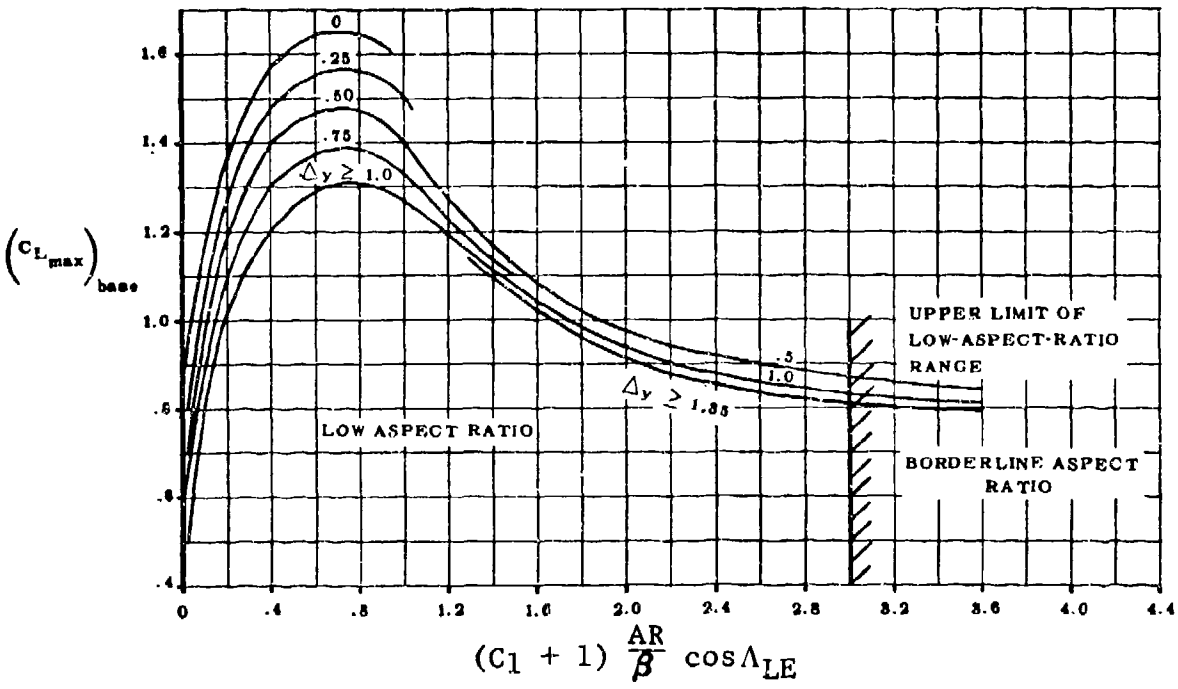

Figure 52 Subsonic Maximum Lift of Low-Aspect-Ratio Wings ($X_T < 35\%$)

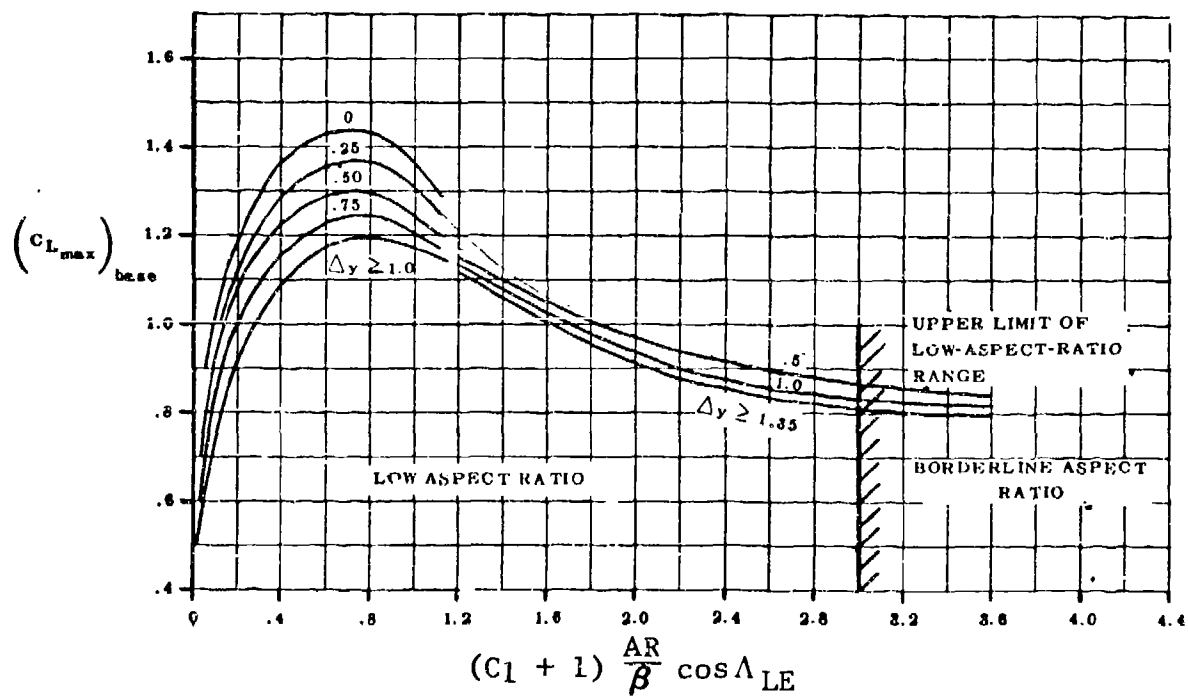

Figure 53 Subsonic Maximum Lift of Low-Aspect-Ratio Wings ($X_T \geq 35\%$)

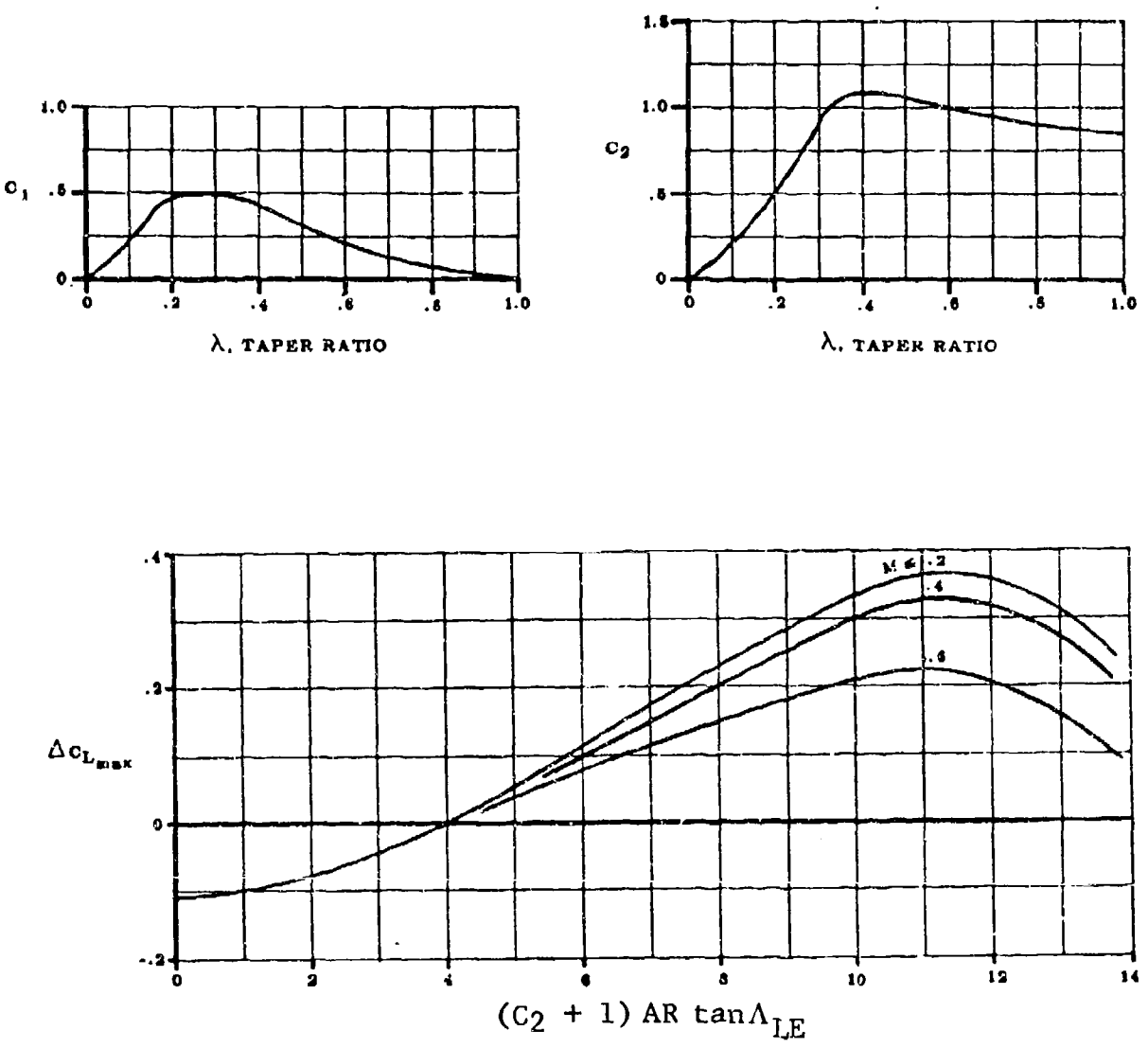

Figure 54 Mach Number Correction for Low-Aspect-Ratio Maximum Lift

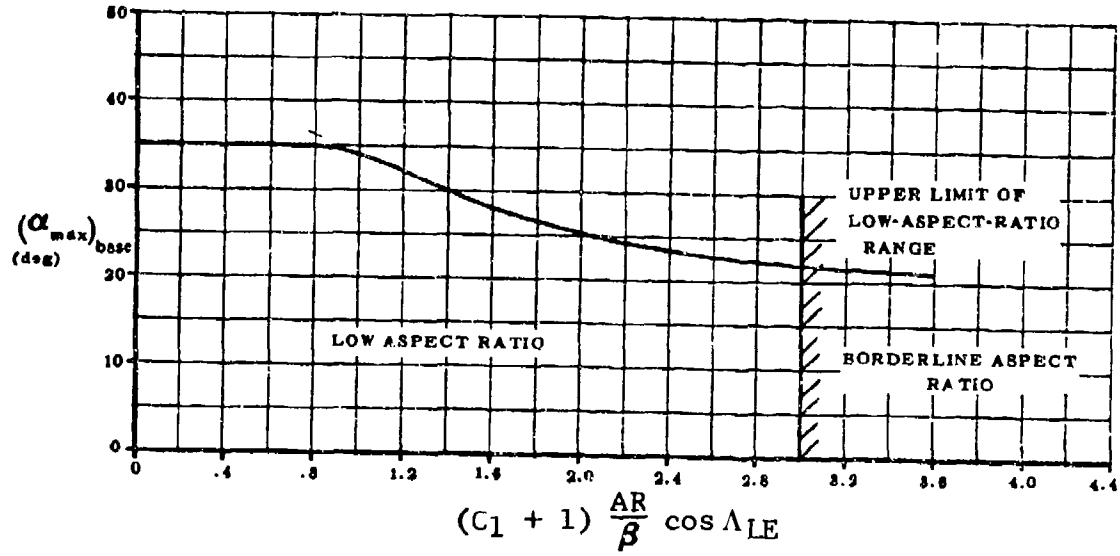

Figure 55 Angle of Attack for Subsonic Maximum Lift of Low-Aspect-Ratio Wing Maximum Lift

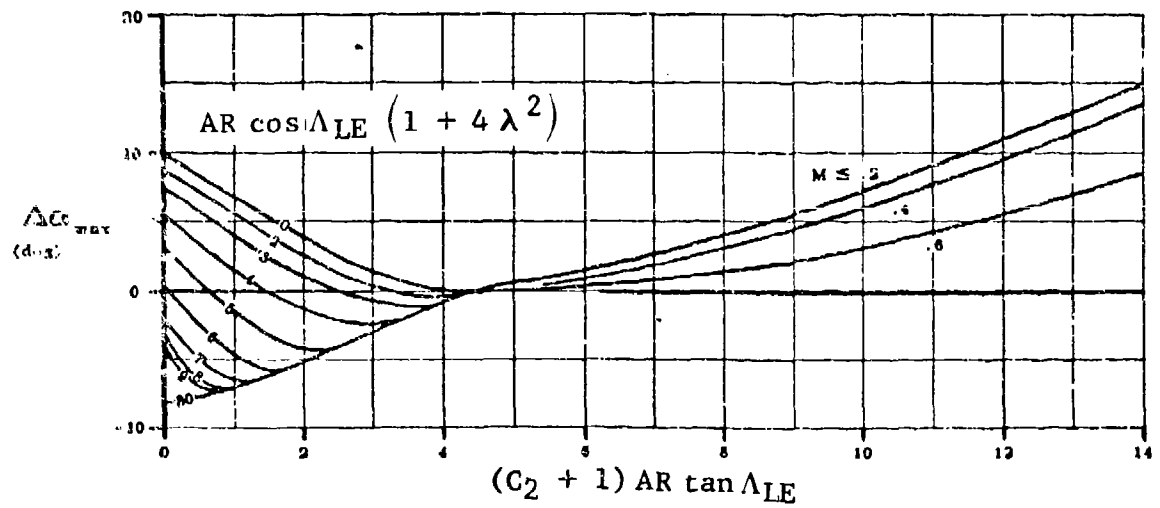

Figure 56 Mach Number Correction for Angle of Attack

7. MOMENT

The moment of a wing-body-tail configuration can be represented by the equation

$$C_m = C_{m_o} + (n - \frac{X_{ac}}{C_{R_e}}) \frac{C_{R_e}}{\bar{c}} C_{L_{WB}} - C_{L_{TAIL}} \cdot \ell_{HT}/\bar{c} \qquad (7\text{-}1)$$

where n is the chordwise distance to the moment reference point measured in exposed wing root chord (C_{R_e}), X_{ac}/C_{R_e} is the aerodynamic center location relative to C_{R_e}, and the last term represents the moment contribution of the tail lift times the moment arm ℓ_{HT}, determined from Equation (2-9).

The following subsections discuss the method used to predict the elements in Equation 7-1 along with a method of determining trimmed lift curves and drag polars.

7.1 Zero-Lift Moment

The method of predicting the zero-lift pitching moment for a wing-body configuration considers only the effect of the wing on C_{m_o} and does not include the effect of an assymmetrical fuselage or the effect of stores and nacelles located near the wing. However, the C_{m_o} prediction method in the Large Aircraft program can be adjusted by input so as to match the test data C_{m_o} on a similar configuration.

The subsonic zero-lift pitching moment for wings with linear twist, up to the critical Mach number, is given in the DATCOM as

$$C_{m_o} = \left\{ (C_{m_o})_{\tau=0} + \left(\frac{\Delta C_{m_o}}{\tau}\right) \tau \right\} \frac{1 + 5.9(t/c)M^5}{\sqrt{1 - M^2 \cos^2 \Lambda_{c/4}}} \qquad (7\text{-}2)$$

where $(C_{m_o})_{\tau=0}$ is the C_{m_o} of an untwisted wing and $(\Delta C_{m_o}/\tau)$ is the change in wing zero-lift pitching moment due to a unit change in wing twist, τ. The parameter $(\Delta C_{m_o}/\tau)$ was obtained from lifting-line theory and is shown in Figure 57.

The C_{m_o} of an untwisted wing is obtained from

$$(C_{m_o})_{\tau=0} = \frac{AR \cos^2 \Lambda_{c/4}}{AR + 2\cos \Lambda_{c/4}} (\bar{C_{m_o}})_{SECT} \qquad (7\text{-}3)$$

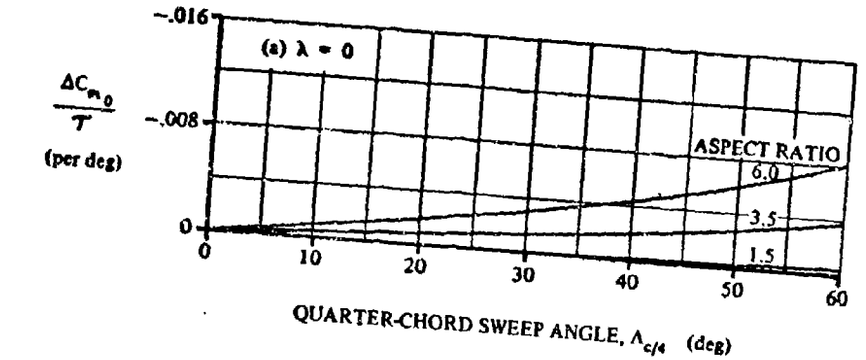

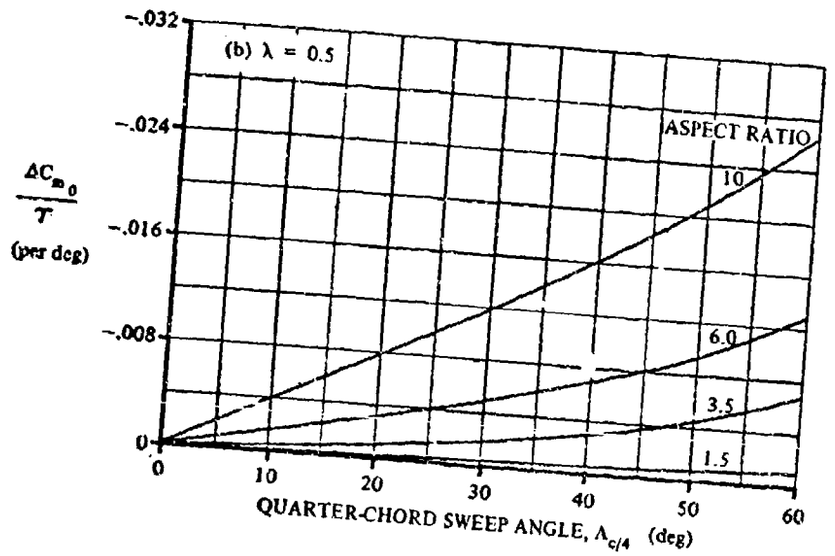

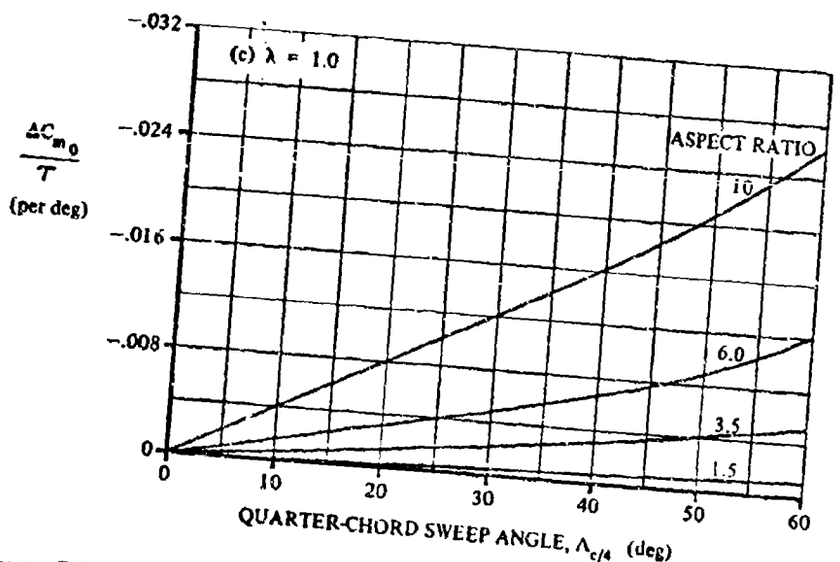

Figure 57 Effect of Linear Twist on the Wing Zero-Lift Pitching Moment

where $(\bar{C}_{m_o})_{SECT}$ is the average section pitching moment coefficient determined by averaging the section C_{m_o} for each wing panel, using

$$(\bar{C}_{m_o})_{SECT} = \frac{\sum_{i=1}^{N} \left(\frac{C_m}{C_{\ell_d}}\right)(C_{\ell_d})_i S_i}{\sum_{i=1}^{N} S_i}$$

where (C_m/C_{ℓ_d}) is the theoretical pitching moment divided by the section design lift of the airfoil camber line obtained from Table 4.1.1-D in the DATCOM.

7.2 Aerodynamic Center

The aerodynamic center location of a wing-body configuration is given in the DATCOM as

$$\frac{X_{ac}}{C_{R_e}} = \frac{\left(\frac{X_{ac}}{C_{R_e}}\right)_N (C_{L_\alpha})_N + \left(\frac{X_{ac}}{C_{R_e}}\right)_{W(B)} (C_{L_\alpha})_{W(B)} + \left(\frac{X_{ac}}{C_{R_e}}\right)_{B(W)} (C_{L_\alpha})_{B(W)}}{(C_{L_\alpha})_N + (C_{L_\alpha})_{W(B)} + (C_{L_\alpha})_{B(W)}} \qquad (7\text{-}4)$$

where the X_{ac}/C_{R_e} terms are the chordwise distances measured in exposed wing-root chords from the apex of the exposed wing to the aerodynamic center, positive aft. The subscripts N, W(B), and B(W) refer to the lift and aerodynamic center contribution of the forebody, exposed wing, and the wing-lift carryover on the body, respectively.

7.2.1 Aerodynamic Center of Forebody

The subsonic location of the aerodynamic center for forebodies with ogive nosecones is approximated in the DATCOM as

$$\left(\frac{X_{ac}}{C_{R_e}}\right)_N = (-0.54)\ \frac{L_N + 1.6(X_{LE} - L_N)}{C_{R_e}} \qquad (7\text{-}5)$$

Figure 58 defines the geometric parameters, L_N, X_{LE}, and C_{R_e}. The supersonic forebody aerodynamic center is obtained from

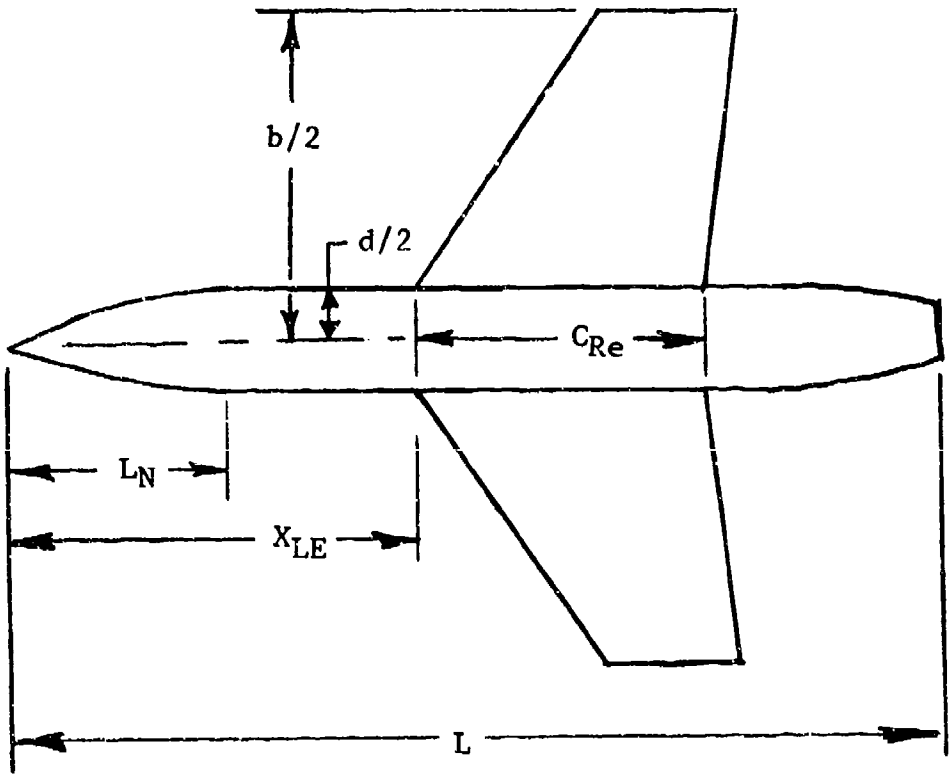

Figure 58 Wing-Body Geometry

$$\left(\frac{X_{ac}}{C_{R_e}}\right)_N = \frac{X_{LE}}{C_{R_e}}\left(\frac{X_{CP}}{\ell_B} - 1\right) \tag{7-6}$$

where the term X_{CP}/ℓ_B is obtained from Figure 59 (Figure 4.2.2.1-23a in DATCOM).

7.2.2 Aerodynamic Center of Wing (Trapezoidal, Single Panel)

The aerodynamic center of the exposed wing is determined from the DATCOM charts presented in Figures 60a through 60f. These charts are valid for subsonic Mach numbers less than Mach critical and supersonic Mach numbers greater than 1.2. For transonic conditions, the data presented in the DATCOM in terms of transonic similarity parameters (Figures 61a through 61d) are used to determine the aerodynamic center position.

The procedure for obtaining aerodynamic center can be summarized as:

$$\text{For } M \lesssim M_{CR};\quad \left(\frac{X_{ac}}{C_{R_e}}\right) = \left(\frac{X_{ac}}{C_{R_e}}\right)' \tag{7-7}$$

For $M_{CR}+.05 \gtrsim M > M_{CR}$,

$$\left(\frac{X_{ac}}{C_{R_e}}\right) = \left(\frac{X_{ac}}{C_{R_e}}\right)' + \left[\left(\frac{X_{ac}}{C_{R_e}}\right)'' - \left(\frac{X_{ac}}{C_{R_e}}\right)'\right]\frac{M-M_{CR}}{.05} \tag{7-8}$$

For $\sqrt{1+(t/c)^{2/3}} > M > M_{CR} + .05$,

$$\left(\frac{X_{ac}}{C_{R_e}}\right) = \left(\frac{X_{ac}}{C_{R_e}}\right)'' \tag{7-9}$$

For $1.2 > M \gtrsim \sqrt{1+(t/c)^{2/3}}$,

$$\left(\frac{X_{ac}}{C_{R_e}}\right) = \left(\frac{X_{ac}}{C_{R_e}}\right)'' + \left[\left(\frac{X_{ac}}{C_{R_e}}\right)'' - \left(\frac{X_{ac}}{C_{R_e}}\right)'\right]\frac{M-\sqrt{1+(t/c)^{2/3}}}{1.2-\sqrt{1+(t/c)^{2/3}}} \tag{7-10}$$

Ref. 2, FIGURE 4.2.2.1-23a

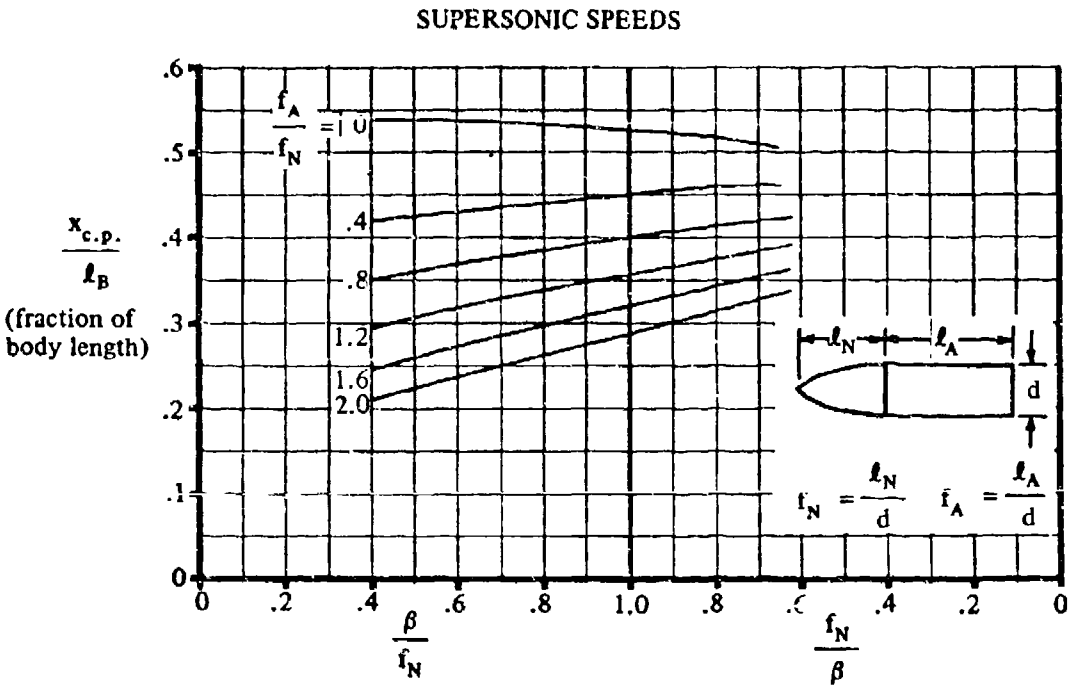

Figure 59 Supersonic Center of Pressure of Ogive with Cylindrical Afterbody

Ref. 2, FIGURE 4.1.4.2-22

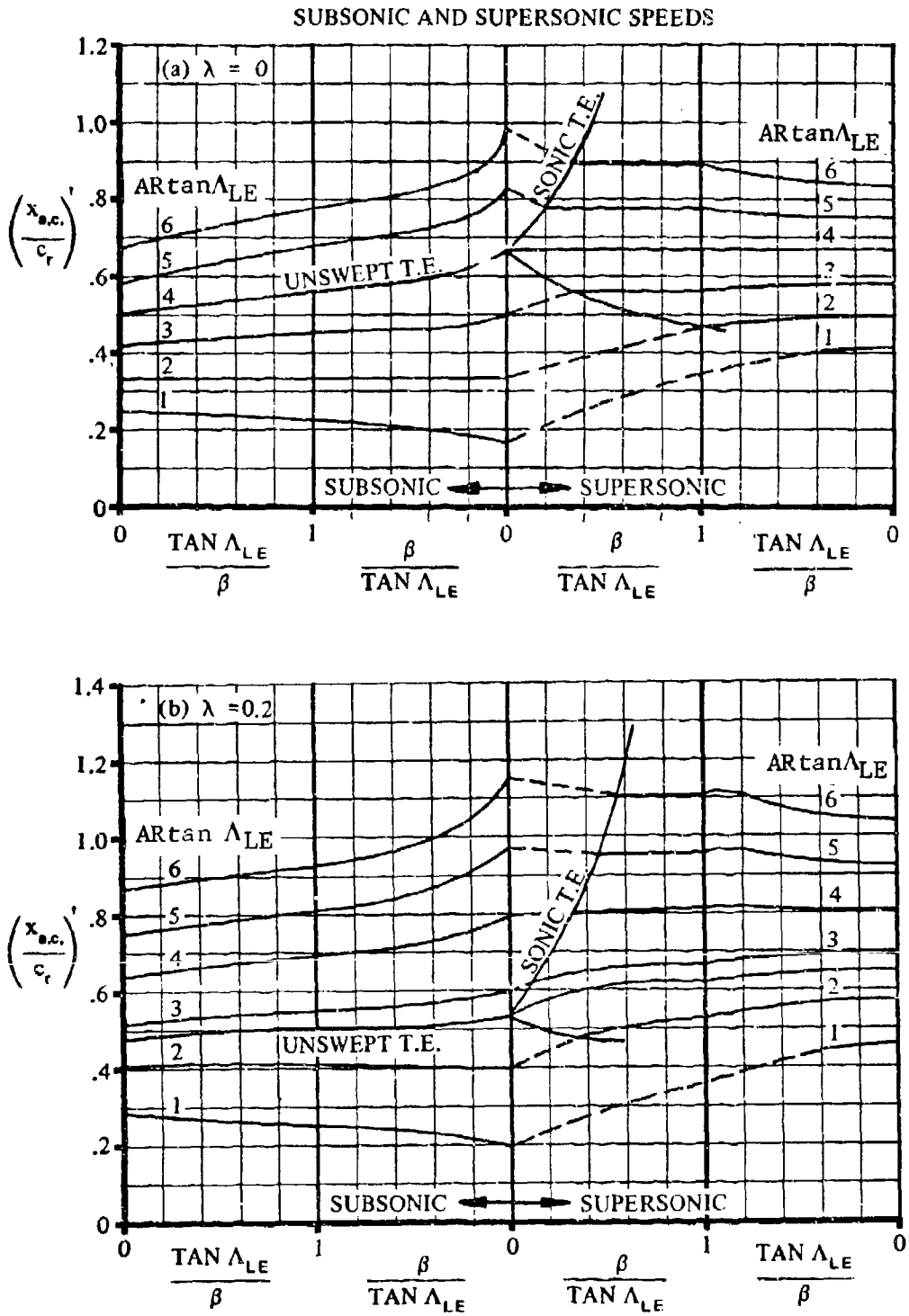

Figure 60 Wing Aerodynamic-Center Position

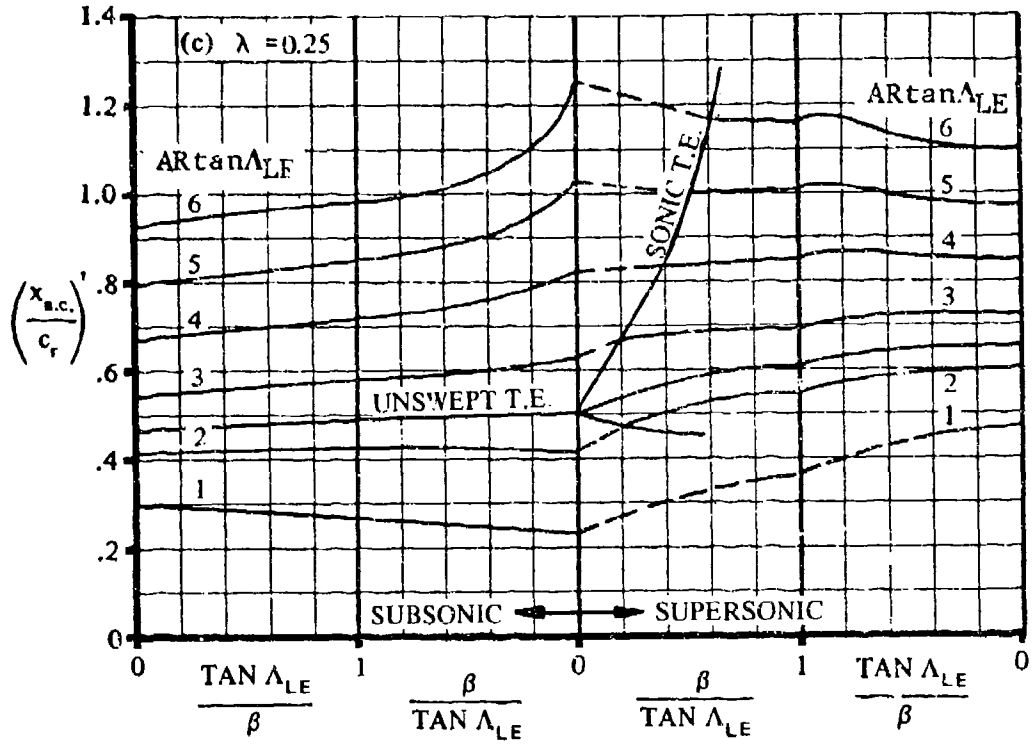

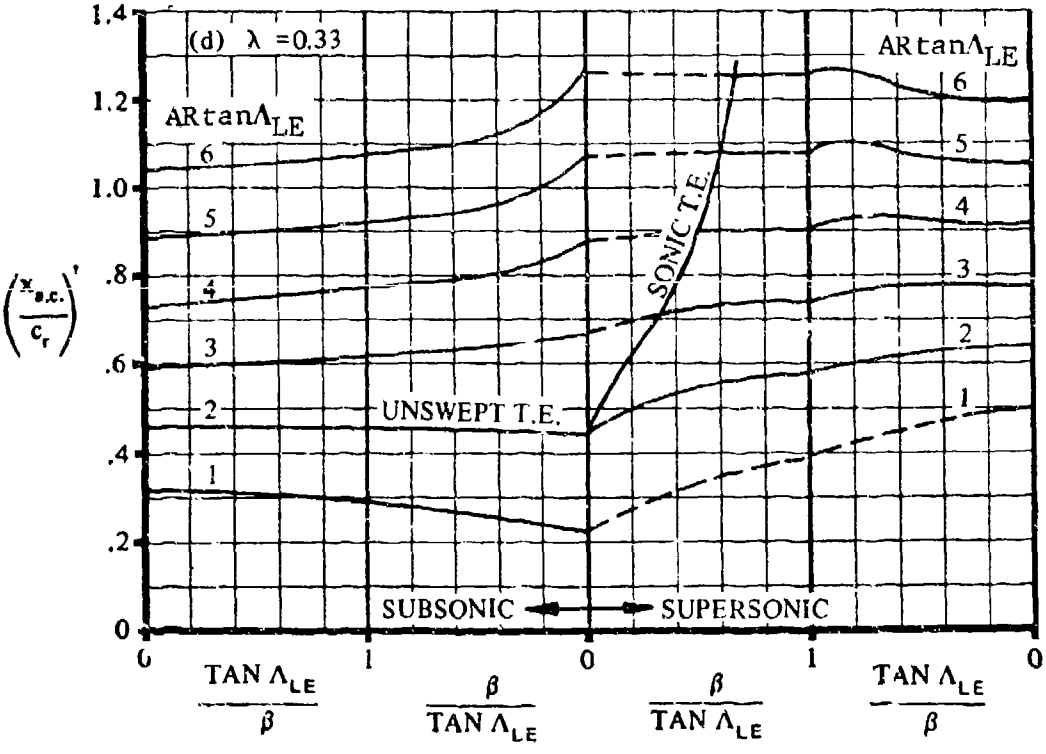

Figure 60 (Cont'd)

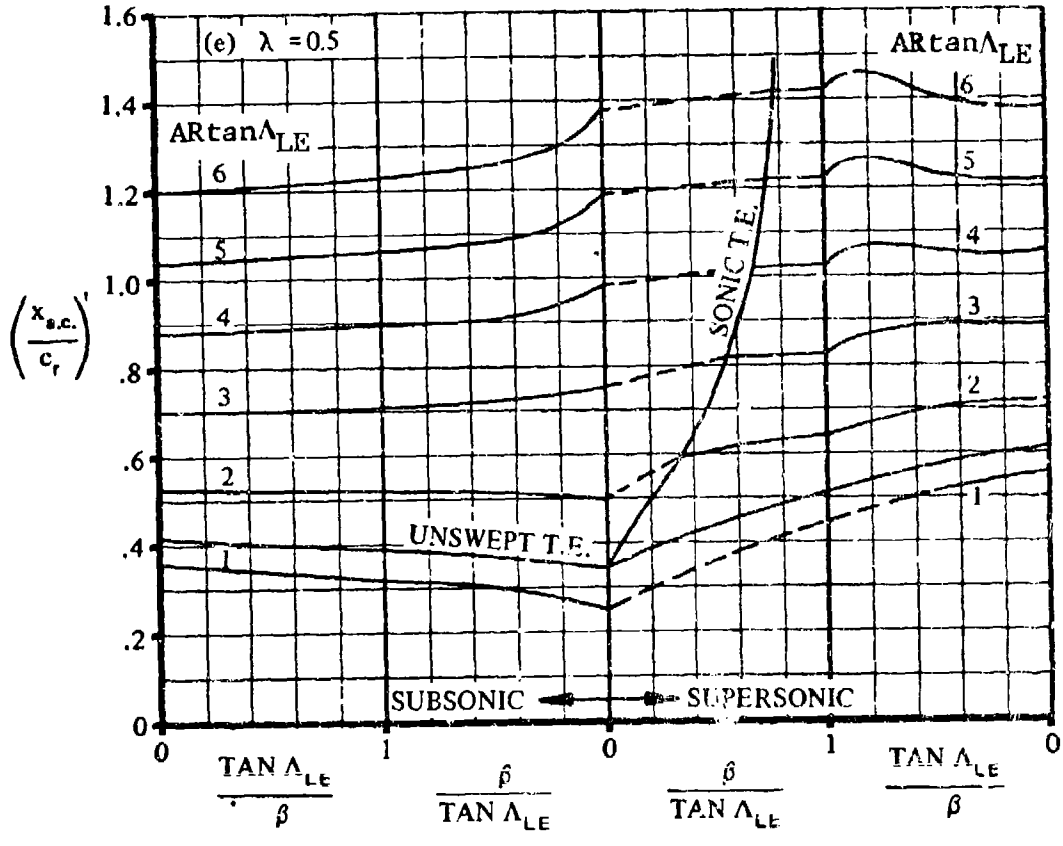

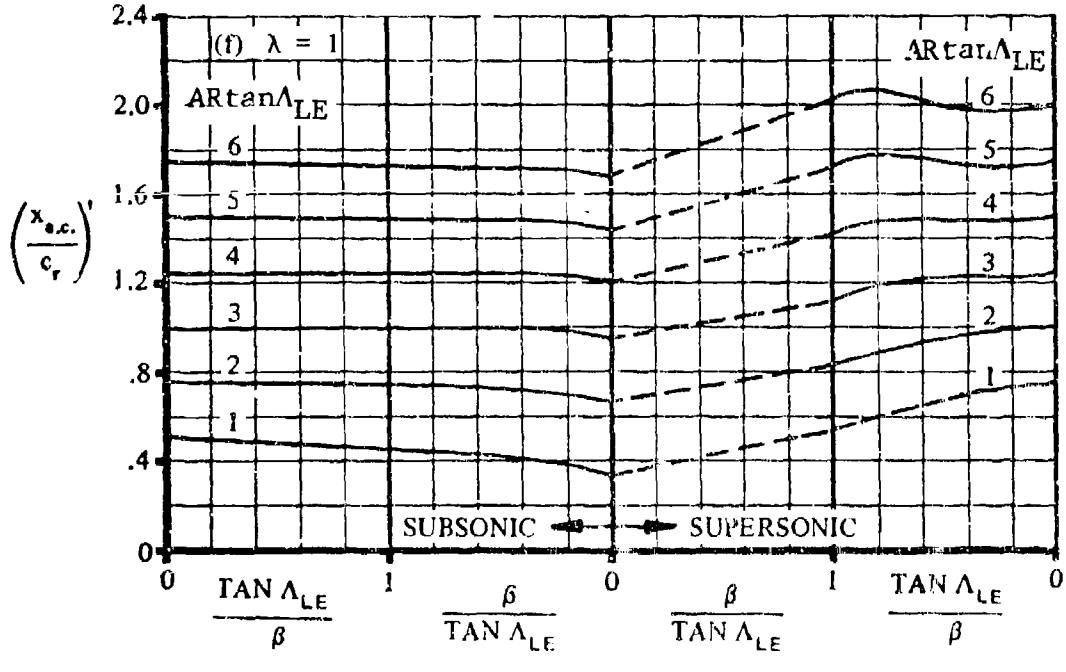

Figure 60 (Cont'd)

Ref. 2, FIGURE 4.1.4.2-25

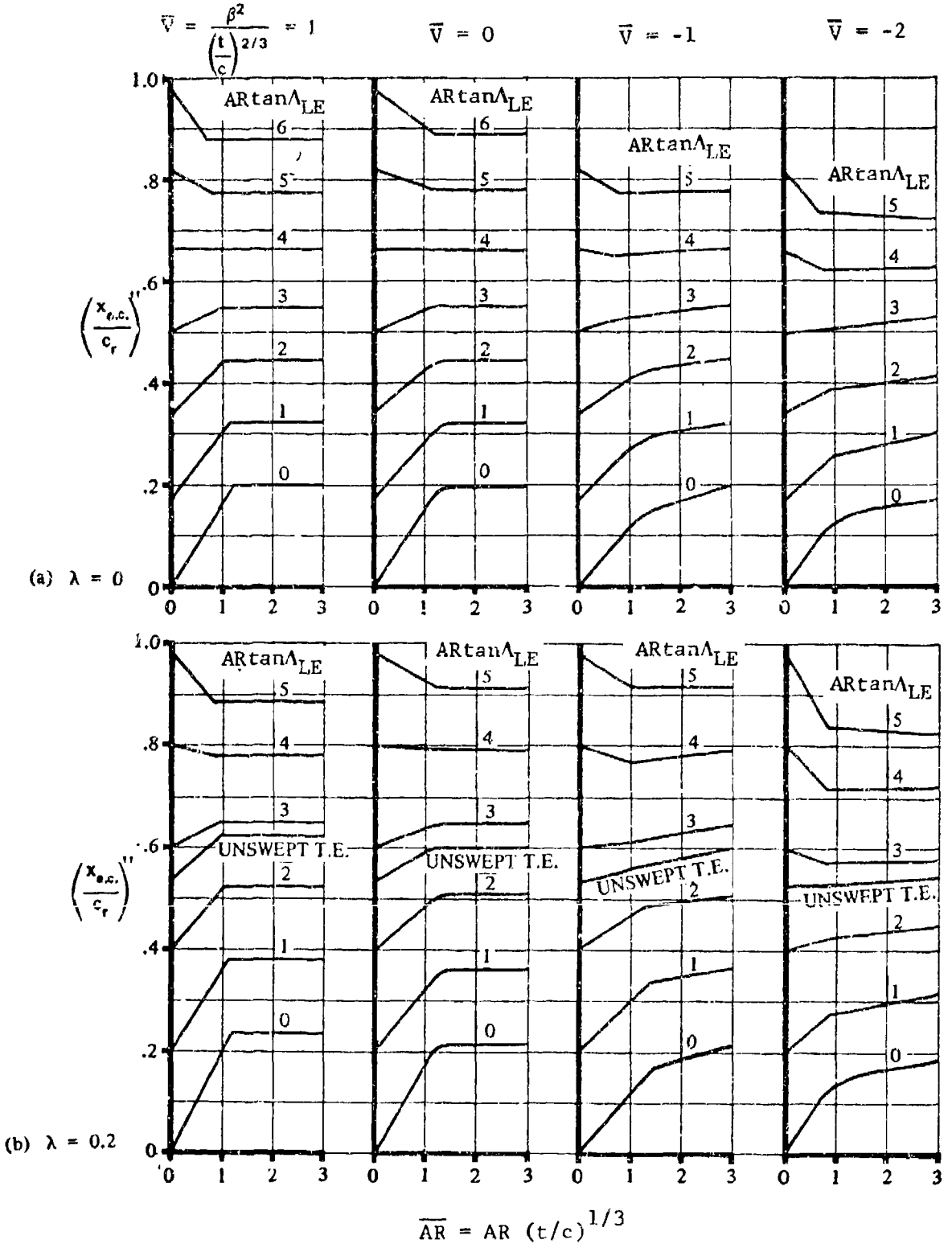

Figure 61 Transonic Wing Aerodynamic-Center Location

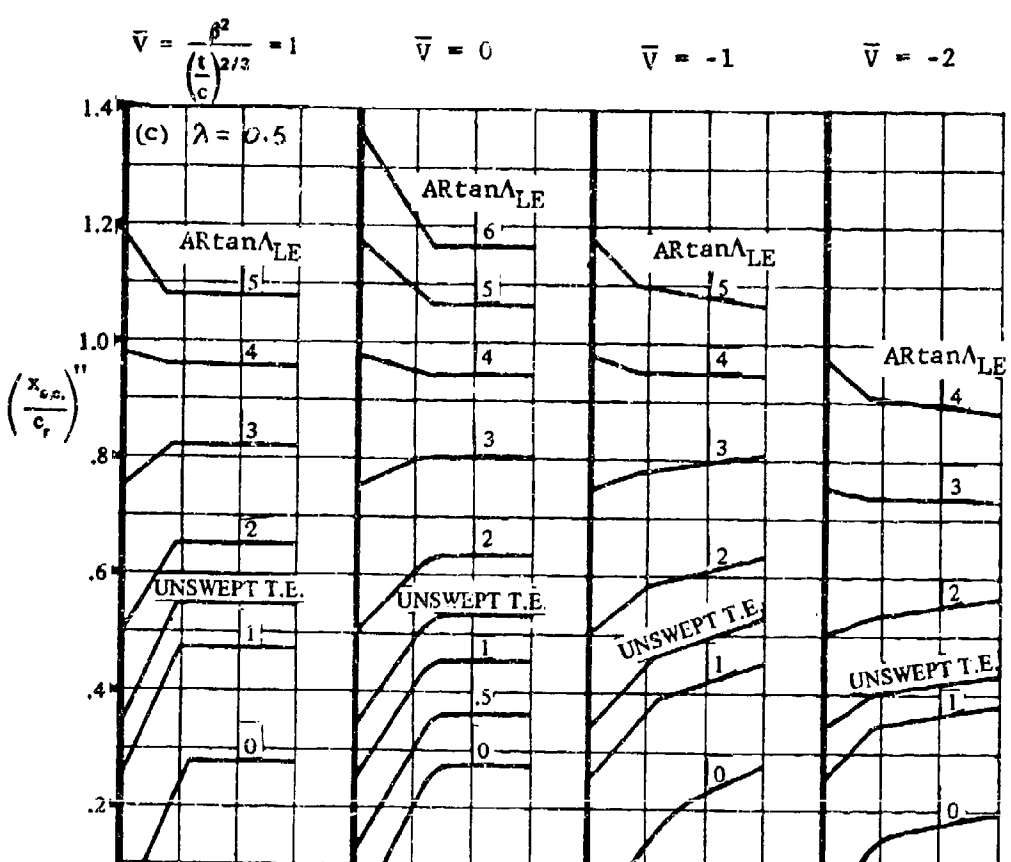

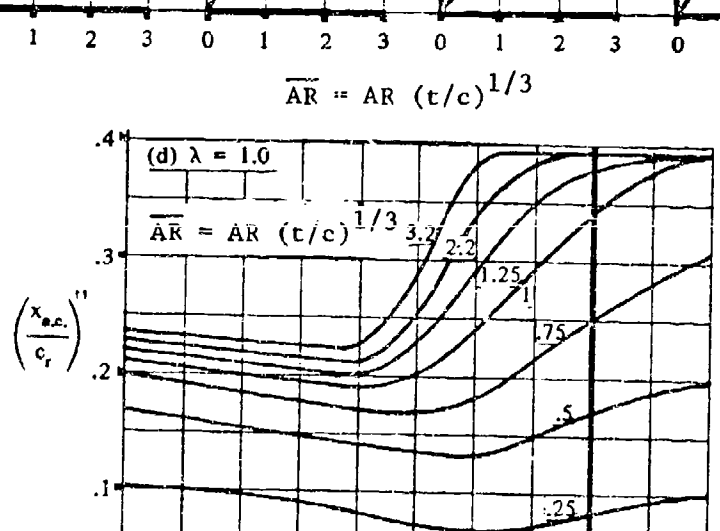

Figure 61 (Cont'd)

For $M \geq 1.2$,

$$\left(\frac{X_{ac}}{C_{R_e}}\right) = \left(\frac{X_{ac}}{C_{R_e}}\right)' \tag{7-11}$$

where $(X_{ac}/C_{R_e})'$ is read from Figure 60 and $(X_{ac}/C_{R_e})''$ is read from Figure 61.

7.2.3 Aerodynamic Center of Wing (Cranked or Double Delta)

The prediction of the a.c. location of cranked or double-delta wings is taken from the method developed at Convair Aerospace as reported in Reference 10. The non-straight-tapered wing is divided into two panels, with each panel having conventional, straight-tapered geometry. The individual lift-curve slope and a.c. are estimated for each panel, using the technique described above for the trapezoidal wing and treating each constructed panel as an isolated wing. The individual lift and a.c. location for each constructed panel are then combined, using an inboard-outboard weighted-area relationship

$$\frac{X_{ac}}{C_{R_e}} = \frac{\left(\frac{\bar{X}_{ac}}{C_{R_e}}\right)_i (C_{L_\alpha})_i S_i + \left(\frac{\bar{X}_{ac}}{C_{R_e}}\right)_o (C_{L_\alpha})_o S_o}{(C_{L_\alpha})_i S_i + (C_{L_\alpha})_o S_o} \tag{7-12}$$

where the outboard wing a.c. is referenced to the inboard root chord length given by

$$\left(\frac{X_{ac}}{C_{R_e}}\right)_o = \left(\frac{X_{ac}}{C_{R_o}}\right)_o \frac{C_{R_o}}{C_{R_e}} - \frac{\Delta\bar{y}}{C_{R_e}} (\tan\Lambda_{LE})_o + \frac{(b/2)_i}{C_{R_e}} (\tan\Lambda_{LE})_i$$

The geometry for the inboard-outboard panel arrangement is illustrated in Figure 62.

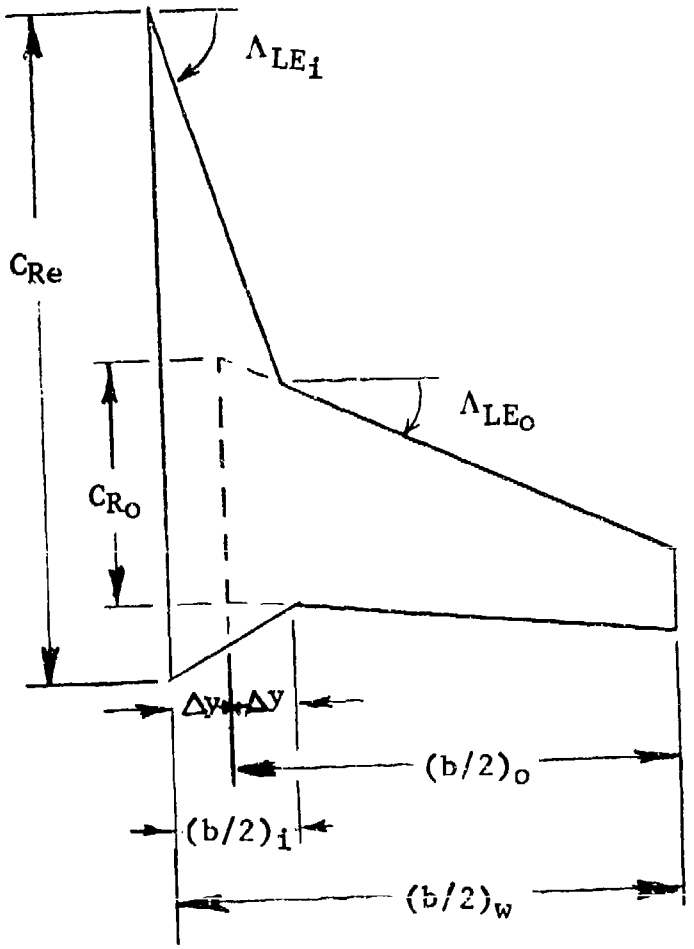

Figure 62 Geometry for Cranked Wing Aerodynamic-Center Prediction

7.2.4 Aerodynamic Center of Wing-Lift Carryover on Body

The location of the a.c. due to the wing-lift carryover on the body is determined by use of the DATCOM method. For $\beta AR_e \geq 4$ the subsonic a.c. location is obtained from

$$\left(\frac{X_{ac}}{C_{R_e}}\right)_{B(W)} = \frac{1}{4} + \frac{b-d}{2C_{R_e}} \tan \Lambda_{c/4} \cdot f(d/b) \qquad (7\text{-}13)$$

where AR_e is the exposed-wing aspect ratio and the factor f(d/b) is shown plotted in Figure 63. For $\beta AR_e < 4$ the a.c. location is determined from

$$\left(\frac{X_{ac}}{C_{R_e}}\right)_{B(W)} = \left[\left(\frac{X_{ac}}{C_{R_e}}\right)'' - \left(\frac{X_{ac}}{C_{R_e}}\right)'\right]\left(\frac{\beta AR_e - 4}{4}\right)^2 + \left(\frac{X_{ac}}{C_{R_e}}\right)' \qquad (7\text{-}14)$$

where $(X_{ac}/C_{R_e})'$ is the a.c. location determined from Equation 7-13 and $(X_{ac}/C_{R_e})''$ is the theoretical location for $\beta AR_e = 0$ determined from the equation

$$\left(\frac{X_{ac}}{C_{R_e}}\right)'' = \frac{1}{8} AR_e(1+\lambda_e) \tan \Lambda_{LE} \qquad (7\text{-}15)$$

where λ_e is the exposed-wing taper ratio. Equation 7-15 is limited to values less than or equal to 0.5. For supersonic conditions the a.c. location is estimated from Figure 64. For transonic conditions the a.c. location is determined by linear interpolation of the a.c. values determined at the critical Mach number and Mach 1.1.

For complex wing planforms the equivalent wing-sweep values are used in the subsonic and supersonic a.c. location methods.

7.3 Effect of Trim Deflection

The effect of trim deflection can be estimated by predicting the incremental change in lift, drag, and moment due to tail deflection along constant angles of attack. The total wing-body-tail lift, drag, and moment can be represented by

$$C_L = C_{L_{WB}} + C_{L_{\alpha_t}}(\alpha - \alpha_{o_t}) + C_{L_\delta} \cdot \delta_{HT} \qquad (7\text{-}16)$$

Ref. 2, FIGURE 4.3.2.1-35

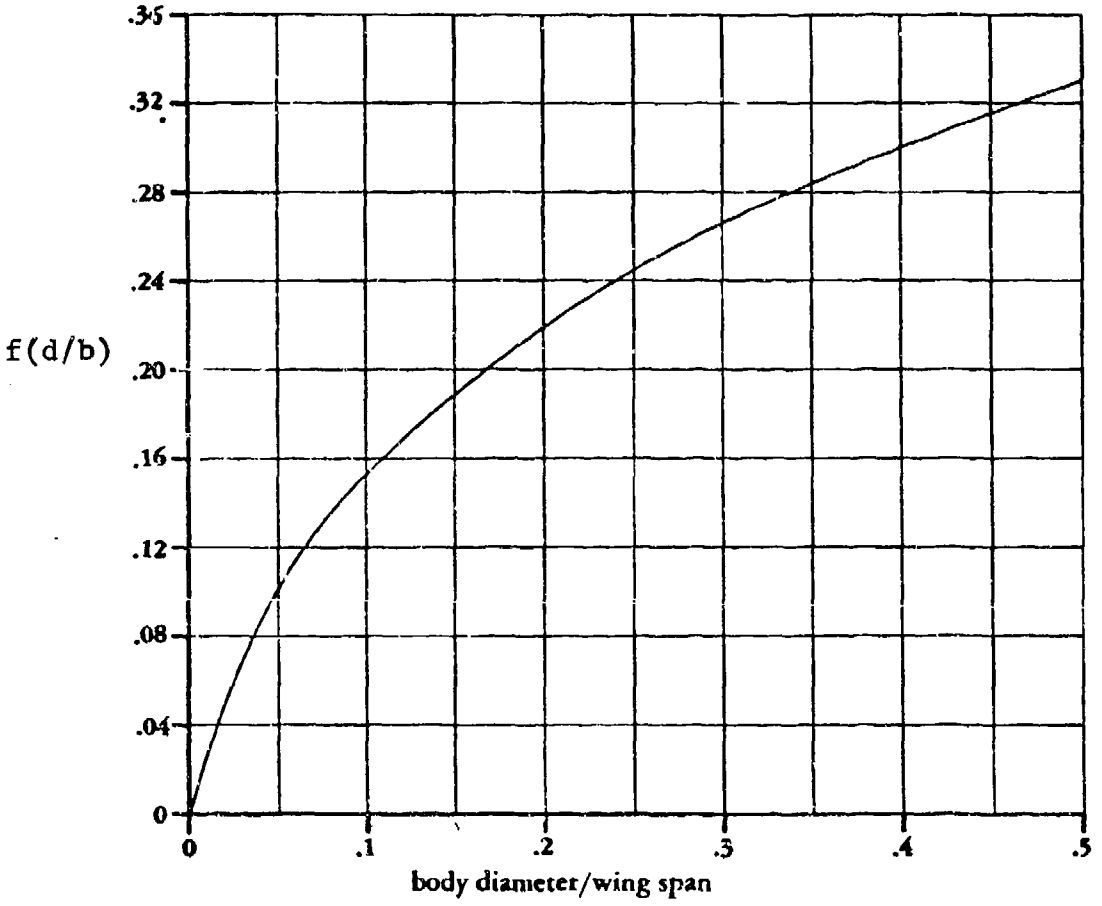

Figure 63 Parameter Used in Accounting for Wing-Lift Carryover on the Body

Ref. 2, FIGURE 4.3.2.1-37

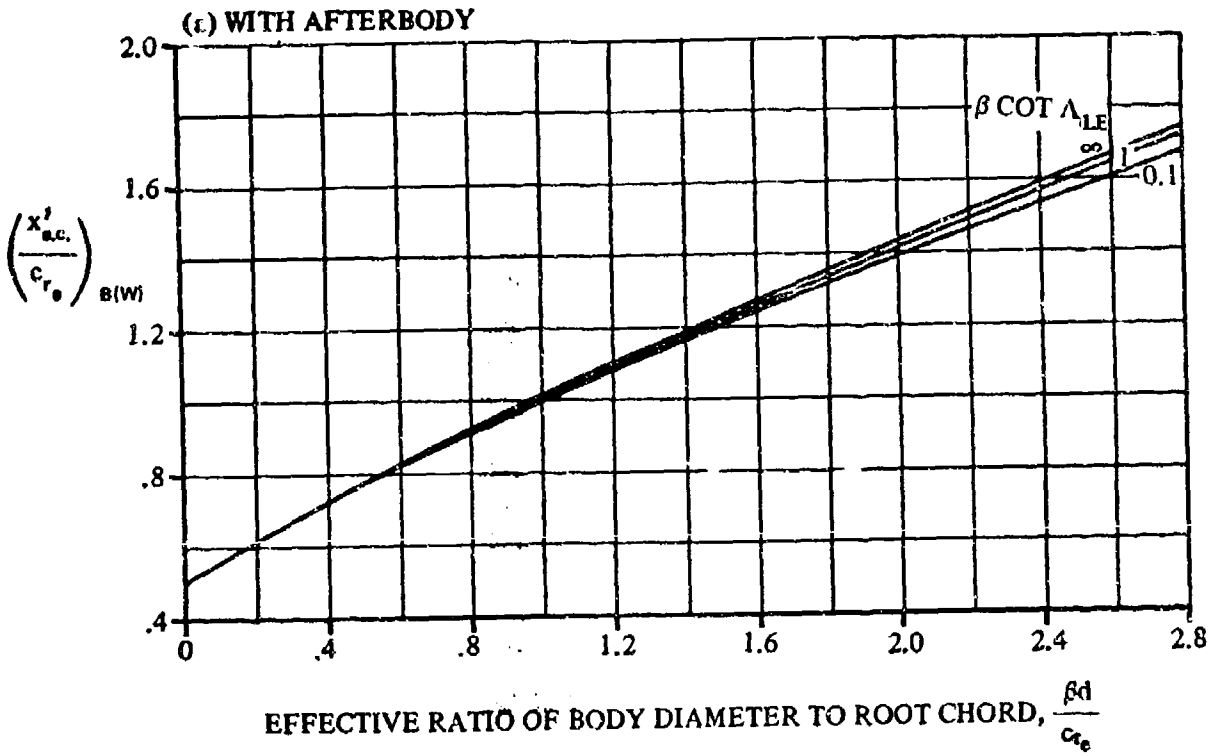

Figure 64 Aerodynamic-Center Locations for Lift Carry-over onto Body at Supersonic Speeds

$$C_D = C_{D_{MIN}}{}_{TOTAL} + (C_{D_L})_{WB} + (C_{D_L})_{HT} \tag{7-17}$$

$$C_m = C_{m_o} + \left(\frac{dC_m}{dC_L}\right)_{W-B} \left\{ C_{L_{\alpha_t}}(\alpha - \alpha_{o_t}) + C_{L_\delta}\ \delta_{HT} \right\} \ell_{HT/\bar{C}} \tag{7-18}$$

where the induced drag of the tail is predicted by use of a tail-induced drag factor K_t times the square of the lift generated by the tail, i.e.

$$(C_{D_L})_{HT} = K_t \left[C_{L_{\alpha_t}}(\alpha - \alpha_{o_t}) + C_{L_\delta}\ \delta_{HT} \right]^2 \tag{7-19}$$

From Equations 7-16 and 7-17, the incremental change in lift and drag <u>at constant α</u> due to a trim deflection can be determined by

$$\Delta C_L = C_{L_\delta} \cdot \delta_{HT} \tag{7-20}$$

$$\Delta C_D = K_t \left[C_{L_{\alpha_t}}(\alpha - \alpha_{o_t}) + C_{L_\delta} \cdot \delta_{HT} \right]^2 - K_t \left[C_{L_{\alpha_t}}(\alpha - \alpha_{o_t}) \right]^2 \tag{7-21}$$

Equation 7-21 can be reduced to

$$\Delta C_D = a\delta_{HT}{}^2 + b\delta_{HT}(\alpha - \alpha_{o_t}) \tag{7-22}$$

where $a = K_t C_{L_\delta}{}^2$

$$b = 2K_t C_{L_{\alpha_t}} \cdot C_{L_\delta}$$

The factor C_{L_δ} for an all-movable horizontal tail is predicted from

$$C_{L_\delta} = (C_{L_\alpha}')_t\ K_{W(B)} \cdot q_t/q_\infty \tag{7-23}$$

where $(C_{L_\alpha}')_t$ is the exposed-area lift-curve estimate for the tail, and $K_{W(B)}$ is the surface lift in the presence of the body factor. The induced drag factor for the tail is determined by the leading-edge suction method described in Section 4, where

$$K_t = \frac{1-R_t}{57.3 K_{W(B)} (C_{L_\alpha}')_t} + \frac{R_t}{\pi AR_{HT}} \frac{S_{REF}}{(S_{EX})_{HT}} \tag{7-24}$$

The Large Aircraft program can predict the lift, moment, and drag for a fixed tail setting or the program can solve for δ_{HT} to trim out the moment. The tail deflection required for trim is obtained by setting Equation 7-18 equal to zero and solving for δ_{HT}.

8. HIGH-LIFT SYSTEM AERODYNAMICS

The empirical methods for predicting lift, drag, and moment of an airplane with flap and slats deployed consist of adding the incremental effects of the high-lift system to the clean airplane aerodynamics. Figure 65 illustrates the manner in which the incremental effects of a flap can be applied to the clean-wing aerodynamics. The following techniques for estimating these increments were derived from DATCOM and References 36 and 37.

8.1 Lift of High-Lift Devices

The untrimmed equation for lift can be expressed as

$$C_L = C_{L_o} + C_{L_\alpha}(\alpha - \Delta\alpha) \tag{8-1}$$

The term $\Delta\alpha$ varies with α according to

$$\Delta\alpha = \begin{cases} 0; & \alpha < (\alpha_{max} - 2\Delta\alpha_{max}) \\ \left(\dfrac{\alpha - \alpha_{max} + 2\Delta\alpha_{max}}{2\Delta\alpha_{max}}\right)^2 \Delta\alpha_{max}; & \alpha > (\alpha_{max} - 2\Delta\alpha_{max}) \end{cases} \tag{8-2}$$

where

$$\alpha_{max} = \frac{C_{L_{max}} - C_{L_o}}{C_{L_\alpha}} + \Delta\alpha_{max}$$

The clean-wing $\Delta\alpha_{max}$ determined in Section 6.9.1 is also used for the case with flaps. The increment in C_{L_o} and $C_{L_{max}}$ caused by a trailing-edge-flap deflection can be estimated from

$$\Delta C_{L_o} = \Delta C_{\ell_o} \left(\frac{C_{L_\alpha}}{C_{\ell_\alpha}}\right) K_c K_b \tag{8-3}$$

$$\Delta C_{L_{max}} = \Delta C_{\ell_{max}} \left(\frac{C_{L_\alpha}}{C_{\ell_\alpha}}\right) K_c K_b \cos\Lambda_{c/2} \tag{8-4}$$

where K_c and K_b are shown plotted in Figures 66 and 67. The factor $C_{L_\alpha}/C_{\ell_\alpha}$, determined from the Polhamus lift equation

$$\frac{C_{L_\alpha}}{C_{\ell_\alpha}} = \frac{AR}{2 + \sqrt{4 + \left(\dfrac{S_{Ref}}{S_{Plan}}\right)^2 \left(\dfrac{AR}{\cos\Lambda_{c/2}}\right)^2}} \tag{8-5}$$

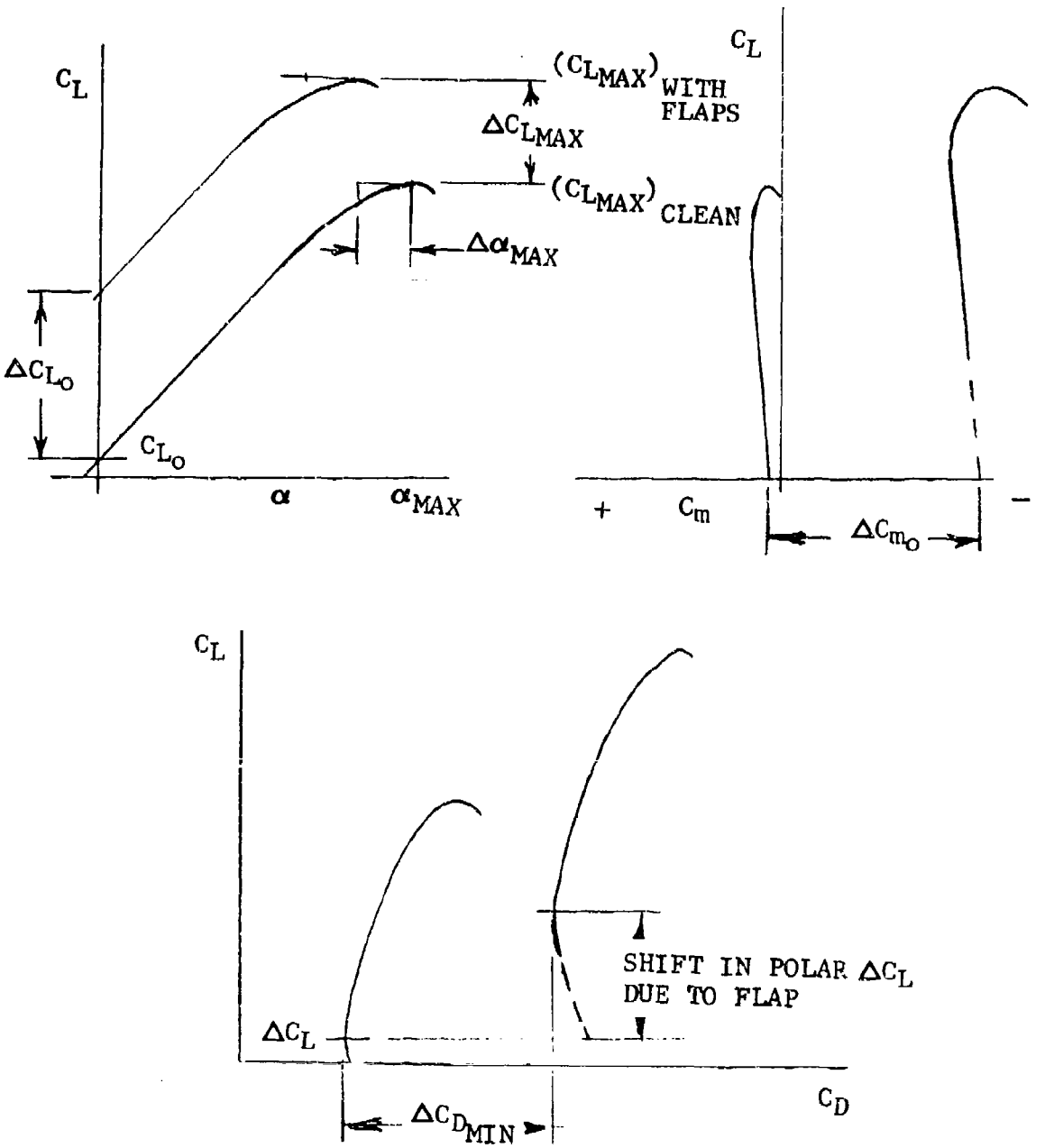

Figure 65 Incremental Effect of Flaps

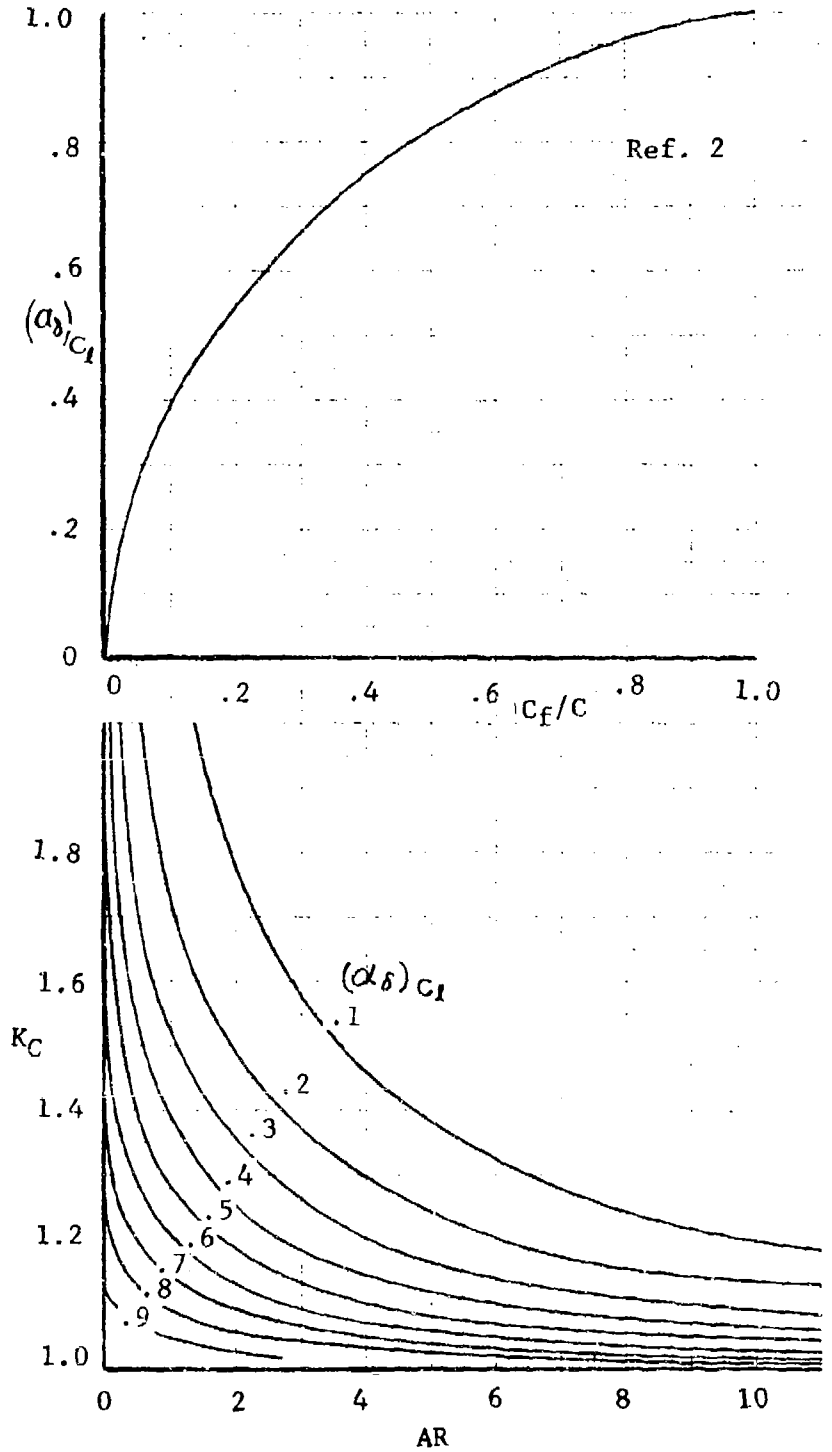

Figure 66 Flap Chord Factor

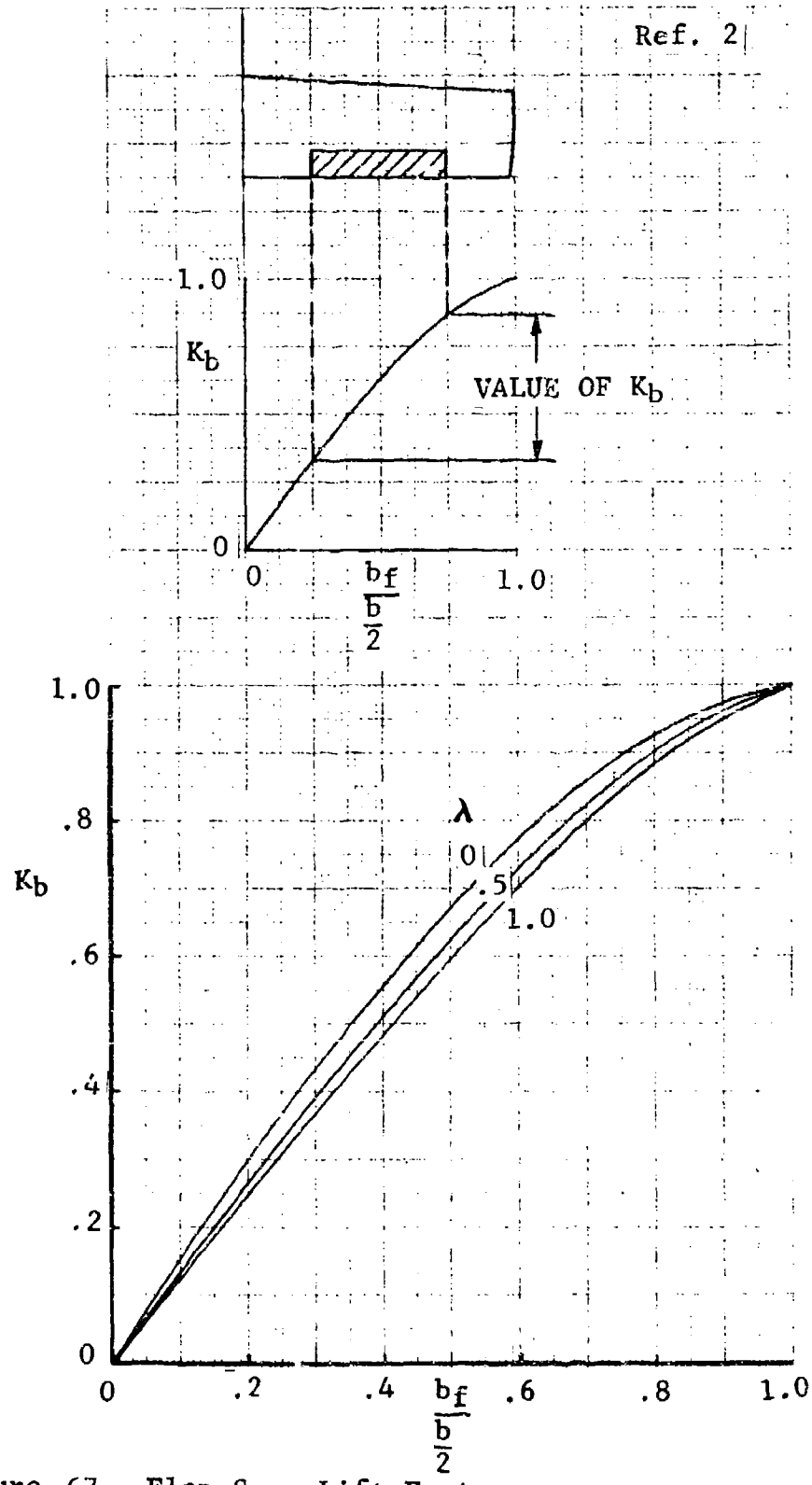

Figure 67 Flap Span Lift Factor

converts the sectional values ΔC_{ℓ_0} and $\Delta C_{\ell_{max}}$ to the three-dimensional case. The sectional values are either obtained from input to the program or generated internally for certain types of high-lift system. The method of generating the section values is discussed in Section 8.4.

The increment in lift at zero angle of attack is approximately zero when a slat is deflected. The slat acts to delay separation from the wing leading edge and thus allows higher angles of attack and, consequently, higher values of maximum lift before the wing stalls. An estimate of the increase in maximum lift of a slat is represented by

$$\Delta C_{L_{max}} = \Delta C_{\ell_{max}} \left(\frac{C_{L_\alpha}}{C_{\ell_\alpha}} \right) K_S \cdot \cos \Lambda_{LE} \qquad (8-6)$$

where the partial span effect, K_S, is shown plotted in Figure 68

8.2 Drag of High-Lift Devices

The untrimmed equation for drag can be expressed by

$$C_D = C_{D_{min}}{}_{Total} + K(C_L - \Delta C_L)^2 \qquad (8-7)$$

The drag-due-to-lift factor, K, with high-lift devices can be estimated by

$$K = K_{Clean} \cdot \frac{S_{Ref}}{S_{Plan}}$$

where K_{Clean} is the clean-airplane polar factor and S_{Plan} is the new planform area of the wing if the flap extends the chord of the wing. The drag due to lift factor remains unchanged until $\alpha > \alpha_{max} - 2 \cdot \Delta\alpha_{max}$, after which K approaches the zero-suction value given by $C_{D_L} = C_L \tan\alpha_{max}$.

Total minimum drag for the high-lift configuration is expressed as

$$C_{D_{min}}{}_{Total} = C_{D_{min}}{}_{Clean} + C_{D_{L.G.}} + C_{D_{Flaps}} + C_{D_{Slats}} + C_{D_I} \qquad (8-8)$$

where increments are summed for the landing gear and the profile

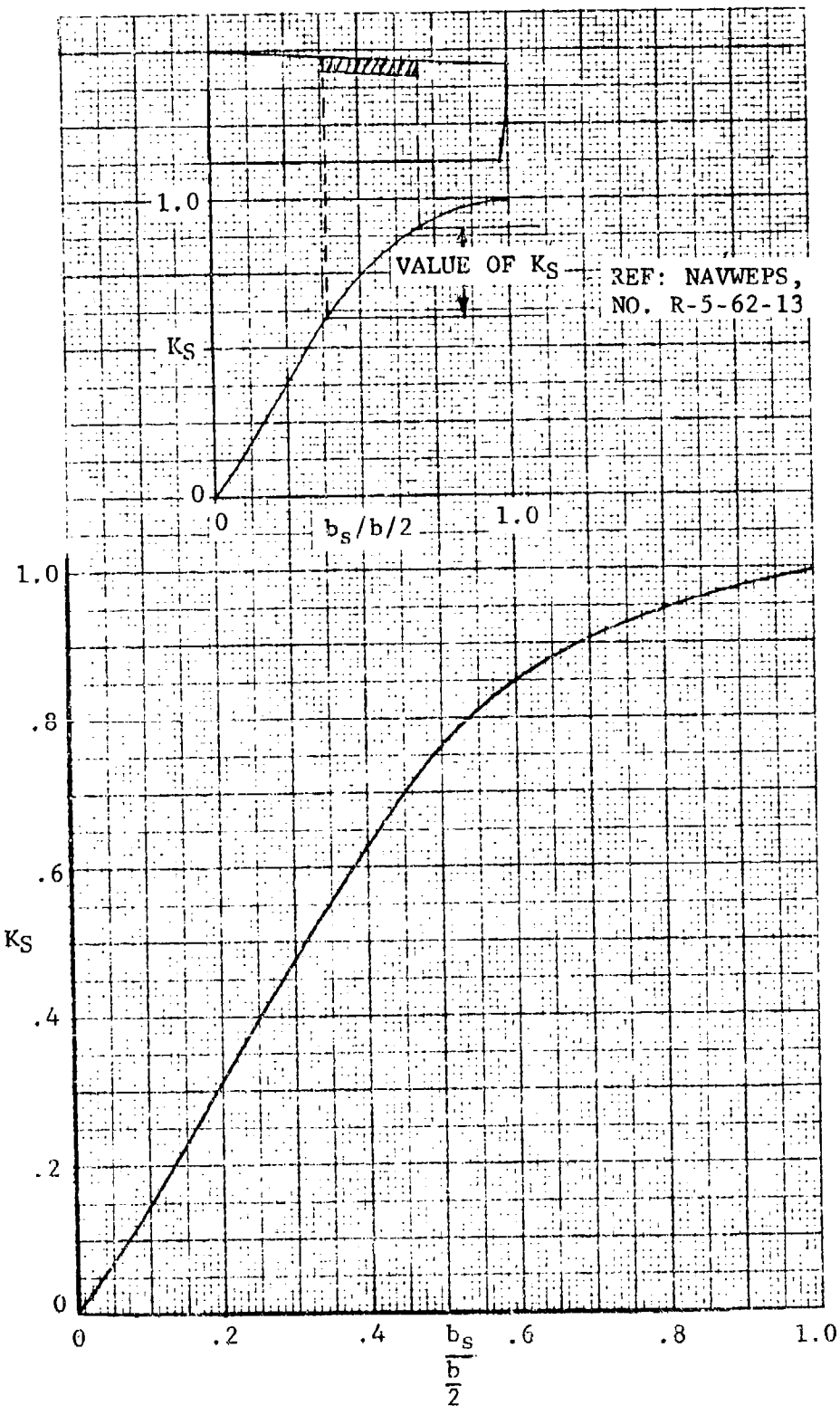

Figure 68 Slat Span Lift Factor

drag caused by the flaps and slats. The increment in profile drag of the flaps and slats can be estimated from sectional drag data, using

$$\Delta C_{D_{Flap}} = \Delta C_{d_f} \cos\Lambda_{HL} \cdot K_d \tag{8-9}$$

$$\Delta C_{D_{Slat}} = \Delta C_{d_s} \cos\Lambda_{LE} \cdot K_d \tag{8-10}$$

where K_d is a partial-span factor, shown plotted in Figure 69. The method for generating section values if given in Section 8.4.

Deflection of a flap produces an increase in lift at zero angle of attack which in turn produces an induced drag given by

$$C_{D_I} = K_a K_f \frac{(\Delta C_{L_o})^2}{\pi AR} \tag{8-11}$$

where K_a and K_f, shown plotted in Figure 70, are factors which account for the non-elliptical span loading of partial-span flaps.

The deflection of a flap increases the camber of the airfoil. In Reference 37, thin-airfoil camber theory is used to relate the displacement of a polar with flaps to the lift increment of the flap at zero angle of attack by the equation

$$\Delta C_L = (\Delta C_L)_{\substack{\text{Clean}\\\text{Wing}}} + (\Delta C_L)_{\substack{\text{Due to}\\\text{Flap}}}$$

where

$$(\Delta C_L)_{\substack{\text{Due to}\\\text{Flap}}} = \frac{(1-\frac{1}{\pi ARK})(\Delta C_{L_o})_{Flap}}{1+1.16\left(\frac{C_{L_\alpha}}{C_{l_\alpha}}\right)(.5-C_f/C)} \tag{8-12}$$

8.3 Moment of High-Lift Devices

The pitching moment increment caused by a flap on a swept wing is represented by

$$C_{M_{\alpha=o}} = \Delta C_{m_{\alpha=o}} \cdot K_m + \frac{1}{2} AR \tan\Lambda_{c/2} \cdot \Delta C_{l_o} \cdot K_{SW} \tag{8-13}$$

where $\Delta C_{m_{\alpha=o}}$ and ΔC_{l_o} are the sectional change in moment and

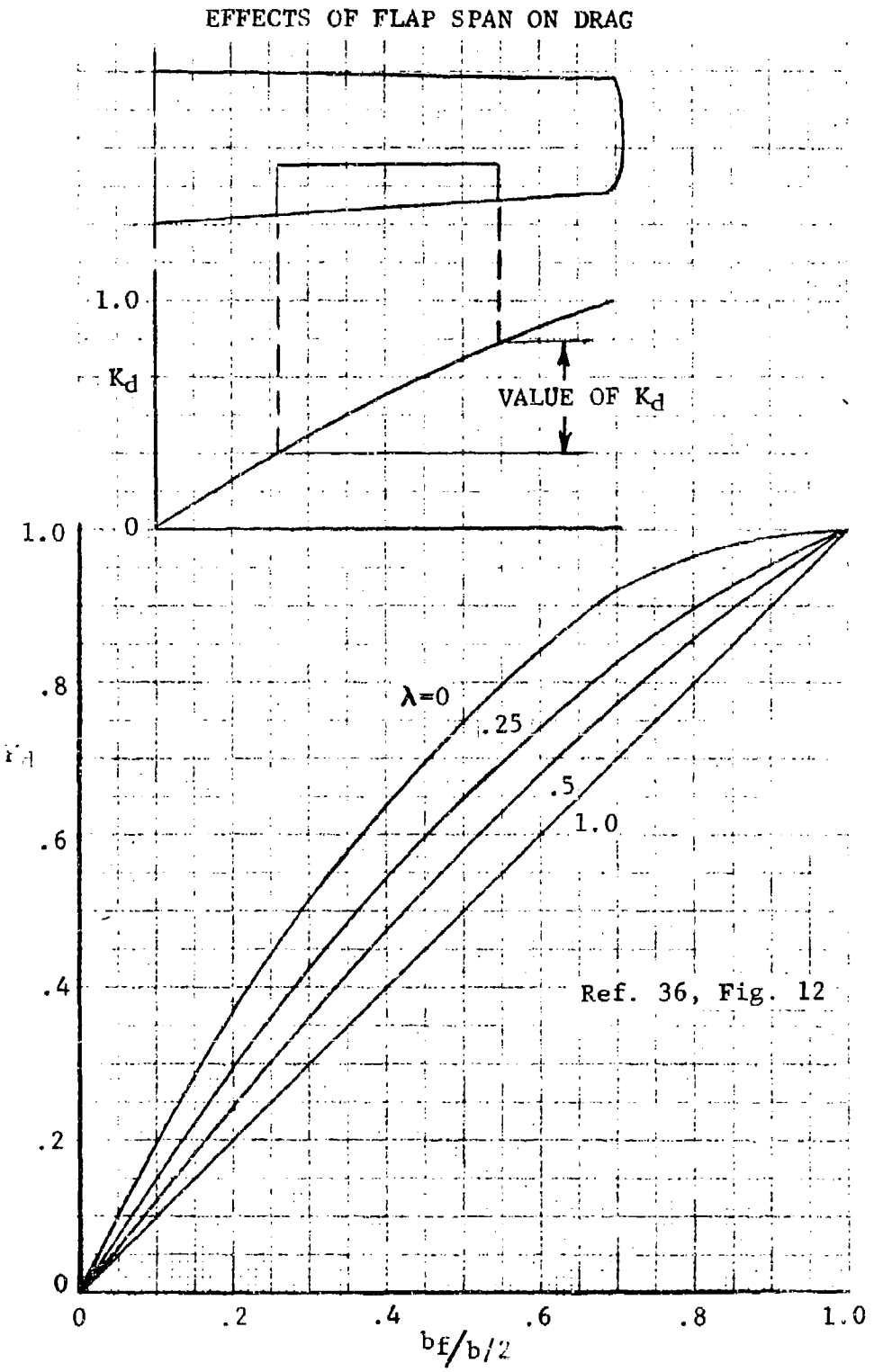

Figure 69 Flap Span Drag Factor

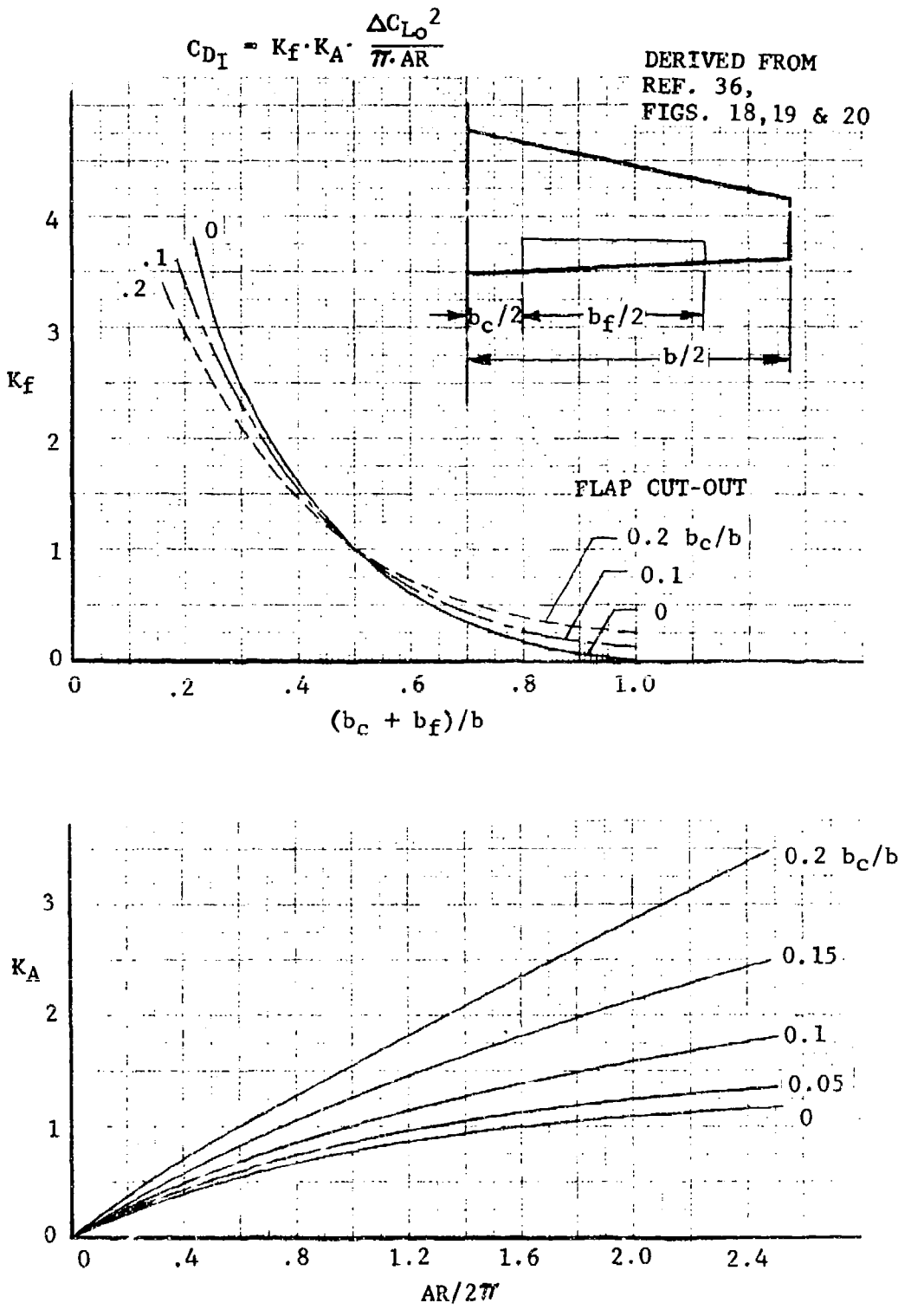

Figure 70 Flap-Induced Drag Factors

lift at zero alpha due to flap deflection. The partial-span factors K_m and K_{SW} are shown plotted in Figures 71 and 72, and the method for generating sectional data is given in Section 8.4.

8.4 Aerodynamic Characteristics of Two-Dimensional High-Lift Devices

The lift effectiveness of plain trailing-edge flaps can be estimated from thin-airfoil theory. The rate of change of lift with flap deflection at a constant angle of attack is given by

$$C_{\ell_\delta} = 2\left[\theta_f + \sin\theta_f\right] \tag{8-14}$$

where

$\cos\theta_f = 1 - 2(C_f/C')$

and C' is the extended chord.

This equation is plotted in Figure 73 as a function of flap-chord ratio. The theory considers only a bent flat plate and does not include effects of thickness or large deflection angles. The effects are accounted for in References 38 and 39 by empirical flap efficiency factors, as shown in Figures 74 through 77. The lift of a plain flap may now be expressed as

$$\Delta C_{\ell_o} = \eta_p \cdot C_{\ell_\delta} \cdot \delta_f \tag{8-15}$$

where

η_p is the plain-flap efficiency factor from Figure 74, depending on the flap deflection angle, δ_f, plus the included angle of the flap trailing edge, ϕ_{TE}.

C_{ℓ_δ} is the rate of change of lift with flap deflection at constant angle of attack from Equation 8-14.

δ_f is the flap deflection angle in radians.

This procedure is extended to slotted flaps with Fowler motion by evaluating C_{ℓ_δ} at a flap-chord ratio based on the extended chord. For double- or triple-slotted Fowler flap segments the lift increment is obtained by summing the incremental lift increments for each flap segment. The result is

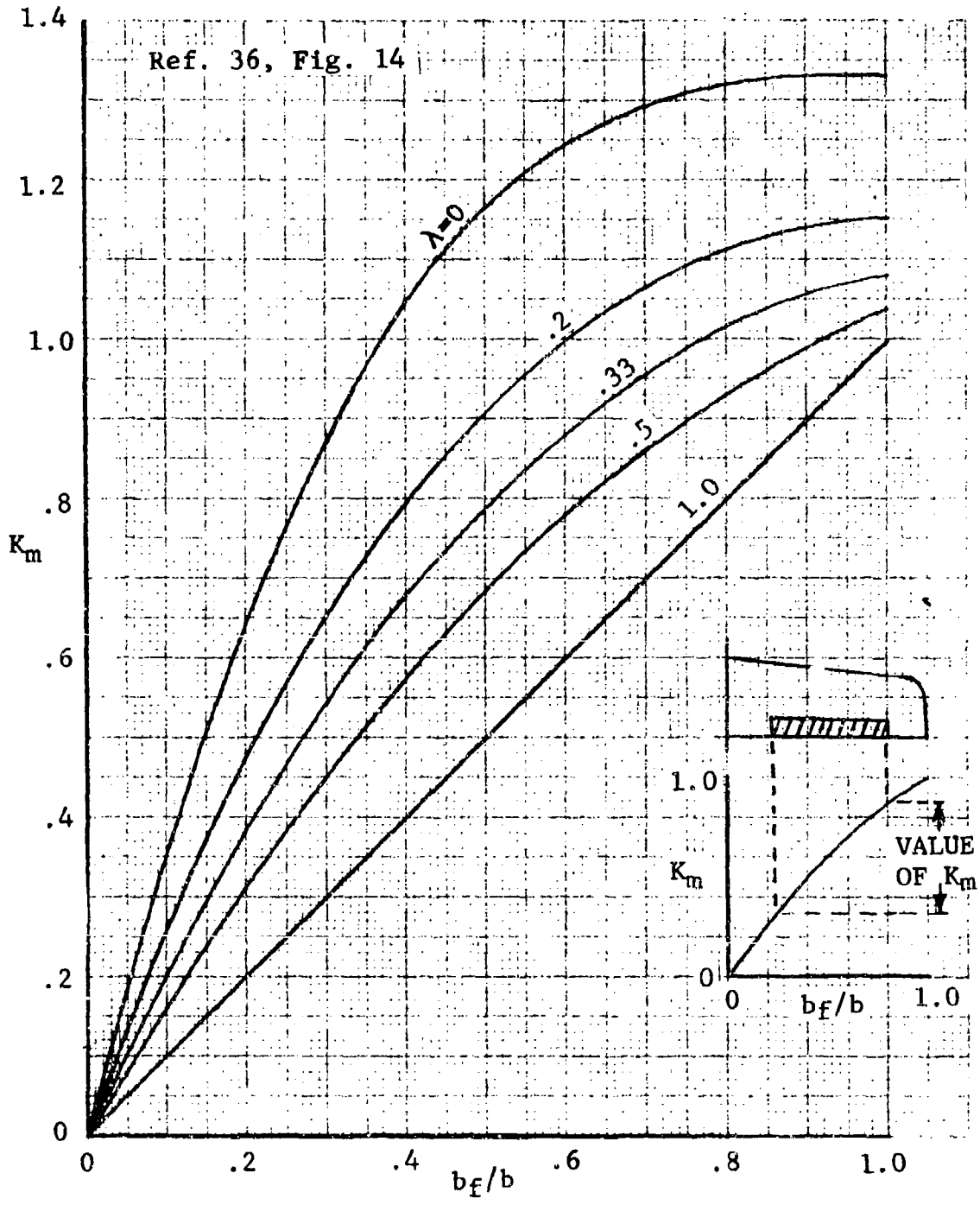

Figure 71 Span Effect on Moments

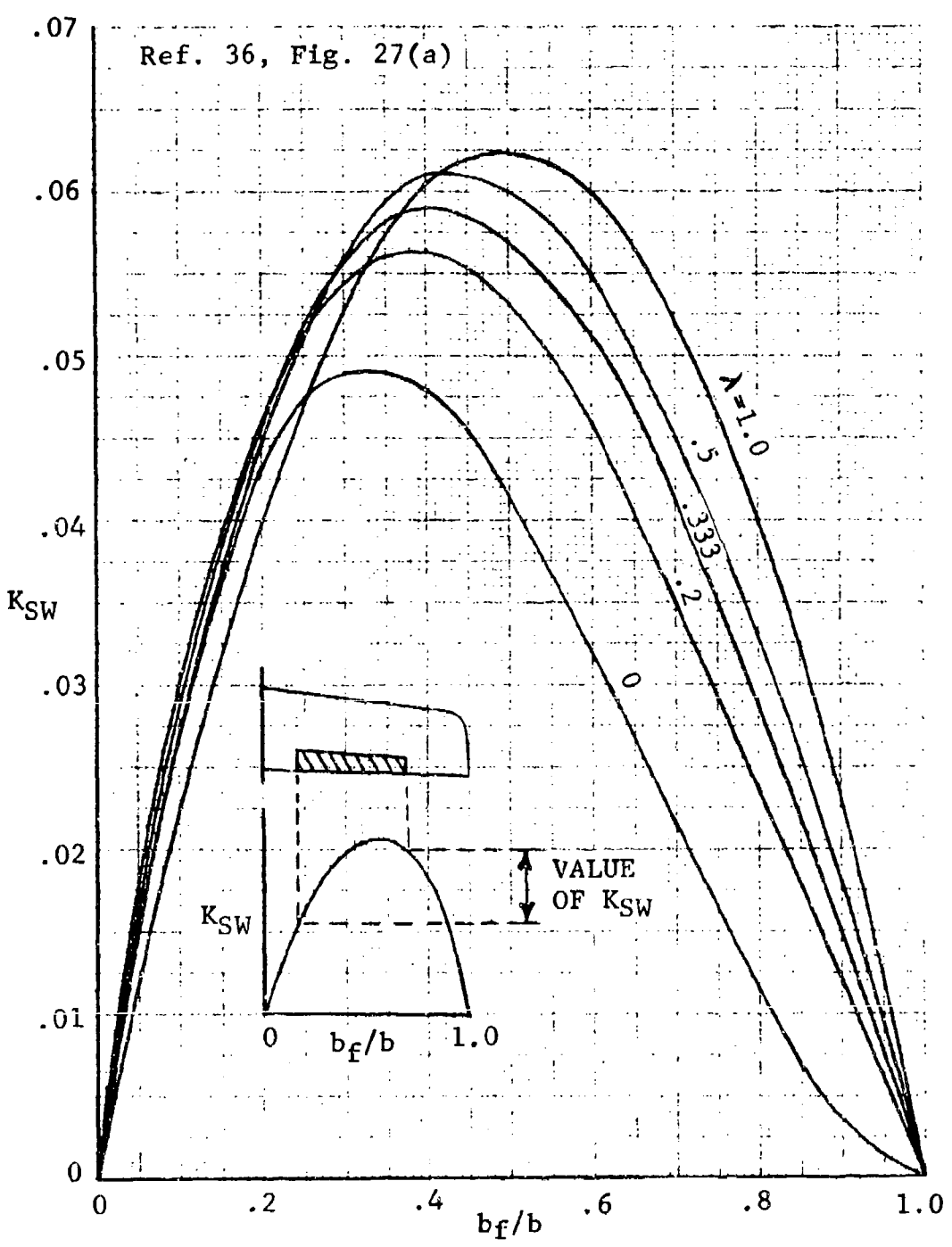

Figure 72 Span Effect on Moments of Sweptback Wings

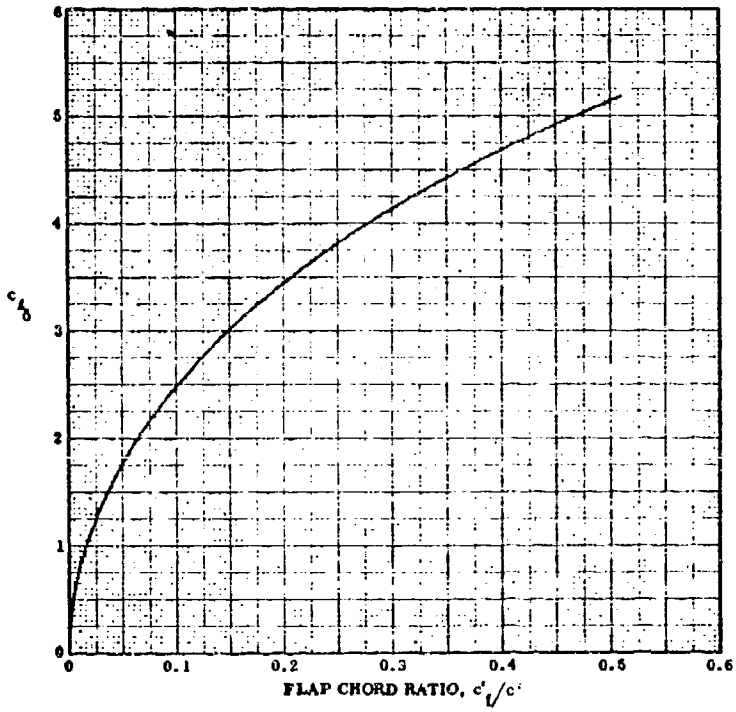

Figure 73 Theoretical Lifting Effectiveness of Trailing-Edge Flaps

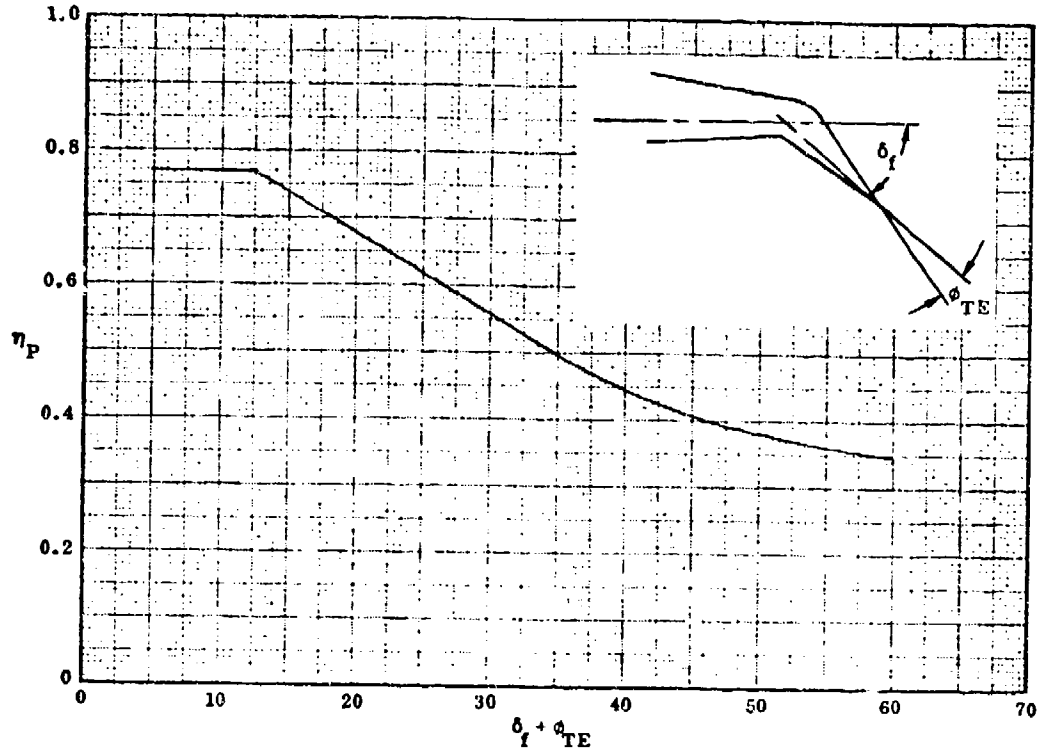

Figure 74 Turning Efficiency of Plain Trailing-Edge Flaps

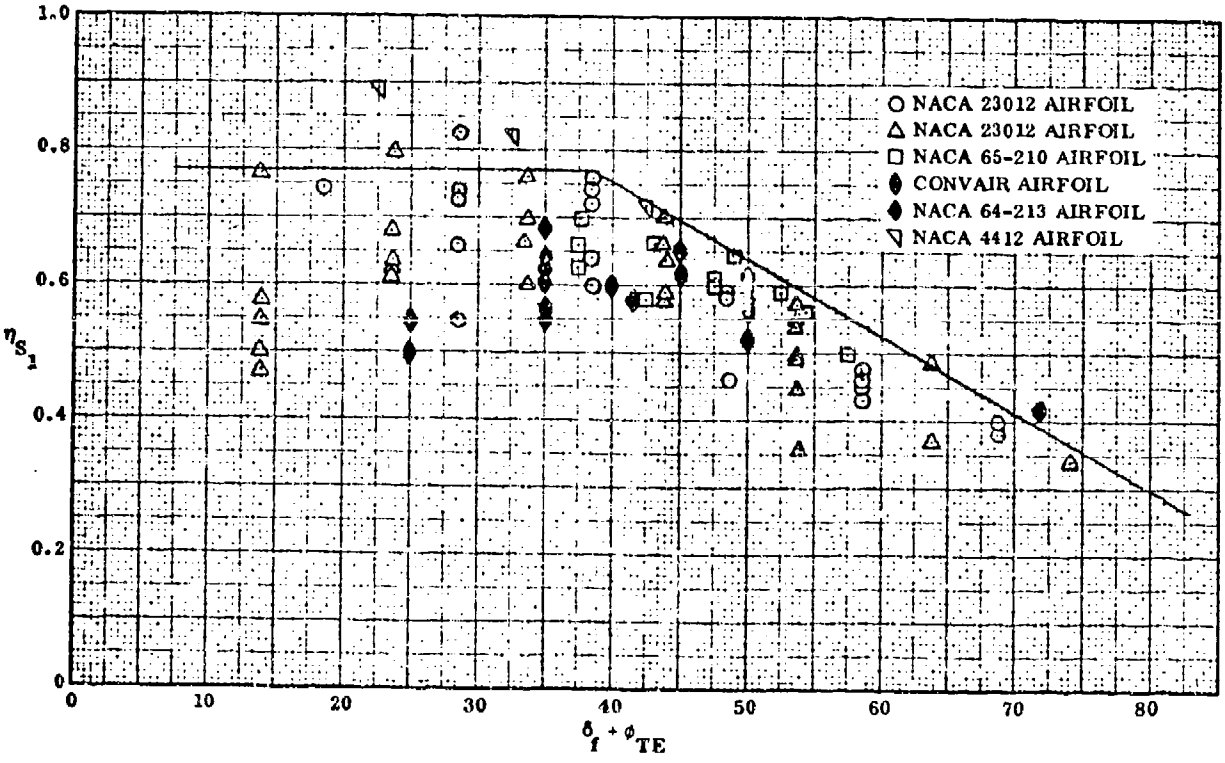

Figure 75 Turning Efficiency of Single-Slotted Flaps

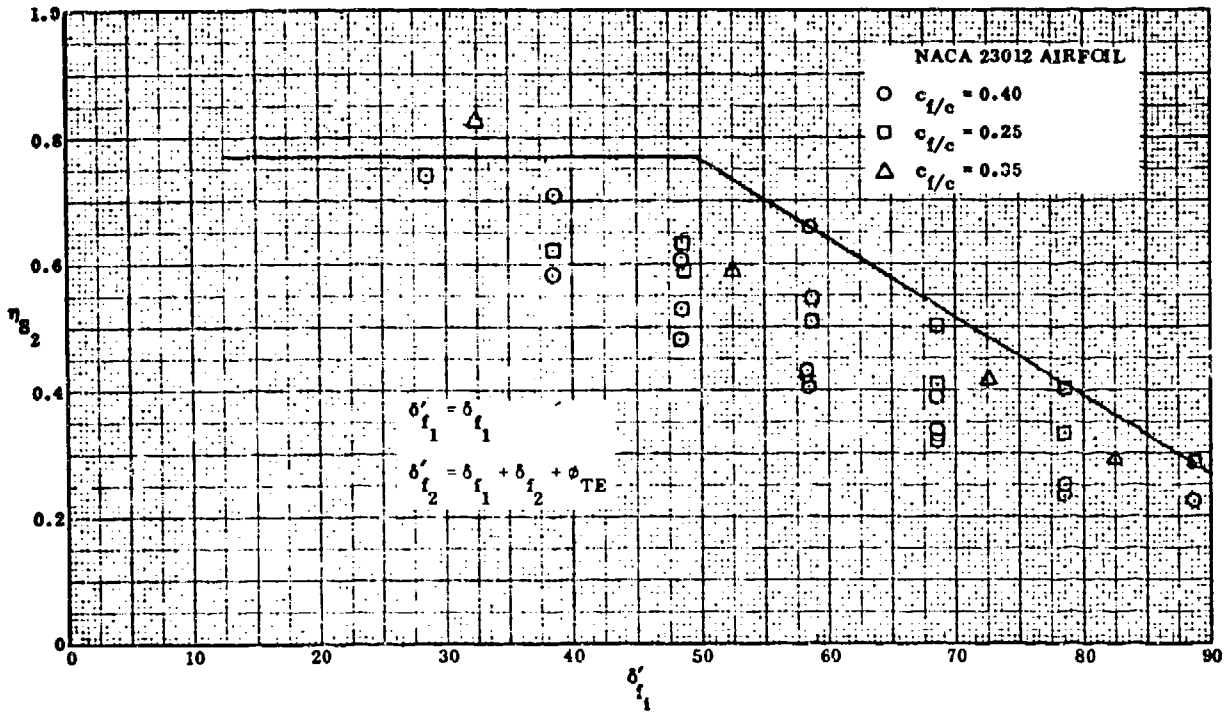

Figure 76 Turning Efficiency of Double-Slotted Flaps

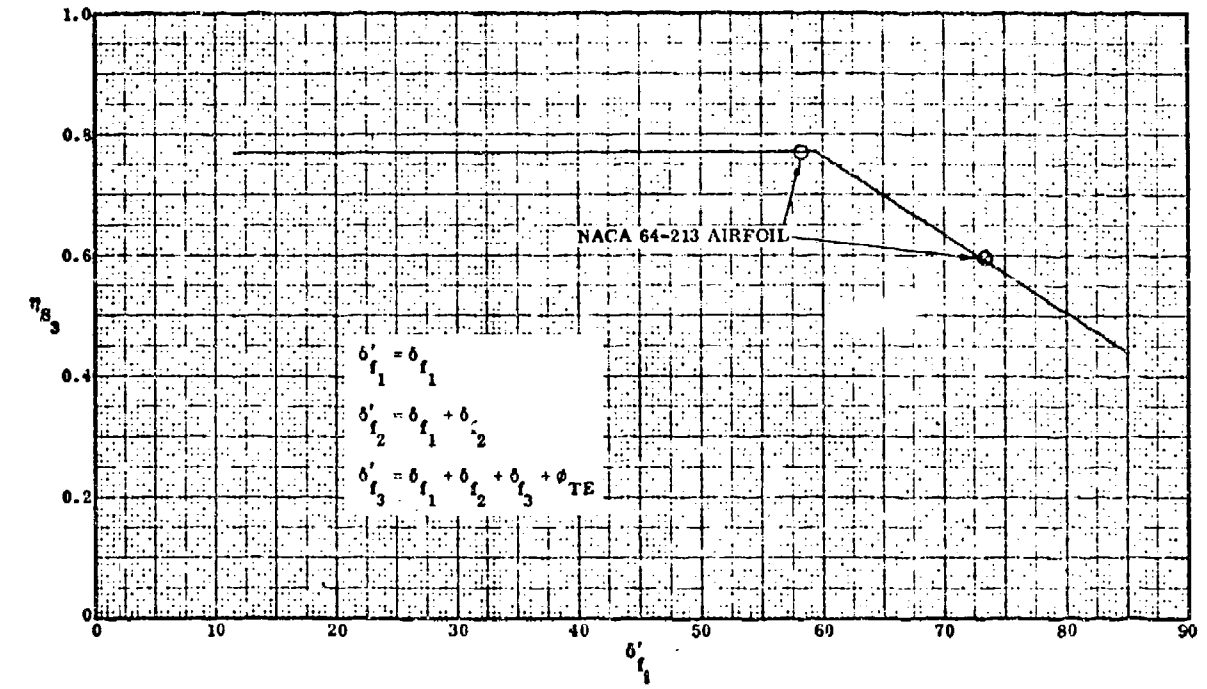

Figure 77 Turning Efficiency of Triple-Slotted Flaps

$$\Delta C_{\ell_o} = \sum_{i=1}^{I} \eta_{SI_i} \cdot C_{\ell_{\delta_i}} \cdot \delta_{f_i} \qquad (8\text{-}16)$$

where

i is a subscript that indicates the 1st, 2nd, 3rd flap segment of the slotted flap

I is the number of slots or segments in the flap system

η_{SI_i} is the slotted-flap efficiency factor from Figures 75, 76, or 77 for the ith flap segment

$C_{\ell_{\delta i}}$ is the lift effectiveness for the ith flap segment

δ_{f_i} is the flap deflection of the ith flap segment.

The method of summation and the geometry definition required to evaluate Equation 8-16 is shown in Figure 78.

The effects of leading-edge high-lift devices on the wing lift at zero angle of attack is estimated from thin-airfoil theory as

$$(C_{\ell_\delta})_{LE} = 2(\sin \theta_{LE} - \theta_{LE}) \qquad (8\text{-}17)$$

where

$$\cos \theta_{LE} = 1 - 2(C_{LE}/C')$$

Unlike trailing-edge flaps, the deflection of a nose flap causes a loss in lift at zero angle of attack. The increment in lift, ΔC_{ℓ_o} is

$$\Delta C_{\ell_o} = (C_{\ell_\delta})_{LE} \cdot \delta_{LE} \qquad (8\text{-}18)$$

where δ_{LE} is the leading-edge flap deflection angle in radians, positive nose down.

The two-dimensional maximum lift increment, $\Delta C_{\ell_{max}}$, due to a trailing-edge plain-flap deflection is given in Reference 38 as

$$\Delta C_{\ell_{max}} = K_T \cdot K_\delta \cdot \Delta C_{\ell_{\alpha=0}} \left(\frac{\Delta C_{\ell_{max}}}{\Delta C_{\ell_{\alpha=0}}} \right) \qquad (8\text{-}19)$$

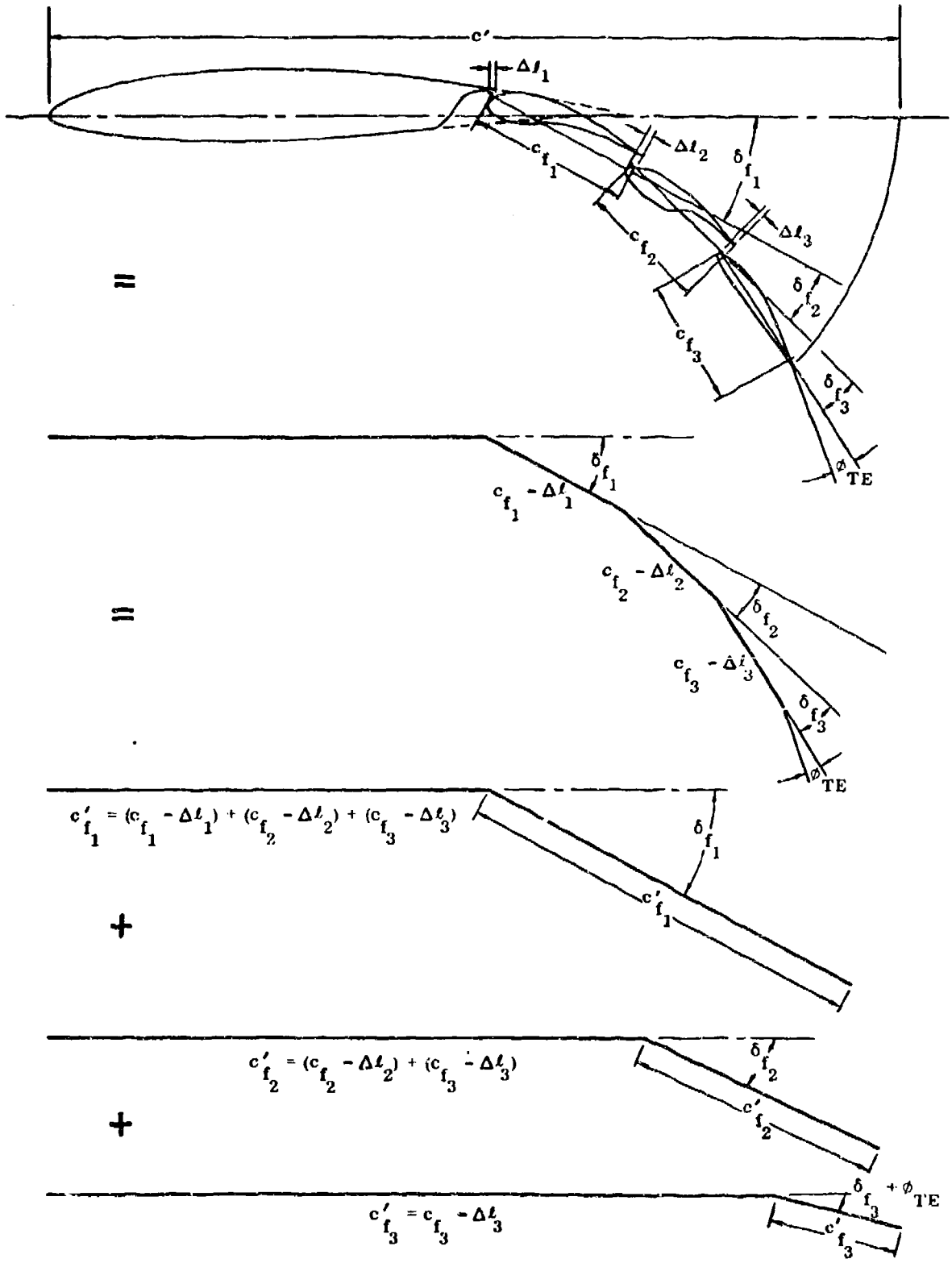

Figure 78 Principle of Superposition Theory and Extended Slotted-Flap Geometry

and, similarly, for single, double- or triple-slotted flaps the equation is

$$\Delta C_{\ell_{max}} = K_T \cdot K_\delta \sum_{i=1}^{I} \left(\Delta C_{\ell_o}\right)_i \left(\frac{\Delta C_{\ell_{max}}}{\Delta C_{\ell_{\alpha=0}}}\right)_i \qquad (8\text{-}20)$$

where

$\left(\Delta C_{\ell_o}\right)_i$ is the predicted lift increment determined for the ith flap segment from Equation 8-18

K_T and K_δ are empirical factors developed from experimental data shown plotted in Figures 79 and 80

$\frac{\Delta C_{\ell_{max}}}{\Delta C_{\ell_{\alpha=o}}}$ is the theoretical relationship between $\Delta C_{\ell max}$ and $\Delta C_{\ell_{\alpha=0}}$ given in Reference 39 as

$$\left(\frac{\Delta C_{\ell_{max}}}{\Delta C_{\ell_{\alpha=o}}}\right) = 1 - \frac{\theta_f}{\theta_f+\sin\theta_f}\left[1 + \frac{\ell n\left|\sin\frac{1}{2}(X+\theta_f)/\sin\frac{1}{2}(X-\theta_f)\right|}{\theta_f \tan X/2}\right] \qquad (8\text{-}21)$$

where $\cos X = 2(X_s/c')-1$ and $\cos\theta_f = 1-2(C_f/c')$. This equation relates the theoretical maximum-lift increment to the chord of the flap and the position of separation, X_s/c', on the airfoil. The choice of the separation point X_s/c' to determine the maximum-lift ratio from Equation 8-21 depends on the leading-edge configuration. For clean leading-edge airfoils, the point of flow separation is assumed at the leading edge, $X_s/c' = 0$. For airfoils with leading-edge high-lift devices, the point of flow separation is assumed to be at the knee of the leading-edge device, $X_s/c' = C_{LE}/c'$.

The two-dimensional increment in maximum-lift coefficient of leading-edge devices is predicted in Reference 38 as follows

$$\Delta C_{\ell_{max}})_{LE} = C_{\ell_{\delta_{LE}}})_{MAX} \cdot \eta_{max} \cdot \eta_\delta \cdot \delta_{LE} \qquad (8\text{-}22)$$

where, according to thin-airfoil theory,

$$C_{\ell_{\delta_{LE}}})_{MAX} = 2 \sin\theta_{LE}$$

and $\cos\theta_{LE} = (1-2C_{LE}/c')$. The $(C_{\ell_{\delta_{LE}}})_{max}$ is presented in Figure 81. The factors η_{max} and η_δ are empirical factors, introduced in Reference 38, to correlate $\Delta C_{\ell max})_{LE}$ with available test

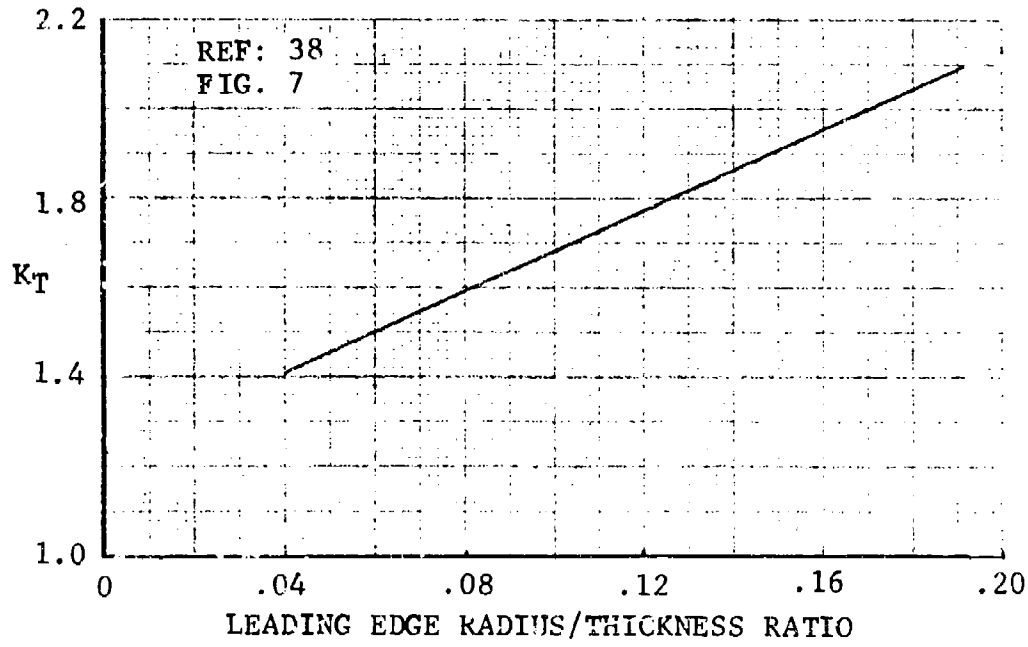

Figure 79 Maximum Lift Correlation Factor for Trailing-Edge Flaps

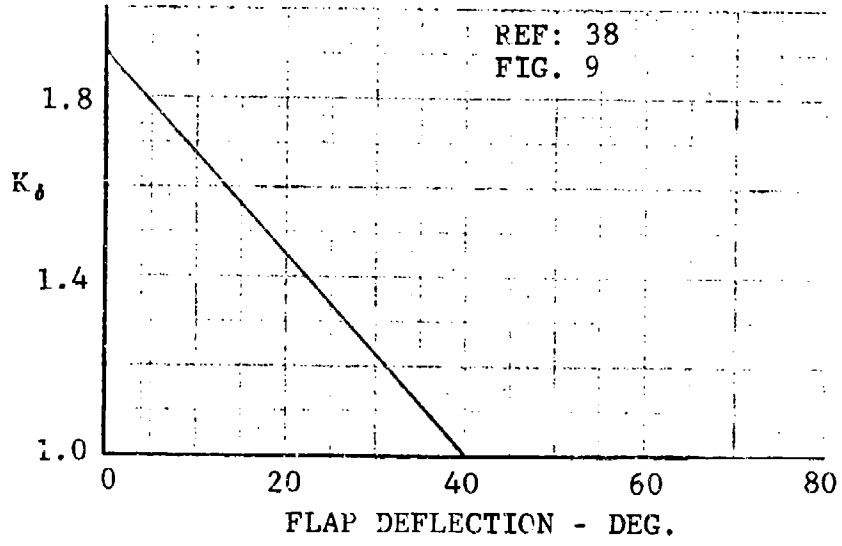

Figure 80 Flap Angle Correlation Factor Versus Flap Deflection

data on airfoils with trailing-edge flaps (Figures 82 and 83). The maximum-lift efficiency factor, η_{max}, depends on the type of leading-edge device and on the ratio of leading-edge radius to maximum airfoil thickness; η_δ is an efficiency factor that accounts for large leading-edge-flap deflections.

In the case of the two-dimensional moment increment, the methodology for predicting the pitching moment is developed parallel to the methods used for estimating the lift increment, which extend thin-airfoil theory to cover multiple-slotted flaps with extendable chords. The trailing-edge-flap pitching-moment increment at zero angle of attack is given in Reference 38 as

$$\Delta C_{m_{\alpha=0}} = \Delta C_{\ell_0} \cdot \left(\frac{C_{m_\delta}}{C_{\ell_\delta}}\right) \cdot K_m' \qquad (8\text{-}23)$$

where

ΔC_{ℓ_0} is the predicted lift increment for either trailing-edge or leading-edge devices

$\left(\frac{C_{m_\delta}}{C_{\ell_\delta}}\right)$ is the theoretical center-of-pressure location from thin-airfoil theory (Figure 84)

K_m' is an empirical factor developed from experimental data (Figure 85)

In the case of the profile drag increment, flap drag increments at $\alpha = 0$ for plain and single-slotted flaps are obtained from Figures 86 and 87. These figures were obtained from Section 6.1.7 in the DATCOM. For double- and triple-slotted flaps, Figure 88 is used to obtain the $\alpha = 0$ drag increment.

8.5 Ground Effect

During takeoff and landing when the clean airplane is close to the ground, the ground proximity produces an increase in the lift-curve slope, a decrease in drag, and reduction of nose-up pitching moment. However, some high-lift configurations may show a loss in lift-curve slope due to ground effect.

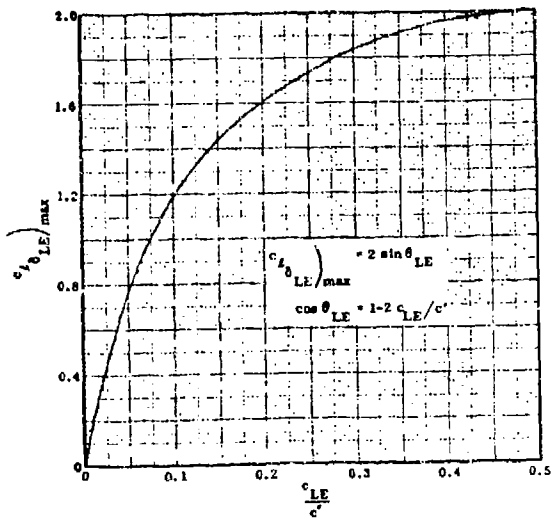

Figure 81 Leading Edge Flap Maximum Lift Effectiveness

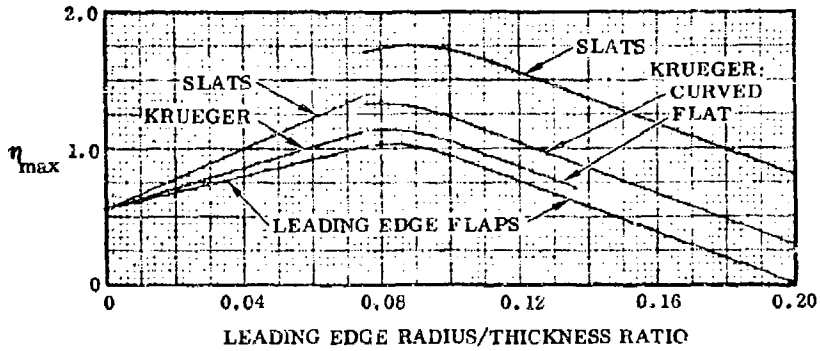

Figure 82 Maximum Lift Efficiency for Leading-Edge Devices

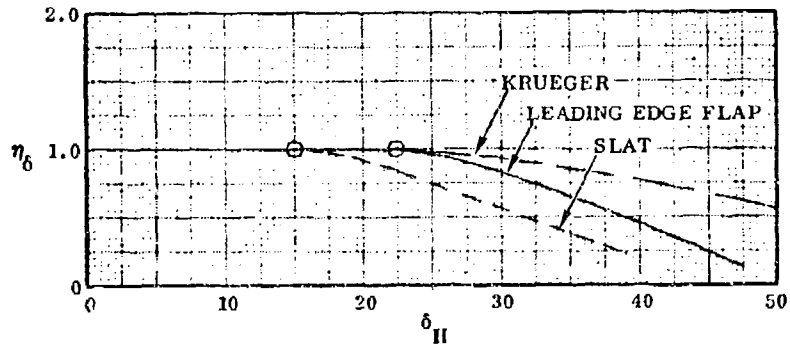

Figure 83 Leading Edge Device Deflection Angle Correction Factor

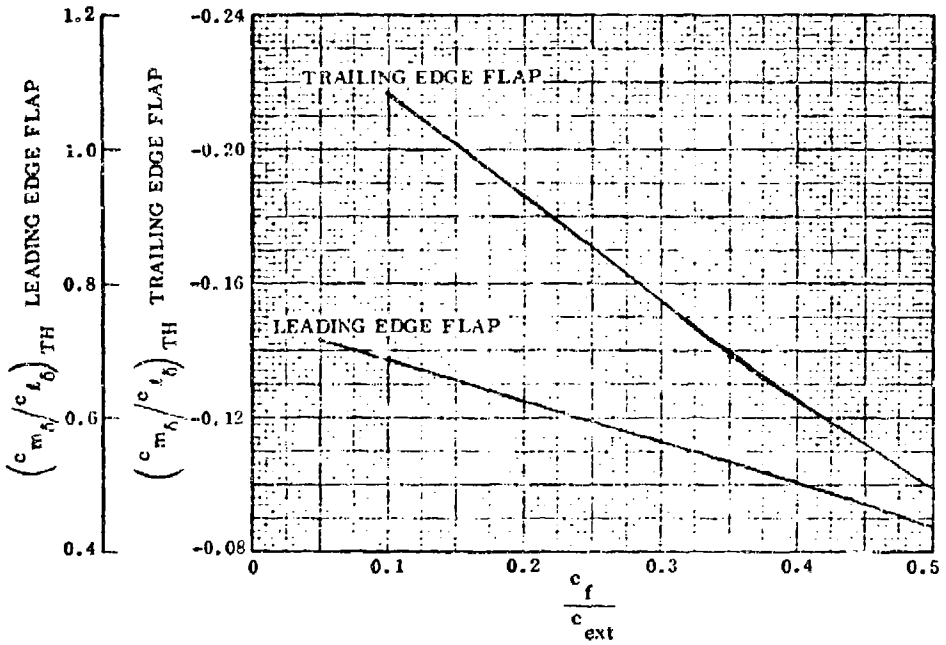

Figure 84 Flap Center of Pressure Location as given by Thin Airfoil Theory

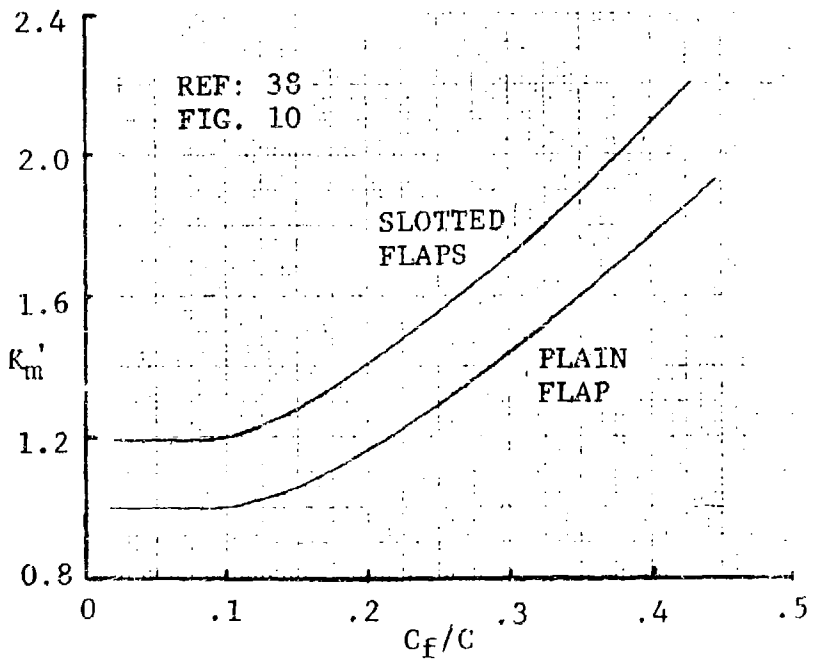

Figure 85 Moment Correlation Factor Versus Flap Chord

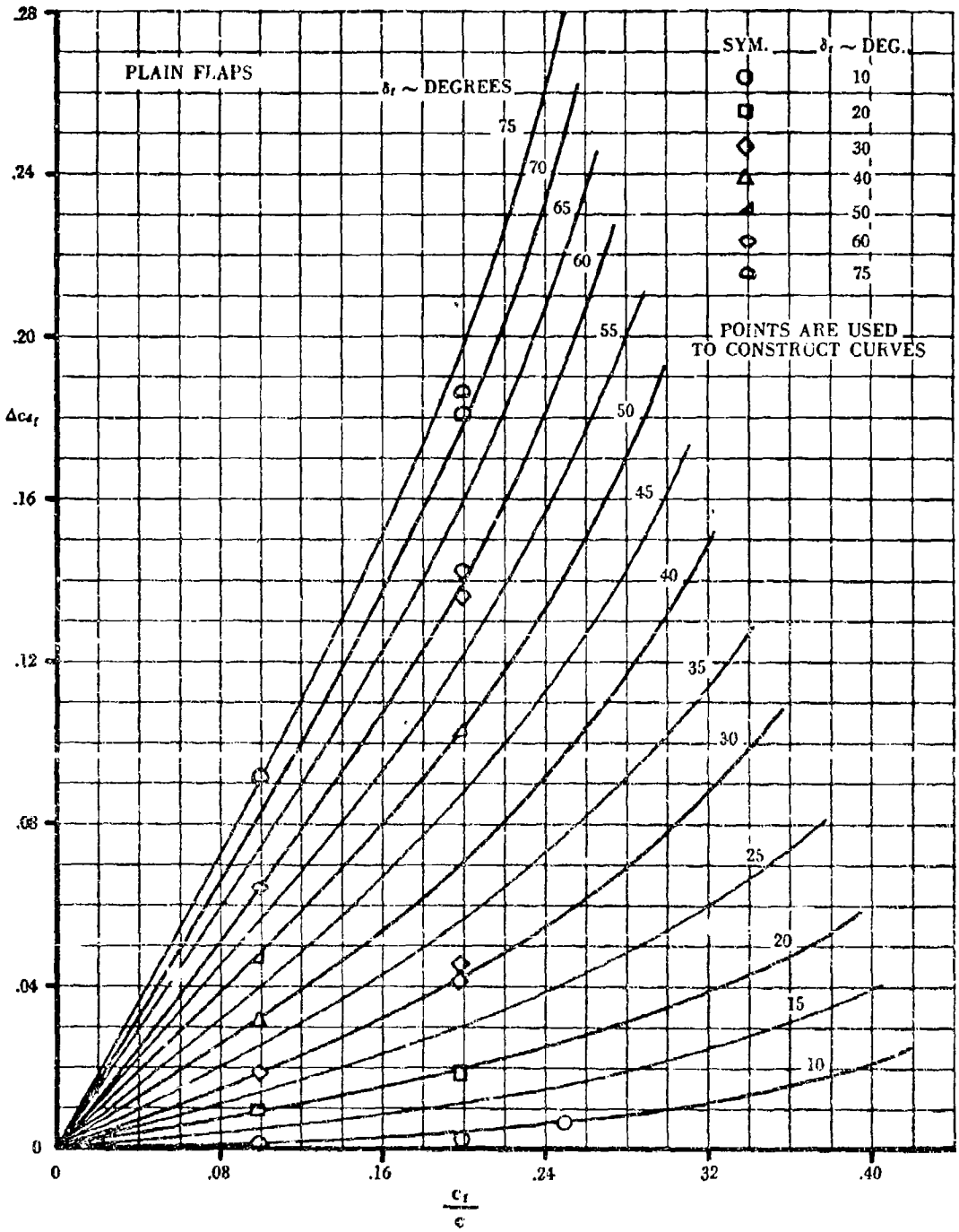

Figure 86 Two-Dimensional Drag Increment Due to Plain Flaps

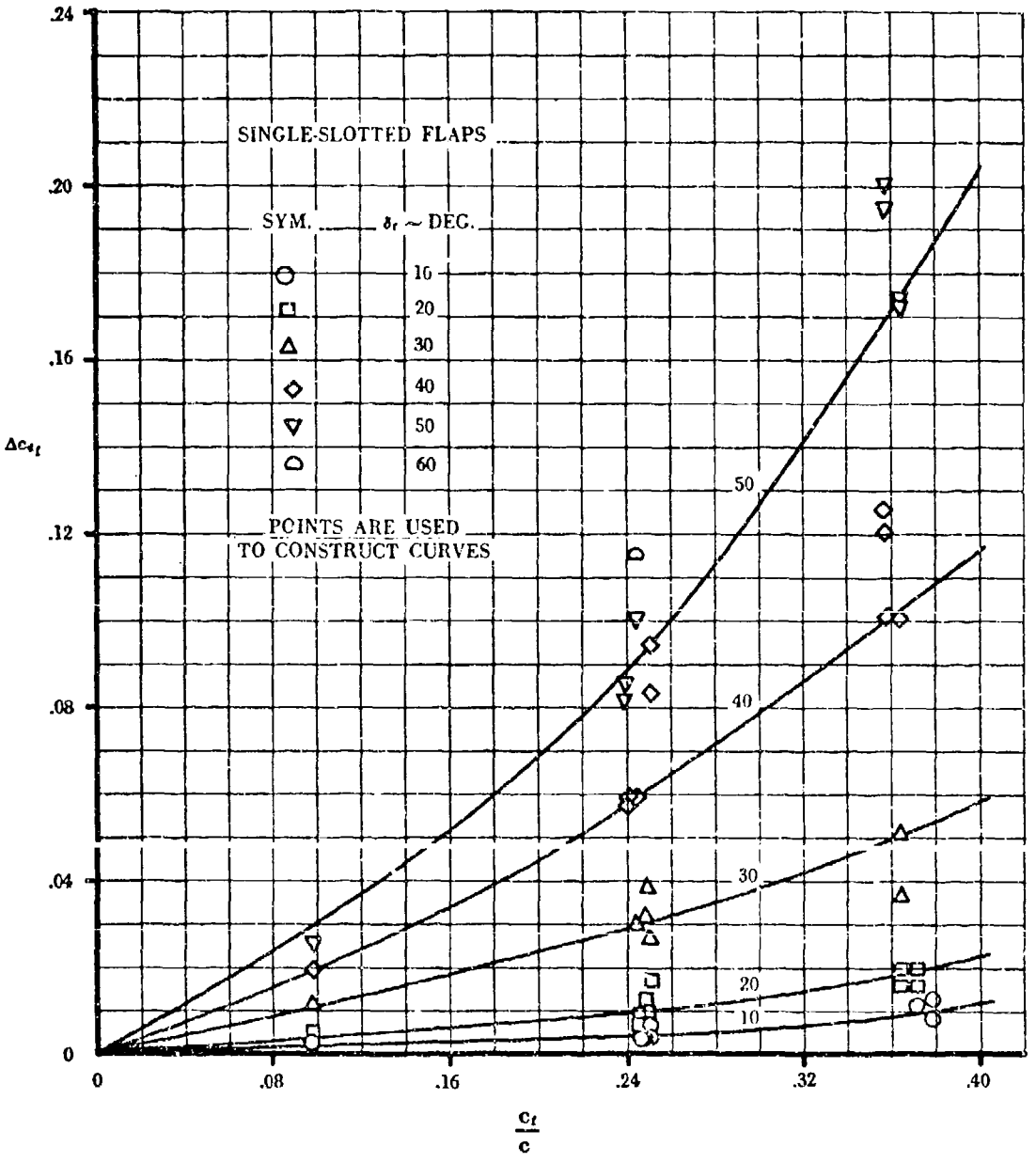

Figure 87 Two-Dimensional Drag Increment Due to Single-Slotted Flaps

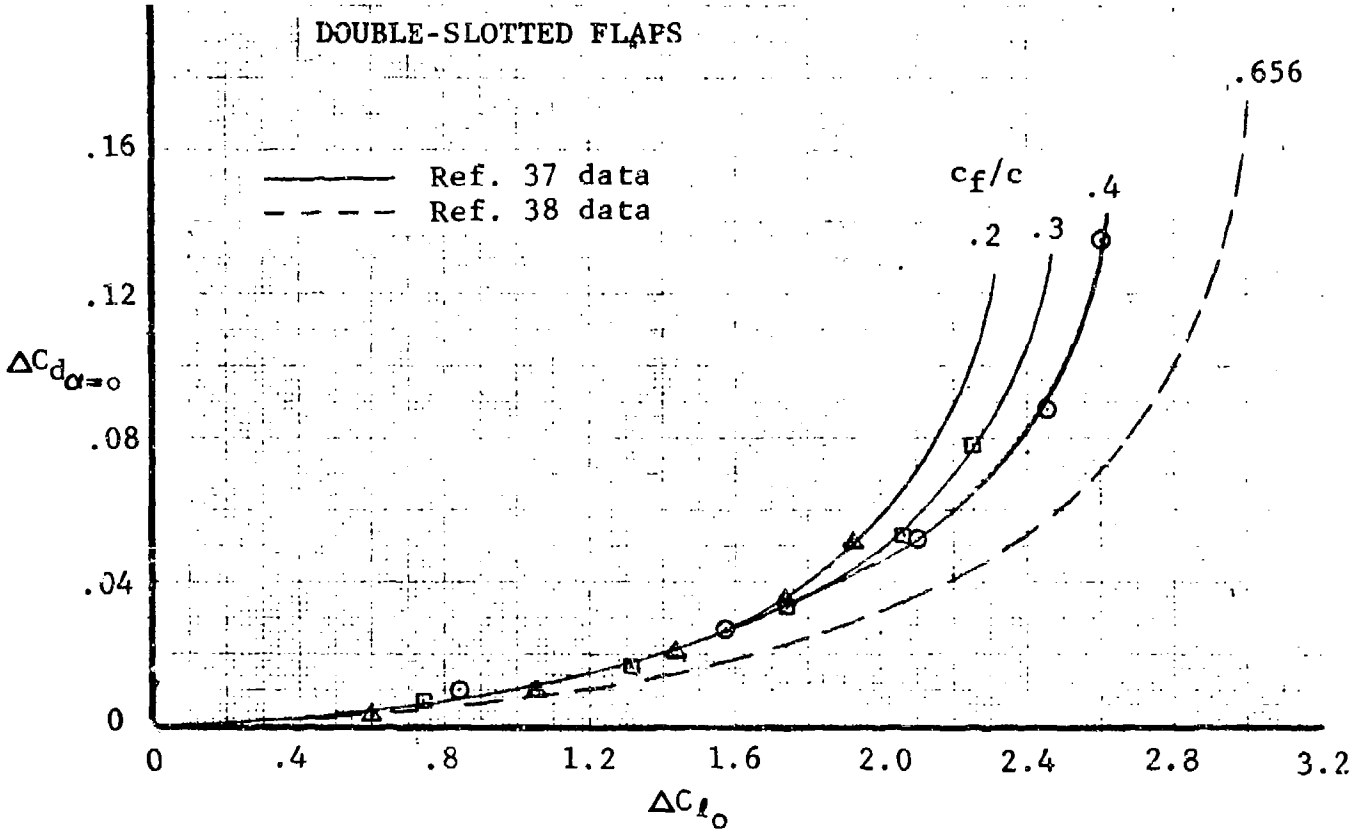

Figure 88 Drag Increment for Double-Slotted Flaps Versus Lift Increment at $\alpha = 0^{\circ}$

A theoretical approach for estimating ground effects would employ an image-vortex system to represent the ground plane. The DATCOM uses a semi-empirical method to estimate the increase in induced upwash at the wing due to the reflected trailing vortices and the change in lift at the wing due to the reflected flap ground effects. The change in wing-body lift moment and drag due to ground effect at a constant angle of attack is given by

$$\Delta C_L = (\Delta C_L)_{WB} + (\Delta C_L)_{HT} \tag{8-24}$$

$$\Delta C_M = \left(\frac{X_{CG}}{\bar{c}} - \frac{X_{ac}}{\bar{c}}\right)(\Delta C_L)_{WB} - (\Delta C_L)_{HT}\, \ell_{HT/\bar{c}} \tag{8-25}$$

$$\Delta C_D = -\frac{\sigma C_L^2}{\pi AR} - \left(C_{D_{\substack{\text{Wing}\\\text{Alone}}}} - \frac{\sigma C_L^2}{AR}\right) \frac{rTC_L}{57.3} \tag{8-26}$$

where σ, r and T are ground-effect parameters, shown plotted in Figures 89, 90, and 91. The term $C_{D_{\text{Wing Alone}}}$ is the minimum drag contribution of the wing plus the drag due to lift of the wing in free air. The increment in lift on the wing due to ground effect is calculated from

$$(\Delta C_L)_{WB} = \left\{\frac{9.12+14.32/(1+\lambda)}{AR}\right\} C_{L_{WB}} (C_{L_\alpha})_{WB} \cdot \sigma'$$

$$+ \frac{r}{1+\lambda}\left(\frac{\Delta L}{L_o}\right) C_{L_{WB}} + \left(\frac{\delta f}{50}\right)^2 \Delta(\Delta C_L)_{Flap} \tag{8-27}$$

where $C_{L_{WB}}$ is the wing-alone lift at angle of attack, and σ', $(\Delta L/L_o)$, and $\Delta(\Delta C_L)_{Flap}$ are shown plotted in Figures 92, 93, and 94. The increment in lift on the horizontal tail due to ground effect is calculated from

$$(\Delta C_L)_{HT} = (\Delta \epsilon)\, C_{L_{\alpha t}} \Big/ \left(1 - \frac{\partial \epsilon}{\partial \alpha}\right) \tag{8-28}$$

where $\Delta\epsilon$ is the change in downwash at the tail given by

$$\Delta \epsilon = \epsilon \left[\frac{b_{eff}^2 + (H_H - H)^2}{b_{eff}^2 + (H_H + H)^2}\right] \tag{8-29}$$

where ϵ is the downwash at the tail in free air, H is the height

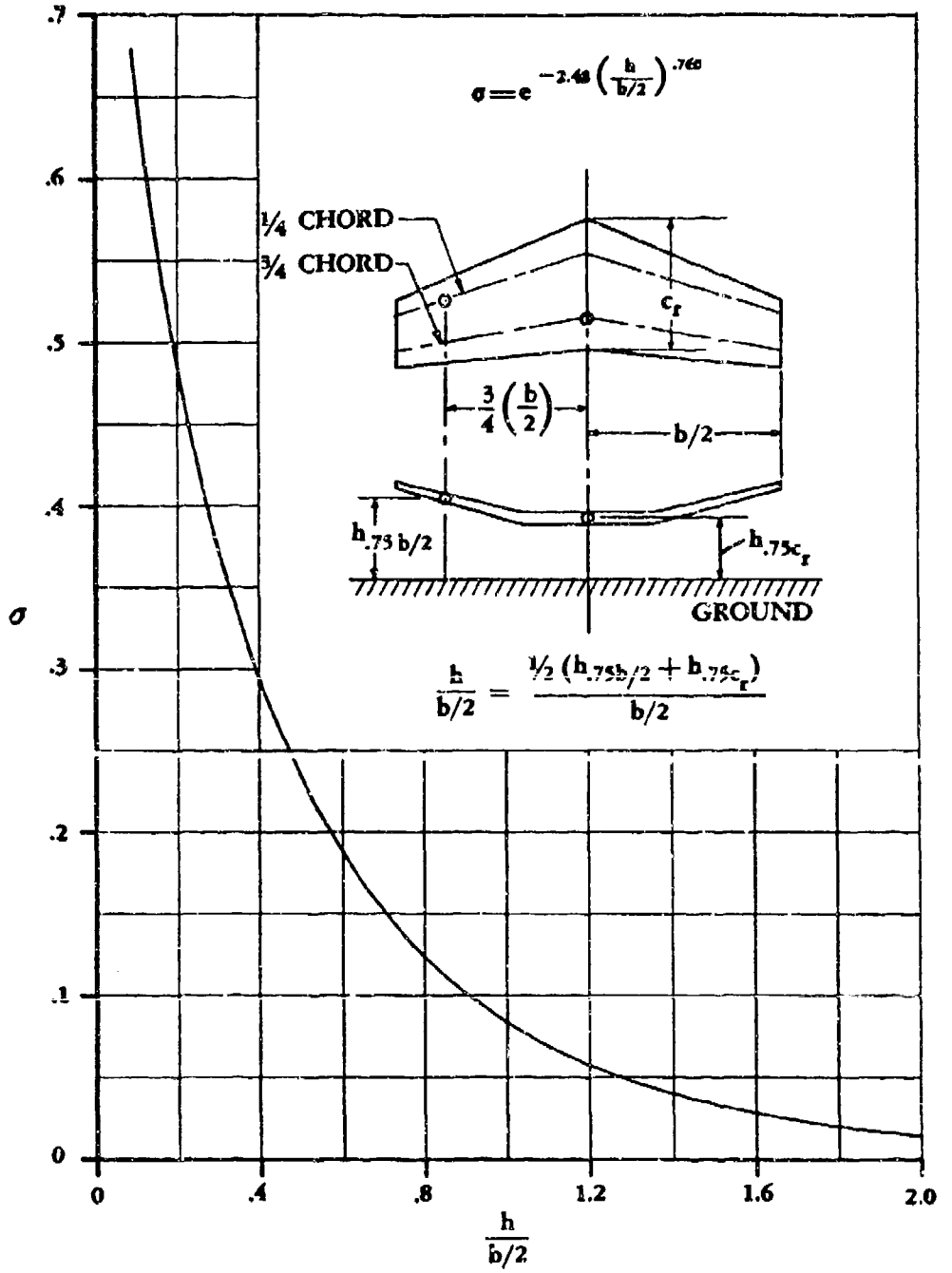

Figure 89 Prandtl's Interference Coefficient

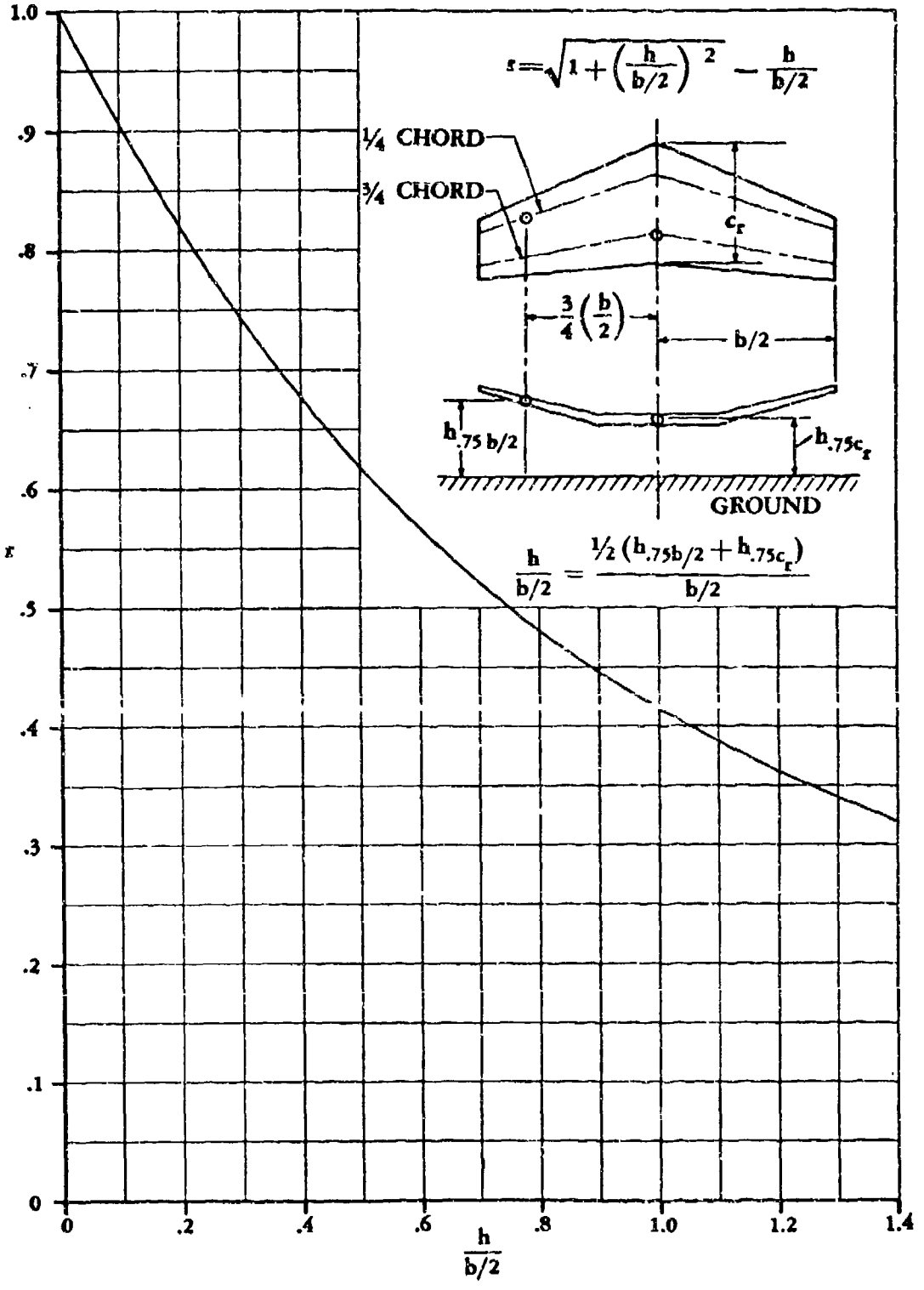

Figure 90 Factor Accounting for Finite Span in Ground Effect

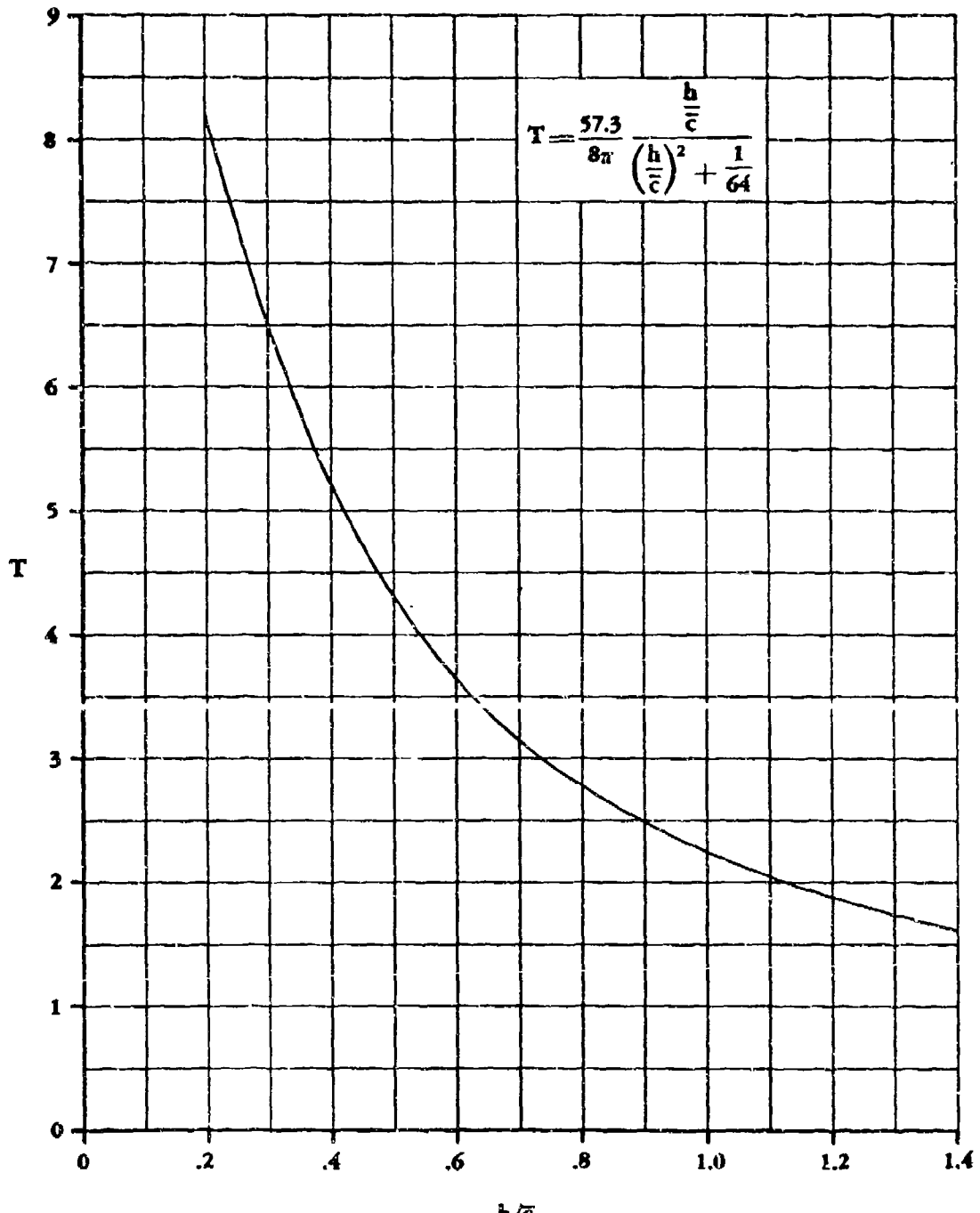

Figure 91 Parameter Accounting for Variation in Longitudinal Velocity with Ground Height

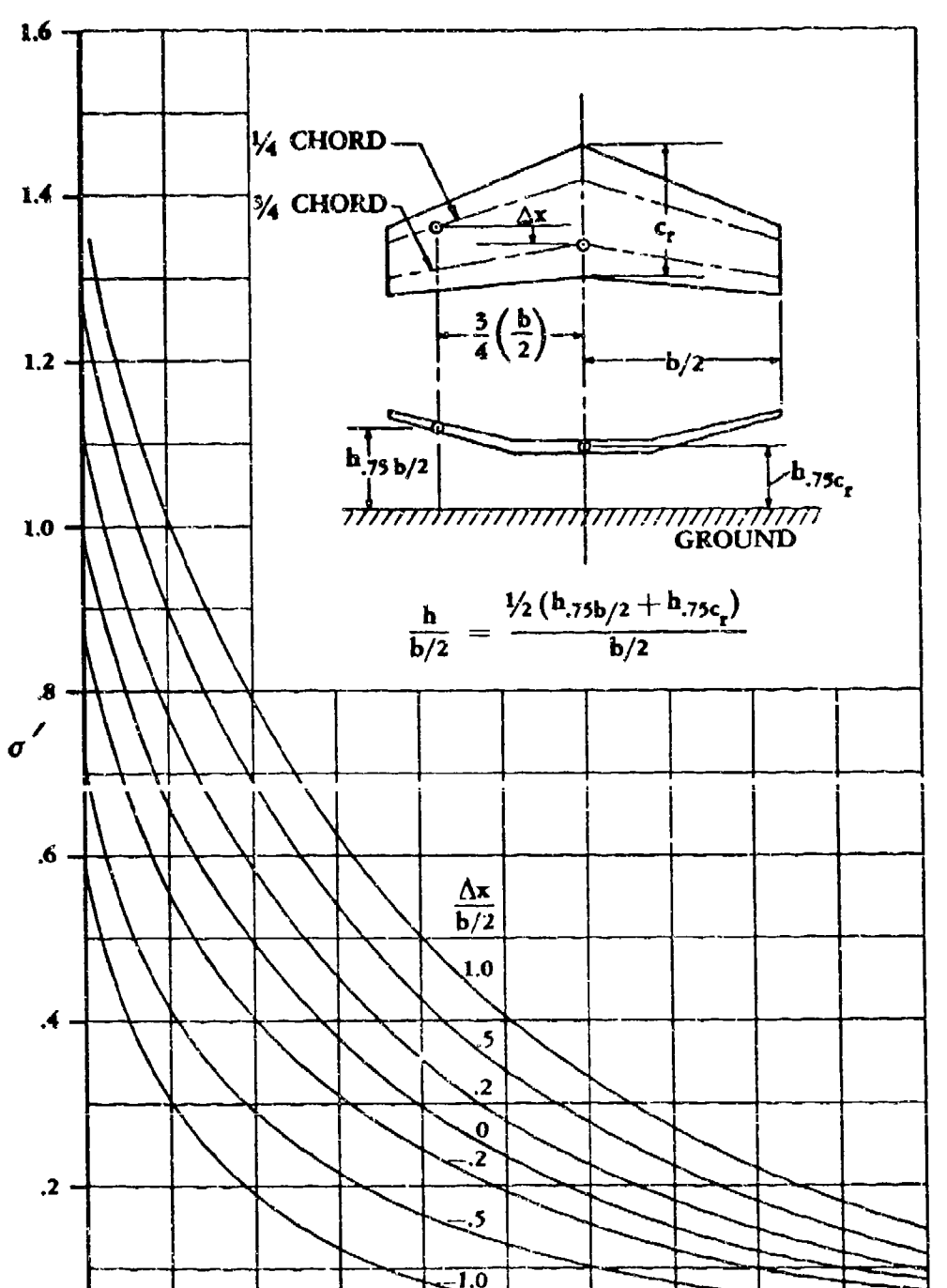

Figure 92 Parameter Accounting for Ground Effect on Lift Due to Trailing Vortices

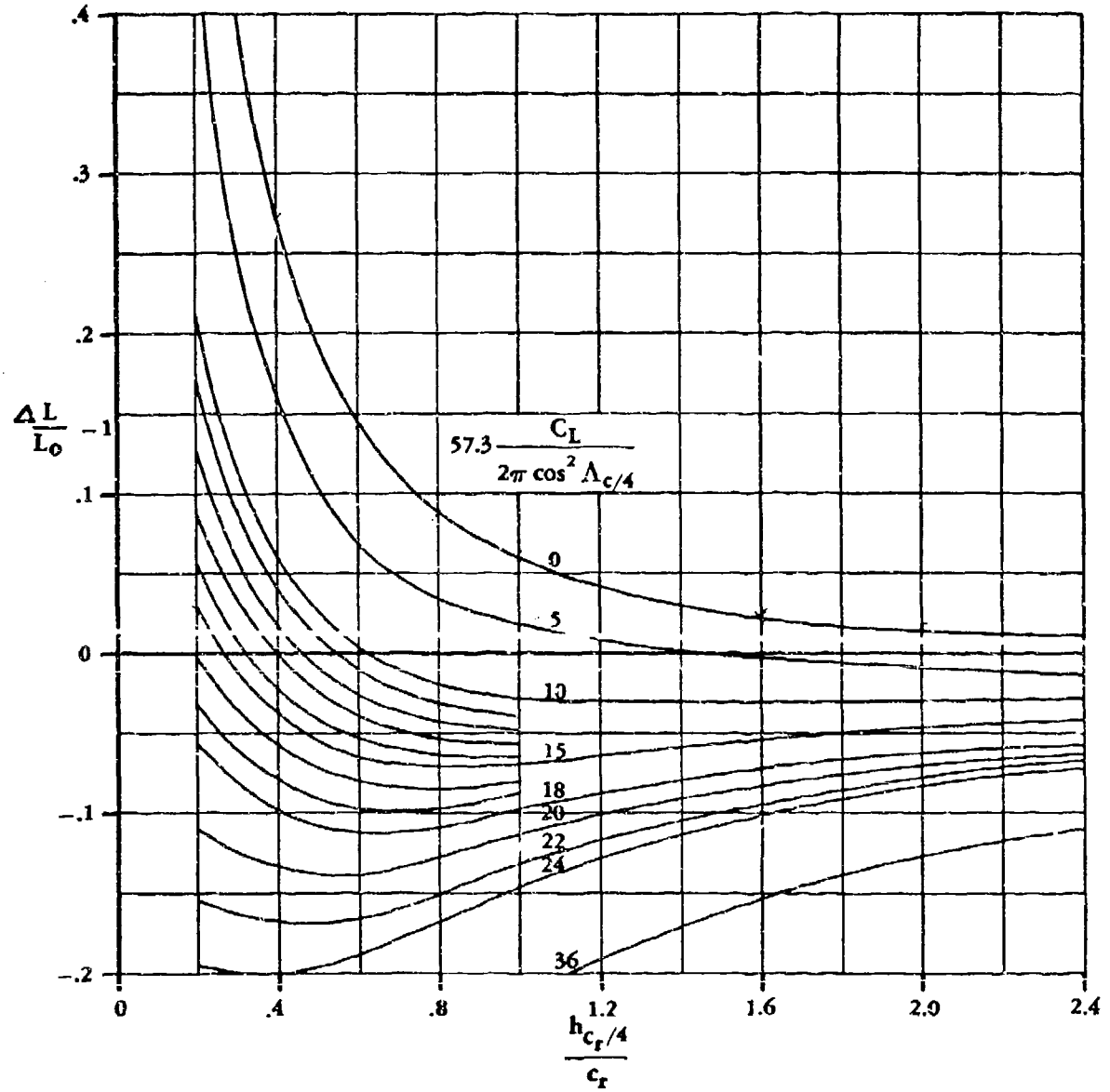

Figure 93 Parameter Accounting for Ground Effect on Lift Due to Bound Vortices

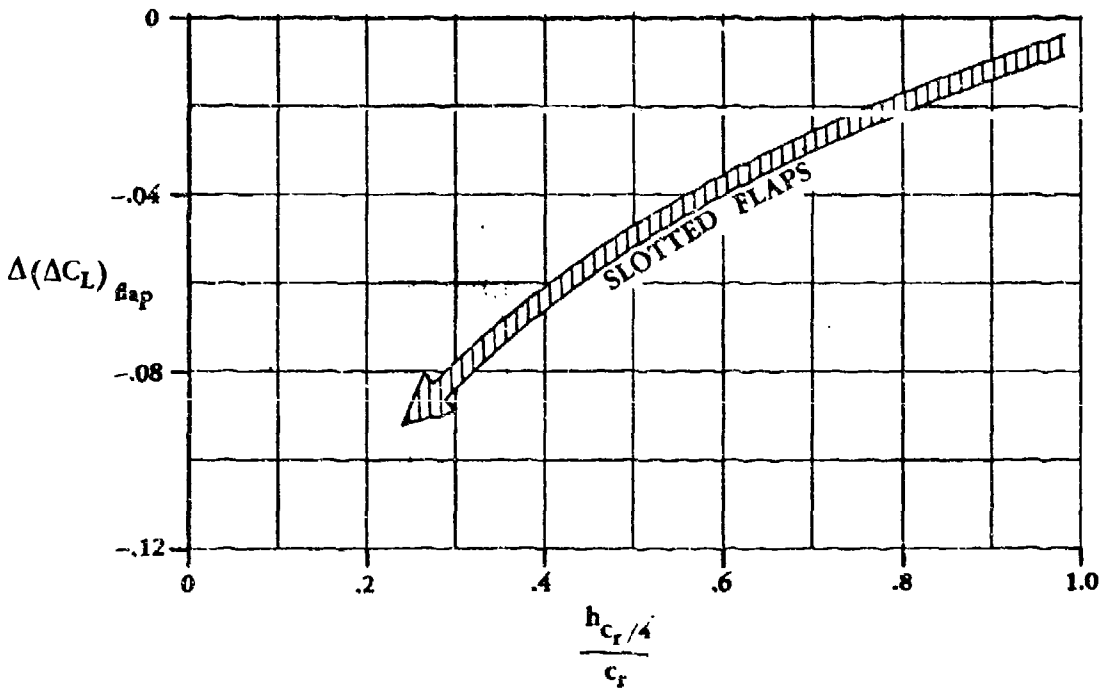

Figure 94 Effect of Flap Deflection on the Ground Influence on Lift

of the $\bar{c}/4$ of the wing above the ground, H_H is the height of the $\bar{c}/4$ of the horizontal tail above the ground, and b_{eff} is the effective wing span, defined as

$$b_{eff} = \frac{C_{Lw_O} + (\Delta C_{L_O})_{Flap}}{\frac{C_{Lw_O}}{b'_w} + \frac{(\Delta C_{L_O})_{Flap}}{b'_f}} \qquad (8\text{-}30)$$

where C_{Lw_O} is the wing lift in free air without flaps, $(\Delta C_{L_O})_{Flap}$ is the change in lift due to the flap, and

$$b'_w = \left(\frac{b'_w}{b}\right) b \qquad b'_f = \left(\frac{b'_f}{b'_w}\right)\left(\frac{b'_w}{b}\right) b$$

The ratio (b'_w/b) is given in Figure 95 as a function of taper ratio, and (b'_f/b'_w) is given in Figure 96 as a function of flap span.

The increments in lift, moment, and drag due to ground effect are calculated at each angle of attack. These effects are then added to the free-air calculations; so that a trimmed condition in ground effect can be calculated.

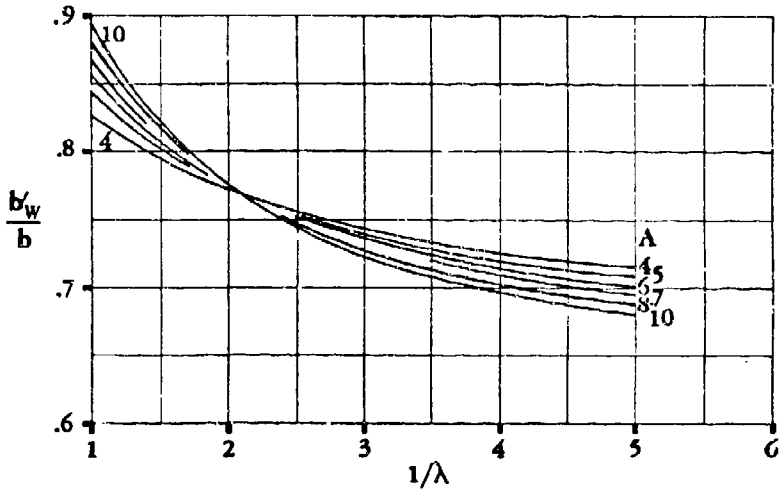

Figure 95 Effective Wing Span in the Presence of the Ground

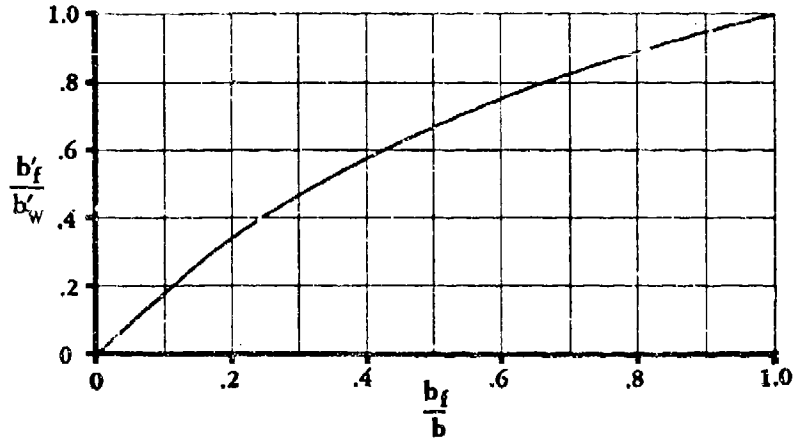

Figure 96 Effective Flap Span in the Presence of the Ground

9. DATA COMPARISONS

This section presents comparisons between predictions using the Large Aircraft program and test data from various sources.

9.1 Systematic Wing Study

Comparison of the predicted lift curves and drag polars with the systematic series of wing reported in Reference 12 are presented in Figures 97 and 98. Reference 12 reported on the tests of 11 wing-body models covering systematic variations of sweep, thickness-to-chord ratio, position of maximum thickness, camber, and aspect ratio. The study was conducted over a Mach range from 0.23 to 0.94. The predictions were made using the geometry presented in Reference 12. The wetted areas of the wing and body were computed internally by the Large Aircraft program and the friction drag solution was for fully turbulent flow.

The predicted drag polar shapes up to lift coefficients slightly greater than the separation lift coefficient comes close to matching the experimental data in most cases. The predicted minimum drag is quite close to experimental levels for most cases except for some test data below 0.3 Mach number. Transition grit was fixed on the leading-edge of the model but its possible that at the low Reynolds and Mach numbers the flow wasn't fully tripped causing the test minimum drags to be low. The predicted polars in the transonic region tended to have too much drag at the higher lift coefficients probably because the drag rise contribution was increasing too fast.

The predicted lift versus alpha curves are in good agreement with experimental data at the low lift coefficients. However, the agreement is poor in the high lift regions, when the predicted maximum lift coefficients don't agree with test data. At the low speed, low Reynolds number condition $C_{L_{MAX}}$ was underpredicted especially for the high sweep and the thin wing conditions. The thick wing lift curve slope was underpredicted at the highest Mach number because the predicted transonic thickness correction became too small.

9.2 Cranked Wing Study

Comparison of the predicted lift curve slope, drag-due-to-lift factor, minimum drag and pitching moment slope with test data for three of the wing models reported in Reference 40 are shown in Figures 99 through 102. Each wing was planer and was mounted separately on a cylindrical body of revolution which had a Sears-Haack nose. Model 1 was a 59 degree leading-edge triangular planform and Model 2 and 3 had two straight line leading edge segments of different sweep angles (referred to as "cranked" planforms). The three models were designed to have the same exposed span and exposed area.

The predictions of the lift curve, drag due-to-lift, minimum drag and moment curve for the Model 1 wing agreed closely with the experimental data except for the moment prediction at Mach 2.94 and the minimum drag at the transonic conditions and at Mach 2.94. The predicted lift curve slope for Models 2 and 3 matched the experimental data at the low subsonic Mach number, but the program did not predict the large increase in lift-curve slope at transonic Mach numbers and the program overpredicted the lift-curve slope for supersonic Mach numbers. The subsonic and transonic predictions of drag due-to-lift, for Models 2 and 3, agrees well with experimental data, but the supersonic values are underpredicted because the lift curve slopes were overpredicted. The predicted pitching moment curve slope was in fair agreement with the test data for Models 1 and 2 up to a Mach number of 1.6; beyond 1.6 Mach the pitching moment was overpredicted. The minimum drag prediction for Model 2 was in fair agreement with experimental data except in the transonic region. The minimum drag predictions for Model 3 were on the average 14 percent higher than the test results.

9.3 C-141A Flight Test Data

Comparison of the C-141A flight test drag polars with full-scale corrected wind-tunnel polars and Large Aircraft program results are shown in Figures 103(a), (b), and (c) for M=0.7, 0.75, and 0.775. These results indicate that the Large Aircraft program predictions are in good agreement with the flight data points at the higher values of C_L and lower values of Mach number. Comparison of the flight test versus predicted drag-rise characteristics are presented in Figure 104 as drag variation with Mach number for constant lift coefficients. These results indicate that the reason why the drag polar was underpredicted at the higher Mach numbers and lower lift coefficients was due primarily to overpredicting the drag rise Mach number, M_{cr}.

The C-141A flight test data shown in Figures 103 and 104 were obtained from Reference 41. The flight test data in Reference 42 are corrected to an equivalent rigid-aircraft condition trimmed at a c.g. location of 0.25 mean aerodynamic chord at a Reynolds number of 55 x 10^6/MAC. The corrected wind tunnel polars shown in Figure 103 were obtained from Reference 42 where fully-corrected model test data was extrapoled to full-scale Reynolds number. The predictions of the Large Aircraft program were made using the full scale C-141A geometry presented in Reference 41. The program predictions are trimmed at a 0.25 MAC c.g. location and 55 x 10^6/MAC Reynolds number condition. The program prediction used a 7 count (0.0007) miscellaneous drag increment in the drag buildup to represent the roughness drag. The 7 count roughness increment was the same as used in Reference 42 to scale model data to full scale.

9.4 High Lift Configurations

Figure 105 shows the lift, drag, and pitching moment predictions for a wing-body configuration compared with test data for a clean wing and a partial and full-span single-slotted flap (Reference 43). The program results are in good agreement with the clean wing lift moment and drag. The increment in lift due to flap deflection is underpredicted at $C_{L_{MAX}}$, but the relative predicted differences between the full-span and partial-span flaps were similar to the test data. The increment in moment due to flap deflection was underpredicted for both the full-span and partial-span cases, while the drag increment for flap deflection was overpredicted only for the full-span condition.

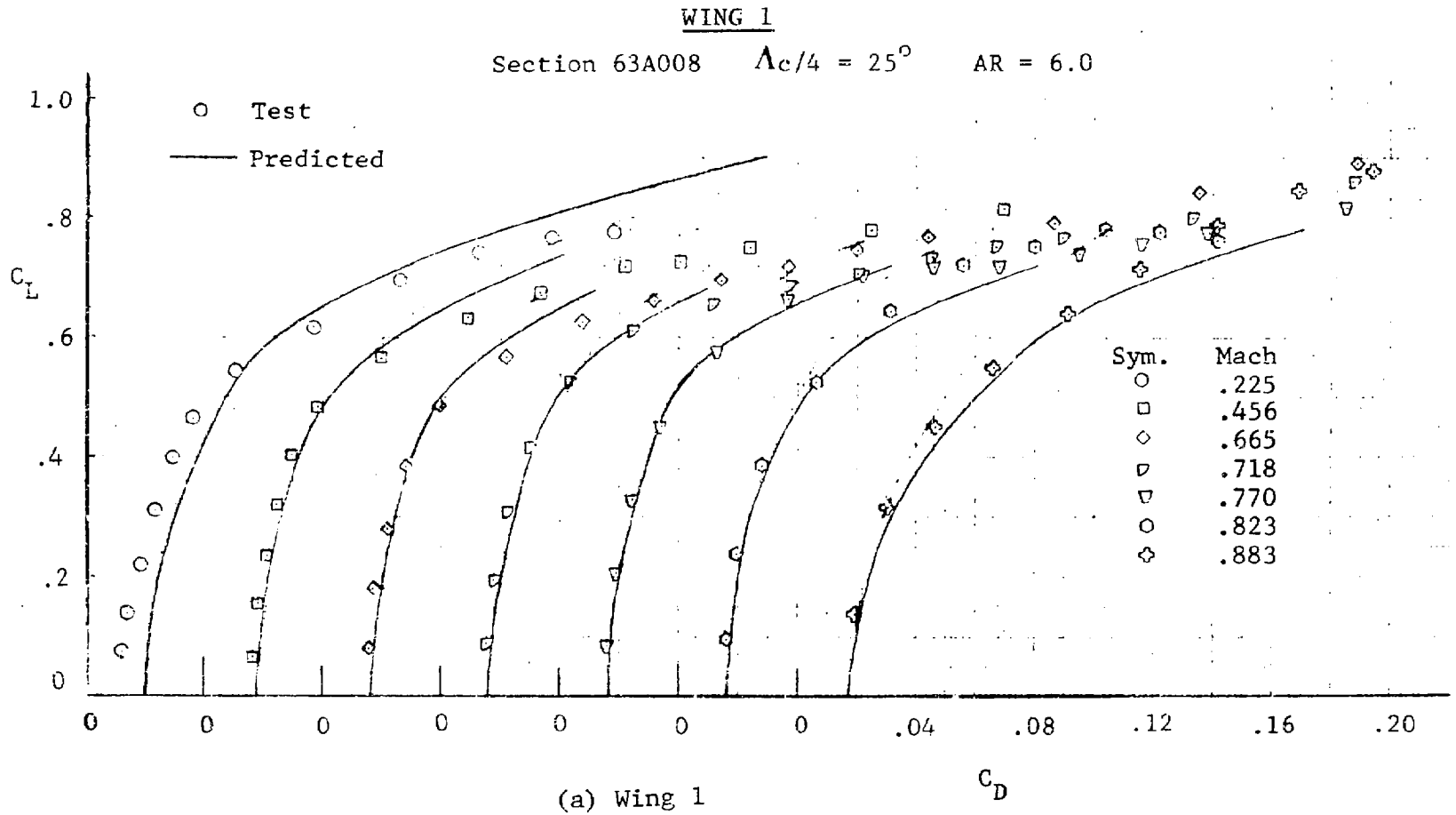

(a) Wing 1

Figure 97 Comparison of Predicted Drag Versus Lift and Test Data

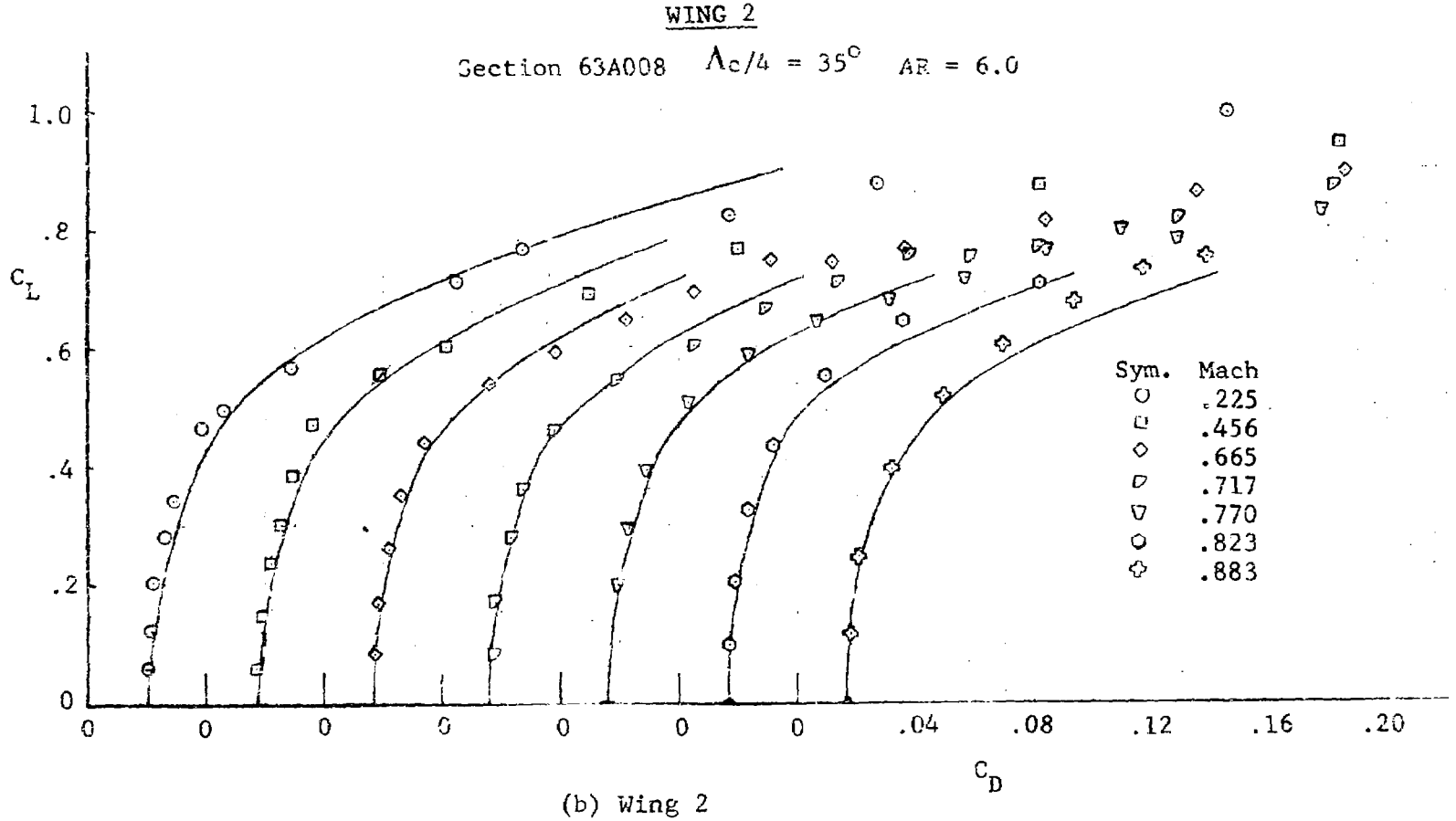

(b) Wing 2

Figure 97 - Continued

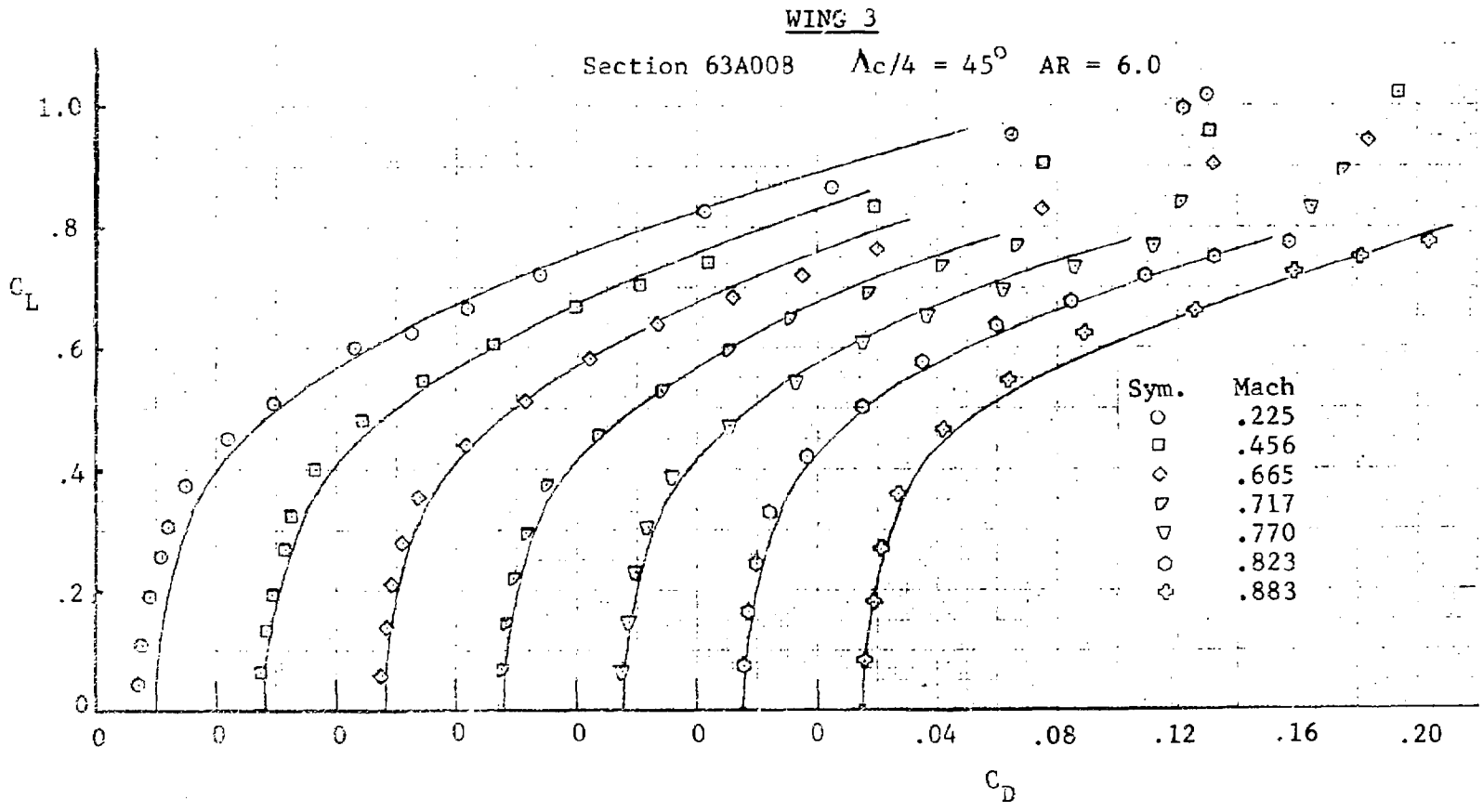

(c) Wing 3

Figure 97 - Continued

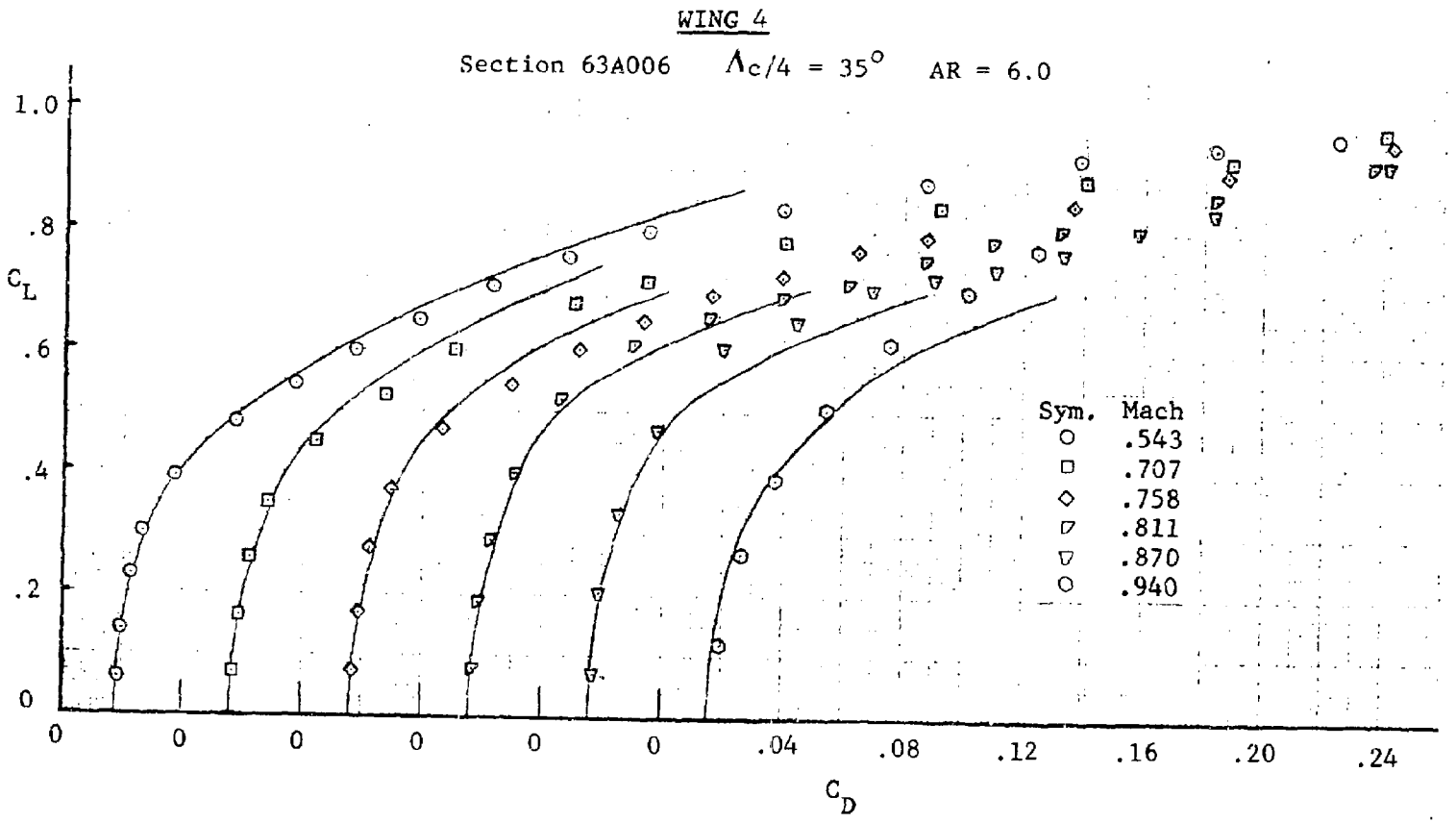

(d) Wing 4

Figure 97 - Continued

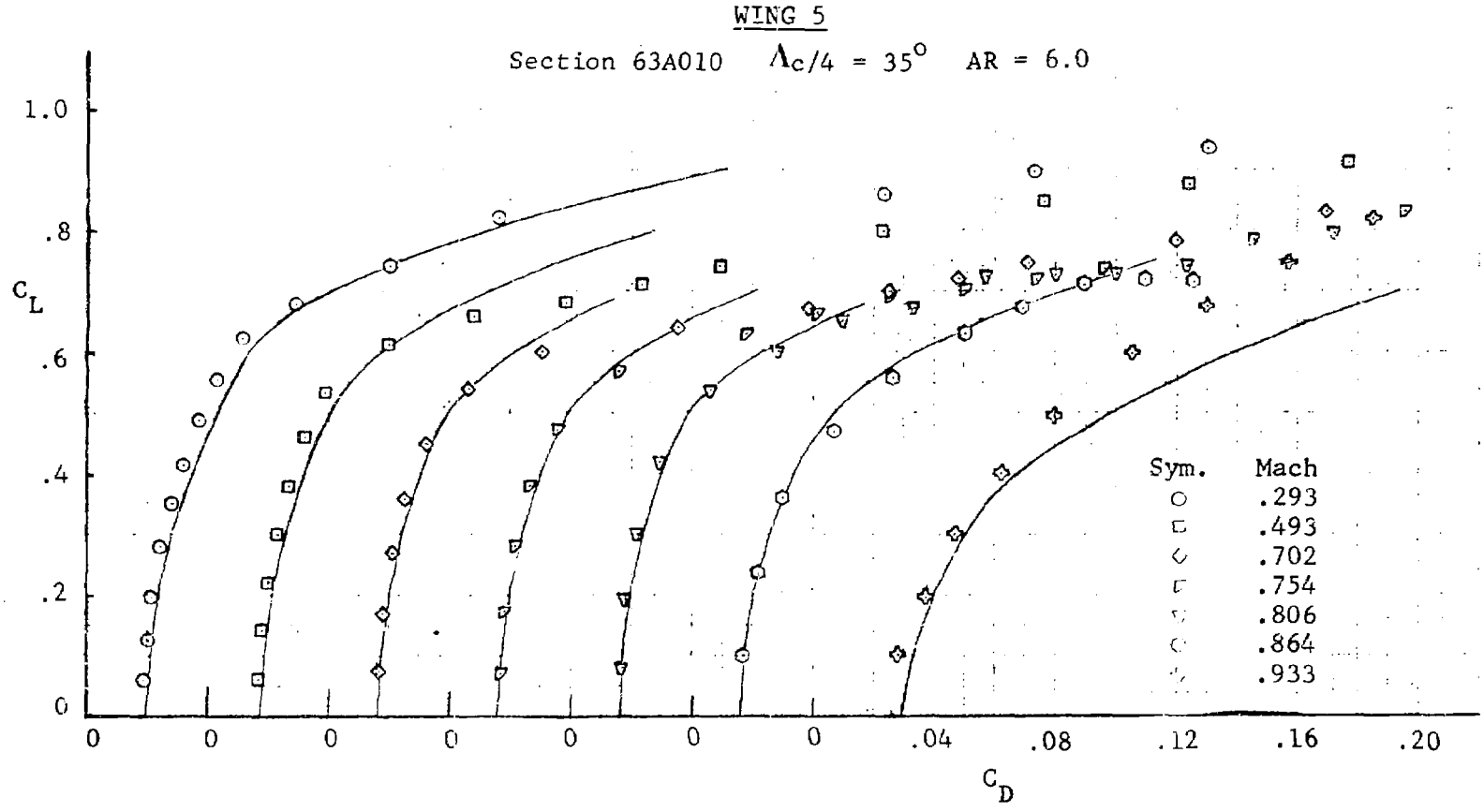

(e) Wing 5

Figure 97 - Continued

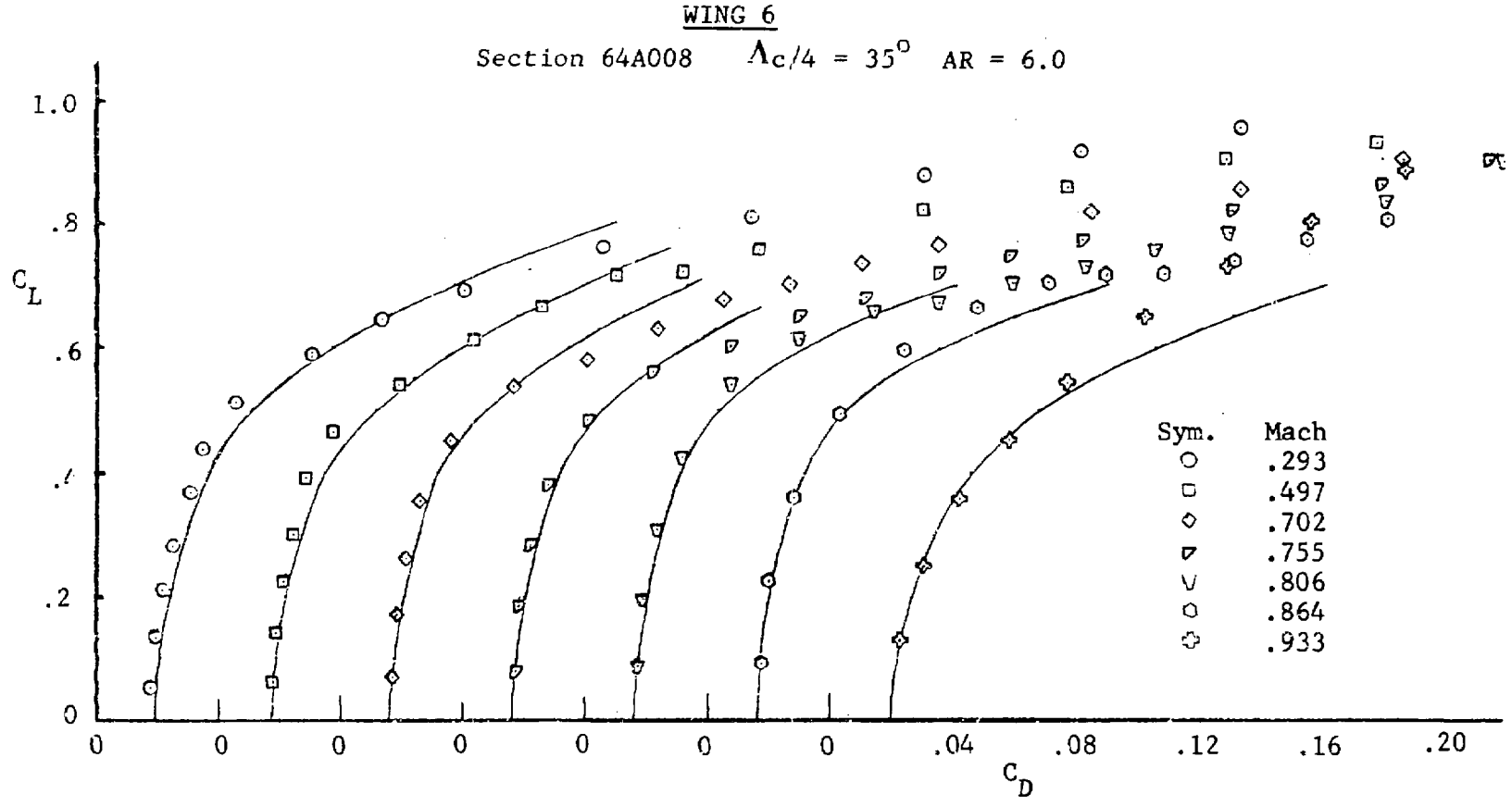

(f) Wing 6

Figure 97 - Continued

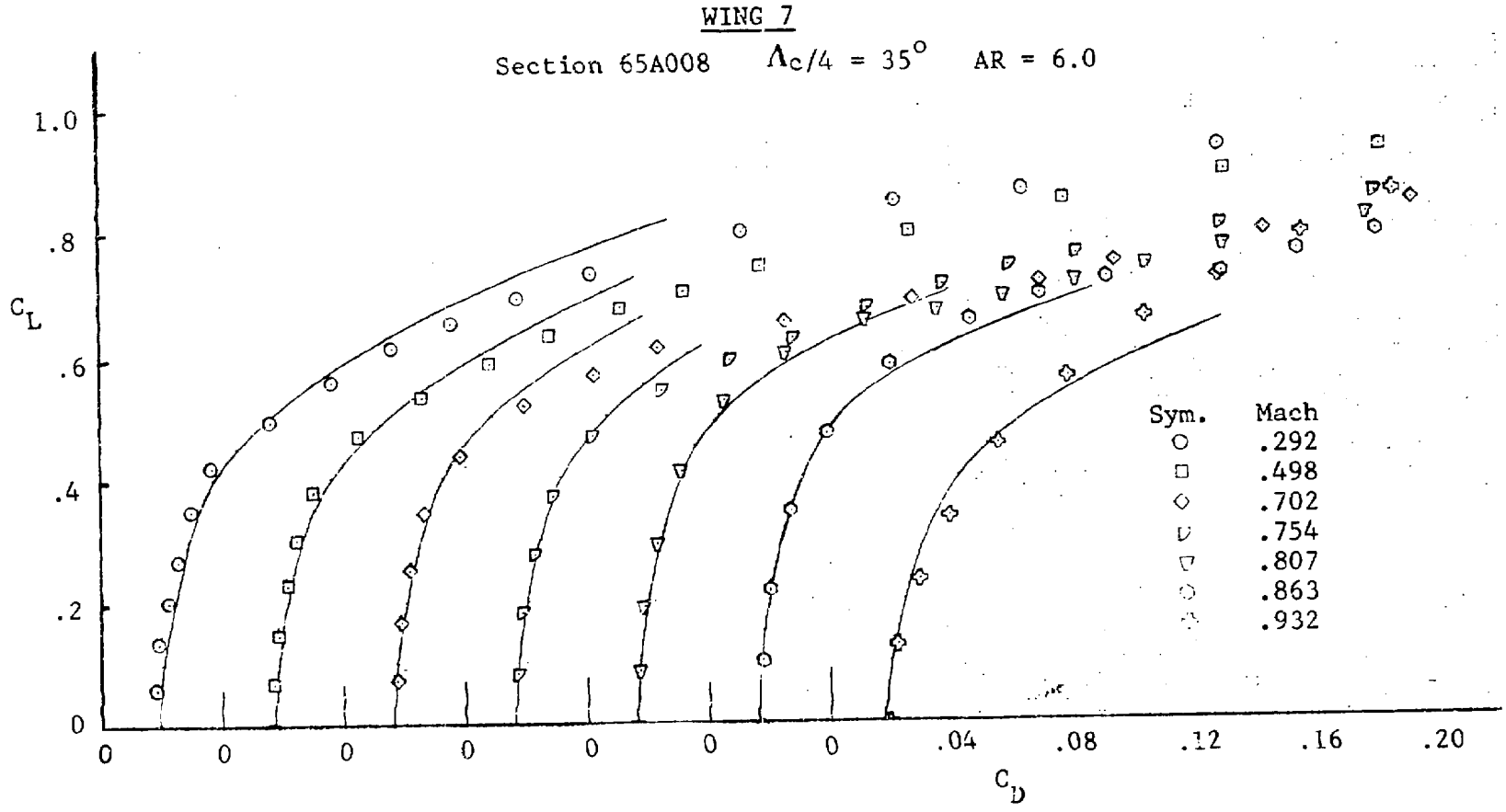

(g) Wing 7

Figure 91 - Continued

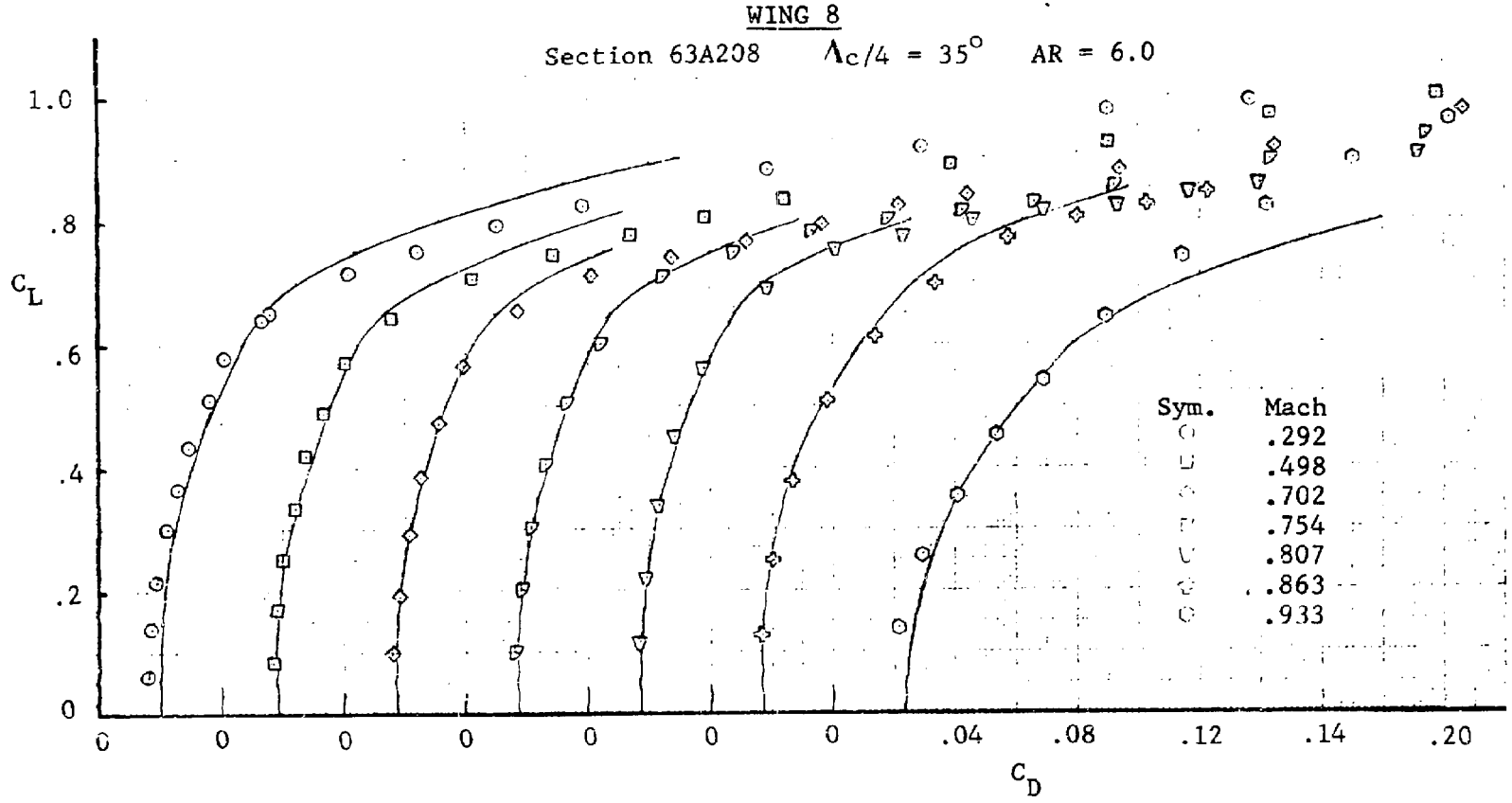

(h) Wing 8

Figure 97 - Continued

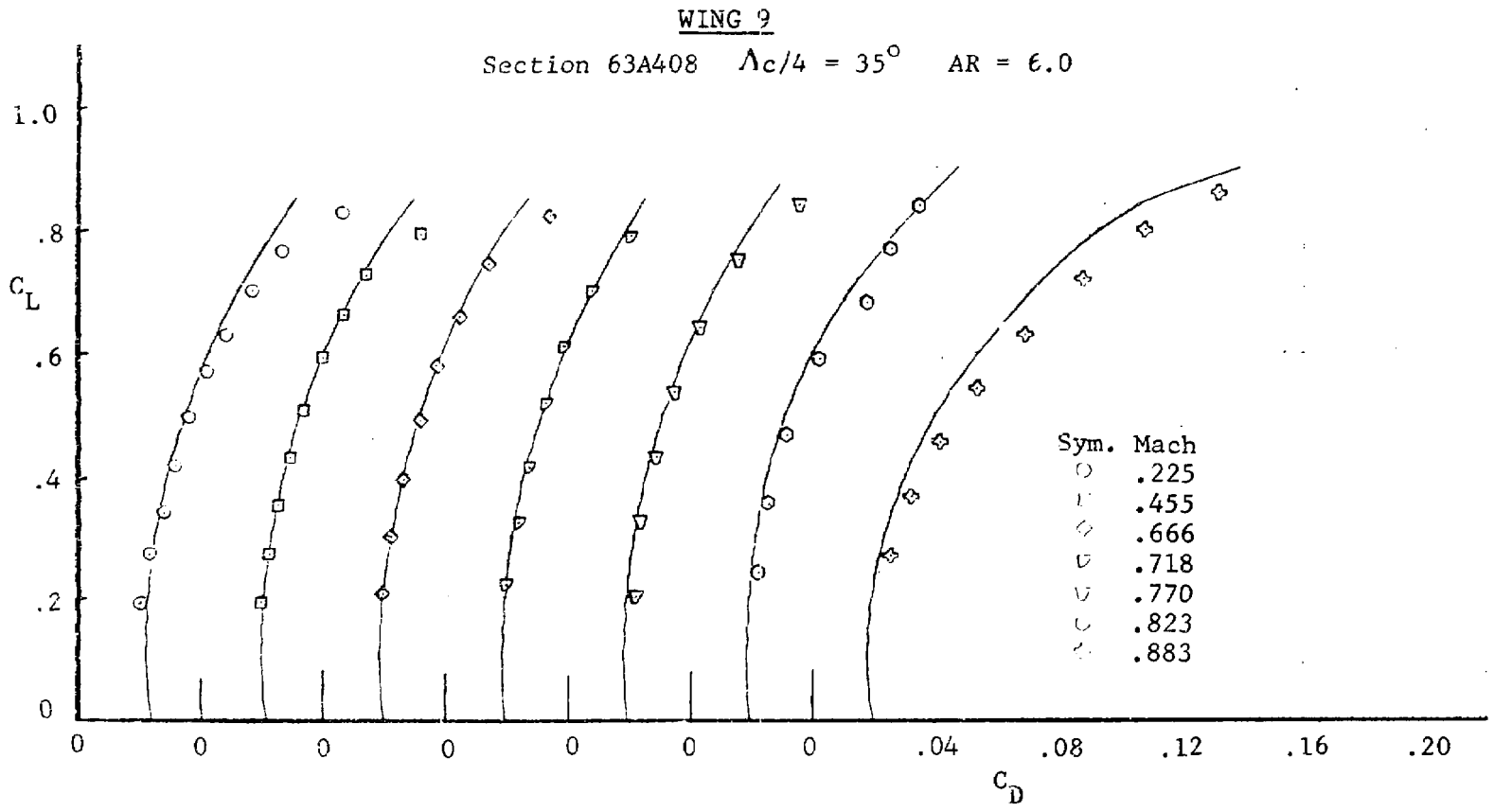

(i) Wing 9

Figure 97 - Continued

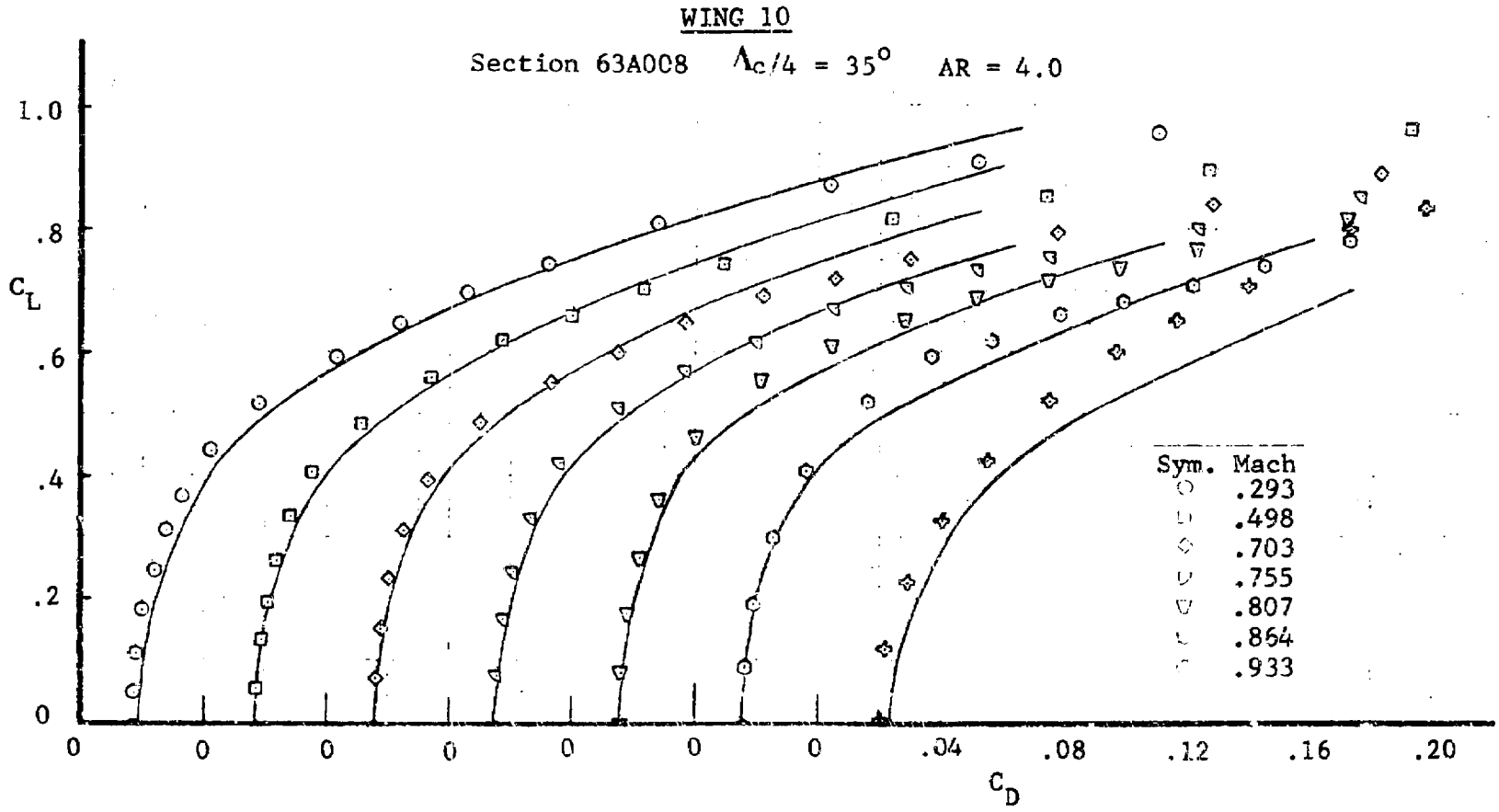

(j) Wing 10

Figure 97 - Continued

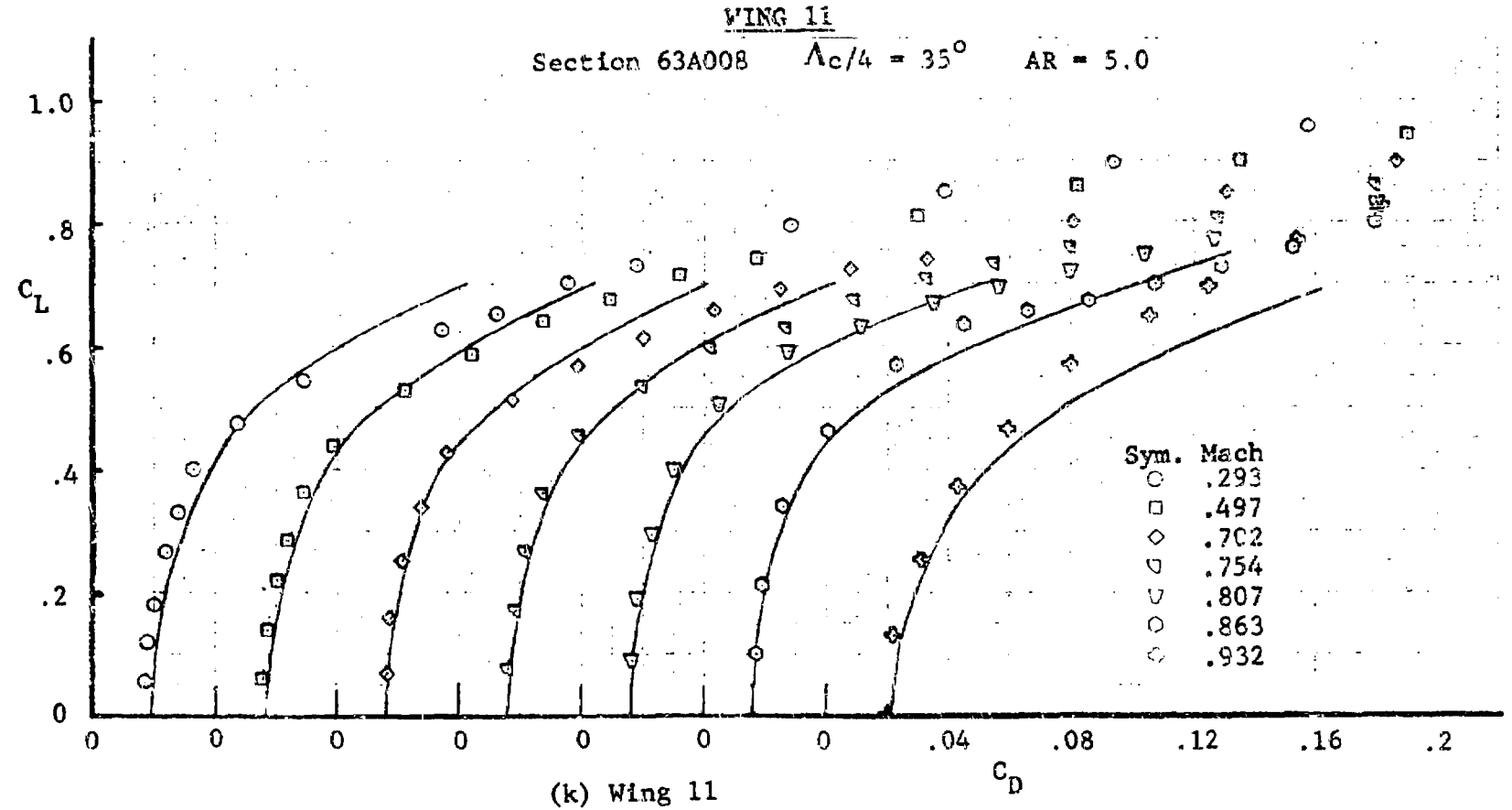

(k) Wing 11

Figure 97 - Concluded

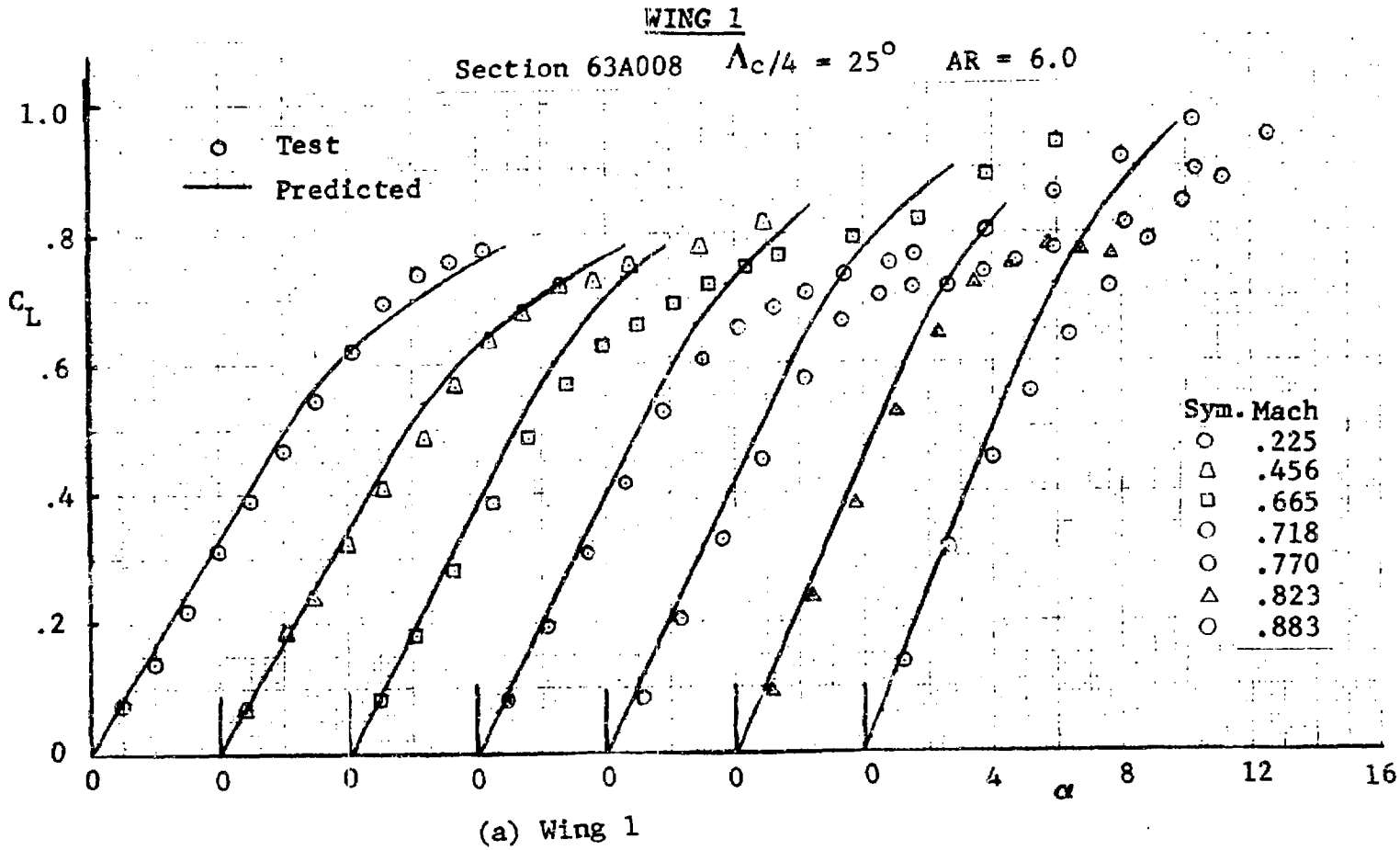

(a) Wing 1

Figure 98 Comparison of Predicted Lift Versus Angle of Attack and Test Data

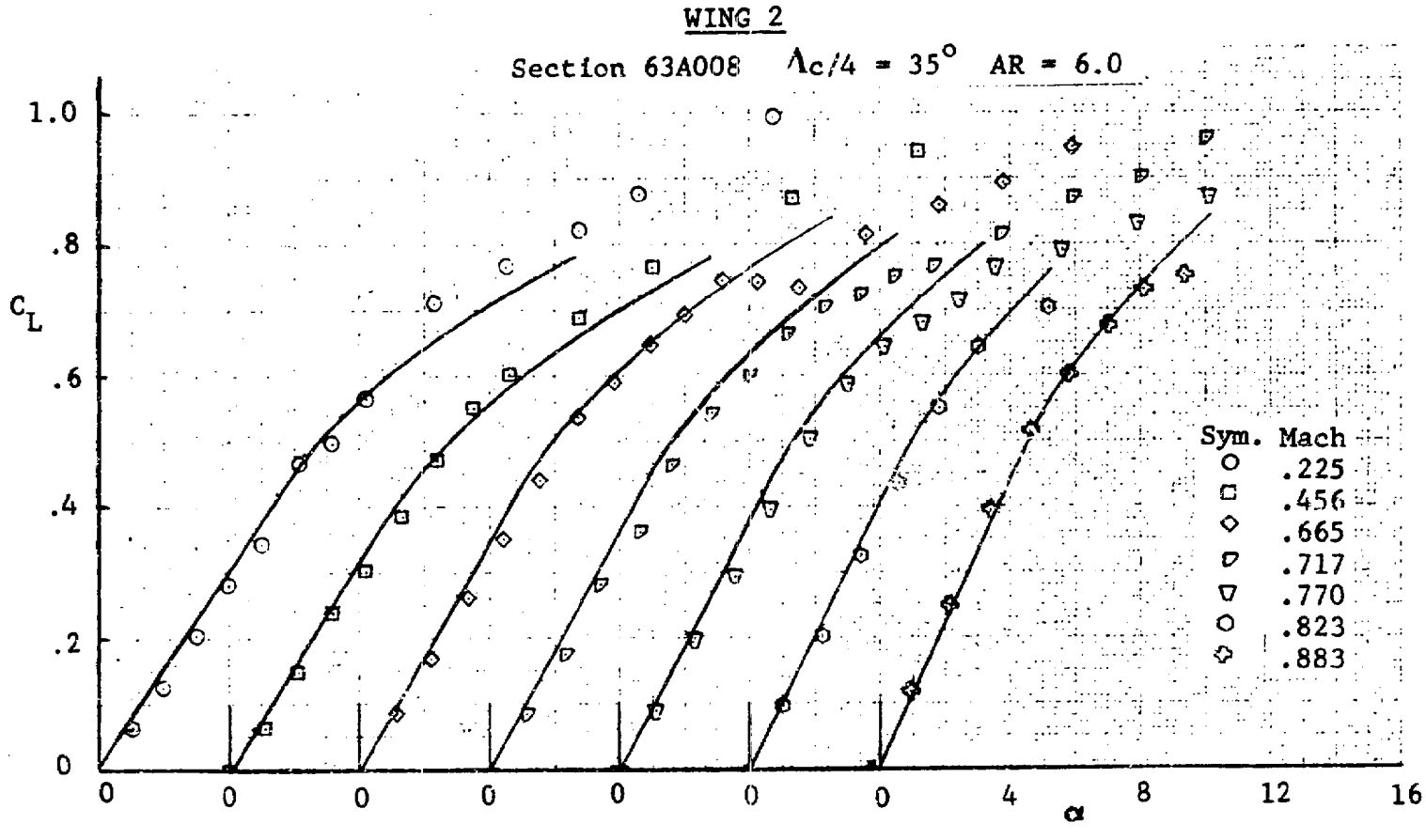

(b) Wing 2

Figure 98 - Continued

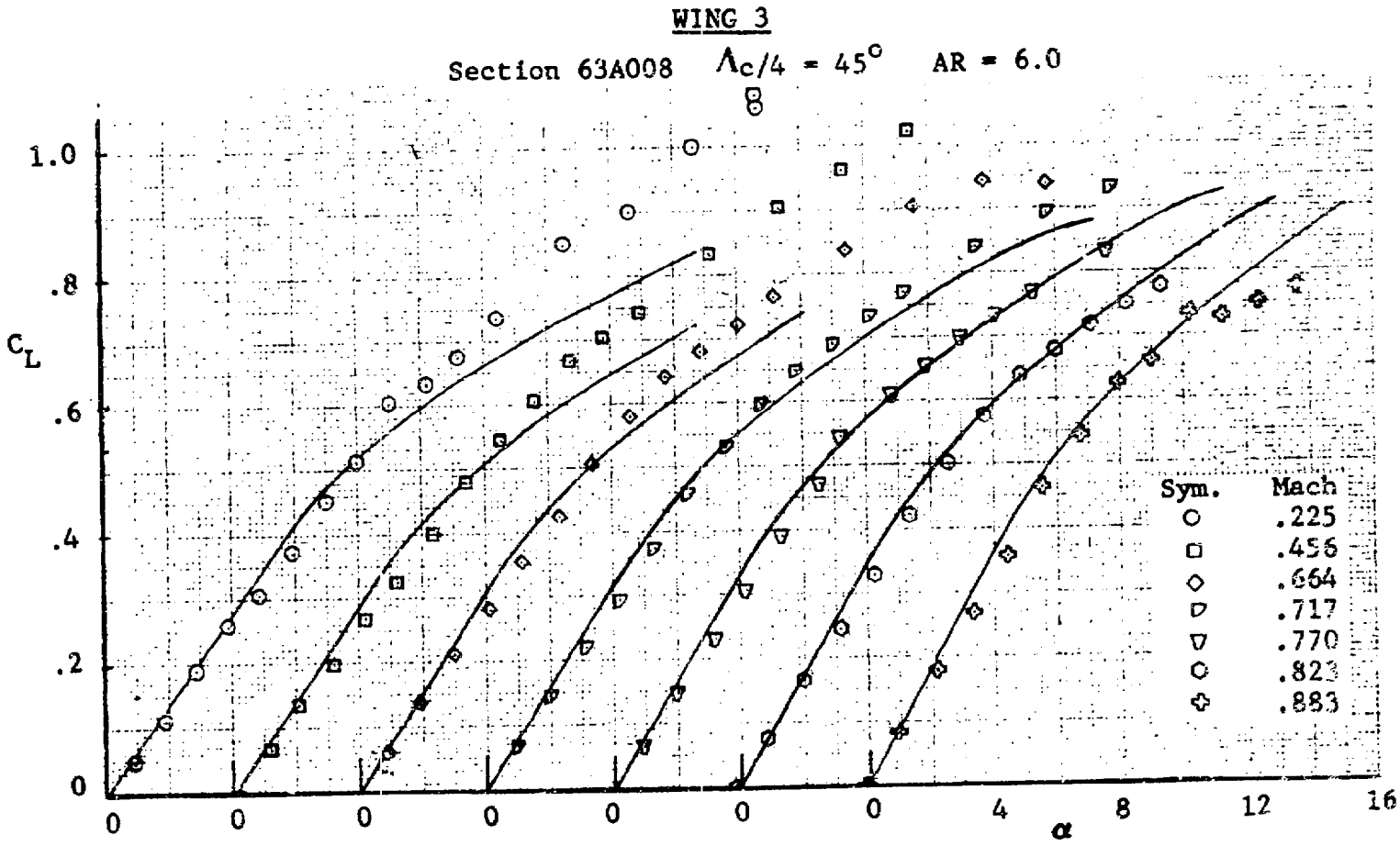

(c) Wing 3

Figure 98 - Continued

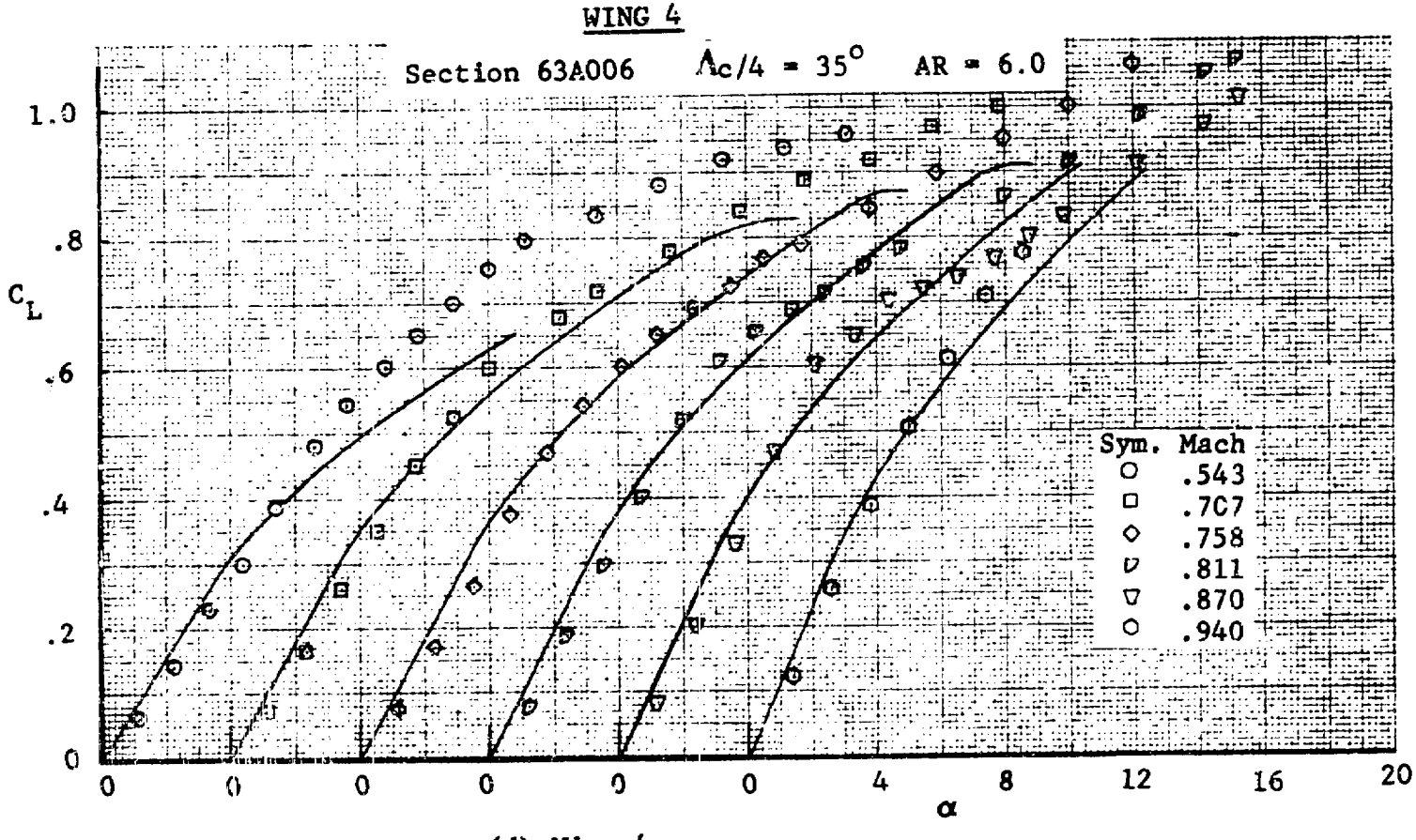

(d) Wing 4

Figure 98 - Continued

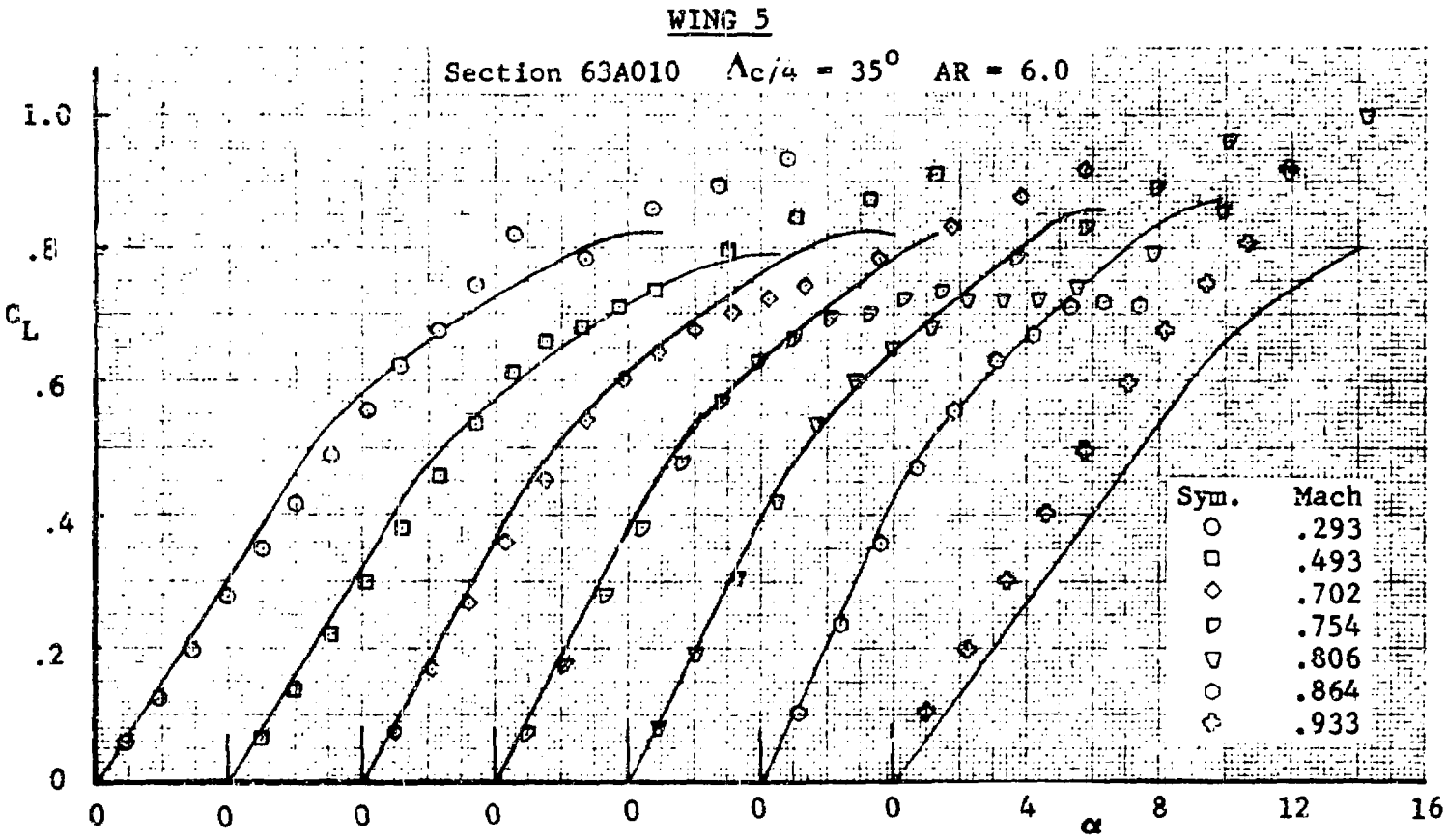

(e) Wing 5

Figure 98 - Continued

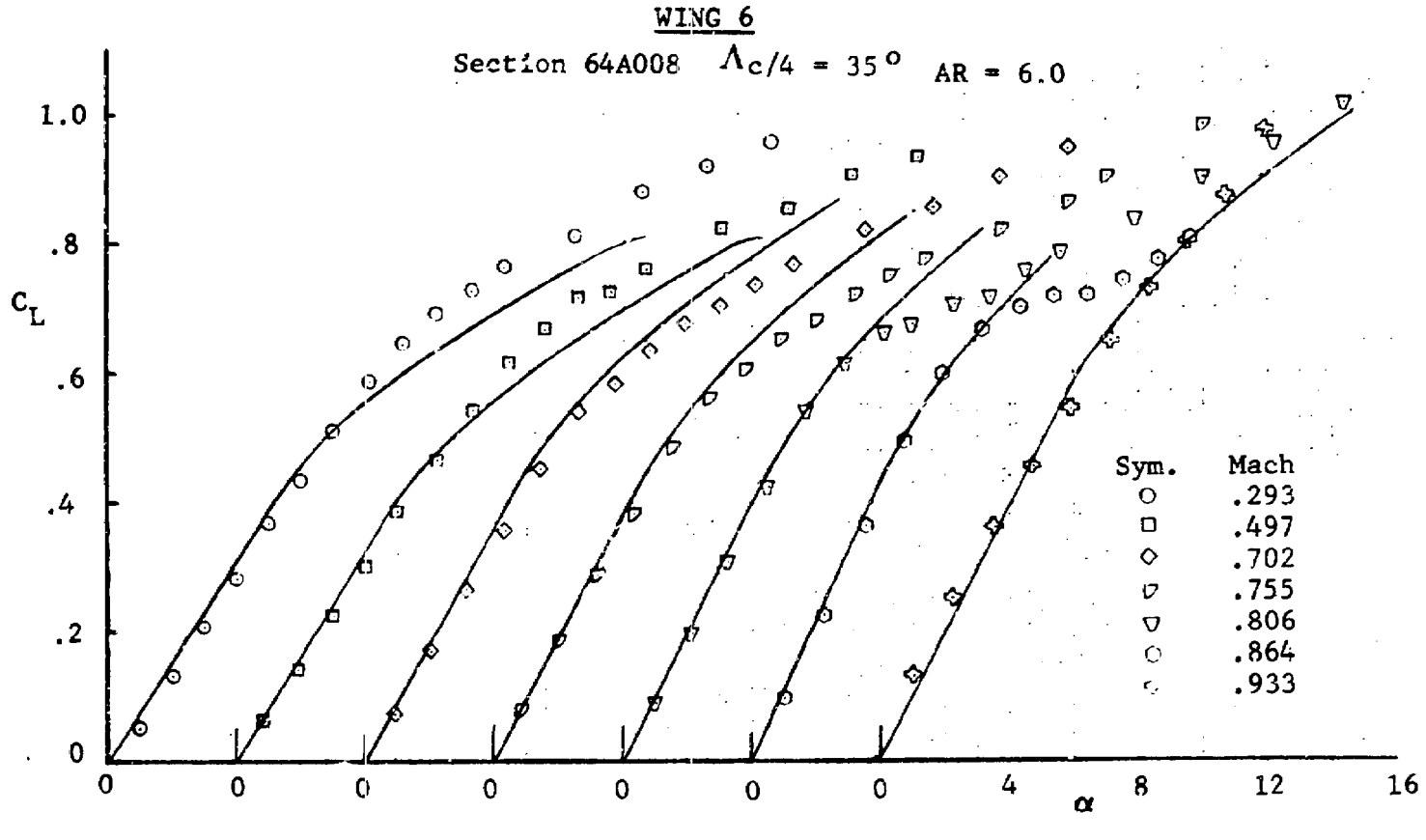

(f) Wing 6

Figure 98 - Continued

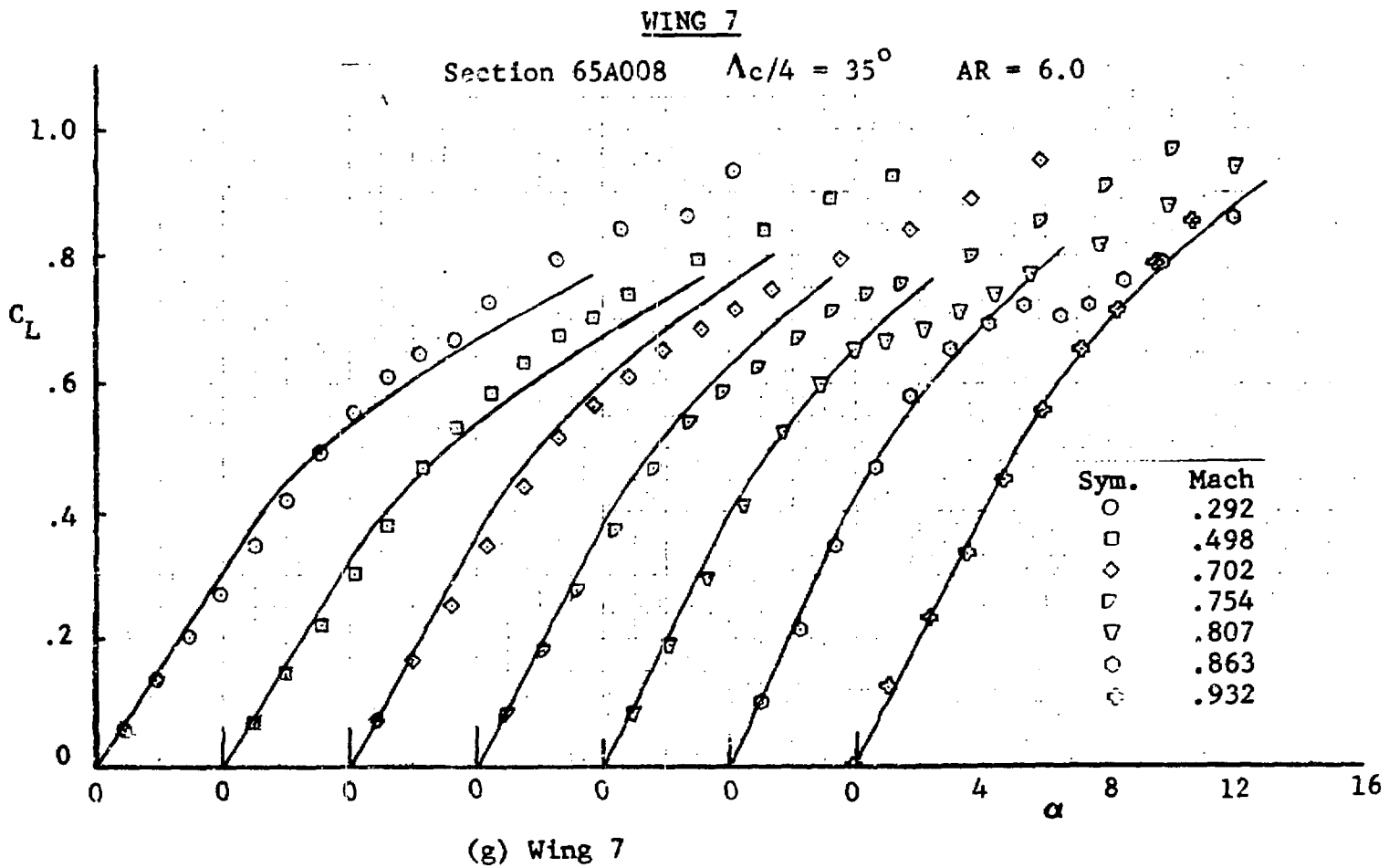

(g) Wing 7

Figure 98 - Continued

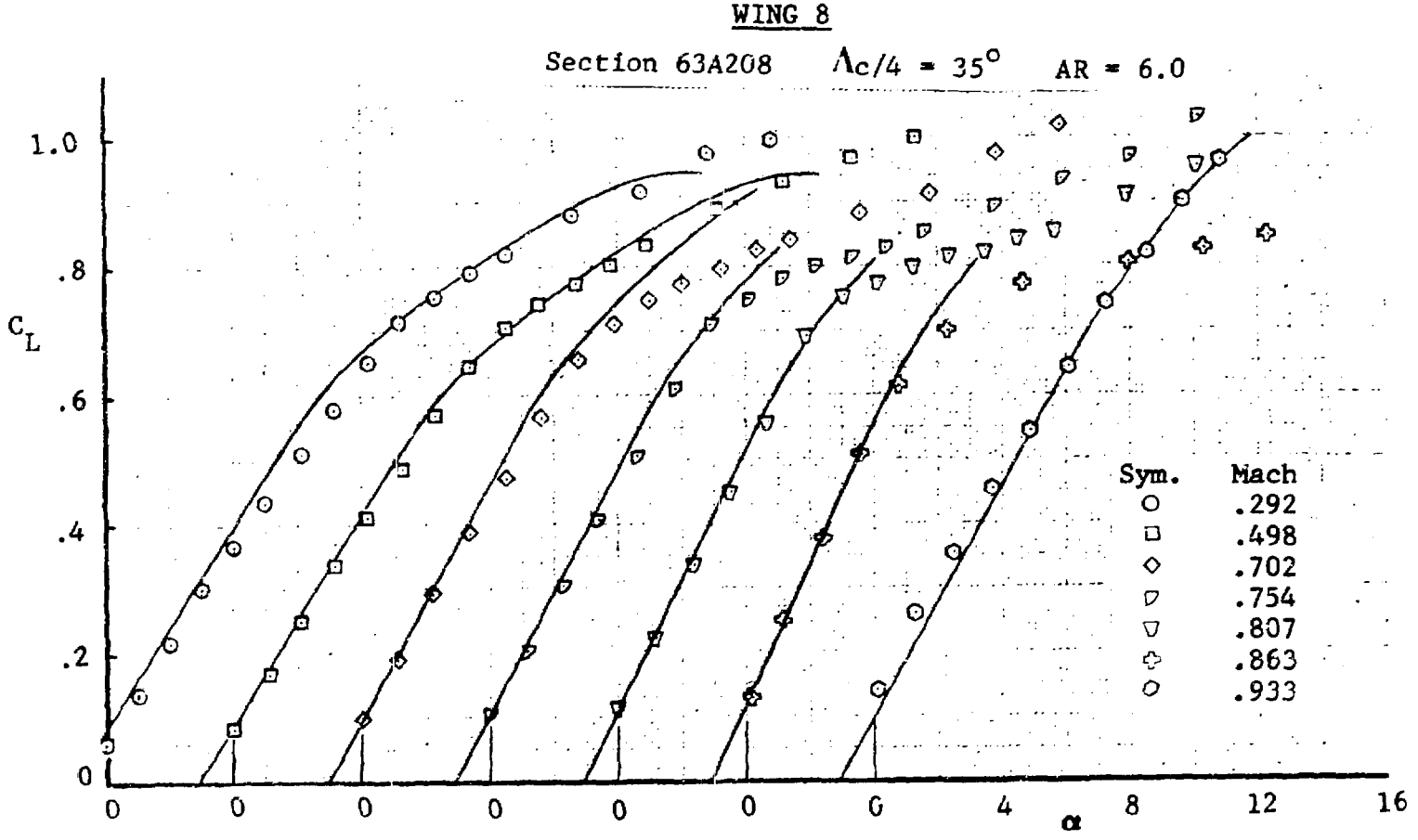

(h) Wing 8

Figure 98 - Continued

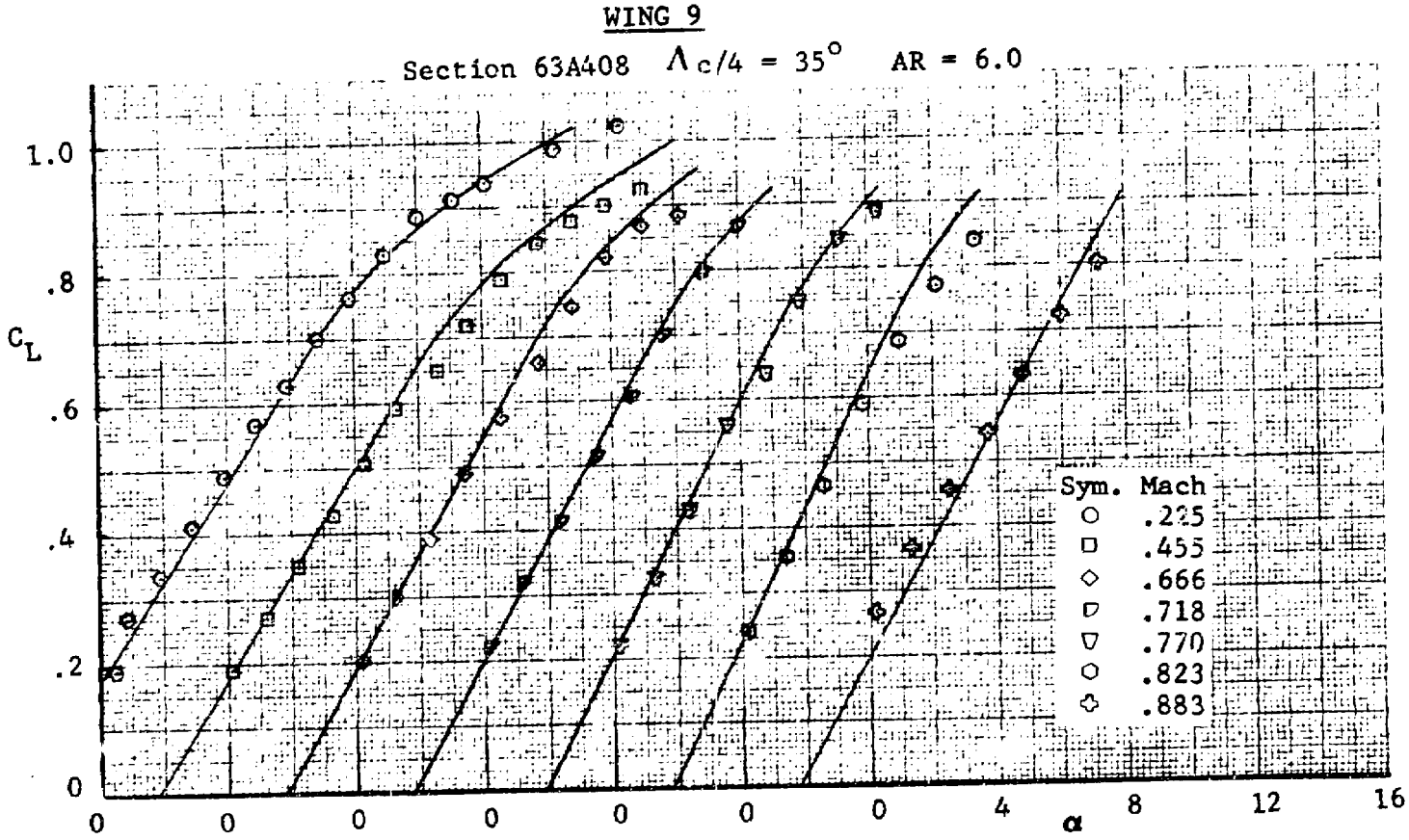

(i) Wing 9

Figure 98 - Continued

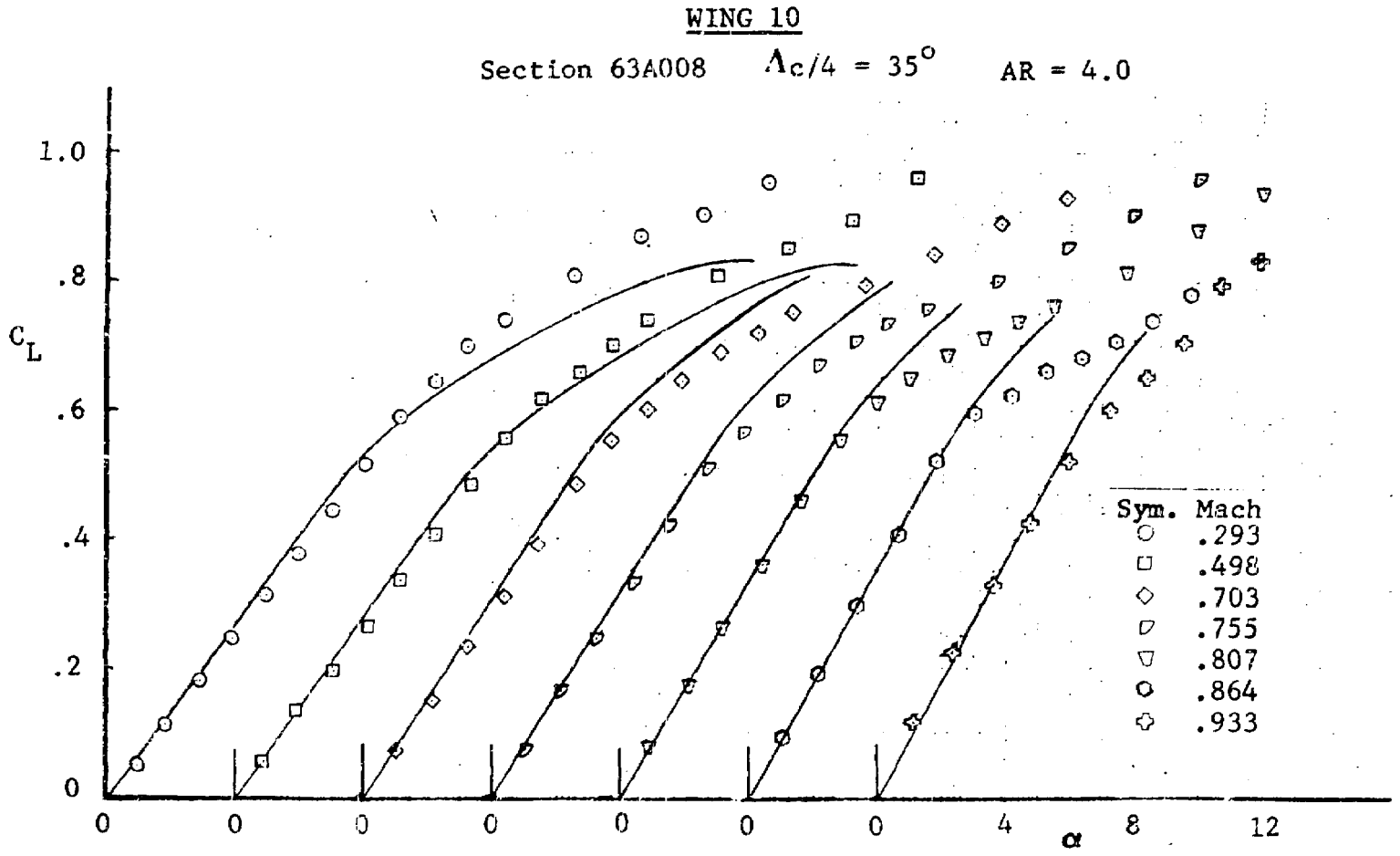

(j) Wing 10

Figure 98 - Continued

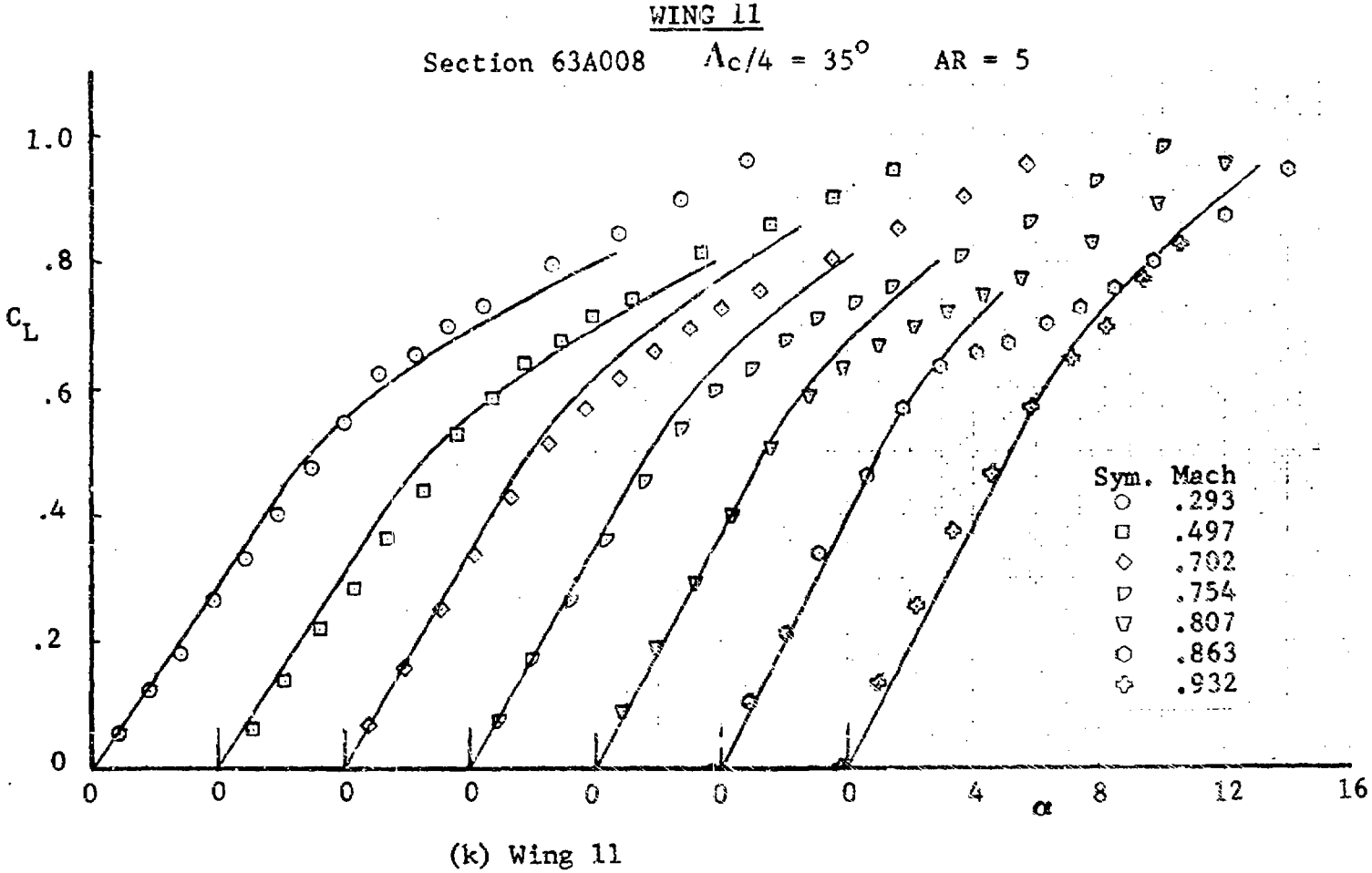

(k) Wing 11

Figure 98 - Concluded

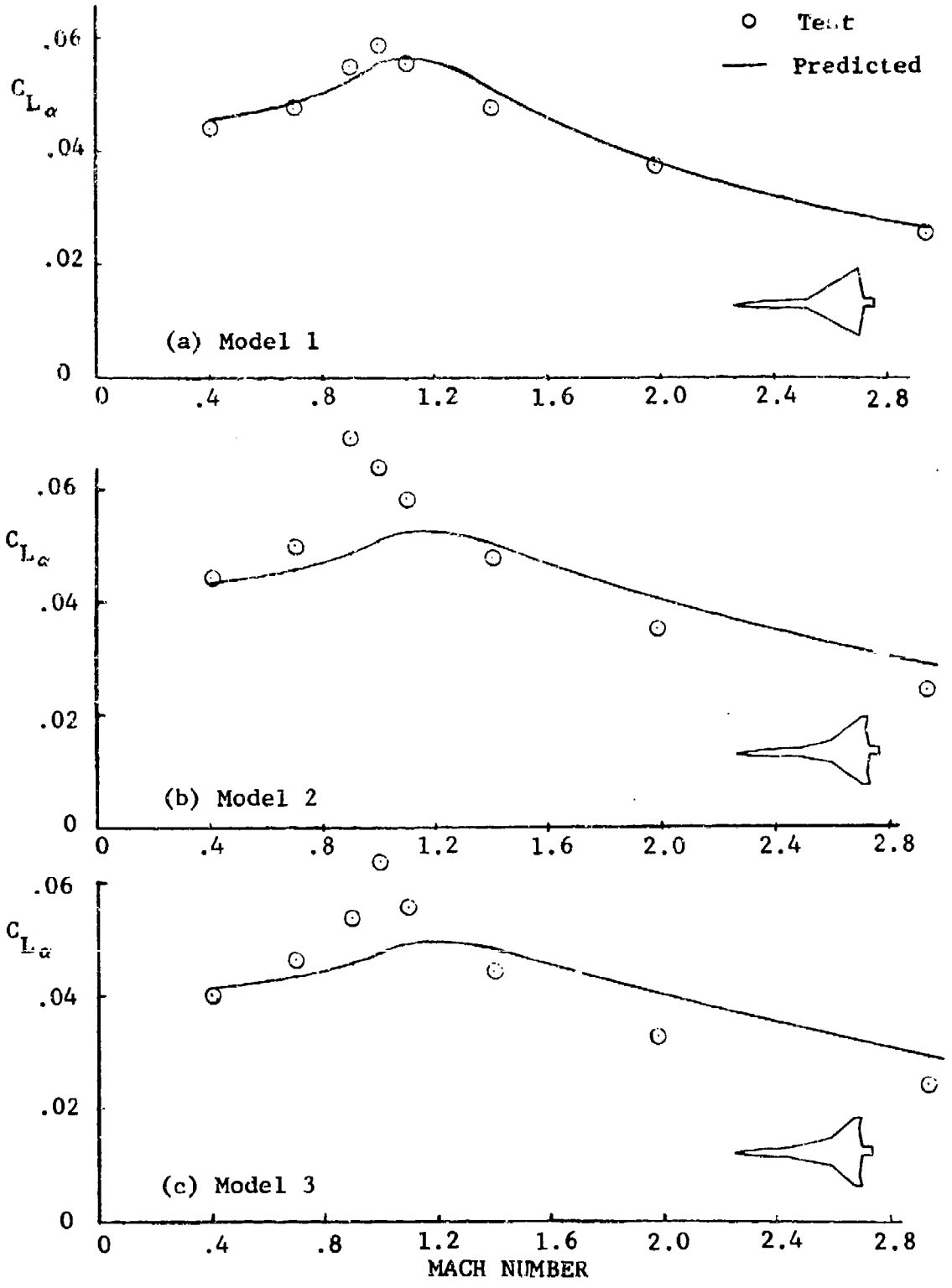

Figure 99 Lift-Curve Slope as a Function of Mach Number

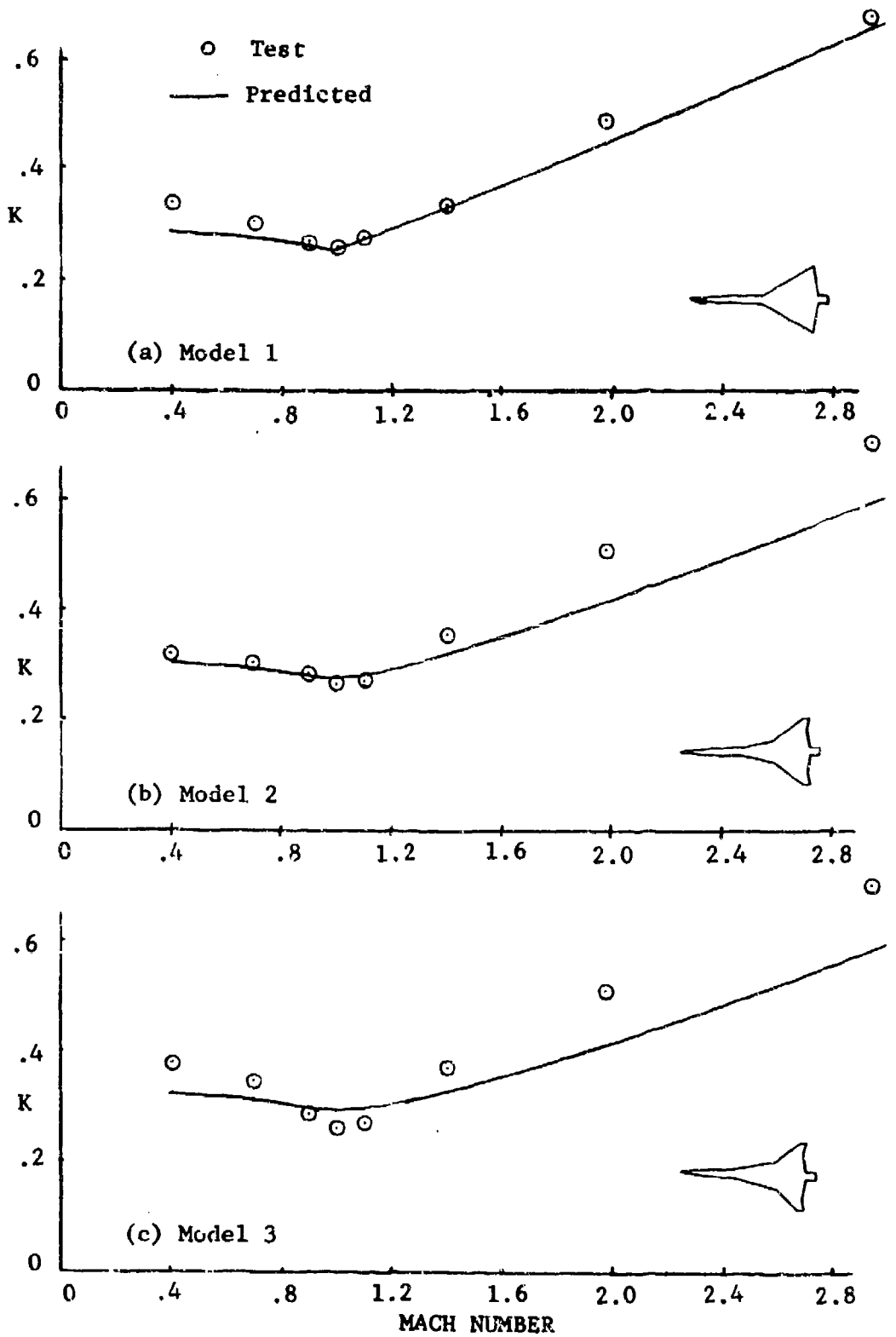

Figure 100 Drag Due-To-Lift Factor as a Function of Mach Number

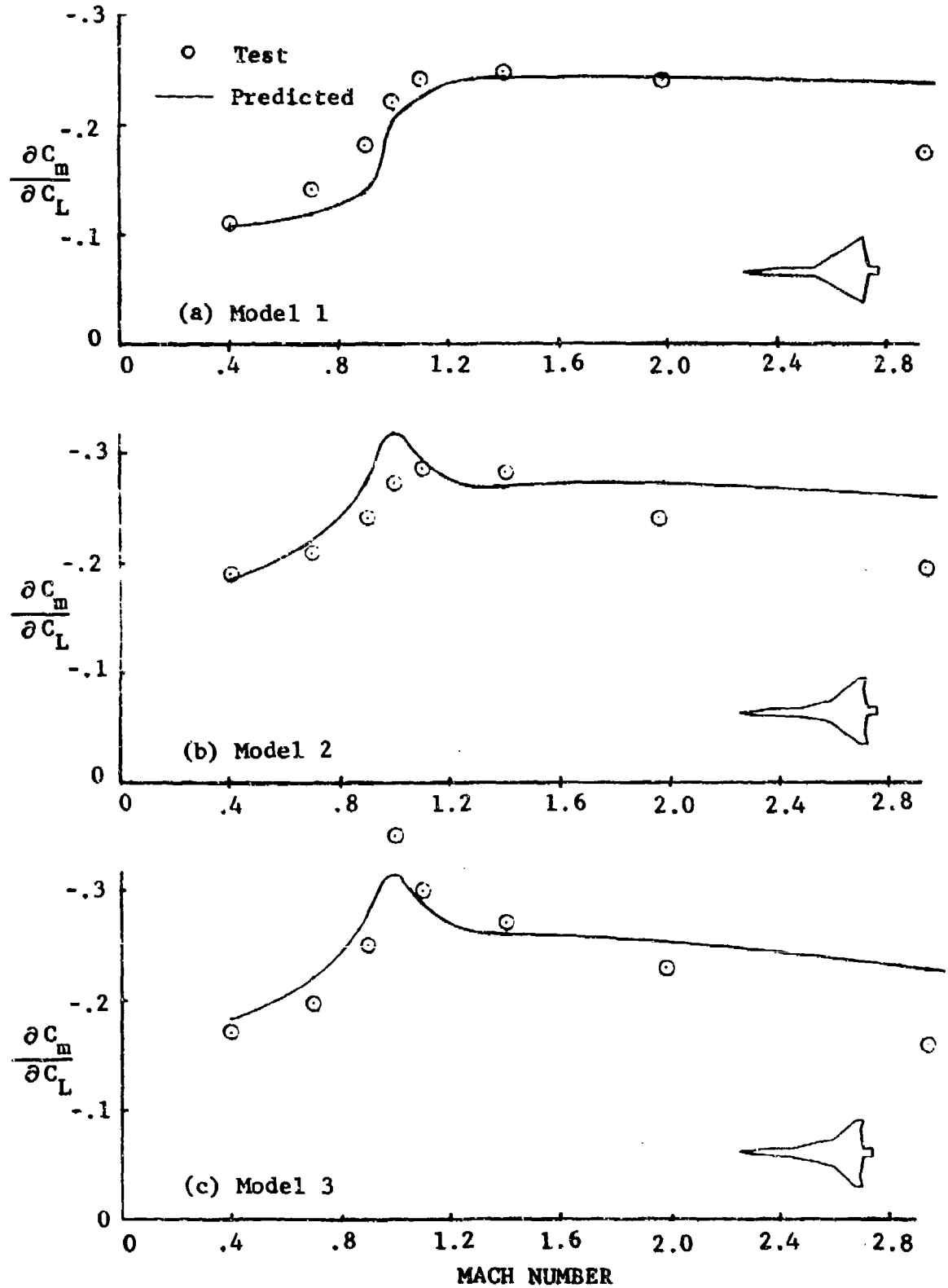

Figure 101 Pitching Moment-Curve Slope as a Function of Mach Number

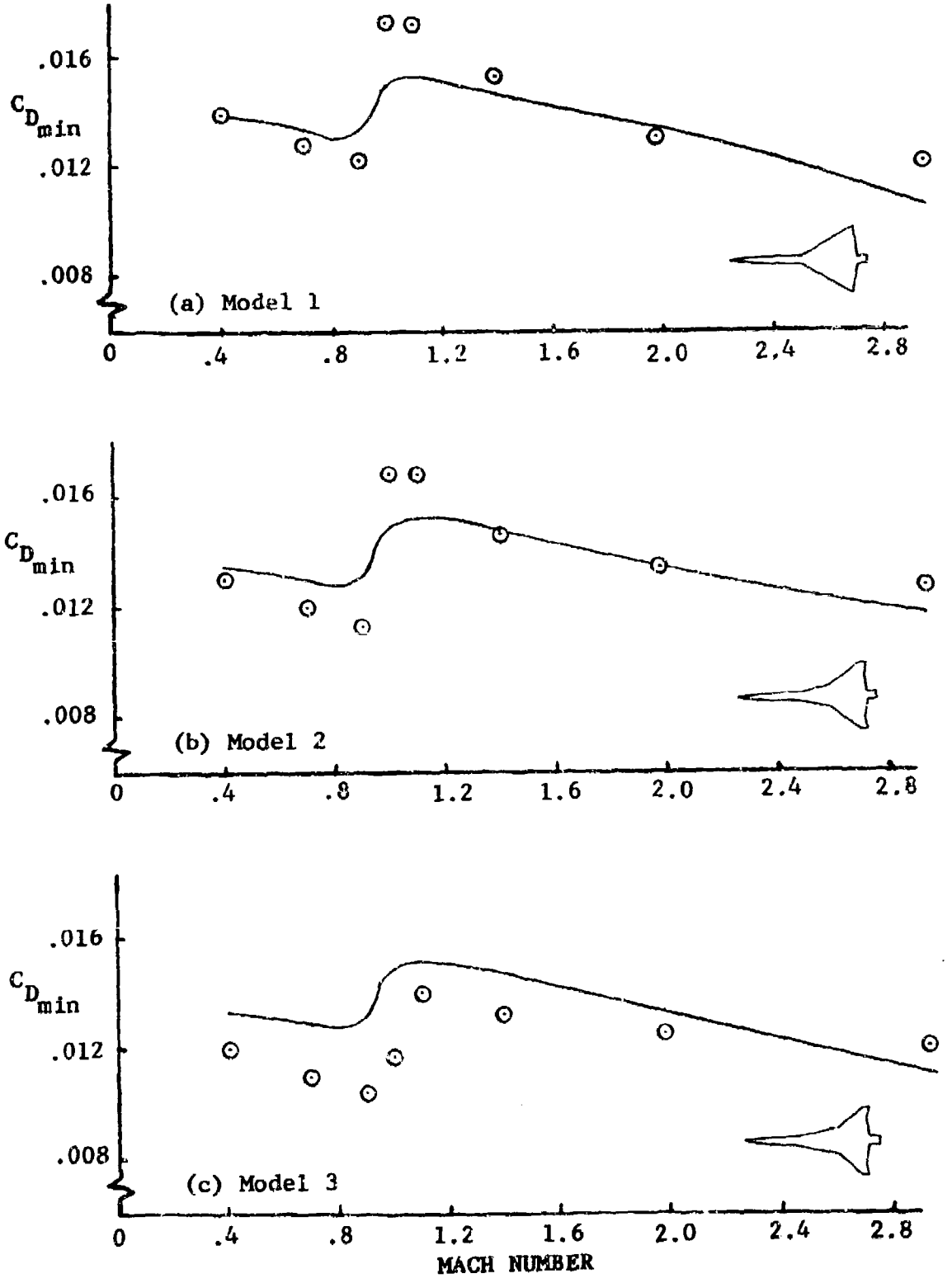

Figure 102 Minimum Drag Coefficient as a Function of Mach Number

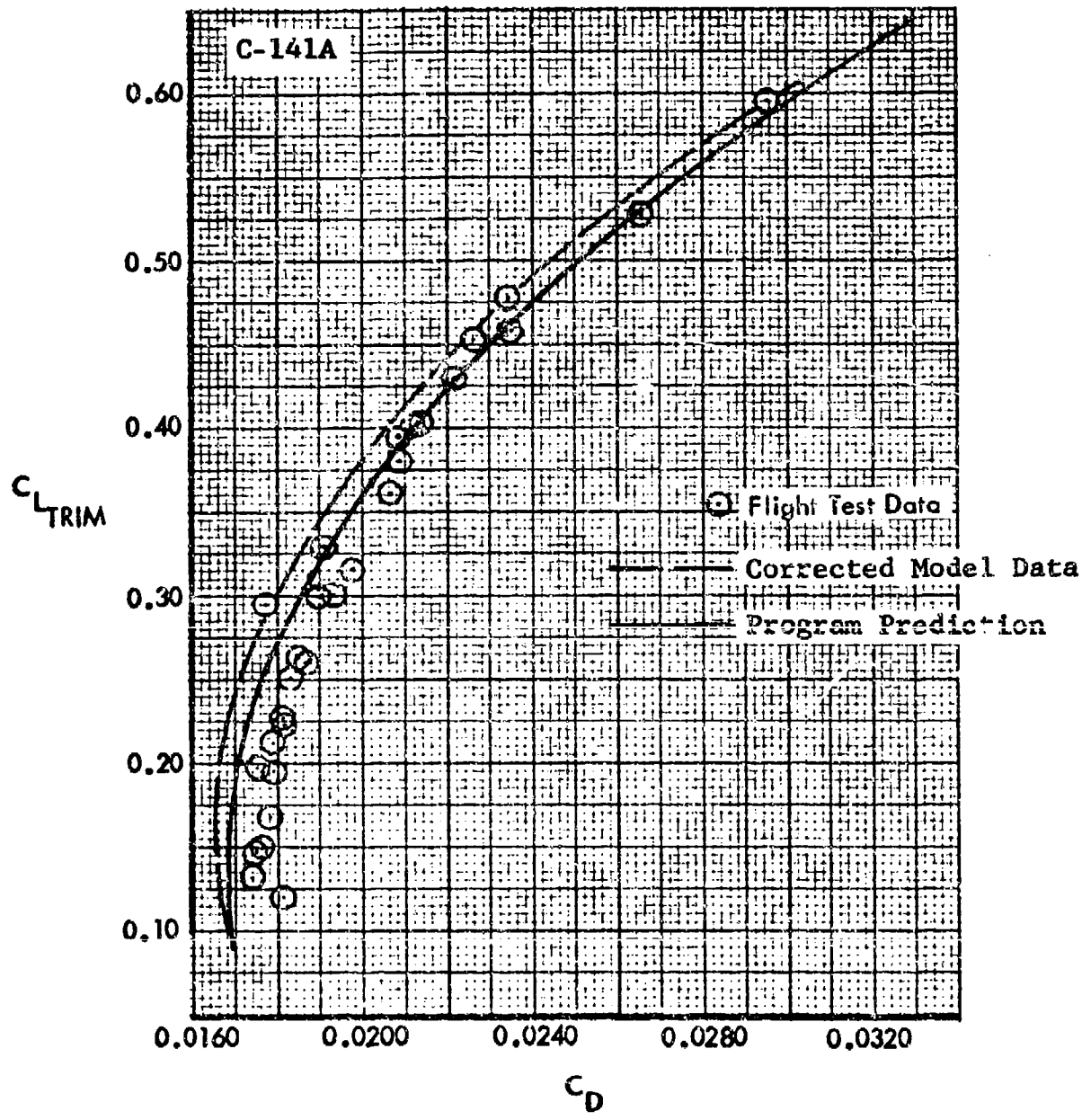

(a) M = 0.700

Figure 103 Correlation of Predicted and Flight Test Drag Polar

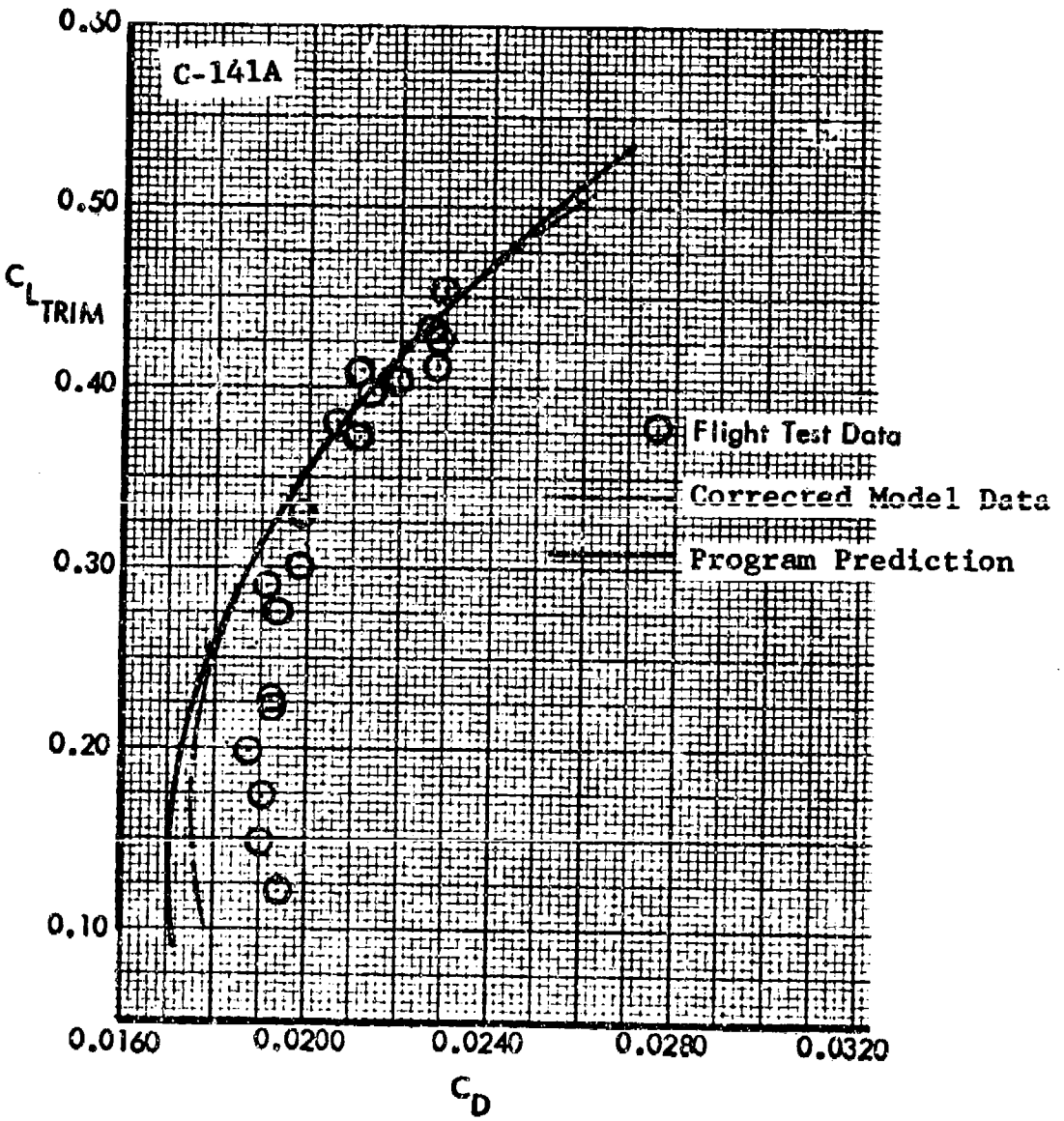

(b) M = 0.750

Figure 103 - Continued

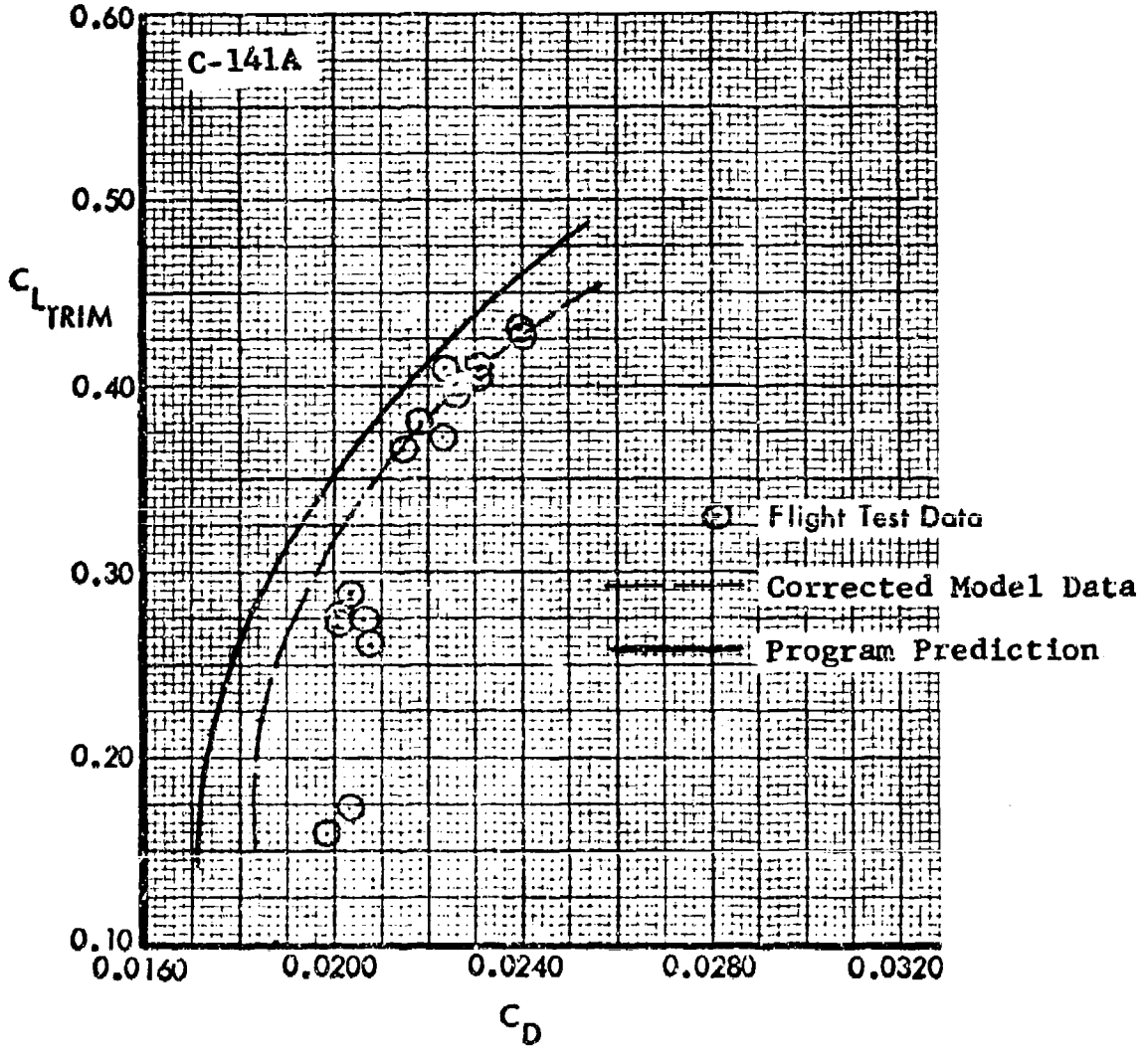

(c) M = 0.775

Figure 103 - Concluded

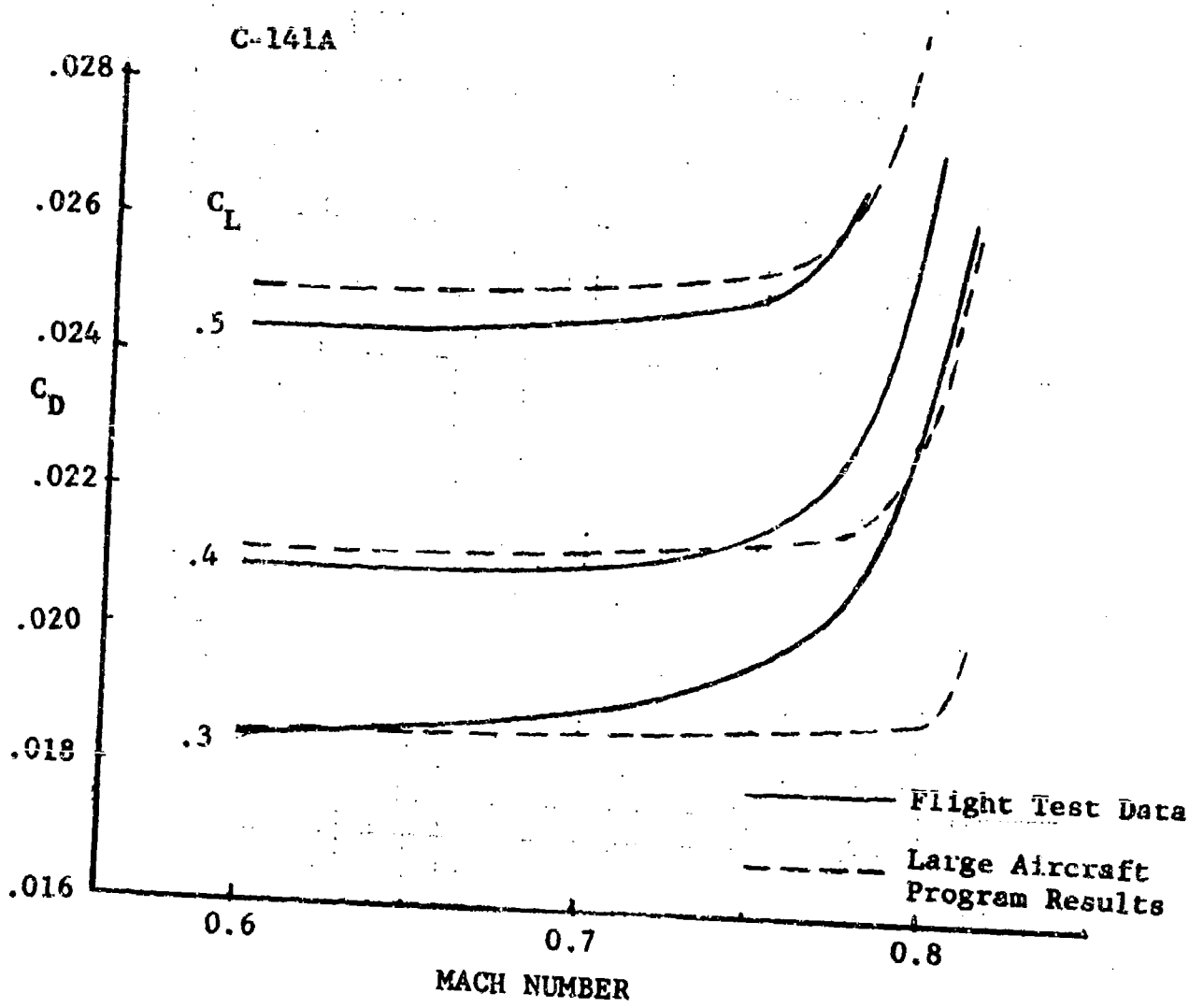

Figure 104 Drag at Constant Lift Coefficient Versus Mach Number

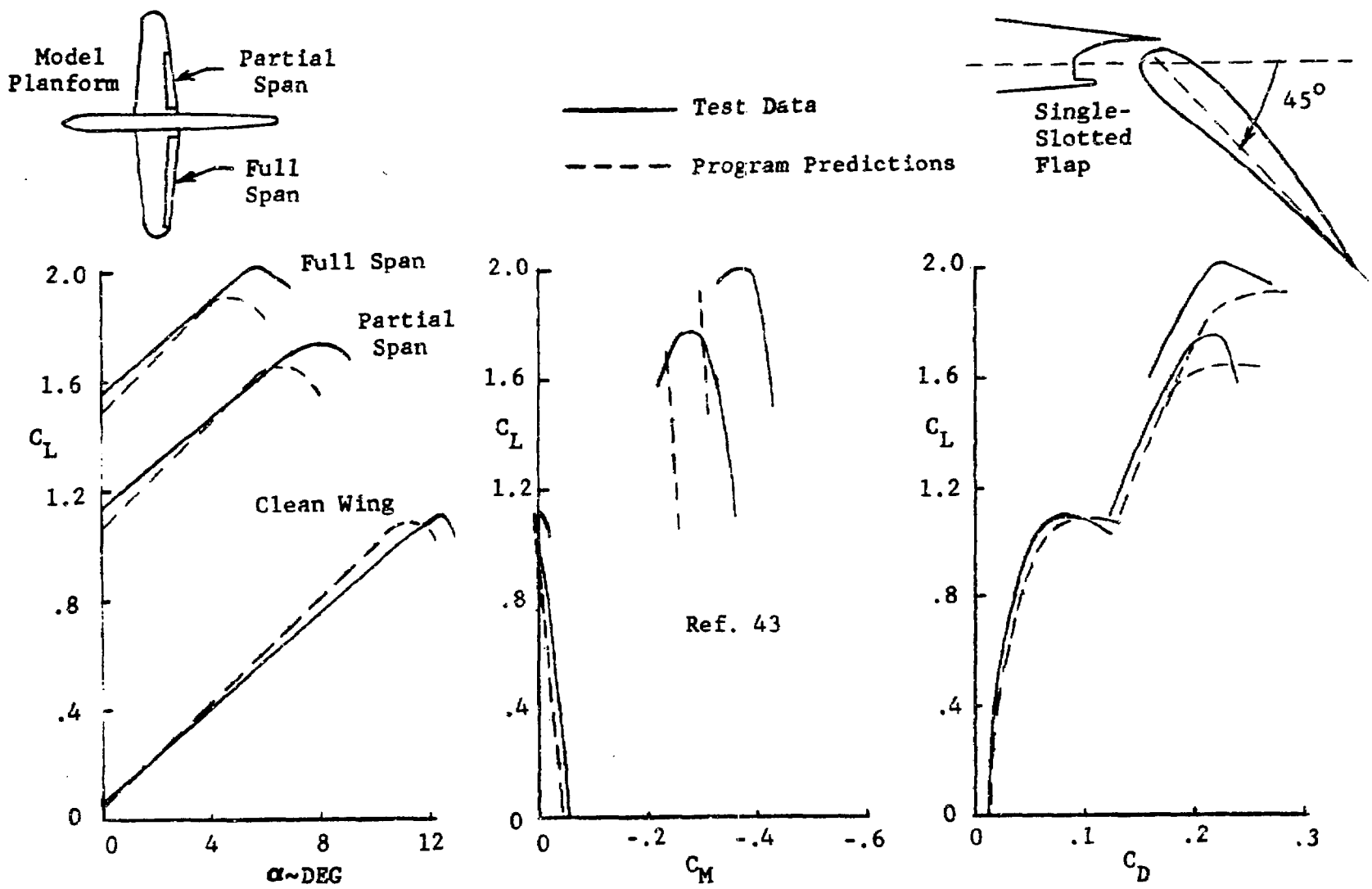

Figure 105 Comparison of Predictions with Test Data, Single-Slotted Flap

10. CONCLUSIONS AND RECOMMENDATIONS

The Large Aircraft Aerodynamic Prediction Program provides the aerodynamicist with a quick-response capability for evaluating the aerodynamic characteristics of arbitrary large aircraft or performing design trade studies. The Large Aircraft program offers a significant improvement over hand calculations based on handbook methods because:

1. The program can consider more complex relationships between geometric and aerodynamic parameters that may be neglected or not feasible in hand calculations.

2. Typical hand calculations require a long series of intermediate calculations and chart lookups that require a great deal of time to perform and are prone to error.

3. The program always performs the calculations in a consistent manner, whereas hand-calculation results may vary between individuals doing the same calculations.

Before using the Large Aircraft program to analyze an arbitrary configuration, the user should familiarize himself with the methods and operation of the program. If a similar-type configuration with test data is available, it should be evaluated first with the program so as to establish limits for credible lift, moment, and drag predictions for those types of configurations.

The modular construction of the Large Aircraft program will allow subroutines to be added or replaced to incorporate new and/or improved aerodynamic prediction procedures as they become available. Future improvements to the Large Aircraft program should extend the program to better handle fighter aircraft by including buffet predictions, transonic maneuvering devices, higher Mach numbers, etc.

REFERENCES

1. Schemensky, R. T., Preliminary Design Aircraft Lift and Drag Analysis Procedure, AeroModule V, General Dynamics' Convair Aerospace Division Report ERR-FW-1363, December 1972.

2. USAF Stability and Control DATCOM, Air Force Flight Dynamics Laboratory, October 1960 (Revised August 1968).

3. White, F. M., and Christoph, G. H., A Simple New Analysis of Compressible Turbulent Two-Dimensional Skin Friction Under Arbitrary Conditions, AFFDL-TR-70-133, February 1971.

4. Aerospace Handbook, Second Edition (C. W. Smith, ed.), General Dynamics' Convair Aerospace Division Report FZA-381-II, October 1972.

5. Hoerner, S. F., Fluid-Dynamic Drag (Published by the author, Midland Park, New Jersey, 1965).

6. Linnell, R. D., Similarity Rule Estimation Methods III, Flow Around Cones and Parabolic Noses, General Dynamics' Convair Aerospace Division Report MR-A-1059, 10 August 1955.

7. Peake, D. J., "Three-Dimensional Flow Separations on Upswept Rear Fuselages," Canadian Aeronautics and Space Journal, Vol. 15 (December 1969), p. 399.

8. Frost, R. C., and Rutherford, R. G., "Subsonic Wind Span Efficiency," AIAA Journal, Vol. 1, No. 4 (April 1963).

9. Benepe, D. B., et al., Aerodynamic Characteristics of Non-Straight-Taper Wings, AFFDL-TR-66-73, October 1966.

10. Henderson, W. P., Studies of Various Factors Affecting Drag Due to Lift at Subsonic Speeds, NASA TN D-3584, October 1966.

11. John, H., On Induced-Drag Calculation of Uncambered and Untwisted Wings as a Function of the Reynolds Number, Boeing Company Report B-819.41, March 1969 (Originally published by VFX, for GDLR Aerodynamics Colliquium, Berlin, October 1968).

12. Ray, E. J., and Taylor, R. T., "Buffet and Static Aerodynamic Characteristics of a Systematic Series of Wings Determined From a Subsonic Wind-Tunnel Study, NASA TN D-5805, June 1970.

13. Simon, W. E., et al., Prediction of Aircraft Drag Due to Lift, AFFDL-TR-71-84, July 1971.

14. A Method of Estimating Drag-Rise Mach Number for Two-Dimensional Aerofoil Sections, Royal Aero. Soc. Transonic Data Memorandum 6407, July 1964.

15. Sinnott, C. S., "Theoretical Prediction of the Transonic Characteristics of Airfoils," Journal of the Aerospace Sciences, Vol. 29, No. 3 (March 1962).

16. Method for Predicting the Pressure Distribution on Swept Wings With Subsonic Attached Flow, Royal Aero. Soc. Transonic Data Memorandum 6312, December 1963.

17. Miller, B. D., Notes on Wing Design Methods for Supercritical Airfoils, General Dynamics' Convair Aerospace Division Report ARM-061, October 1971.

18. Drag-Rise Mach Number of Aerofoils Having a Specified Form of Upper-Surface Pressure Distribution: Charts and Comments on Design, Royal Aero. Soc. Transonic Data Memorandum 67009, January 1967.

19. Lowry, J. G., and Polhamus, E. C., A Method for Predicting Lift Increments Due to Flap Deflection at Low Angles of Attack in Incompressible Flow, NACA TN 3911, 1957.

20. Spencer, B., Jr., A Simplified Method for Estimating Subsonic Lift-Curve Slope at Low Angles of Attack for Irregular Planform Wings, NASA TM X-525, May 1961.

21. Polhamus, E. C., Summary of Results Obtained by Transonic-Bump Method on Effects of Planform and Thickness on Lift and Drag Characteristics of Wings at Transonic Speeds, NACA RM L51H30, 30 November 1951.

22. Nelson, W. H., and McDevitt, J. B., The Transonic Characteristics of 17 Rectangular, Symmetrical Wing Models of Varying Aspect Ratio and Thickness, NACA RM A51A12, 10 May 1951.

23. Tinling, B. E., and Kolk, W. R., The Effects of Mach Number and Reynolds Number on the Aerodynamic Characteristics of Several 12-Percent-Thick Wings Having 35 Degrees of Sweepback and Various Amounts of Camber, NACA RM A50K27, 23 February 1951.

24. Donlan, C. J., and Weil, J., Characteristics of Swept Wings at High Speeds, NACA RM L52A15, January 1952.

25. Hoerner, S. F., The Lift of a Body-Wing Combination, Wright-Patterson Air Force Base Air Documents Division Report F-TR-1187-ND, September 1948.

26. Schemensky, R. T., Braymen, W. W., and Crosthwait, E. L., Aerodynamic Configuration Analysis Procedure, AeroModule, Version IA, General Dynamics' Fort Worth Division Report ERR-FW-931, 31 December 1969.

27. Pitts, W., Nielsen, J., and Kaattari, G., Lift and Center of Pressure of Wing-Body-Tail Combinations at Subsonic, Transonic, and Supersonic Speeds, NACA TR 1307, 1957.

28. Sherrer, H. J., Jr., and Crosthwait, E. L., The Prediction of Lift Considering Body Cross Section and Complete Configuration Planform, General Dynamics' Fort Worth Division Report AIM-261, 17 September 1969.

29. Gilman, B. G., and Burdges, K. P., "Rapid Estimation of Wing Aerodynamic Characteristics for Minimum Induced Drag," Journal of Aircraft, Vol. 4, No. 6 (November-December 1967).

30. Polhamus, E. C., "Prediction of Vortex-Lift on Leading-Edge Suction Analogy," AIAA Paper No. 69-1133, October 1969.

31. Schemensky, R. T., Prediction of the Lift Characteristics of Low Aspect Ratio Wings, General Dynamics' Convair Aerospace Division Report ARM-098, 14 November 1972.

32. Polhamus, E. C., Charts for Predicting the Subsonic Vortex-Lift Characteristics of Arrow, Delta, and Diamond Wings, NASA TN D-6243, April 1971.

33. Benepe, D. B., Analysis of Nonlinear Lift of Sharp- and Round-Leading-Edge Delta Wings, General Dynamics' Fort Worth Division Report ERR-FW-799, December 1968.

34. Küchemann, D., A Simple Method for Calculating the Span and Chordwise Loading on Straight and Swept Wings of any Given Aspect Ratio at Subsonic Speeds, A.R.C. Technical Report R&M No. 2935, August 1952.

35. Emerson, H. F., Wind-Tunnel Investigation of the Effect of Clipping the Tips of Triangular Wings of Different Thickness, Camber, and Aspect Ratio – Transonic Bump Method, NASA TN-3671, June 1956.

36. Young, A. D., The Aerodynamics Characteristics of Flaps, Royal Aircraft Establishment, Farnborough, RAE Report No. Aero. 2185, February 1947.

37. Schemensky, R. T., High-Lift Prediction Techniques, General Dynamics' Fort Worth Division Report AIM-170, 12 February 1969.

38. Hebert, J., et al., Effects of High-Lift Devices on V/STOL Aircraft Performance, USAAVLABS Technical Report 70-33A, October 1970.

39. Hebert, J., et al., STOL Tactical Aircraft Investigation, Volume II - Design Compendium, AFFDL-TR-73-21, 13 January 1973

40. Hopkins, E. J., Hicks, R. M., and Carmichael, R. L., "Aerodynamic Characteristics of Several Cranked Leading-Edge Wing-Body Conbinations at Mach Numbers From 0.4 to 2.94" NASA TN D-4211, October 1967.

41. Paterson, J. H. et al., "An Analysis of Flight Test Data on the C-141A Aircraft," NASA CR-1558, June 1970.

42. MacWilkinson, D. G., Blackerby, W. T., and Paterson, J.H., "Correlation of Full-Scale Drag Predictions with Flight Measurements on the C-141A Aircraft," Lockheed-Georgia Company Report LG73ER0058, June 1973.

43. Sivells, J. C. and Spooner, S. H., "Investigation in the Langley 19-Foot Pressure Tunnel of Two Wings of NACA 65-210 and 64-210 Airfoil Sections with Various Type Flaps," NACA TR 942, 1949.